2022

Integration of Spectroscopic and Mass Spectrometric Tools for the Analysis of Novel Psychoactive Substances in Forensic and Toxicology Applications

Travon Cooman
West Virginia University (WVU), tc0057@mix.wvu.edu

Integration of Spectroscopic and Mass Spectrometric Tools for The Analysis of Novel Psychoactive Substances in Forensic and Toxicology Applications

Travon Cooman

Dissertation submitted to the Eberly College of Arts and Sciences at
West Virginia University
in partial fulfilment of the requirements for the degree of

Doctor of Philosophy in

Forensic Science

Luis Arroyo, Ph.D., Chair

Sadie Bergeron, Ph.D.

Patrick Callery, Ph.D.

Tatiana Trejos, Ph.D.

Department of Forensic and Investigative Science

Morgantown, West Virginia

2022

Keywords: Raman spectroscopy, seized drugs, machine learning, neural networks, zebrafish, metabolism, high resolution mass spectrometry, valerylfentanyl, fentanyl

Abstract

Integration of spectroscopic and mass spectrometric tools for the analysis of novel psychoactive substances in forensic and toxicology applications

Travon Cooman

Analytical methods aiming the detection of novel psychoactive substances are continuously revised due to their utility in the seized drug and toxicology realms. One method frequently employed for the preliminary identification of illicit materials is portable Raman spectroscopy. Even when a substance in possession of an offender is identified, conclusive evidence that it may have been consumed requires additional confirmatory work and further toxicological evaluation of a biological specimen. Many times, the substance consumed may not be detected in the analyzed specimen due to its extensive metabolism. It is therefore challenging to rule out the identity of the drug ingested if metabolic studies have not been performed on a particular substance. This research aims to evaluate portable Raman as a quick, safe, non-destructive method for rapid drug analysis using the instrument's built-in algorithms and in-house machine and deep learning algorithms. Furthermore, metabolic and toxicologic studies using zebrafish and human liver microsomes are used to elucidate selected opioids.

In the first part of this research, a portable Raman instrument—TacticID was validated according to the United Nations Office on Drugs and Crime guidelines using 14 drugs and 15 cutting agents commonly encountered in seized drugs. Analysis was performed through glass and plastic packaging. In-house binary mixtures (n=64) at the following ratios—1:4, 1:7, 1:10, and 1:20 were evaluated and the results compared to direct analysis in real-time mass spectrometry (DART-MS). Whereas Raman performed better at detecting diluents which consisted of the majority in the mixtures, DART-MS resulted in higher identification for easily ionizable drugs which were present in lower percentages. To minimize the weaknesses in each technique, both methods were combined, resulting in 96% accuracy. However, analysis of 15 authentic adjudicated cases resulted in 83% accuracy using the combined methods, demonstrating the usefulness of these methods as preliminary tests over traditional subjective techniques as color tests.

In instances where a portable Raman instrument is used for drug screening, its accuracy as a single technique is crucial. In this study, the correct identification of the instrument detecting both drug and diluent in binary mixtures was 19%. Therefore, machine and deep learning methods such as naïve bayes, k-nearest neighbors, support vector machine, random forest, neural network (NN), and convolutional neural networks (CNN) were explored as alternatives to the instrument's built-in hit quality index algorithm. The findings in this research demonstrated NN and CNN superior to the other algorithms, increasing the correct identification of both compounds to 65 and 64%, respectively. Furthermore, ternary and quaternary mixtures were simulated using data augmentation methods and 100% accuracy was observed with CNN models. Similar accuracies were observed when the substances were reported by their drug classes. This work demonstrated

how the contribution of machine learning can help improve the accuracy of analytical instruments outputs, thereby increasing confidence in compounds reported.

In the second part of this research, zebrafish which share 70% of gene similarity to humans, were used as a toxicity model to provide information about drug effects on a living system. Fentanyl was selected as a model drug and zebrafish (0 – 96 hours post fertilization) were dosed at 0.01 – 100 µM. Major dose dependent phenotypic effects included pericardial malformations, spine and yolk extension malformation, all of which inhibited the normal growth and development of the larvae. This has laid the foundation for future studies to understand the mechanisms of action. Furthermore, three metabolites—4-ANPP, norfentanyl, and β-hydroxyfentanyl, were detected in the zebrafish assay. All the observed metabolites have been reported in human specimens.

The final aim of this work was to elucidate an uncharacterized opioid—valerylfentanyl using zebrafish and human liver microsomes as a comparative model. Although valerylfentanyl carboxy metabolite is sold as a metabolite, a complete metabolic study was not found in the literature. Therefore, the well-studied microsome model was used to compare the results to zebrafish (30 days post fertilization). Although 19 metabolites were detected in the microsome model, and fewer in the zebrafish assay, the major marker metabolite valeryl norfentanyl was consistent in both studies, demonstrating zebrafish can be used to study opioid metabolism.

Acknowledgements

My journey in graduate school started with Dr. Suzanne Bell encouraging me to pursue a doctoral degree but it would have been impossible without support from my key research advisor, mentor and friend Dr. Luis Arroyo who welcomed me to the Arroyo Research Group in 2019. I am grateful to him for always challenging me to explore new areas of forensic science that helped me gain skills I thought might have been beyond my own capabilities.

I am thankful to my committee members Dr. Tatiana Trejos, Dr. Sadie Bergeron, and Dr. Patrick Callery for providing guidance and feedback throughout the duration of this project. Their dedication and time investment will forever be appreciated.

I will forever be grateful to Dr. Aldo Romero for challenging me to explore as many machine learning techniques as possible to process Raman data. Other collaborators who made this project possible included Dr. Edward Sisco of the National Institute of Standards and Technology, Ms Amber Burns of the Maryland State Police, Dr. Piero Gardinali and Dr. Natalia Quinete of Florida International University. I am thankful for their valuable input.

Personnel of Dr. Sadie Bergeron and Dr. Eric Horstick Zebrafish Laboratories at the West Virginia University including Heather Price, Dr. Rebecca Coltogirone, Alexandra Schmidt, and Casey Showman were extremely helpful and patient with me as I learned zebrafish husbandry and setting up our own zebrafish satellite facility and I am thankful to them. I also appreciate the zebrafish microinjection training and tips from Dr. Brittany Seman. I am sincerely thankful to my undergraduate researchers Brianna Sauvé, Brianna Hoover, Katherine Davis, and Collin Kustera who were diligent in assisting in fish care and data analysis, and my lab mates—Alexis Wilcox, Colby Ott, Dr. Joseph Cox, Kourtney Dalzell, Kylea Mathison, and Sharon Kalb who contributed to the success of this project.

This research would have also been impossible without funding through the National Institute of Justice, National Science Foundation Major Research Instrumentation Program, and support from Dr. Casper Venter and the Forensic and Investigative Science Department at the West Virginia University.

Finally, I thank God for preserving me, keeping me enthusiastic about the impact of this research in the field of forensic science, and for His grace in completing my graduate studies. I am most grateful to my family and loved ones who always provided encouraging words and wishes during this journey.

Table of Contents

Table of Figures

List of Tables

List of Symbols, Abbreviations

4-ANPP	4-anilino-N-phenethylpiperidine
4-MEC	4-methylethcathinone
4-MMC	4-methylmethcathinone
Adam	Adaptive moment estimation
ANOVA	Analysis of variance
ARRIVE	Animal Research Reporting of In Vivo Experiments
BB22	1-(cyclohexylmethyl)-1H-indole-3-carboxylic acid 8-quinolinyl ester
BH	Benjamini and Hochberg
$CaCl_2$	Calcium chloride
CNN	Convolutional neural network
CV	Coefficient of variation
CYP	Cytochrome P450
Da	Dalton
DART-MS	Direct analysis in real time mass spectrometry
dpf	days post fertilization
FDR	False discovery rate
FFT	Fast Fourier transformation
F_n	False negative
FN	False negative
F_p	False positive
FP	False positive
FTIR	Fourier Transform Infrared
Fu-BAP	Furanoyl-1-benzyl-4-anilinopiperidine
GC-MS	Gas chromatography mass spectrometry
HEPES	4-(2-hydroxyethyl)-1-piperazineethanesulfonic acid
HLM	Human liver microsomes
hpd	hours post dosing

HQI	Hit quality index
HRMS	High-resolution mass spectrometer
HSD	Honestly significant differences
JWH-122	(4-methyl-1-naphthalenyl)(1-pentyl-1H-indol-3-yl)-methanone
KCl	Potassium chloride
kNN	k-nearest neighbors
LDA	Linear discriminant analysis
MDMA	Methylenedioxymethamphetamine
$MgSO_4$	Magnesium sulfate
MLA	Machine learning algorithm
MRM	Multiple reaction monitoring
MS-222	Tricaine
MSP-FSD	Maryland State Police Forensic Sciences Division
NaCl	Sodium chloride
NADPH	Nicotinamide adenine dinucleotide phosphate
NB	Naïve bayes
NMR	Nuclear magnetic resonance
nM	Nano Molar
NN	Neural network
NSO	Novel synthetic opioids
OECD	Organization for Economic Cooperation and Development
P	Precision
PB-22	1-pentyl-1H-indole-3-carboxylic acid 8-quinolinyl ester
PCA	Principal component analysis
PEG	Polyethylene glycol
QqQ	Triple quadrupole mass spectrometer
R	Recall
ReLU	Rectified Linear Unit
RF	Random forest
RT	Retention time
SERS	Surface enhanced Raman spectroscopy

SORS	Spatially offset Raman spectrometer
SVM	Support vector machine
SWGDRUG	Scientific Working Group for the Analysis of Seized Drugs
THC	Δ^9- Tetrahydrocannabinol
TL	Tupfel long-fin
T_n	True negative
TN	True negative
TNR	True negative rate
T_p	True positive
TP	True positive
TPR	True positive rate
UDPGA	Uridine 5'-diphosphateglucuronic acid
UNODC	United Nations Office on Drugs and Crime
ww PTFE	Water wettable hydrophilic polytetrafluoroethylene

Introduction

Novel psychoactive substances (NPS) have flooded the illegal market over the last decade and pose a challenge for their detection by forensic chemists and toxicologists. Their extensive metabolism, lack of metabolite elucidation, and limited availability of standards suggest that these emerging drugs of abuse can go undetected or unconfirmed using existing screening technologies. Even when some NPS and other drugs of abuse have been thoroughly studied and reported in the literature, it may take several months for a crime lab to finalize casework due to the limited number of certified reference materials for these chemical entities and their metabolites. The incorporation of a fast, easy, and accurate onsite method for screening these substances and knowledge of their metabolism can help decrease case turnaround times.

This research project aims to develop a comprehensive study in two critical areas: seized drug analysis in forensic chemistry, and drug metabolism of NPS within forensic toxicology. Chapter 1 focuses on utilizing a portable Raman instrument to screen common drugs of abuse and diluents in seized drugs mixtures. To improve the accuracy of the portable Raman instrument, selected machine learning techniques are discussed in chapter 2. Chapter 3 presents zebrafish as a toxicology and metabolism model for fentanyl, and chapter 4 extends this knowledge to valerylfentanyl by comparing human liver microsomes data to zebrafish.

Current methods for onsite drug screening include color tests [1, 2], mass spectrometry [3], and electrochemistry [4], amongst others [5]. Whereas many of these methods require opening packages for sampling, putting operators at risk of exposure, Raman spectroscopy is capable of through packaging analysis. Raman spectroscopy, a well-established, nondestructive technique used to analyze drugs of abuse, is the study of inelastic scattering of UV, visible or near infrared light. When light strikes a molecule, elastic—no change in photon frequency and inelastic scattering—shift in photon frequency, occurs. Inelastic scattering of radiation was experimentally discovered by Chandrashekhara Venkata Raman in 1928 [6, 7] and it is the principle on which Raman was developed. When light in the ultraviolet or visible spectrum strikes a molecule, an electronic transition occurs as shown in **Figure 1**. For a molecule to absorb light, the energy of the light must be equivalent to the energy band gaps. Light in the mid-IR range (2.5 to 49 μm) causes molecules to vibrate through a stretching or bending motion. Depending on the structure of the molecule, it may undergo symmetric or asymmetric stretching as shown in **Figure 2**, or any of the

four bending modes–scissoring, rocking, wagging, and twisting, as shown in **Figure 3**. Stretching modes usually have higher energy than bending modes and are denoted by ν and σ respectively [8]. Molecules excited to a virtual energy state may scatter light back to the ground state at the same frequency as the incident light, this phenomenon is called Rayleigh scattering. Rayleigh scattering is usually more intense and is filtered in Raman spectrometers. When molecules gain vibrational energy, the resulting scattered light is higher than that of the incident light giving rise to anti-Stokes Raman scattering [6]. Stokes- Raman scattering, a fairly weak process, results when molecules are excited to a virtual state, attain an induced dipole and emit photons at a different frequency than that of the incident light as shown in **Figure 1**.

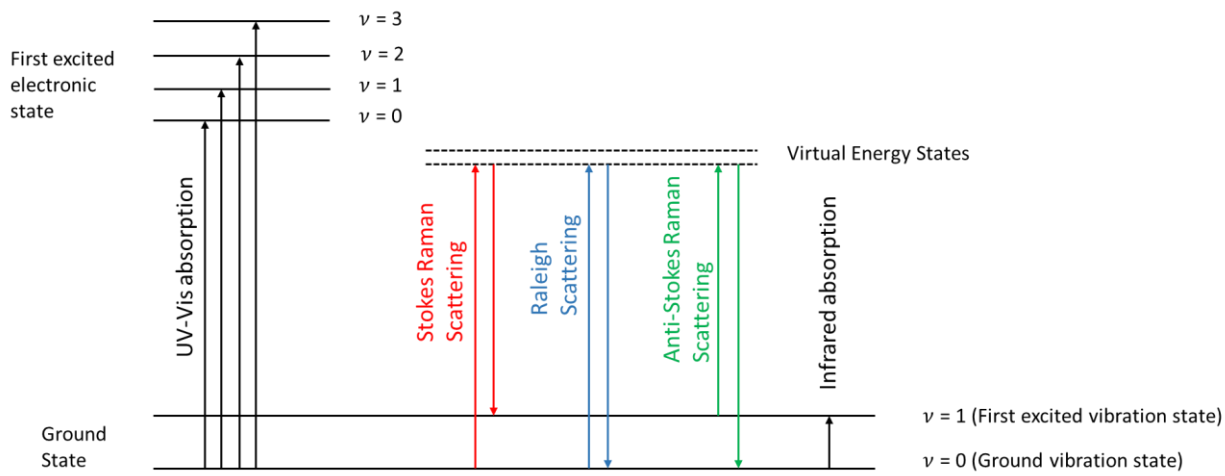

Figure 1. Diagram showing the excitation of molecules in the presence of visible light and infra-red light.

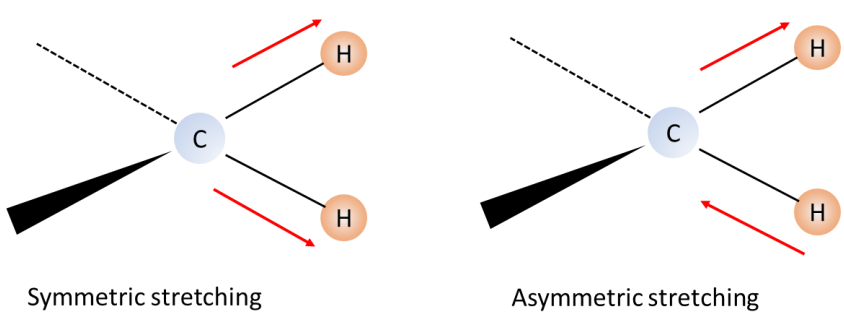

Figure 2. Different modes of stretching for a CH_2 group.

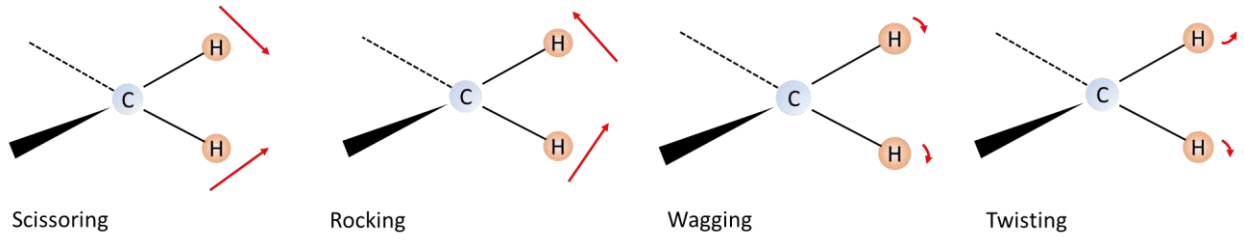

Figure 3. Different modes of bending for a CH_2 group.

The two major Raman techniques are Dispersive and Fourier Transform (FT) Raman spectroscopy. Dispersive systems filter scattered light through a notch filter or edge filter and removes the laser line. The light is shone on a diffraction grating where the wavelengths of scattered light are separated and focused on a detector–usually a Peltier cooled charge-coupled device (CCD) array detector. Fourier Transform systems contain an interferometer which allows for a fast, simultaneous measurement of all frequencies and result in an interferogram which is converted to a spectrum using Fast Fourier Transformation calculations performed by the software. FT- Raman systems use a 1064 nm laser as the excitation source to minimize fluorescence whereas dispersive systems use a 785 nm laser. Lasers are selected based on their excitation efficiency, and fluorescence capabilities. Raman scattering is inversely proportional to the fourth order of excitation wavelength (λ^{-4}) implying lasers with shorter wavelengths are more efficient and sensitive than longer wavelengths [9]. The scan time is also shorter when short wavelength lasers are used.

The major drawbacks of Raman spectroscopy include: the occurrence of photodecomposition–where the sample is destroyed before data is obtained making dark samples unsuitable for analysis, and Raman signals are masked by the background and fluorescence interfering with analysis. A background spectrum is not normally required as this is a scattering technique unlike when Fourier Transform Infrared spectroscopy is used. However, Raman spectroscopy is considered a Category A technique by the Scientific Working Group for the Analysis of Seized Drugs indicating it has the highest discriminatory power [10]. Raman is highly selective, provides specific functional group information, does not interfere with water, allowing for analysis of aqueous samples, and provides rapid analysis.

The construction of low-cost, battery-powered, portable Raman spectrometers have increased the versatility of Raman [11]. For example, portable devices have been used in the analysis of explosives [12], drugs [7, 13], paints [14], and inks [15] due to very little to no sample preparation being required for testing. Portable Raman instruments have also been used at ports of entry for the identification of chemicals and biohazards using a non-contact approach in comparison to ion mobility spectroscopy and other techniques which require contact with these substances [13, 16]. A noncontact approach helps reduce exposure risks to workers. Although drugs such as cocaine, amphetamine, and methylenedioxymethamphetamine (MDMA) have been studied with portable Raman systems, novel psychoactive substances and mixtures have been a challenge to identify. To successfully identify a compound, it must first be present in the instrument's library, and the search algorithm must be accurate and account for mixtures and other interferences. Novel psychoactive substances can be structurally similar to each other, and although the change in one functional group can result in unique spectra, there is a need for it to be evaluated.

Therefore, the main goal of chapter 1 was to evaluate the performance of a portable Raman instrument—TacticID as a screening technique, through analysis of pure powdered substances, mixtures and adjudicated cases. Fifteen common drugs of abuse and 15 diluents were analyzed as pure substances and mixtures comprising of various ratios after validating the instrument. The accuracy through glass and plastic packaging was 91% and 89%, respectively. A subset of the samples was analyzed using direct analysis in real time mass spectrometry (DART-MS) and when combined with the Raman data, the accuracy increased to 96%. Analysis of authentic case samples resulted in 83% correct identification when the two techniques were combined, hence providing a rapid and accurate method for drug screening. Chapter 1 was published in the Journal of Forensic Chemistry.

The limitations of portable Raman instruments continue to make it a challenge in forensic science. Some limitations include: its low sensitivity to drugs in small concentrations, fluorescence from samples interfering with signals, unsuitable for dark samples and complex matrices, fluctuation from the laser source, and its limited use for qualitative analysis [17]. Chemometrics and machine learning have sought to improve some of these challenges especially the analysis of multicomponent mixtures. Guirguis used principal component analysis (PCA)—a data reduction and exploratory technique as a classification method for the analysis of NPS using a hand-held

Raman with a 1064 nm laser and reported 89% correct classification [18]. Omar et al also used PCA to distinguish fentanyl, cathinone, and synthetic cannabinoids in seized Customs samples by comparing three hand-held Raman instruments—Progeny (1064 nm laser), Cora 5600 (1064 nm laser) and Bravo (785- 1000 nm laser) but did not provide classification rates although each drug class formed separate clusters [19]. Weng et al used PCA followed by discriminant algorithms to classify methamphetamine and 3,4-methylenedioxy methamphetamine with accuracy >95% using surface-enhanced Raman spectroscopy [20]. Although the selected algorithm can affect misclassification rates, preprocessing of the data is important as spectral peak overlap, fluorescence, and variable Raman intensities can influence this process. O'Connell et al reported correct classification rates of about 90% after using the first derivative of the Raman spectrum as a preprocessing technique [21].

Simple methods such as PCA or linear discriminant analysis do not perform as well with mixtures which are commonly encountered in seized materials. Therefore, chapter 2 builds on the research in chapter 1 and focuses on methods that can improve detection of compounds by portable Raman instruments. A database was created containing simulated binary, ternary, and quaternary mixtures. This data was used to explore machine learning algorithms to classify compounds by their drug class and drug name. The models improved the correct classification of binary mixtures from 19% using the instrument's hit quality index algorithm to 64% using convolutional neural networks. Therefore, incorporating machine learning algorithms in portable instruments, can improve the detection of unknown substances with high accuracies. Chapter 2 was published in Chemical Physics Letters.

Although Raman spectroscopy can be used to detect NPS, their metabolism and toxicity are not always extensively studied. Therefore chapters 3 and 4 discusses zebrafish as an alternative drug metabolism and toxicology model. Zebrafish (*Danio rerio),* one of 45 *Danio* species are a small teleost (3-4 cm) first used in genetic studies in the 1980s [22]. The name is derived from the stripes on the side of their body. They are typically found in standing or slow-moving water such as ponds, lakes, ditches or rice paddies [23–25]. Zebrafish exhibit a circadian pattern of daytime activity and night-time rest similar to mammals; and possess all the classes of senses—taste, touch, smell, balance, vision, and hearing [26]. Their natural diet consists mainly of zooplankton and insects [27] and they are surface feeders. At 5 days post fertilization (dpf) they can feed on their own,

using pharyngeal 'jaws' with tooth rows in the back of the throat. Zebrafish are broadcast spawners that release eggs and sperm in a cloud over a substrate [28]. A female generally produces around 100 transparent eggs 1.0 to 1.5 mm in a single spawning [29]. **Figure 4** shows the different stages of the zebrafish life cycle. At 0- 72 hours post fertilization (hpf)—embryos, 72 hpf to 13 dpf—early larvae, 14 dpf to 29 dpf—mid larvae, 30 dpf to 3 or 4 months—adults [30].

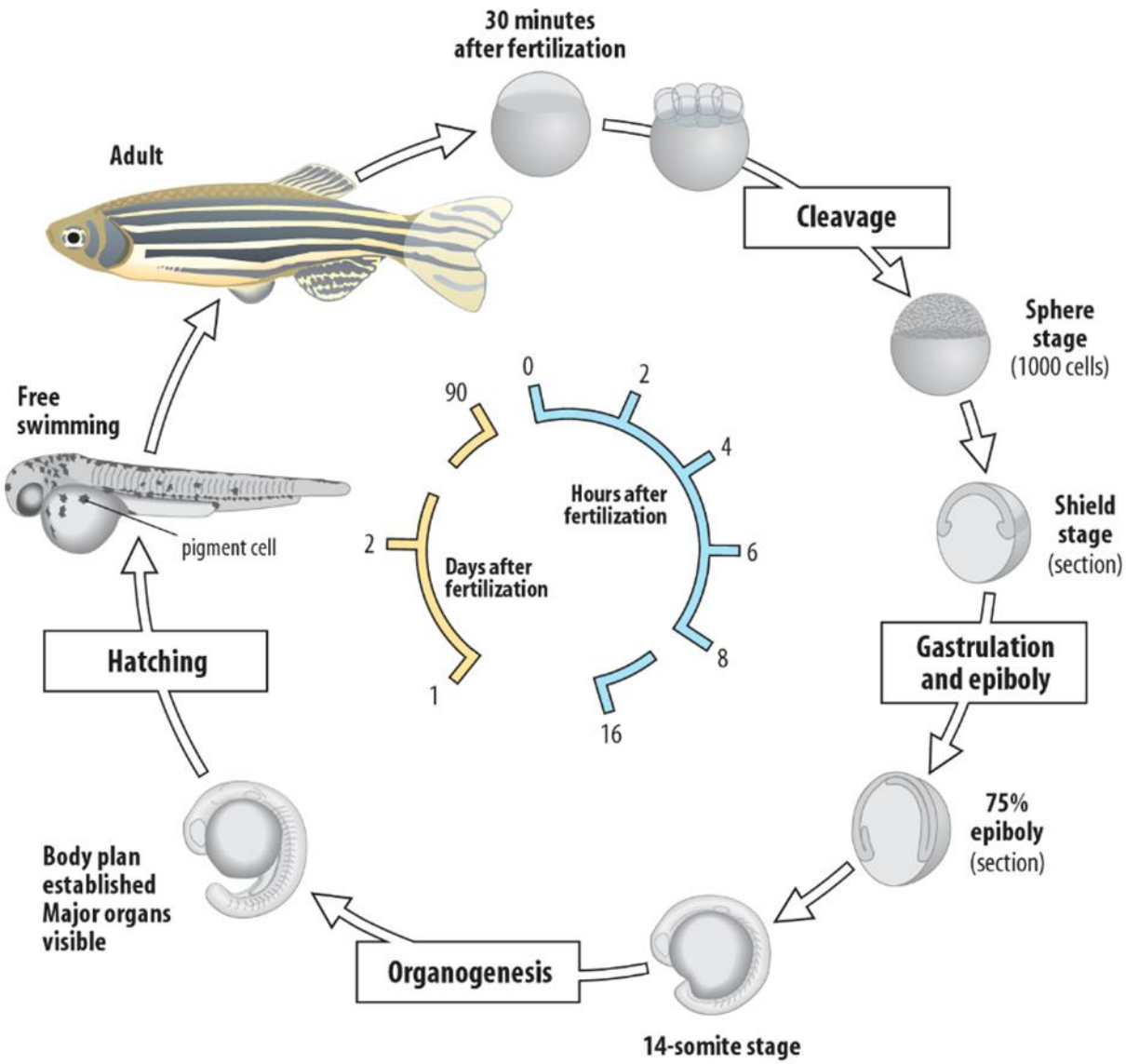

Figure 4. Zebrafish developmental stages (adapted from http://www.mun.ca/biology/desmid/brian/BIOL3530/DEVO_03/ch03f09.jpg)

Their small size, high reproductive rate [31], low cost and easy maintenance make zebrafish a rapidly increasing model to study toxicity and *in vivo* drug metabolism. Assessment of toxicity is critical for drug discovery and scheduling of NPS. Zebrafish embryo is accepted as a toxicity test [32, 33] and is used to determine acute toxicity of chemicals on embryonic stages of fish—maximum tolerated concentration. This concentration can be used for dosing regimens since therapeutic concentrations for humans may not necessarily be the same in zebrafish. Additionally, dosing embryos until 96 to 120 hpf has been performed to evaluate developmental defects in zebrafish and used as a model to predict toxicity in humans. Zoupa and Machera evaluated the effects of triadimefon—a fungicide used in agriculture by measuring several effects in zebrafish—hatching rate, body length, spinal defects, heart shape and other deformities, and compared their findings to previous studies in mammals [34]. Cornet et al., developed an assay to predict the cardiotoxicity, neurotoxicity and hepatotoxicity for twenty compounds with known effects in humans by exposing observing developmental defects and mortality rates of embryos exposed to drugs of varying concentrations. Specificity was reported as 89%, sensitivity was 68%, and accuracy, 78%, confirming zebrafish embryo assays are promising to extend toxicity to humans [35]. Gonzalez-Nunez and Rodriguez performed developmental studies which demonstrated zebrafish expressed opioid receptors fundamentally similar to those found in mammals and can be extrapolated to higher vertebrates but did not perform toxicity studies [36].

The complexities of rodent and mammalian models for *in vivo* drug metabolism have resulted in alternative models being explored. The zebrafish model has been used for both targeted—known metabolites monitored and untargeted—comprehensive, metabolomics—study of metabolite profiles [37]. Metabolomics have been combined with analytical techniques such as gas chromatography- mass spectrometry (GC/MS), and nuclear magnetic resonance (NMR), but liquid chromatography high-resolution mass spectrometry has been most useful in evaluating metabolic profiles since it provides higher sensitivity and mass accuracy information of compounds as metabolites are in low concentrations and most times unconfirmed without reference standards.

Zebrafish contain cytochrome P450 (CYP) enzymes and approximately 70% of human genes have a zebrafish orthologue [38], suggesting metabolic profiles from zebrafish may be similar to mammals. However, differences have been observed in metabolites in zebrafish and humans. For example, Jones et al., investigated the metabolism of ibuprofen in zebrafish larvae and reported

the absence of carboxy-ibuprofen and the glycoconjugate metabolites observed in human [39]. In another study by Chng et al., the differences between zebrafish liver microsomes, human liver microsomes and zebrafish larvae were observed [40]. The major metabolite in larvae was 6β-hydroxytestosterone and unique metabolites of zebrafish were observed only in zebrafish. Differences are expected because the enzymes in zebrafish may interact with certain substrates differently since the genetic makeup is not a complete match to humans.

There is wide variability in the stage of zebrafish development when metabolism studies are performed. The age of zebrafish used in previous studies include 4 dpf [41], 5 dpf [32, 40], and 3 to 8 months [42, 43]. Studies report that zebrafish liver—a major site for metabolism, starts developing 24 hpf and is complete between 3 and 5 dpf [44, 45] and cytochrome P450 activity dramatically increases at 3 dpf [46]. **Figure 5** shows the difference in the size of the liver in larvae and an adult. Verbueken et al., compared the drug metabolizing capability of embryos from 5 hpf to 120 h and compared the results with zebrafish liver microsomes and adult zebrafish assays [47]. The authors reported that zebrafish embryos have poor CYP- related metabolizing capacity with benzyloxy-methyl-resorufin—a mammalian CYP substrate but this statement needed to be evaluated with other CYP substrates. Considerations for the age of zebrafish are important because in some countries larvae are not considered animals until 120 hpf or when they develop independently feeding capacity [48]. Studies which focus on early stage (<96 hpf) zebrafish metabolism result in a shorter wait time for results compared to waiting >30 days for the fish to become adults before performing metabolism studies. However, the capability of both larvae and adult zebrafish for metabolism studies have been demonstrated.

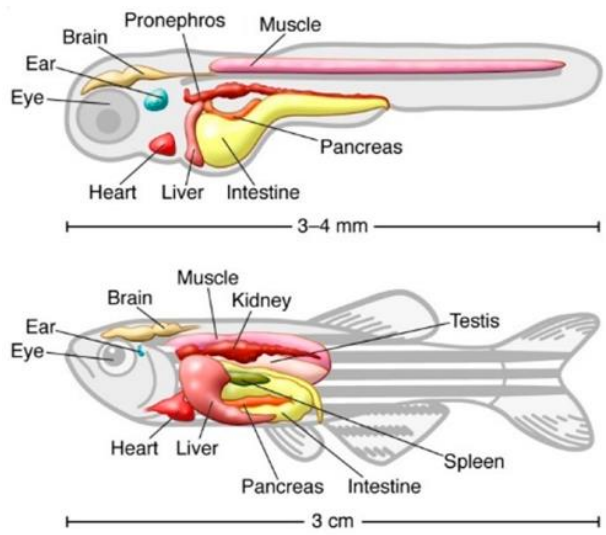

Figure 5. General anatomy of a larval—3 to 5 dpf (top) and adult (bottom) zebrafish (adapted from Santoriello and Zon [49]).

The incubation time, dosing methods and number of zebrafish are also variable. Rodrigues Matos et al., used 18 adult zebrafish dosed via bath application and collected water samples for analysis of xylazine metabolites at 0, 1, 3, 6, 24, 48, 72, 96, 120, 144, 168 hours [43]. In a similar experiment with stanozolol and sibutramine, de Souza Anselmo et al. used 12 adult zebrafish [50]. Richter et al. used ten 4 dpf zebrafish and administered the drug via microinjection in the yolk sac and analyzed the incubation media and zebrafish tissue after 24 hours [41]. In another study, 16 5-dpf larvae were dosed with meta-chlorophenylpiperazine (mCPP) and collected 0.25, 1, 3, 6, 8, and 10 hours after exposure [32]. Although bath application seems to be the easiest method of dosing, the solubility of the drug must be evaluated, and it must be ensured that most of the drug does not adhere to particles in the water. Microinjection requires personnel training, but this is the only method to ensure the fish receives the desired dose.

Like other models, zebrafish models have their limitations. There are substantial differences in organ/ body size between zebrafish and mammals, the differences in the biological environment may affect metabolism, the mode of drug delivery does not always reflect the method of intake by mammals, and zebrafish are maintained at a lower temperature than mammals [37].

The most common *in vitro* models used to evaluate the pharmacodynamics and pharmacokinetics of drugs in humans include hepatocytes and human liver microsomes (HLM). Hepatocytes, or liver cells play a key role in detoxification and biotransformation of xenobiotics and contain both phase

I and II enzymes. However, they are expensive, difficult to obtain, and the isolation of viable cells is challenging [51]. HLMs are subcellular fractions derived from the endoplasmic reticulum of hepatic cells after liver homogenization and differential centrifugation [52, 53]. Although they contain mainly phase I enzymes, uridine diphosphate glucuronic acid (UDPGA) can be added to the assay to observe phase II enzymes conjugation [54]. The list of enzymes in HLMs include cytochrome P450s, flavin monooxygenases, carboxyl esterases and epoxide hydrolase, and UDP glucuronyl transferases. The low cost, easy, multiple use from freeze-thaw cycles, high stability of enzymes after being stored for many years make HLMs a good model. In addition to metabolic data, microsomes can also provide half-life data which can be used to optimize incubation times for metabolism.

Therefore, chapter 3, focuses on using early-stage zebrafish larvae to assess the toxic effects of fentanyl and to evaluate the larvae's ability to metabolize fentanyl. Fertilized eggs were exposed to fentanyl concentrations ranging from 0.01 to 100 µM and observed until 96 hours. Phenotypic observations for toxicity included egg coagulation, somite formation, heartbeat, tail and yolk morphology, pericardial formation, and swim bladder inflation. The incubation media was analyzed for the presence of metabolites using a targeted metabolomics approach. Fentanyl concentration caused significant effects on survival and development, with notable defects to the tail, yolk, and pericardium at 50 and 100 µM. Despropionyl fentanyl (4-anilino-*N*-phenethylpiperidine, 4-ANPP), β-hydroxy fentanyl, and norfentanyl were detected in zebrafish larvae. Chapter 3 was published in the Journal of Applied Toxicology.

The metabolism of valerylfentanyl—a novel synthetic opioid, less potent than fentanyl, is elucidated in chapter 4. Although valerylfentanyl is less potent than fentanyl, it was previously detected in postmortem samples [55, 56], but its metabolism was not elucidated in the literature. An *in vitro*—HLM model was compared to an *in vivo*—zebrafish model. Nineteen metabolites were detected with *N*-dealkylation as the most abundant metabolite—valeryl norfentanyl being observed followed by hydroxy valerylfentanyl. The major metabolites in HLM were also detected in 30 dpf zebrafish. An authentic liver specimen which tested positive for valerylfentanyl, among other opioids and stimulants, revealed the presence of a metabolite which shared transitions and retention time as the hydroxylated metabolite of valerylfentanyl but could not be confirmed

without reference standards. 4-ANPP—a common metabolite to other fentanyl analogues was also detected. Chapter 4 was published in Drug Testing and Analysis.

The overall contribution of this work has: (1) highlighted the importance of validating portable instruments for seized drug analysis and demonstrated in one of the first studies of its kind that the combination of Raman and DART-MS can improve the detection of drugs of abuse in street samples, (2) demonstrated machine and deep learning algorithms for the detection of unknown compounds and their class performed better than a portable Raman instrument's built-in algorithm, (3) elucidated the toxicity and metabolism of fentanyl using a single early stage zebrafish assay and, (4) fully characterize the metabolic pathway of valerylfentanyl using zebrafish and human liver microsomes.

Objectives

Chapter 1

The main goal of chapter 1 was to evaluate the performance of a portable Raman instrument in comparison to direct analysis in real time mass spectrometry (DART-MS) using seized drugs samples, and to evaluate their combined performance for orthogonal analysis. The central hypothesis of this chapter is the combination of Raman and DART-MS improves the correct identification of components in a seized drug sample.

Task 1.1: The first task was to review the literature for common drugs of abuse and diluents. Selected binary ratios based on the literature search were created using powdered drug-diluent samples.

Task 1.2: The second task was to validate a portable Raman instrument—TacticID, according to the United Nations Office on Drugs and Crime guidelines for handheld Raman field identification devices for seized material. Validation parameters included library verification, repeatability/ reproducibility, interference studies, and matrix effects.

Task 1.3: Selected binary mixtures from Task 1.1 were analyzed using DART-MS and the performance compared to Raman.

Task 1.4: Adjudicated case samples from the Maryland State Police were analyzed using both Raman and DART-MS. The performance of each technique was evaluated independently, and in combination with each other.

Chapter 2

The main aim of chapter 2 was to explore machine learning algorithms to improve the correct identification of components in seized materials analyzed using the TacticID portable Raman. The central hypothesis of this chapter is that machine learning algorithms perform better than the built-in algorithm of the TacticID instrument.

Task 2.1: Spectra from chapter 1 were compiled and used for data augmentation by creating binary, ternary, and quaternary mixtures.

Task 2.2: Machine learning and deep learning algorithms were selected to evaluate spectra by compound name and drug class. Algorithms included artificial neural network, convolutional neural network, k-nearest neighbor, naïve bayes, random forest, and support vector machine.

Task 2.3: The machine learning algorithms in Task 2.2 were evaluated on authentic datasets consisting of single compounds and binary mixtures and the correct classification was compared to the hit quality index algorithm built into the TacticID portable Raman instrument.

Task 2.4: Proposed a workflow that can be implemented in portable Raman instruments.

Chapter 3

Chapter 3 evaluated zebrafish larvae as a model to investigate the toxic effects of fentanyl while providing metabolism data. The central hypotheses of this chapter are that fentanyl causes toxic effects to zebrafish in a dose dependent manner, and zebrafish larvae are capable of metabolizing fentanyl.

Task 3.1: Administered fentanyl (0.01 to 100 µM) to 0 dpf zebrafish until 96 hpf and observed phenotypes indicative of toxicity.

Task 3.2: Performed a targeted metabolism study through analysis of zebrafish incubation media for fentanyl metabolites—norfentanyl, β-hydroxyfentanyl, and 4-ANPP.

Chapter 4

Chapter 4 elucidated the metabolic pathway of valerylfentanyl using zebrafish and human liver microsomes. The central hypothesis of chapter 4 is that metabolites observed in zebrafish and human liver microsomes are similar.

Task 4.1: Incubated valerylfentanyl with human liver microsomes and performed metabolite analysis using high-resolution mass spectrometry (Q-Exactive Orbitrap).

Task 4.2: Incubated valerylfentanyl with 30 dpf zebrafish and performed analysis using a Q-Exactive Orbitrap mass spectrometer.

Task 4.3: Proposed structures of valerylfentanyl metabolites using mass spectra data.

Chapter 1: Screening of Seized Drugs Utilizing Portable Raman Spectroscopy and Direct Analysis in Real Time-Mass Spectrometry (DART-MS)

Reproduced with additions and permission from Travon Cooman, Colby E. Ott, Kourtney A. Dalzell, Amber Burns, Edward Sisco, Luis E. Arroyo, *Forensic Chemistry*, Vol. 25 (2021): 100352 and Elsevier. DOI: 10.1016/j.forc.2021.100352

1.1. Introduction

Forensic chemists rely on an assortment of analytical techniques and instrumentation to reach conclusions when dealing with unknown seized compounds. However, every year forensic laboratories in the United States are burdened by over one million submissions of suspected drugs [57], requiring significant time and resources despite often limited budgets. To alleviate these problems and improve the speed of analysis, rapid screening of samples is a logical first step. Current screening practices often involve the use of color tests. This approach is prone to subjective, visual, judgments from the chemist [1, 2] and requires the use of different chemicals, some of which are toxic [58]. Furthermore, sensitivity and selectivity problems are common, especially for impure or low concentration samples and with novel substances [6, 58]. Also of issue is the collection and submission of unknown samples to the forensic laboratory that, upon analysis, turn out to be harmless or legal substances. To address these concerns, innovative, safer, and more cost-effective methods for screening unknown seized substances are needed both within the laboratory and in the field.

Raman spectroscopy, a well-established, nondestructive technique is attractive because it can provide high discrimination between drug structures. The selectivity of Raman spectroscopy is superior to chemical color tests, increasing the ability to reliably differentiate and identify a wider range of compounds. The use of Raman spectroscopy for the identification of drugs of abuse has been well documented using both conventional desktop models [19, 59, 60] and portable instrumentation [13, 59, 61–63]. The implementation of low-cost, battery powered, portable Raman spectrometers in forensic drug chemistry casework has harnessed their versatility as a fast and safe option [11], simplifying the testing process, eliminating the need for sample preparation, and opening the door to a wider range of materials and packaging types [7, 16, 63].

Another means of improving drug screening has been the use of mass spectrometry techniques such as high-resolution mass analyzers coupled with ambient ionization. Direct analysis in real time mass spectrometry (DART-MS) has been shown to provide rapid, and sensitive analysis of a wide range of materials, including drugs of abuse, through direct introduction of small sample amounts with minimal to no sample preparation [3, 64–66]. In addition, recent literature reports have demonstrated the ability of DART-MS to detect trace drug residues on the outside of packaging, allowing prediction of the internal contents prior to opening the packaging [67, 68]. The combination of the DART ionization source with high-resolution mass spectrometry results in accurate mass measurements, providing more confident screening of drug compounds.

Combining the results from the orthogonal techniques for the detection of 15 common drugs of abuse and 15 diluents is presented herein. After establishing bias, precision, and reproducibility of portable Raman spectroscopy, a suite of pure and binary mixture samples was analyzed to determine the accuracy of this approach. A subset of these samples and mixtures was analyzed using DART-MS to establish the accuracy of the technique by itself and when these results were combined with portable Raman. To demonstrate real-world utility, this combination of screening techniques was used to analyze a set of authentic samples provided by the Maryland State Police Forensic Sciences Division (MSP-FSD).

1.2. Materials and Methods

1.2.1 Reagents and Materials

A total of 15 drugs of abuse and 15 diluents were purchased, as neat materials with a minimum purity of 99 % from a number of chemical suppliers. Drug purity was verified using GC-MS. All drugs were purchased from Cayman Chemical (Ann Arbor, MI), and the identities of the compounds and the suppliers for the diluents are listed in **Table 1.1**.

Table 1. 1. Analyte panel for drugs and diluents. Abbreviations or alternate, common, names are shown in parenthesis next to the name. Compounds with an asterisk (*) were purchased as hydrochloride salts. For the diluents, superscript letters indicate chemical supplier.

Drugs	Diluents
4-Methylethcathinone (4-MEC)	Acetaminophen[b]
4-Methylmethcathinone (Mephedrone)	Benzocaine[b]
Alprazolam	Boric Acid[e]
Buprenorphine*	Caffeine[e]
Cocaine*	Diltiazem*[c]
Codeine	Hydroxyzine*[d]
Fentanyl	Levamisole*[c]
Heroin	Lidocaine*[b]
Methamphetamine*	Maltose[f]
Mitragynine	myo-Inositol[h]
Morphine	Phenacetin[a]
Naltrexone*	Phenolphthalein[g]
PB-22	Procaine*[c]
Sufentanil	Sorbitol[d]
Δ9-Tetrahydrocannabinol (THC)	Starch[i]

Suppliers: [a]TCI Chemicals (Portland, OR), [b]Millipore-Sigma (St. Louis, MO), [c]Acros Organics (Geel, Belgium), [d]Spectrum Chemical MFG (New Brunswick, NJ), [e]Baker (Radnor, PA), [f]MPBio (Salon, OH), [g]Fisher Chemical (Fairlawn, NJ), [h]Alfa Aesar (Ward Hill, MA), [i]Kroger (Morgantown, WV).

1.2.2 Instrumentation

Raman spectra were obtained using a TacticID portable 785 nm laser Raman instrument from B&W Tek (Newark, DE). The unit was operated at either 20 %, 60 %, or 90 % laser power. Spectra were acquired between the range of 176 cm^{-1} and 2900 cm^{-1} with 9 cm^{-1} resolution. Spectra were automatically compared with the stored instrument library, as well as an in-house library created using the same instrument. Assessment of spectral similarity was determined by the hit-quality-index (HQI) with the low-end cut-off set to the instrument's default of 85 %. A polystyrene

reference material was utilized daily to verify the performance of the instrument before any further measurements.

DART-MS spectra were acquired in positive ionization mode using an IonSense DART-SVP ion source (Saugus, MA) with a JEOL AccuTOF 4G LC-plus mass spectrometer (Peabody, MA). DART analysis was performed using the parameters outlined in **Table 1.2**. Direct sampling was implemented by first placing the closed end of a capillary tube within the DART gas stream for several seconds. Following brief cooling, the capillary was dipped and swirled into the powdered sample before being introduced to the ion source. To perform drift compensation, polyethylene glycol (PEG) was used. Resulting mass spectra were extracted and background subtracted using an area of the chronogram where samples were not analyzed in msAxel. Spectra were assessed manually, as well as through use of Mass Mountaineer (Fineview, NY) software with an in-house library of over 600 compounds provided by the National Institute of Standards and Technology (NIST). Search parameters for mixture analysis included a minimum peak height of 5 % relative intensity, to minimize the potential for false positive identification, and an *m/z* agreement of ±0.005 Da, based on the MS manufacturers tolerance. DART-MS is a well-established technique in forensic seized drug analysis and therefore a validation of the technique was not required [69, 70].

Table 1. 2. DART-MS parameters for analysis.

DART Temperature	400 °C
DART Gas	He
Orifice 1 Voltage	30 V, 60 V, 90 V switching at 0.2 s/scan
Ring Voltage	5 V
Orifice 2 Voltage	20 V
Ion Guide	500 V
m/z Scan Range	*m/z* 50 – *m/z* 800

1.2.3 Establishing Bias, Precision, & Reproducibility for the Portable Raman

Establishment of bias, precision, and reproducibility of the portable Raman instrument was performed following ASTM E1683-02 [71], ASTM E1840-96 [72], and United Nations Office on Drugs and Crime (UNODC) guidelines [17] by investigating interference from different types of packaging, variability between analysts, mixture analysis, and verification of libraries within the instrument. For these studies only a diluent panel was used for testing. Pure diluents were analyzed inside glass vials and 2 mil plastic bags. The point-and-shoot adapter was used for analysis through plastic bags and no adaptor for analysis through glass. Spectra were acquired in triplicate at both 60 % and 90 % laser power. Reproducibility and repeatability were established through triplicate analysis performed by a total of three different operators. Analysis of variance (ANOVA) was used to evaluate within and between operator variability. The instrument's accuracy when analyzing pure drugs and diluents was reported.

1.2.4 Assessment of Mixtures

A total of 64 mixtures of target drugs and common diluents were created to simulate street samples and are shown in **Table 1.3**. Mixtures and ratios were selected based on published literature [73–78]. As an example, a 1:4 ratio was prepared by mixing 10 mg of target drug with 40 mg of diluent. All mixtures were analyzed via Raman through the plastic bags in triplicate at different areas to account for variability in the sample. The mixture analysis setting was used for all mixtures, to allow for identification of multiple compounds, with the number of hits—high spectrally correlated compounds, set to 5 and the ratio threshold set to 15 %.

Previous studies have shown that DART-MS is an established technique for drugs of abuse analysis [64, 67, 79, 80]. Therefore, a subset of 25 samples of the original 64 mixtures, highlighted in **Table 1.3**, was selected to demonstrate the applicability of DART-MS for mixture analysis. The accuracy of DART-MS, the TacticID instrument, and the orthogonal combination of both techniques were determined. The combined accuracy was determined when the compounds were correctly reported by either DART-MS or Raman. For example, if the drug was only reported from the DART-MS results and the diluent reported with Raman, a correct identification of both drug and diluent resulted for that particular mixture.

Table 1. 3. Mixtures of drugs and diluents investigated in this study. Ratios with a checkmark were analyzed using the portable Raman system (n = 64). Samples with an asterisk (*) were also analyzed using DART-MS (n = 25).

Mixture	**Mass Ratio (Drug : Diluent)**			
	1:4	**1:7**	**1:10**	**1:20**
Heroin HCl / acetaminophen	✓*	✓		✓
Fentanyl HCl / caffeine				✓
Fentanyl HCl / methamphetamine HCl	✓			
Cocaine HCl / levamisole	✓*			
Fentanyl HCl / cocaine HCl	✓			
Methamphetamine HCl / levamisole	✓*	✓		
Methamphetamine HCl / caffeine	✓*			
Cocaine HCl / benzocaine	✓*			
Alprazolam / caffeine	✓*	✓*		
Alprazolam / levamisole	✓	✓		
4-MMC HCl / maltose	✓*			✓
4-MMC HCl / lidocaine		✓*	✓	
4-MEC HCl / maltose	✓*	✓		
4-MEC HCl / benzocaine		✓*	✓	
PB-22 / lidocaine	✓			
Sufentanil / caffeine	✓			
Codeine / acetaminophen	✓	✓	✓	✓
Codeine / maltose	✓*	✓*	✓*	✓*
Morphine / maltose	✓*	✓*	✓*	✓
Naltrexone HCl / maltose	✓*	✓*	✓*	✓*
Buprenorphine HCl / starch	✓*	✓*	✓*	✓
Cocaine HCl / caffeine	✓	✓	✓	✓
Cocaine HCl / diltiazem	✓	✓	✓	✓
Cocaine HCl / hydroxyzine	✓		✓	
Cocaine HCl / lidocaine	✓	✓		✓
Cocaine HCl / maltose		✓		✓
Cocaine HCl / procaine	✓	✓	✓	
Cocaine HCl / boric acid			✓	

1.2.5. Authentic Samples

Fifteen adjudicated case samples were provided by the Maryland State Police Forensic Sciences Division and analyzed via both the portable Raman system and DART-MS. Samples were assessed in triplicate using both methods and compared against their respective libraries. The Raman laser power was altered based on the color of the test material—20 % or 60 % for colored samples and 90 % power for white powders. Analysis of the authentic samples by DART was performed as described previously in **Table 1.2**. Samples were prepared following MSP-FSD protocols by dissolving 1 mg to 2 mg of powder in ≈1 mL of methanol. The averaged mass spectrum was obtained for each sample from the triplicate analyses and used for identification in MassMountaineer with a tolerance of ±0.005 Da and threshold of 5 %, which was lowered to 1 % for differentiation of isomers. A multi-point drift compensation with tetracaine was used for calibration to serve as a positive control.

1.3. Results and Discussion

1.3.1 Portable Raman

1.3.1.1 Laser Power and Operator Reproducibility

The hit quality index (HQI)—a common spectral comparison method [81, 82], is a measure of the spectral correlation between the known library spectrum and the unknown test spectrum. Rodriguez *et al*. described HQI by **Equation 1.1** [83]. The Raman system reports the HQI as a percentage where a value closer to 100 % represents higher similarity and a value closer to 0 % represents poor similarity. Validation of the instrument was performed with diluents only as a cost saving option. **Figure 1.1** shows the distribution of the HQI for the diluents at 60 % (**Figure 1.1A**) and 90 % (**Figure 1.1B**) power for three operators. All HQI values were greater than 90 % although there was higher variation with Operator 3. ANOVA results showed myo-inositol with the highest variation in the HQI value—2 % coefficient of variation (CV) observed between and within operators. The percent CV for all other compounds was less than 2 %.

$$HQI = \frac{(Library*Test)^2}{(Library*Library)(Test*Test)} \qquad \textbf{Equation (1.1)}$$

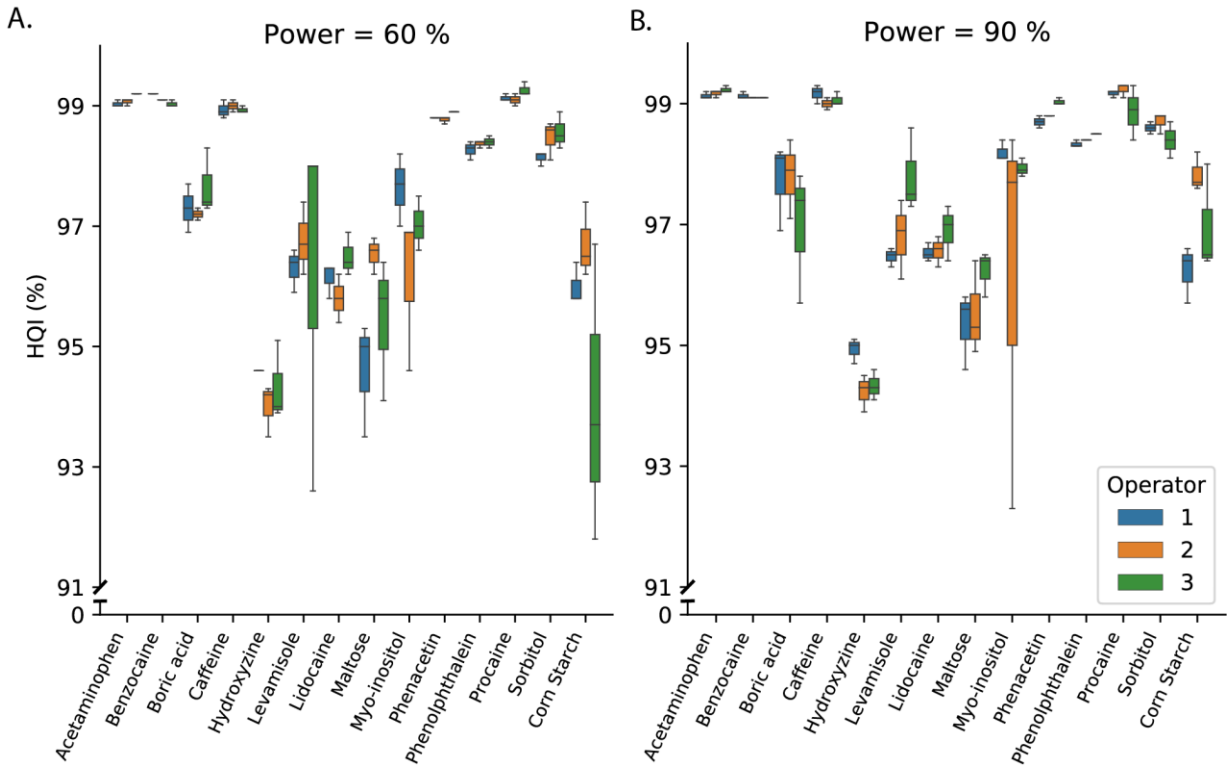

Figure 1. 1. Boxplots showing the distribution of the HQI (%) between three operators when the portable Raman was operated at 60 % (A) and 90 % (B) power. All diluents were powders and analyzed through plastic. Results for diltiazem are not shown because it was not present in the instrument library. Each box and whisker plot represents nine total measurements.

1.3.1.2 Packaging Container

Figure 1.2 shows the distribution of HQIs when the diluents were measured through glass (**Figure 1.2(A)**) and plastic (**Figure 1.2(B)**) at 60 % and 90 % power as part of the instrument validation. Although all HQI values were greater than 85 %, there was higher variation when the packaging material was glass at both laser powers. Analysis of corn starch through glass only returned a result using the mixture setting on the instrument and was not plotted in **Figure 1.2**. However, the portable Raman instrument returned all the pure diluents tested as the top hit through both glass and plastic. The instrument is designed to analyze compounds through transparent glass vials <5 mm diameter thickness, as used in this study. The thickness of the plastic bags used in this study was 2 mil (0.0508 mm), which provided more consistent spectral intensities, and therefore

typically higher HQIs compared to glass. Most of the drugs analyzed in this study were white powders and the laser power selected for subsequent analysis was 90 % because of the lower variation in the observed HQIs.

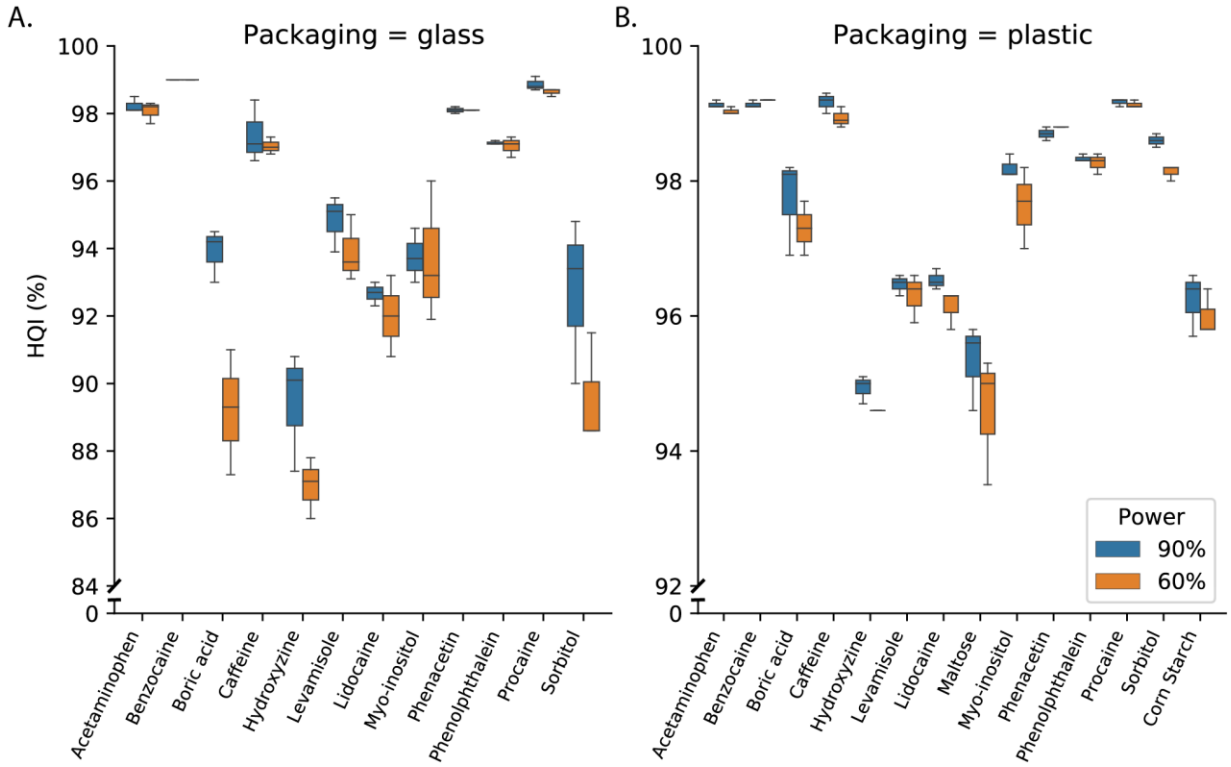

Figure 1. 2. Boxplot comparing the type of packaging—glass (A), and plastic (B), through which the diluents were analyzed when the instrument was operated at 60 % and 90 % power, by three operators. Diltiazem is not plotted as it was not present in the instrument's library and returned a "no match" result. Corn starch and maltose are not shown for glass (A) since the mixture setting was used to get a hit and the mixture setting provides a spectral weight percentage instead of an HQI. Note the differences between the y-axes, where (A) is from 84 % to 100 % and (B) is from 92 % to 100 %.

1.3.1.3. Performance Measures

The performance of an instrument in relation to a particular purpose is important to understand, especially the false identification rates within a forensic context. Given that portable Raman systems can be used for field applications or laboratory case work, the ability to correctly identify compounds through glass or plastic packaging was investigated. A true positive (TP) was defined as the instrument correctly associating the spectrum of the drug with the spectrum of the drug in

its library; a true negative (TN) was defined as the instrument returning a "no match" result when the drug was absent from the library or no drug was present in the sample; a false positive (FP) was defined as the instrument erroneously returning a match for a drug that was not present; and a false negative (FN) was defined as the instrument returning a "no match" result or failing to detect a drug when it was present and its spectrum was in the library. **Equations 1.2– 1.5** were used to calculate the accuracy, sensitivity, specificity, and precision for pure target drugs and diluents. When the compounds listed in **Table 1.1** (except for THC) were analyzed through plastic, the accuracy was 89 %, the true positive rate (TPR) was 100 %, the true negative rate (TNR) was 23 % and the precision was 88 %. When analysis was performed through glass, these values were 91 %, 100 %, 38 %, and 90 %, respectively. Although the portable Raman instrument demonstrated high accuracy and TPR, the high false positive rate is one reason it is regarded as a preliminary method. For this reason, we explored the potential of combining the portable Raman technique with DART-MS.

$$Accuracy = \frac{(TP+TN)}{(TP+FN+FP+TN)} \qquad \textbf{Equation (1.2)}$$

$$Sensitivity(TPR) = \frac{TP}{(TP+FN)} \qquad \textbf{Equation (1.3)}$$

$$Specificity(TNR) = \frac{TN}{(TN+FP)} \qquad \textbf{Equation (1.4)}$$

$$Precision = \frac{TP}{(TP+FP)} \qquad \textbf{Equation (1.5)}$$

When binary diluent–diluent mixtures were analyzed, both compounds were correctly identified in 17 % of the samples as shown in **Figure 1.3(A)**. For drug-diluent mixtures as shown in **Figure 1.3(B)**, both compounds were correctly identified in 19 % of the samples. In one instance, the drug-diluent mixture of naltrexone-maltose (1:7 ratio), both compounds were incorrectly identified. The mixtures at 1:4 and 1:7 ratios produced greater success in observing both compounds, possibly due to the more equal proportions of each compound.

Cocaine is one of the most prevalent drugs of abuse. A study conducted in Austria reported 10 % of seized samples analyzed contained cocaine as the active ingredient [84] with purities ranging from 30 % to 60 % based on the geographic location [74, 85, 86]. Cocaine seizures in the European

Union increased by more than 42 tonnes in 2018 from the previous year, the highest level recorded [87]. A 2020 midyear report in the US ranked cocaine as the third most popular drug of abuse comprising 13 % of drug seizures [88]. To gain a better understanding of the ability to identify binary mixtures involving cocaine using portable Raman, the 90 % laser power data was analyzed separately. **Figure 1.3(C)** shows both cocaine and the diluent were correctly identified in 14 % of the tested mixtures. However, cocaine was reported as the detected drug in only 24 % of the samples while the diluent was correctly identified 90 % of the time. **Figure 1.4** presents the Raman spectra obtained using the TacticID for cocaine, levamisole, and a ratio 1:4 cocaine-levamisole, demonstrating areas of congruence for both compounds within the mixture. The peaks at 1000 cm^{-1}, 1024 cm^{-1}, 1276 cm^{-1}, 1600 cm^{-1}, and 1716 cm^{-1} are attributed to symmetric stretching of aromatic ring breathing, asymmetric stretching of the aromatic ring, C-N stretching, C=C stretching of the aromatic ring, and C=O symmetric stretching, respectively in cocaine HCl [89]. The levamisole spectrum is marked by the absence of a peak at 1716 cm^{-1} present in the mixture and the cocaine spectra. Although cocaine and levamisole have a peak at 1260 cm^{-1} – 1276 cm^{-1}, representing CN stretching, it is weaker in levamisole. Similarly, cocaine has a stronger peak at 1600 cm^{-1} than levamisole.

Fentanyl remains a drug of interest especially in the United States due to the ongoing opioid crisis. Three mixtures containing fentanyl were investigated in this study, but the portable Raman system was only able to detect fentanyl in one sample. Possible reasons for the missed detections include the limited amount of sample used in preparing the mixtures due to the high exposure risk associated with fentanyl, and fluorescence. Surface-enhanced Raman spectroscopy (SERS) was used by Haddad, Green and Lombardi to detect fentanyl in binary cocaine mixtures at 65 ppm [90], overcoming the low concentrations of fentanyl found in street samples [74]. Green *et al.* also compared the sensitivity of immunoassay based fentanyl testing strips, a TruNarc™ Raman spectrometer and a Bruker Alpha™ Fourier-Transform Infrared (FTIR) spectrometer for detecting fentanyl in street samples [91]. The TruNarc system resulted in an overall sensitivity of 25.7 %, and 81.9 % sensitivity with FTIR for all test compounds including fentanyl. Although the immunoassay test strips produced a higher sensitivity than both TruNarc and FTIR, they do not discriminate between fentanyl and its analogues.

Several portable Raman instruments are currently on the market for forensic applications. For a comparison of the specifications between some of these instruments, refer to the Forensic Technology Center of Excellence report [92]. Although the Scientific Working Group for the Analysis of Seized Drugs (SWGDRUG) lists Raman spectroscopy as a category A technique indicating it has the highest discriminatory power [10], some laboratories consider portable Raman spectroscopy as category B due to the challenge in detecting all components in mixture samples. For example, Spicher *et al.* reported an accuracy of 97.6 % when certified reference materials were analyzed with a portable Raman, but 76.9 % accuracy for case samples [93] which usually contain several compounds and have the controlled substance as the minor ingredient. The overall accuracy of the portable Raman system in our study was 32 % in detecting the target drug, 89 % in detecting the diluent, and 19 % in detecting both compounds in the binary mixtures analyzed above, highlighting the need for complementary techniques that also provide results just as fast as Raman and with minimal sample preparation.

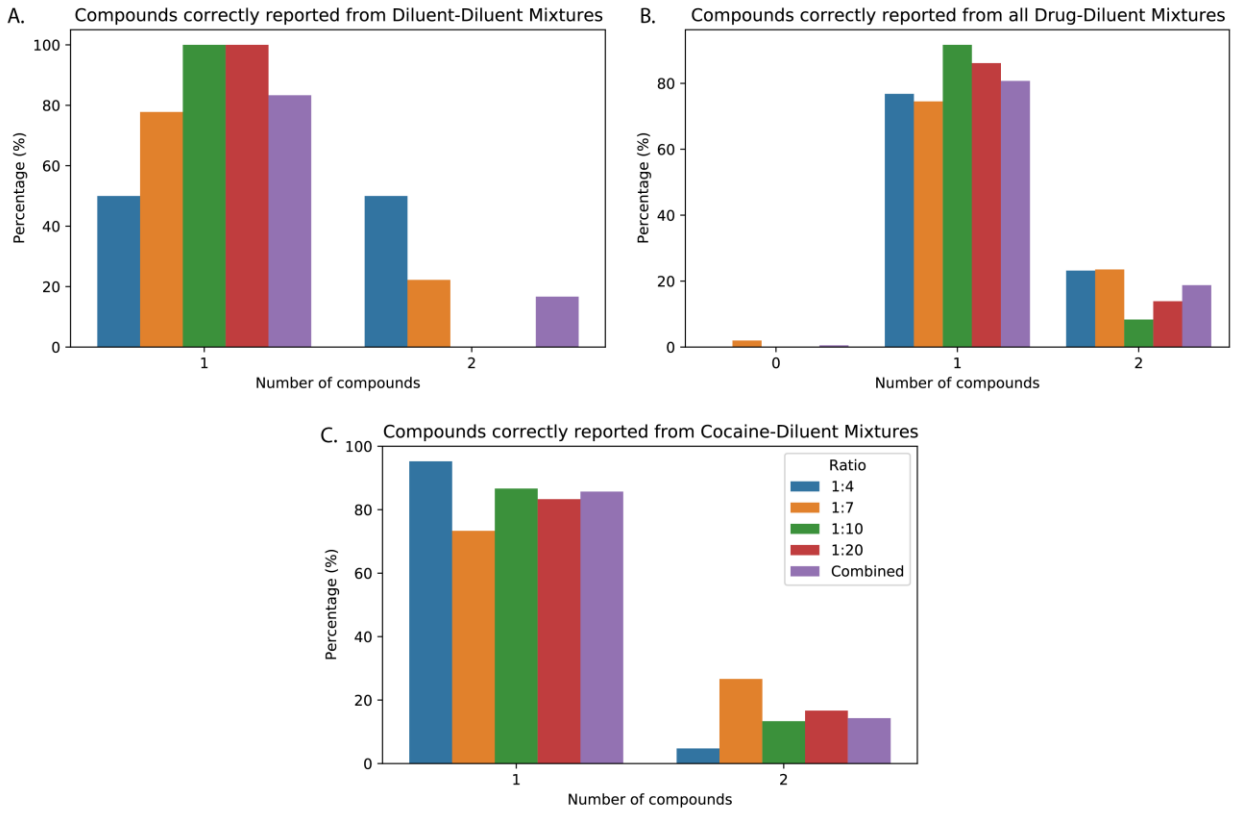

Figure 1. 3. (A)— Percent of correctly reported compounds for each ratio and the total dataset (purple) by the portable Raman system for diluent-diluent mixtures (ratios 1: 4 and 1:20, n = 6;

ratios 1:7 and 1:10, n = 9). 83 % of correctly identified substances matched 1 compound and 17 % matched for both compounds as shown by the purple bars; (B)—Percent of correctly reported compounds by the portable Raman for drug-diluent mixtures (ratio 1: 4, n = 69; ratio 1:7, n = 51; ratios 1:20 and 1:10, n = 36). 81 % of the identified substances returned a hit for 1 compound, and 19 % for both compounds in binary mixtures; (C)—Percent of correctly identified compounds in cocaine- diluent mixtures (ratio 1:4, n = 21; ratios 1:10 and 1:7, n = 21; ratio 1:20, n = 12). All mixtures were analyzed with 90 % laser power. The combined ratio is the overall percentage for the number of identified compounds calculated from the total number of samples.

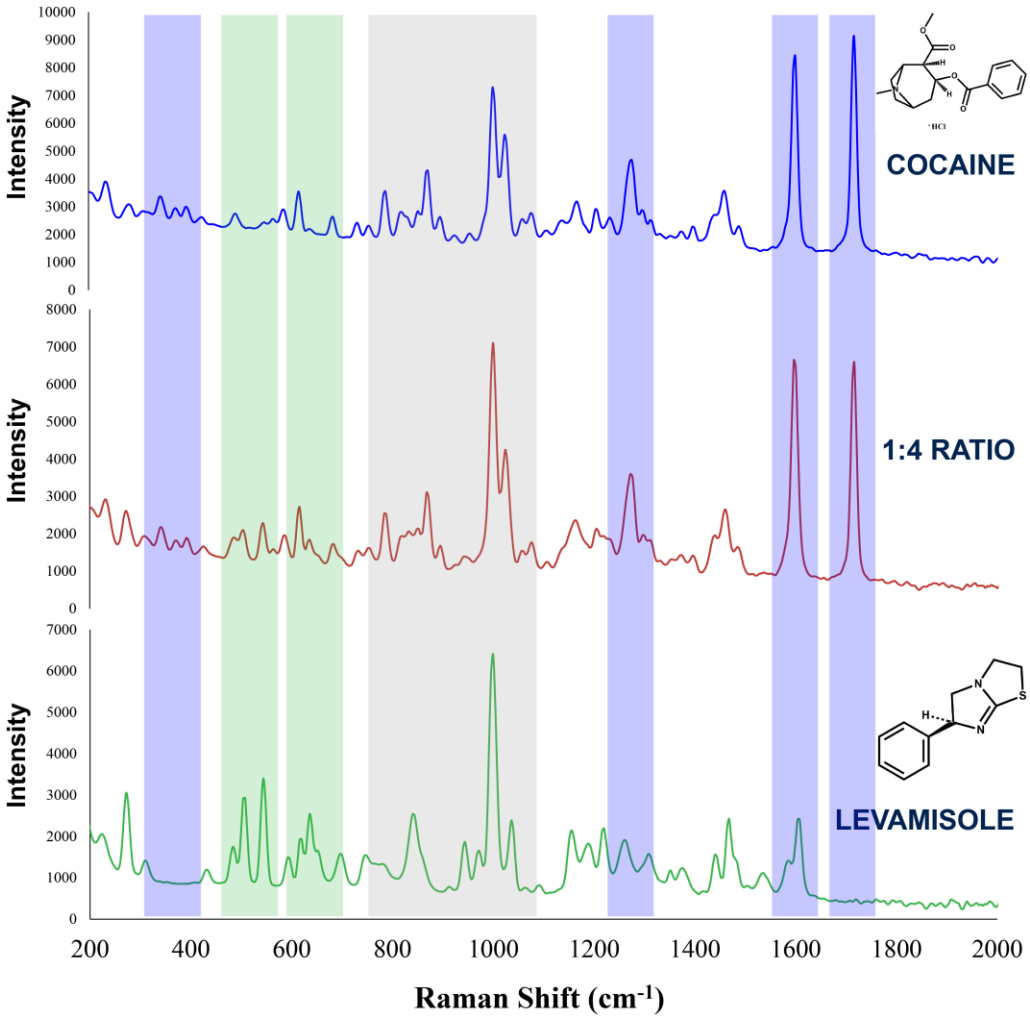

Figure 1. 4. Raman spectra of solid powders within plastic bags for cocaine, levamisole, and a mixture ratio of 1:4, cocaine-levamisole. Areas of congruence with levamisole are highlighted in

green and with cocaine are highlighted in blue to demonstrate spectral regions for each analyte compared to the mixture. The area highlighted in gray represents contributions from both levamisole and cocaine.

1.3.2. DART-MS

DART-MS was utilized as an orthogonal detection method for the samples tested by portable Raman. SWGDRUG lists mass spectrometry as a category A technique [10], but like portable Raman, DART-MS is used as a screening method. A polyethylene glycol standard was run on the instrument to account for drift compensation. For analysis by traditional DART sampling, *m/z* 283.17513 was chosen for drift compensation by the software. **Figure 1.5** shows a representative DART-MS spectrum for a 1:4 mixture ratio of cocaine-levamisole mixture analyzed using traditional microcapillary sampling.

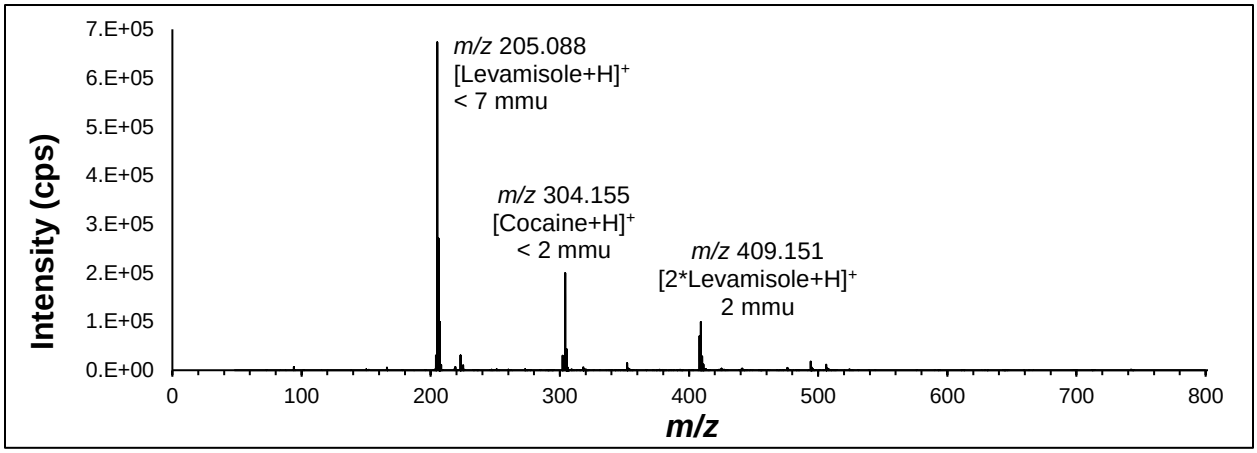

Figure 1. 5. Representative DART mass spectrum of a 1:4 mixture ratio of cocaine to levamisole. Peaks of interest are labeled based on MassMountaineer identification along with the difference in milli-mass units (mmu) between the library and the spectrum. Due to high concentration, the levamisole peak fell outside of the ±5 mmu window, which was widened to encompass this peak. For simplicity, only the spectrum collected at the 30 V voltage is shown.

Identification was based on manual inspection of the mass spectrum for each sample run in triplicate and using MassMountaineer data analysis software (Rev: 5.0.7.0) with an in-house library as demonstrated. Due to the structural properties of maltose and starch, these molecules do ionize easily and were therefore not observed in the DART-MS spectra. Previous work has demonstrated the ability to analyze carbohydrates via DART-MS; however, the authors utilized an

in situ permethylation step to allow positive mode analysis [94]. In our proposed protocol, a generic drug screening method was used with direct analysis and minimal sample preparation. When considering positive identification of both the drug and diluent, the samples where the diluent was not identified contained either maltose or starch, while the remaining samples had positive identifications for the diluent, representing the loss of carbohydrate information due to the ionization mode rather than instrument ability. As such, performance of the DART analysis was judged by positive identification of the drug of abuse. The true positive rate was determined to be 93 % with false negative rate of 7 %.

In many cases, peaks not corresponding to the protonated molecule were present in the mass spectrum. Upon analysis, the majority of these peaks were easily explained through the presence of dimers and loss of water. Codeine, acetaminophen, naltrexone, caffeine, levamisole, and alprazolam demonstrated the formation of dimers while –OH losses were observed for buprenorphine, morphine, and codeine. In one instance, methamphetamine was not identified in the sample due to the 5 % peak threshold set by the search algorithm. Manual examination of the mass spectrum easily revealed the methamphetamine peak of *m/z* 150 (**Figure 1.6**).

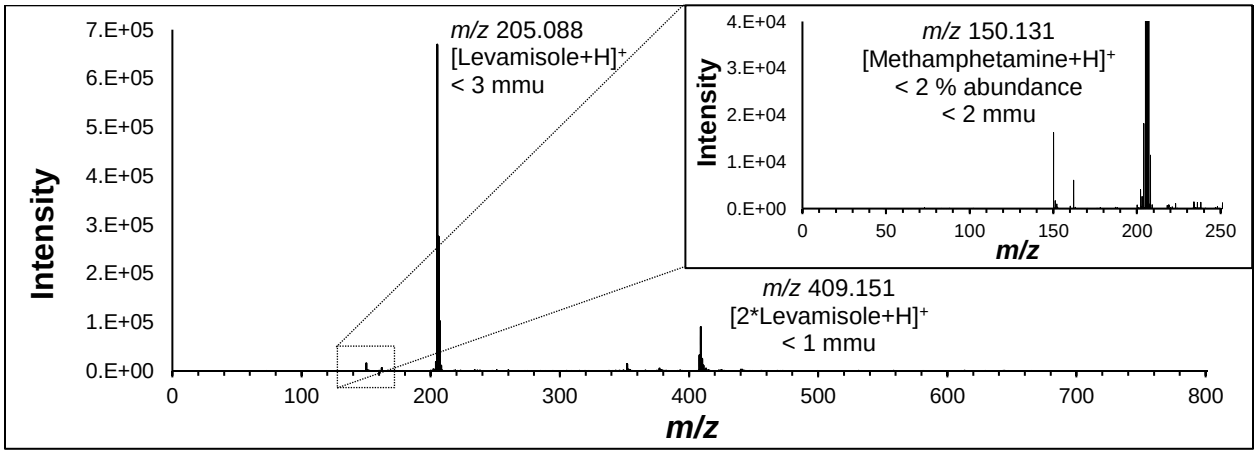

Figure 1. 6. Demonstration of the lack of identification of the methamphetamine peak in the MassMountaineer software due to the peak threshold value of 5 %. MassMountaineer identifications are shown along with the milli-mass unit difference between the library and the spectrum. Methamphetamine m/z 150 can be seen when zooming into the group of peaks present near m/z 150. Abundance of less than 2 %. The relative abundance window was widened to

observe the methamphetamine peak. For simplicity, only the spectrum collected at the 30 V voltage is shown.

1.3.3. Orthogonal Detection

Analytical schemes which leverage orthogonal techniques to provide complimentary identification data have demonstrated improved reliability and accuracy, and therefore the data from the portable Raman and DART-MS were combined to compare the performance rates of the orthogonal approach. It is important to note that although Raman spectroscopy and mass spectrometry are considered SWGDRUG category A techniques, these instruments are being assessed as rapid screening techniques. Although the portable Raman initially struggled to identify the drug analyte in dilute mixture ratios, the diluent was correctly identified 100 % of the time in the subset of mixtures used for the orthogonal detection study. In contrast, DART-MS excelled at detecting both drug and diluent compounds; however, many diluents were not identified due to analysis in positive mode. Therefore, the combination of both techniques yielded high accuracy for both drug and diluent compounds in all the analyzed samples, demonstrating the combined strength and enhanced reliability through orthogonal combination. **Table 1.4** presents the comparison of overall performance rates for the samples assessed orthogonally, first by portable Raman and followed by DART-MS analysis. Specificity does not apply because the instruments always returned a match based on the library search. Performance measures were determined using **Equations 1.2-1.5**. Accuracy for both analytes (drug + diluent) was determined by the sum of the samples producing identifications for both the drug and diluent divided by the total number of samples. Lastly, the accuracy of the combination of the two instruments was assessed as the sum of the samples producing the respective identifications by either portable Raman and/or DART-MS divided by the total number of samples (**Table 1.4**).

Table 1. 4. Comparison of accuracy between Raman, DART-MS, and the orthogonal combination when mixtures were analyzed. The accuracy of the Raman shown below is only for the 25 mixtures that were also analyzed by DART-MS. Specificity is not applicable as there were no True negatives in this study.

	Raman			**DART-MS**			**Combined**
	Drug	**Diluent**	**Both Analytes**	**Drug**	**Diluent***	**Both Analytes***	**Both Analytes**
Accuracy	48 %	100 %	56 %	85 %	33 %	26 %	96 %
Sensitivity	56 %	100 %	56 %	92 %	36 %	28 %	96 %
Specificity	NA	NA	NA	NA	NA	NA	NA
Precision	78 %	100 %	100 %	92 %	82 %	78 %	100 %

** Diluents measured by DART-MS were acetaminophen, benzocaine, caffeine, levamisole, lidocaine, maltose, and starch.*

1.3.4. Authentic Sample Results

To investigate how the orthogonal approach worked for real samples, fifteen authentic adjudicated case samples were obtained from the Maryland State Police Forensic Sciences Division. The majority of the samples were white powders or white crystalline samples and several samples were off-white to gray-brown. All samples were analyzed by portable Raman through plastic bags or through capsules. **Table 1.5** provides the results of the portable Raman and DART-MS analyses along with the ground-truth results which were obtained using GC-MS analysis. Accuracy was defined as the ability of the instrument to detect those compounds assigned as ground truth for each respective group (drug, diluent, or all analytes). For example, if the ground truth contained two diluents, both needed to be detected for a positive result for diluent accuracy. In this manner, detection of all ground truth compounds was required. The overall accuracy of the portable Raman was 44 % for all analytes, whereas the accuracy of the DART-MS analysis was 74 % for all analytes. The failure of the portable Raman instrument to detect some controlled substances due to their low proportion, was compensated for with DART-MS as the combination of the two techniques resulted in 83 % accuracy in the detection of all ground truth compounds for the authentic samples. It is important to note that while both instruments performed well, in one instance, both instruments were needed to yield a full profile of the unknown substance as

demonstrated by case #1. Some diluents can foul the GC-MS source, therefore most drug chemistry laboratories screen samples for controlled substances but do not always report diluents. In one case, #3, a diluent was detected by both Raman and DART-MS but not observed by GC-MS. Given that the diluent was mannitol it is expected as GC-MS is not sensitive to sugar alcohols.

Table 1. 5. Summary of authentic samples analyzed through Raman and DART-MS and ground truth as observed from GC-MS. An explanation is provided for compounds detected via DART-MS but not observed via GC-MS analysis.

Case	GC-MS Results (Ground Truth)	Portable Raman Results	DART-MS Result
1	Heroin Mannitol Quinine 6-Monoacetylmorphine	-- Mannitol -- -- **Additional Hits:** Hydrogen peroxide Sodium azide JWH-122	Heroin -- Quinine 6-Monoacetylmorphine
2	Cocaine Levamisole	Cocaine HCl Levamisole HCl	Cocaine Levamisole
3	Fentanyl Caffeine Diphenhydramine Quinine	-- Caffeine -- -- **Additional Hits:** Erythromycin Mannitol Sodium azide	Fentanyl Caffeine -- Quinine **Additional Hits:** Levamisole Mannitol
4	MDMA	MDMA HCl **Additional Hits:** Centrophenoxine Buprenorphine HCl	MDMA

Case	GC-MS Results (Ground Truth)	Portable Raman Results	DART-MS Result
		2-*N*,*N*-diethylamino-1-(4-methoxyphenyl)-1-propanone	
5	Fentanyl Acetaminophen	-- Acetaminophen	Fentanyl Acetaminophen **Additional Hits:** Xylitol
6	Cocaine Levamisole Phenacetin	Cocaine base Levamisole Phenacetin	Cocaine Levamisole Phenacetin
7	Caffeine	Caffeine Starch	Caffeine
8	Caffeine Mannitol Quinine	-- Mannitol --	Caffeine Mannitol Quinine
9	No Drugs of Abuse	Maleic anhydride Hexobarbitone	Caffeine
10	Fentanyl Acetylsalicylic Acid Benzocaine Caffeine *N*-Phenylpropamide Quinine	-- Acetylsalicylic Acid -- -- -- --	Fentanyl Acetylsalicylic Acid -- Caffeine -- Quinine
11	Cocaine Levamisole Phenacetin Inositol	Cocaine base -- Phenacetin -- **Additional Hits:** Thebaine	Cocaine Levamisole Phenacetin --
12	Phentermine	Phentermine HCl	Phentermine
13	Methamphetamine Ketamine Phenacetin	-- Ketamine HCl Phenacetin **Additional Hits:**	Methampehtamine Ketamine

Case	GC-MS Results (Ground Truth)	Portable Raman Results	DART-MS Result
		Dimethyl sulfone	
14	Heroin 6-Monoacetylmorphine Mannitol Quinine 6-Acetylcodeine	-- -- Mannitol -- -- **Additional Hits:** Sorbitol Hydrogen peroxide Hydroxyzine pamoate Codeine	Heroin 6-Monoacetylmorphine Mannitol Quinine --
15	Cocaine Benzoylecgonine	Cocaine HCl --	Cocaine --

Table 1. 6. The accuracy results for the authentic case samples. The calculation of the accuracy was performed in similar fashion as described above in section 1.3.5. Sample #9 was not included since it was a true negative sample.

Performance Measure	Raman	DART-MS	Combined
Drug Accuracy	41 %	82 %	82 %
Diluent Accuracy	45 %	68 %	83 %
Accuracy for All Analytes	44 %	74 %	83 %

1.4. Conclusions

On-site drug testing can help reduce drug backlogs, but the safety of personnel conducting the tests is important due to the increasing potency of illicitly manufactured substances. Portable Raman analysis allows for testing without opening certain types of packing, thereby reducing potential drug exposures. It produces high confidence in results when analyzing pure substances, but

accuracy suffers when mixtures are present, as demonstrated in this study. The use of orthogonal techniques such as DART-MS can help resolve some of the challenges encountered in Raman analysis.

In this study, a portable Raman spectrometer was validated according to the UNODC guidelines on a panel of 15 commonly encountered drugs of abuse and 15 diluent compounds. The HQI for pure diluents through plastic was higher than that for glass, >90 % and >86 %, respectively. The between-operator precision was low at ≤2 %. Analysis through plastic resulted in an accuracy of 89 % and precision of 88 %, while analysis through glass resulted in an accuracy of 91 % and precision of 90 %. The system excelled at identification of analytes in their pure form and in higher percent ratio but demonstrated some difficulty in detection the analyte at low concentrations. In comparison, DART-MS demonstrated high accuracy and sensitivity for the drug analytes of interest and many of the diluent compounds. However, DART-MS struggled with diluent compounds that perform better in negative mode (only positive mode was used). Although these techniques are strong on their own, the combination of both instruments resulted in a drug accuracy of 96 %, diluent accuracy of 100 %, and overall accuracy for two-part mixtures of 96 %. Analysis of authentic case samples using both techniques resulted in 44 % accuracy by Raman, 74 % by DART-MS, and 83 % accuracy when both techniques were combined. This combination of orthogonal data demonstrates the improved reliability and accuracy possible when both techniques are used in screening. The ability to detect both drug and diluent analytes provides useful information for drug intelligence operations that can be performed rapidly for improved investigative leads and real-time decision making.

Chapter 2: Implementing Machine Learning for the Identification and Classification of Compound and Mixtures in Portable Raman Instruments

Reproduced with additions and permission from Travon Cooman, Tatiana Trejos, Aldo H. Romero, Luis E. Arroyo, *Chemical Physics Letters*, Vol. 787 (2022): 139283, and Elsevier. DOI: 10.1016/j.cplett.2021.139283

2.1.0 Introduction

Portable instruments are becoming more prevalent due to their ability to provide quick results on-the-spot [2, 5, 16, 95–97]. While data can be acquired in a short time, the specificity and accuracy of these instruments and the safety of the operators remain important. Portable analytical techniques for on-site applications include electrochemical systems [4], paper-based analytical devices [98, 99], mass spectrometry methods [3, 100–102], and spectroscopy methods [2, 103–105]. In scenarios where analysis requires packages to be opened at point-of-contact areas, the risk of exposure to unknown substances by personnel remains high. Raman spectroscopy provides unique advantages over other techniques due to its ability to be noninvasive [106–108] and even to analyze substances through packaging [109–111], thereby minimizing the risk of exposure to operators. For example, the Agilent Resolve Handheld Raman—a spatially offset Raman spectrometer (SORS) which allows subsurface analysis, is capable of analyzing explosives, drug precursors, toxic industrial chemicals, chemical warfare agents, and narcotics through packaging such as colored plastic and glass, paper, sacks, cardboard and fabric [110]. Conventional Raman systems are better suited for analysis through clear plastic bags and vials, and translucent packaging. Portable Raman systems have proved useful for the molecular identification of minerals [112, 113], analysis of biomaterials [114], food quality monitoring [115–118], and analysis of drugs [5, 13, 119, 120]. Raman spectroscopy is broadly applied in chemistry, biochemistry, biology, and medicine [121–123] due to its ability to provide a structural fingerprint by which molecules can be identified. Nonetheless, the instrument's accuracy is dependent on the incorporated algorithms that return an identification for an unknown compound.

Organic molecules, when stimulated by an excitation source such as a laser, results in a photon frequency shift due to the vibration produced by the interaction between the applied electromagnetic field and the electronic charge, which is unique to the molecule. Depending on the functional groups in the molecule, it may undergo symmetric, asymmetric stretching, or

bending. These factors influence the Raman shifts and peak shapes and intensities observed in the resulting Raman spectrum. Unknown compounds can be compared to the vibrational signatures in a library. A common metric used for spectral comparisons is the hit quality index (HQI) where 1.0 represents a perfect correlation and 0.0 represents poor correlation [83]. A threshold for a 'match' or 'no match' result can be predetermined by the user based on the application. For example, in forensic science where mixtures are commonly encountered in seized drugs, a threshold of 85% for the HQI may be selected, but in the pharmaceutical industry where purer substances are encountered, the threshold might be 95% [82]. Spectra can be preprocessed to reduce the baseline by computing the first derivative to allow for higher discrimination [83]. One drawback to using the HQI is that incorrect identifications of similar compounds with small spectra differences may result [124]. Other metrics for spectral comparison include Pearson's correlation—where a value of 1 represents a perfect correlation and -1 represents a poor correlation, and cosine similarity—where 0 represents poor correlation and 1 represents perfect correlation [125]. However, these methods work well when there is a linear relationship between spectral features but can perform poorly with complex spectra of multiple mixtures.

One method used to recognize spectral features, otherwise difficult to visualize by the naked eye, is machine learning. Developed algorithms are trained to extract relevant features or patterns in complex spectra and predict the classes of new compounds, thereby improving detection, identification, and classification. Several supervised and unsupervised algorithms have been used in combination with spectroscopic data, including principal component analysis, k-nearest neighbors, random forests, support vector machines and deep learning methods [126–129]. Principal component analysis (PCA)—a dimensionality reduction technique, can also be used for classification, although it is not a preferred technique, or it can be used as a pipeline for discriminant analysis and other classification techniques [19, 120, 130, 131]. k-nearest neighbors (kNN) which performs classification by assigning unlabeled data to a class most similar to the labeled data [132] has been used to classify drugs of abuse [126], tablets [128, 129], and solvents [127]. Support vector machines (SVM) use a decision boundary to separate classes by maximizing their distance using a hyperplane [133]. High accuracy was achieved with SVM when analyzing mixtures of acetaminophen with sugars and inorganic materials [134], adulterated olive oil [135], and the differentiation between human and animal blood [136].

A less commonly used classifier for spectral classification is the naïve bayes (NB) which computes the probability that an unknown sample belongs to a class [137]. A drawback of the NB algorithm is that it assumes each spectral feature is independent which is not the case for spectral data [134]. A commonly used classifier due to its robustness and ability to handle regression and multiclass classification is random forests [126, 127, 138, 139]. Random forests (RF) consist of tree-like classifiers where an input spectrum receives a vote for a class by each tree and assigned to the most popular class determined by the trees [140].

Deep learning methods—an important branch of machine learning, are becoming more prevalent over traditional classification methods due to their ability to extract relevant information about labeled data in more complex datasets which contain non-linearly separable classes. Two algorithms used for Raman spectroscopy include artificial neural networks (NN) and convolutional neural networks (CNN) which are mathematically modeled after the nervous system [141]. CNNs are preferably used for image classification and object recognition over NNs—which can lead to overfitting, making CNNs ideal for spectral comparison [142] as spectra can be considered fingerprints of molecules or crystalline materials. A smart Raman spectrometer was developed to analyze pure compounds, binary and ternary mixtures with 99.9%, 96.7%, and 85.7% accuracy, respectively using a CNN [143].

Whereas many of these techniques have been used post acquisition of the spectra [120, 130, 131][128, 144–148], few have incorporated these methods in portable Raman instruments [143][82, 149]. Additionally, the combination of existing spectral comparison methods with classification techniques have not been explored. When machine learning algorithms are utilized, the main goal is to report a compound, but misclassification is common when new compounds are absent from the instrument's library, or the trained model has not seen the new compound.

In this study, we evaluate the accuracy of six machine learning algorithms— kNN, NB, RF, SVM, NN, and CNN, on pure drug spectra, binary, ternary and quaternary mixtures and compare their accuracy to a recently validated portable Raman instrument which uses a HQI algorithm [150]. The findings presented here can be easily adapted to many other materials and applications.

2.2.0 Methods

2.2.1 Spectra Acquisition

Spectra were acquired using a TacticID portable Raman spectrometer with a 300 mW, 785 nm laser, and 9 cm^{-1} resolution (B&W Tek, Newark, DE). As previously described [150], spectra were measured for 14 drugs—4-methylethcathinone (4-MEC), 4-methylmethcathinone (4-MMC), alprazolam, buprenorphine, cocaine, codeine, fentanyl, heroin, methamphetamine, mitragynine, morphine, naltrexone, PB-22, sufentanil and 15 diluents— acetaminophen, benzocaine, boric acid, caffeine, diltiazem, hydroxyzine, levamisole, lidocaine, maltose, myo-inositol, phenacetin, phenolphthalein, procaine, sorbitol, starch, using a laser power of 60% and 90%. The powder samples were measured through glass vials and 2 mil plastic bags. A total of 444 pure spectra were collected.

The spectra were baseline corrected and truncated to include Raman shifts from 176 to 2000 cm^{-1}. A Savitsky-Golay filter [151] was applied to smooth the spectra with a 5 point window length and third order polynomial.

2.2.2 Spectral Comparison

The cosine similarity and Pearson's correlation were used to compare an authentic test set of pure compounds (referred to as authentic pure set). These compounds included acetaminophen, benzocaine, boric acid, caffeine, diphenhydramine, levamisole, lidocaine, maltose, mannitol, myo-inositol, phenacetin, and procaine. Spectra were acquired in triplicate through 2 mil plastic bags and the instrument was operated at 90% power. A second database was created comprising of the first derivative of the spectra from **section 2.2.1** and comparisons to the test spectra were reported.

2.2.3 Pure Spectra Algorithms

To increase the number of spectra used for training and testing the algorithms, 444,000 spectra were created by multiplying each spectrum by 1000 random numbers between 0 and 1. This introduced variation in the spectra and simulated instances where there might be suppression of signals, hence training the algorithms under the worst-case scenario. Data augmentation is common when spectra are limited for training machine learning algorithms (MLA) [146, 152, 153]. Each spectrum was normalized to its maximum intensity.

Six machine learning algorithms including k-nearest neighbors (kNN), naïve bayes (NB), support vector machine (SVM), random forest (RF), neural network (NN), and convolutional neural network (CNN) were explored. *Scikit-learn v 0.24.1* [154] in python was used for kNN, NB, SVM and RF classifiers. NN and CNN were based on *Keras v 2.4.0* with *Tensorflow v 2.4.1* backend [155]. Two models were created for each algorithm—one based on the compounds (n = 29) where the output is the compounds listed in **Table 2.1** and the second based on the compounds' class (n = 17), also listed in **Table 2.1.** Training was performed on 80% of the data in each class and testing on 20% using the *stratify* argument in the *train_test_split* function in *Scikit-learn*. The optimized parameters selected for the algorithms included *neighbors = 2* for kNN, RF— *estimators = 1000, max depth = 20*, and SVM— *kernel = linear*, regularization parameter -*C =0.09*.

Table 2. 1. The compounds and their designated class used for training the pure spectra algorithms.

Compounds	**Class**
4-MEC	Cathinone
4-MMC	Cathinone
Acetaminophen	Analgesic
Alprazolam	Benzodiazepine
Benzocaine	Anesthetic
Boric acid	Acid
Buprenorphine	Opioid
Caffeine	Stimulant
Cocaine	Cocaine
Codeine	Opioid
Diltiazem	Calcium channel blocker
Fentanyl	Opioid
Hydroxyzine	Antihistamine
Levamisole	Anthelmintic
Lidocaine	Anesthetic
Maltose	Sugar
Methamphetamine	Amphetamine
Mitragynine	Opioid

Compounds	**Class**
Morphine	Opioid
Myo-inositol	Sugar
Naltrexone	Opiate antagonist
PB-22	Cannabinoid
Phenacetin	Analgesic
Phenolphthalein	Dye
Procaine	Anesthetic
Sorbitol	Sugar
Starch	Carbohydrate
Sufentanil	Opioid

The CNN architecture was the same for the compound model and compound class model. The entire spectrum of shape 457x1 was used as the input with 200 3x1 filters in the first convolutional layer, followed by a 2x1 *MaxPooling* layer, a second convolutional layer with 100 3x1 filters, a 2x1 *MaxPooling* layer, a *Flatten* layer and an output layer with 29 units for the compound model and 17 units for the compound class model. The *ReLU* activation function was used in the convolutional layers whereas the *softmax* function was used in the output layer. The model was compiled using the *categorical cross entropy* loss function and the *adam* optimizer function. Early stopping was implemented and the *batch size* for the fitted models was 5.

Two fully connected NN models were created—one for compound, and another for compound class prediction. The compound model contained 457 neurons in the first hidden layer, 20% *dropout* to prevent overfitting [156], 128 and 114 neurons in the second and third hidden layers, respectively, with 10% *dropout* in both layers, the output layer contained 29 units. The compound class model contained 457 neurons in the first hidden layer with 20% *dropout*, 100 neurons in the second, third and fourth layers with 20% *dropout* in the second layer, and 10% in the third and fourth layers. The output layer contained 17 units. Both models used the *sigmoid* activation function in the output layer, the *ReLU* activation function in the hidden layers, a *batch size* of 32 for fitting the model, and implemented early stopping.

The authentic pure set was used to evaluate the models. Two drugs—diphenhydramine (antihistamine), and mannitol (sugar) were not included in the training data and misclassification of these substances were expected with the models trained based on the compounds. However, we evaluated their classification based on the drug class.

2.2.4 Binary Mixture Algorithms

Simulated binary mixtures of the drugs and diluents from **Section 2.2.2** were created using **Equation 2.1**.

$$Mixture = (drug * r) + \left(diluent * (1 - r)\right) \qquad \textbf{Equation 2.1}$$

Where r = [0.05, 0.10, 0.15, 0.20, 0.25, 0.30, 0.35, 0.40, 0.45, 0.50, 0.55, 0.60, 0.65, 0.70, 0.75, 0.80, 0.85, 0.90, 0.95], drug and diluent are the spectrum of each drug or diluent, respectively, and mixture is the resulting spectrum. Machine learning algorithms including SVM, kNN, CNN, NN, NB and RF were first evaluated on this simulated dataset (binary mix #1). A second dataset (binary mix #2) was created by applying a Fast Fourier transformation (FFT) to the spectra and multiplying each intensity by a random number between 0.8 and 1.2 as an additional data augmentation technique, adding unequal variation to the spectra. The two datasets were combined, and algorithms were selected to evaluate the data based upon the reported accuracy on binary mix #1 and the time taken to train the models. Therefore, NB was not selected due to poor accuracy and RF due to longer training times. The combined binary mixtures dataset contained 1,152,312 spectra with 224 unique binary compound mixtures and 88 binary compound class mixtures. A list of the mixtures can be found in **Table 2.2.**

Table 2. 2. Compound mixtures and class mixtures used for binary mixtures algorithms.

Compound Mixtures	Compound Class Mixtures
4-MEC – Acetaminophen	Cathinone – Analgesic
4-MEC – Benzocaine	Cathinone – Anesthetic
4-MEC – Boric acid	Cathinone – Acid
4-MEC – Caffeine	Cathinone – Stimulant
4-MEC – Diltiazem	Cathinone – Calcium Channel Blocker
4-MEC – Hydroxyzine	Cathinone – Antihistamine
4-MEC – Levamisole	Cathinone – Anthelmintic

Compound Mixtures	Compound Class Mixtures
4-MEC – Lidocaine	Cathinone – Anesthetic
4-MEC – Maltose	Cathinone – Sugar
4-MEC – Morphine	Cathinone – Opioid
4-MEC – Myo-inositol	Cathinone – Sugar
4-MEC – Phenacetin	Cathinone – Analgesic
4-MEC – Phenolphthalein	Cathinone – Dye
4-MEC – Procaine	Cathinone – Anesthetic
4-MEC – Sorbitol	Cathinone – Sugar
4-MEC – Starch	Cathinone – Carbohydrate
4-MMC – Acetaminophen	Cathinone – Analgesic
4-MMC – Benzocaine	Cathinone – Anesthetic
4-MMC – Boric acid	Cathinone – Acid
4-MMC – Caffeine	Cathinone – Stimulant
4-MMC – Diltiazem	Cathinone – Calcium Channel Blocker
4-MMC – Hydroxyzine	Cathinone – Antihistamine
4-MMC – Levamisole	Cathinone – Anthelmintic
4-MMC – Lidocaine	Cathinone – Anesthetic
4-MMC – Maltose	Cathinone – Sugar
4-MMC – Morphine	Cathinone – Opioid
4-MMC – Myo-inositol	Cathinone – Sugar
4-MMC – Phenacetin	Cathinone – Analgesic
4-MMC – Phenolphthalein	Cathinone – Dye
4-MMC – Procaine	Cathinone – Anesthetic
4-MMC – Sorbitol	Cathinone – Sugar
4-MMC – Starch	Cathinone – Carbohydrate
Alprazolam – Acetaminophen	Benzodiazepine – Analgesic
Alprazolam – Benzocaine	Benzodiazepine – Anesthetic
Alprazolam – Boric acid	Benzodiazepine – Acid
Alprazolam – Caffeine	Benzodiazepine – Stimulant
Alprazolam – Diltiazem	Benzodiazepine – Calcium Channel Blocker
Alprazolam – Hydroxyzine	Benzodiazepine – Antihistamine
Alprazolam – Levamisole	Benzodiazepine – Anthelmintic

Compound Mixtures	Compound Class Mixtures
Alprazolam – Lidocaine	Benzodiazepine – Anesthetic
Alprazolam – Maltose	Benzodiazepine – Sugar
Alprazolam – Morphine	Benzodiazepine – Opioid
Alprazolam – Myo-inositol	Benzodiazepine – Sugar
Alprazolam – Phenacetin	Benzodiazepine – Analgesic
Alprazolam – Phenolphthalein	Benzodiazepine – Dye
Alprazolam – Procaine	Benzodiazepine – Anesthetic
Alprazolam – Sorbitol	Benzodiazepine – Sugar
Alprazolam – Starch	Benzodiazepine – Carbohydrate
Buprenorphine – Acetaminophen	Opioid – Analgesic
Buprenorphine – Benzocaine	Opioid – Anesthetic
Buprenorphine – Boric acid	Opioid – Acid
Buprenorphine – Caffeine	Opioid – Stimulant
Buprenorphine – Diltiazem	Opioid – Calcium Channel Blocker
Buprenorphine – Hydroxyzine	Opioid – Antihistamine
Buprenorphine – Levamisole	Opioid – Anthelmintic
Buprenorphine – Lidocaine	Opioid – Anesthetic
Buprenorphine – Maltose	Opioid – Sugar
Buprenorphine – Morphine	Opioid – Opioid
Buprenorphine – Myo-inositol	Opioid – Sugar
Buprenorphine – Phenacetin	Opioid – Analgesic
Buprenorphine – Phenolphthalein	Opioid – Dye
Buprenorphine – Procaine	Opioid – Anesthetic
Buprenorphine – Sorbitol	Opioid – Sugar
Buprenorphine – Starch	Opioid – Carbohydrate
Cocaine – Acetaminophen	Cocaine – Analgesic
Cocaine – Benzocaine	Cocaine – Anesthetic
Cocaine – Boric acid	Cocaine – Acid
Cocaine – Caffeine	Cocaine – Stimulant
Cocaine – Diltiazem	Cocaine – Calcium Channel Blocker
Cocaine – Hydroxyzine	Cocaine – Antihistamine
Cocaine – Levamisole	Cocaine – Anthelmintic
Cocaine – Lidocaine	Cocaine – Anesthetic

Compound Mixtures	Compound Class Mixtures
Cocaine – Maltose	Cocaine – Sugar
Cocaine – Morphine	Cocaine – Opioid
Cocaine – Myo-inositol	Cocaine – Sugar
Cocaine – Phenacetin	Cocaine – Analgesic
Cocaine – Phenolphthalein	Cocaine – Dye
Cocaine – Procaine	Cocaine – Anesthetic
Cocaine – Sorbitol	Cocaine – Sugar
Cocaine – Starch	Cocaine – Carbohydrate
Codeine – Acetaminophen	Opioid – Analgesic
Codeine – Benzocaine	Opioid – Anesthetic
Codeine – Boric acid	Opioid – Acid
Codeine – Caffeine	Opioid – Stimulant
Codeine – Diltiazem	Opioid – Calcium Channel Blocker
Codeine – Hydroxyzine	Opioid – Antihistamine
Codeine – Levamisole	Opioid – Anthelmintic
Codeine – Lidocaine	Opioid – Anesthetic
Codeine – Maltose	Opioid – Sugar
Codeine – Morphine	Opioid – Opioid
Codeine – Myo-inositol	Opioid – Sugar
Codeine – Phenacetin	Opioid – Analgesic
Codeine – Phenolphthalein	Opioid – Dye
Codeine – Procaine	Opioid – Anesthetic
Codeine – Sorbitol	Opioid – Sugar
Codeine – Starch	Opioid – Carbohydrate
Fentanyl – Acetaminophen	Opioid – Analgesic
Fentanyl – Benzocaine	Opioid – Anesthetic
Fentanyl – Boric acid	Opioid – Acid
Fentanyl – Caffeine	Opioid - Stimulant
Fentanyl – Diltiazem	Opioid – Calcium Channel Blocker
Fentanyl – Hydroxyzine	Opioid – Antihistamine
Fentanyl – Levamisole	Opioid – Anthelmintic
Fentanyl – Lidocaine	Opioid – Anesthetic
Fentanyl – Maltose	Opioid – Sugar

Compound Mixtures	Compound Class Mixtures
Fentanyl – Morphine	Opioid – Opioid
Fentanyl – Myo-inositol	Opioid – Sugar
Fentanyl – Phenacetin	Opioid – Analgesic
Fentanyl – Phenolphthalein	Opioid – Dye
Fentanyl – Procaine	Opioid – Anesthetic
Fentanyl – Sorbitol	Opioid – Sugar
Fentanyl – Starch	Opioid – Carbohydrate
Heroin – Acetaminophen	Opioid – Analgesic
Heroin – Benzocaine	Opioid – Anesthetic
Heroin – Boric acid	Opioid – Acid
Heroin – Caffeine	Opioid – Stimulant
Heroin – Diltiazem	Opioid – Calcium Channel Blocker
Heroin – Hydroxyzine	Opioid – Antihistamine
Heroin – Levamisole	Opioid – Anthelmintic
Heroin – Lidocaine	Opioid – Anesthetic
Heroin – Maltose	Opioid – Sugar
Heroin – Morphine	Opioid – Opioid
Heroin – Myo-inositol	Opioid – Sugar
Heroin – Phenacetin	Opioid – Analgesic
Heroin – Phenolphthalein	Opioid – Dye
Heroin – Procaine	Opioid – Anesthetic
Heroin – Sorbitol	Opioid – Sugar
Heroin – Starch	Opioid – Carbohydrate
Methamphetamine – Acetaminophen	Amphetamine – Analgesic
Methamphetamine – Benzocaine	Amphetamine – Anesthetic
Methamphetamine – Boric acid	Amphetamine – Acid
Methamphetamine – Caffeine	Amphetamine – Stimulant
Methamphetamine – Diltiazem	Amphetamine – Calcium Channel Blocker
Methamphetamine – Hydroxyzine	Amphetamine – Antihistamine
Methamphetamine – Levamisole	Amphetamine – Anthelmintic
Methamphetamine – Lidocaine	Amphetamine – Anesthetic

Compound Mixtures	Compound Class Mixtures
Methamphetamine – Maltose	Amphetamine – Sugar
Methamphetamine – Morphine	Amphetamine – Opioid
Methamphetamine – Myo-inositol	Amphetamine – Sugar
Methamphetamine – Phenacetin	Amphetamine – Analgesic
Methamphetamine – Phenolphthalein	Amphetamine – Dye
Methamphetamine – Procaine	Amphetamine – Anesthetic
Methamphetamine – Sorbitol	Amphetamine – Sugar
Methamphetamine – Star	Amphetamine – Carbohydrate
Mitragynine – Acetaminophen	Opioid agonist – Analgesic
Mitragynine – Benzocaine	Opioid agonist – Anesthetic
Mitragynine – Boric acid	Opioid agonist – Acid
Mitragynine – Caffeine	Opioid agonist – Stimulant
Mitragynine – Diltiazem	Opioid agonist – Calcium Channel Blocker
Mitragynine – Hydroxyzine	Opioid agonist – Antihistamine
Mitragynine – Levamisole	Opioid agonist – Anthelmintic
Mitragynine – Lidocaine	Opioid agonist – Anesthetic
Mitragynine – Maltose	Opioid agonist – Sugar
Mitragynine – Morphine	Opioid agonist – Opioid
Mitragynine – Myo-inositol	Opioid agonist – Sugar
Mitragynine – Phenacetin	Opioid agonist – Analgesic
Mitragynine – Phenolphthalein	Opioid agonist – Dye
Mitragynine – Procaine	Opioid agonist – Anesthetic
Mitragynine – Sorbitol	Opioid agonist – Sugar
Mitragynine – Starch	Opioid agonist – Carbohydrate
Morphine – Acetaminophen	Opioid – Analgesic
Morphine – Benzocaine	Opioid – Anesthetic
Morphine – Boric acid	Opioid – Acid
Morphine – Caffeine	Opioid – Stimulant
Morphine – Diltiazem	Opioid – Calcium Channel Blocker
Morphine – Hydroxyzine	Opioid – Antihistamine
Morphine – Levamisole	Opioid – Anthelmintic

Compound Mixtures	Compound Class Mixtures
Morphine – Lidocaine	Opioid – Anesthetic
Morphine – Maltose	Opioid – Sugar
Morphine – Morphine	Opioid – Opioid
Morphine – Myo-inositol	Opioid – Sugar
Morphine – Phenacetin	Opioid – Analgesic
Morphine – Phenolphthalein	Opioid – Dye
Morphine – Procaine	Opioid – Anesthetic
Morphine – Sorbitol	Opioid – Sugar
Morphine – Starch	Opioid – Carbohydrate
Naltrexone – Acetaminophen	Opiate antagonist – Analgesic
Naltrexone – Benzocaine	Opiate antagonist – Anesthetic
Naltrexone – Boric acid	Opiate antagonist – Acid
Naltrexone – Caffeine	Opiate antagonist – Stimulant
Naltrexone – Diltiazem	Opiate antagonist – Calcium Channel Blocker
Naltrexone – Hydroxyzine	Opiate antagonist – Antihistamine
Naltrexone – Levamisole	Opiate antagonist – Anthelmintic
Naltrexone – Lidocaine	Opiate antagonist – Anesthetic
Naltrexone – Maltose	Opiate antagonist – Sugar
Naltrexone – Morphine	Opiate antagonist – Opioid
Naltrexone – Myo-inositol	Opiate antagonist – Sugar
Naltrexone – Phenacetin	Opiate antagonist – Analgesic
Naltrexone – Phenolphthalein	Opiate antagonist – Dye
Naltrexone – Procaine	Opiate antagonist – Anesthetic
Naltrexone – Sorbitol	Opiate antagonist – Sugar
Naltrexone – Starch	Opiate antagonist – Carbohydrate
PB-22 – Acetaminophen	Cannabinoid – Analgesic
PB-22 – Benzocaine	Cannabinoid – Anesthetic
PB-22 – Boric acid	Cannabinoid – Acid
PB-22 – Caffeine	Cannabinoid – Stimulant
PB-22 – Diltiazem	Cannabinoid – Calcium Channel Blocker
PB-22 – Hydroxyzine	Cannabinoid – Antihistamine
PB-22 – Levamisole	Cannabinoid – Anthelmintic

Compound Mixtures	Compound Class Mixtures
PB-22 – Lidocaine	Cannabinoid – Anesthetic
PB-22 – Maltose	Cannabinoid – Sugar
PB-22 – Morphine	Cannabinoid – Opioid
PB-22 – Myo-inositol	Cannabinoid – Sugar
PB-22 – Phenacetin	Cannabinoid – Analgesic
PB-22 – Phenolphthalein	Cannabinoid – Dye
PB-22 – Procaine	Cannabinoid – Anesthetic
PB-22 – Sorbitol	Cannabinoid – Sugar
PB-22 – Starch	Cannabinoid – Carbohydrate
Sufentanil – Acetaminophen	Opioid – Analgesic
Sufentanil – Benzocaine	Opioid – Anesthetic
Sufentanil – Boric acid	Opioid – Acid
Sufentanil – Caffeine	Opioid – Stimulant
Sufentanil – Diltiazem	Opioid – Calcium Channel Blocker
Sufentanil – Hydroxyzine	Opioid – Antihistamine
Sufentanil – Levamisole	Opioid – Anthelmintic
Sufentanil – Lidocaine	Opioid – Anesthetic
Sufentanil – Maltose	Opioid – Sugar
Sufentanil – Morphine	Opioid – Opioid
Sufentanil – Myo-inositol	Opioid – Sugar
Sufentanil – Phenacetin	Opioid – Analgesic
Sufentanil – Phenolphthalein	Opioid – Dye
Sufentanil – Procaine	Opioid – Anesthetic
Sufentanil – Sorbitol	Opioid – Sugar
Sufentanil – Starch	Opioid – Carbohydrate

Models were created to evaluate the prediction of compound mixtures and compound class mixtures. The number of *estimators* used for the RF algorithms was 1000, and the depth of each tree set to 20. A *linear* kernel with a regularization parameter of *0.09* were selected for the SVM models.

The entire spectrum of size 457x1, was used as the input for the CNN models. The first convolutional layer contained 200 3x1 filters, followed by a 2x1 *MaxPooling* layer, a convolutional layer with 100 3x1 filters, a second 2x1 *MaxPooling* layer, a *Flatten* layer and a fully connected layer with 224 output units for the compound mixtures model and 88 units for the compound class mixtures model. The minimum *validation loss* was monitored, and the best model used to evaluate the test data. The model was fitted using a *batch size* of 5.

Fully connected NN models were created with 457 neurons in the first hidden layer with 20% *dropout*, 114 neurons in the second and third layers with 20% *dropout* in the second layer and 10% *dropout* in the third, 36 neurons in the fourth layer with 10% *dropout*, and the output layer with 224 units for the compound mixtures model and 88 for the compound class mixtures model. The *batch size* for both fitted models were 64.

To demonstrate the accuracy of the models, spectra from authentic in-house binary drug: diluent mixtures (n = 186) previously acquired using the TacticID instrument [150] were used to evaluate the algorithms and to compare with the instrument's reported results. The drug: diluent ratios were 1:4, 1:7, 1:10, and 1:20. As an example, for a 1:7 ratio, 10 mg of the drug and 70 mg of the diluent were mixed prior to analysis. Selected classifiers which included SVM, kNN, NN, and CNN were used to test the authentic in-house mixtures. The accuracy of the predictions was based on the three highest probabilities that a compound belonged to a class.

2.2.5 Ternary Mixture Algorithms

Selected ternary mixtures were created from the spectra in **Section 2.2.1**. using **Equation 2.2.**

$$Ternary\ Mixture = (drug * 0.05) + \left(diluent1 * \frac{(1-0.05)}{2}\right) + \left(diluent2 * \frac{(1-0.05)}{2}\right) \quad \textbf{Equation 2.2}$$

The resulting spectra were processed using the Fast Fourier Transformation (FFT) and multiplied by a random number between 0.8 and 1.2 as a data augmentation technique which introduced unequal variations in peak intensities. A total of 829,440 spectra were created and there were 60 ternary compound mixtures and 50 ternary compound class mixtures. A list of the mixtures can be found in **Table 2.3 and 2.4.** The evaluated algorithms included CNN, kNN, NN, and SVM. A *linear* kernel was used for the SVM models, with a regularization parameter of *0.09* for both the compound mixtures model and compound class mixtures model. The CNN models contained 200 3x1 filters in the first convolutional layer, a 2x1 *MaxPooling* layer, a convolutional layer with 100

3 x 1 filters, a *MaxPooling* layer, a *Flatten* layer, and a fully connected layer with a *softmax* activation function. The *ReLU* activation function was used in all convolutional layers. The model was compiled using the *categorical cross entropy* loss function and *adam* optimizer function. Early stopping allowed for the best model to be saved based on the minimum *validation loss*, with the *patience* parameter set to 10, and the *batch size* to 5.

Table 2. 3. Ternary compound mixtures.

4MEC – Acetaminophen – Benzocaine	Cocaine– Benzocaine – Maltose	Methamphetamine– Acetaminophen – Levamisole
Alprazolam – Acetaminophen – Benzocaine	Codeine– Benzocaine – Maltose	PB22– Acetaminophen – Levamisole
4MEC– Acetaminophen – Caffeine	Cocaine – Caffeine – Maltose	Methamphetamine – Benzocaine – Caffeine
Alprazolam – Acetaminophen – Caffeine	Codeine – Caffeine – Maltose	PB22– Benzocaine – Caffeine
4MEC– Acetaminophen – Maltose	Cocaine – Diltiazem– Levamisole	Methamphetamine – Benzocaine – Levamisole
Alprazolam – Acetaminophen – Maltose	Codeine – Diltiazem – Levamisole	PB22– Benzocaine – Levamisole
4MEC– Benzocaine – Caffeine	Cocaine – Diltiazem – Lidocaine	Methamphetamine – Caffeine – Levamisole
Alp– Benzocaine – Caffeine	Codeine – Diltiazem – Lidocaine	PB22– Caffeine – Levamisole
4MEC– Benzocaine – Maltose	Cocaine – Diltiazem – Phenacetin	Fentanyl– Acetaminophen – Caffeine
Alprazolam – Benzocaine – Maltose	Codeine – Diltiazem – Phenacetin	Heroin – Acetaminophen – Caffeine
4MEC– Caffeine – Maltose	Cocaine – Levamisole– Lidocaine	Fentanyl– Acetaminophen – Lidocaine

Alprazolam – Caffeine – Maltose	Codeine – Levamisole – Lidocaine	Heroin – Acetaminophen – Lidocaine
Cocaine – Acetaminophen – Benzocaine	Cocaine – Levamisole – Phenacetin	Fentanyl – Acetaminophen – Procaine
Codeine– Acetaminophen – Benzocaine	Codeine – Levamisole – Phenacetin	Heroin – Acetaminophen – Procaine
Cocaine – Acetaminophen – Caffeine	Cocaine – Lidocaine – Phenacetin	Fentanyl – Caffeine – Lidocaine
Codeine – Acetaminophen – Caffeine	Codeine – Lidocaine – Phenacetin	Heroin – Caffeine – Lidocaine
Cocaine – Acetaminophen – Maltose	Methamphetamine – Acetaminophen – Benzocaine	Fentanyl – Caffeine – Procaine
Codeine – Acetaminophen – Maltose	PB22– Acetaminophen – Benzocaine	Heroin – Caffeine – Procaine
Cocaine – Benzocaine – Caffeine	Methamphetamine – Acetaminophen – Caffeine	Fentanyl – Lidocaine – Procaine
Codeine – Benzocaine – Caffeine	PB22– Acetaminophen – Caffeine	Heroin– Lidocaine– Procaine

Table 2. 4. Ternary compound class mixtures.

Cathinone-Analgesic-Anesthetic	Cocaine-Anesthetic-Sugar	Amphetamine-Analgesic-Anthelmintic
Benzodiazepine-Analgesic-Anesthetic	Opioid-Anesthetic-Sugar	Cannabinoid-Analgesic-Anthelmintic
Cathinone-Analgesic-Stimulant	Cocaine-Stimulant-Sugar	Amphetamine-Anesthetic-Stimulant
Benzodiazepine-Analgesic-Stimulant	Opioid-Stimulant-Sugar	Cannabinoid-Anesthetic-Stimulant
Cathinone-Analgesic-Sugar	Cocaine-Calcium Channel Blocker-Anthelmintic	Amphetamine-Anesthetic-Anthelmintic
Benzodiazepine-Analgesic-Sugar	Opioid-Calcium Channel Blocker-Anthelmintic	Cannabinoid-Anesthetic-Anthelmintic
Cathinone-Anesthetic-Stimulant	Cocaine-Calcium Channel Blocker-Anesthetic	Amphetamine-Stimulant-Anthelmintic
Benzodiazepine-Anesthetic-Stimulant	Opioid-Calcium Channel Blocker-Anesthetic	Cannabinoid-Stimulant-Anthelmintic

Cathinone-Anesthetic-Sugar	Cocaine-Calcium Channel Blocker-Analgesic	Opioid-Stimulant-Anesthetic
Benzodiazepine-Anesthetic-Sugar	Opioid-Calcium Channel Blocker-Analgesic	Opioid-Anesthetic-Anesthetic
Cathinone-Stimulant-Sugar	Cocaine-Anthelmintic-Anesthetic	
Benzodiazepine-Stimulant-Sugar	Opioid-Anthelmintic-Anesthetic	
Cocaine-Analgesic-Anesthetic	Cocaine-Anthelmintic-Analgesic	
Opioid-Analgesic-Anesthetic	Opioid-Anthelmintic-Analgesic	
Cocaine-Analgesic-Stimulant	Cocaine-Anesthetic-Analgesic	
Opioid-Analgesic-Stimulant	Opioid-Anesthetic-Analgesic	
Cocaine-Analgesic-Sugar	Amphetamine-Analgesic-Anesthetic	
Opioid-Analgesic-Sugar	Cannabinoid-Analgesic-Anesthetic	
Cocaine-Anesthetic-Stimulant	Amphetamine-Analgesic-Stimulant	
Opioid-Anesthetic-Stimulant	Cannabinoid-Analgesic-Stimulant	

The NN models for compound mixtures and compound class mixtures were fully connected with 457 neurons in the first hidden layer, 20% dropout, 114 neurons in the second layer, 20% dropout, 114 neurons in the third layer, 10% dropout, and 36 neurons in the fourth layer with 10% dropout. The output layer contained 60 units for the compound mixtures model and 50 units for the compound class mixtures model using the *sigmoid* activation function. The *ReLU* activation function was used for all other layers. Early stopping was implemented and the model with the minimum *validation loss* was saved. The model was fitted with the *patience* parameter of 5, and *batch size* of 16 for the compound mixtures model and 24 for the compound class mixtures model.

2.2.6 Quaternary Mixture Algorithms

Three subsets of quaternary mixtures were created from the spectra in **Section 2.2.1** using **Equation 2.3.** The value 0.05 was selected to simulate the effect of high signal suppression of the drug in comparison to the diluents, as is usually the case in street drug mixtures, although this methodology can be easily generalized to other compounds. The spectra were also processed using the FFT prior to evaluation using machine learning algorithms created for classification by compound mixture and compound class mixture. SVM, kNN, CNN and NN were used to evaluate

the data. A *linear* kernel with *0.09* regularization was used for all SVM models. The number of layers, neurons and batch size were optimized for each model.

$$Quaternary\ Mixture = (drug * 0.05) + \left(diluent1 * \frac{(1-0.05)}{3}\right) + \left(diluent2 * \frac{(1-0.05)}{3}\right) + \left(diluent3 * \frac{(1-0.05)}{3}\right) \quad \textbf{Equation 2.3}$$

2.2.6.1 Subset 1

Subset 1 contained 4 quaternary mixtures of cocaine with acetaminophen, diltiazem, and hydroxyzine. See **Table 2.5** for additional information about the mixtures. A total of 663,552 spectra were created in this set. The entire Raman spectrum (457x1) was used as the input for the CNN models. The first convolutional layer for the compound mixtures model contained 200 3x1 filters with *ReLU* activation, a *MaxPooling* layer, followed by another convolutional layer with 100 3x1 filters, a second *MaxPooling* layer, a *Flatten* layer, followed by a fully connected layer with the *softmax* activation function, and compiled with *categorical cross entropy* loss and the *adam* optimizer function. Early stopping was implemented where the best model was saved for the minimum validation loss, with *patience* set to 10 and *batch size* to 5. The same parameters were selected for the CNN compound class mixtures model.

Table 2. 5. Subset 1 mixtures.

Compound Mixtures	**Compound Class Mixtures**
Cocaine- Acetaminophen-Diltiazem-Hydroxyzine	Cocaine- Analgesic- Calcium channel blocker-Antihistamine
Cocaine- Acetaminophen-Diltiazem-Procaine	Cocaine- Analgesic-calcium channel blocker-Anesthetic
Cocaine- Acetaminophen-Hydroxyzine-Procaine	Cocaine- Analgesic- Antihistamine-Anesthetic
Cocaine- Diltiazem-Hydroxyzine-Procaine	Cocaine-Calcium Channel Blocker-Antihistamine-Anesthetic

A fully connected NN was created for both the compound mixtures model and compound class mixtures model, with the same architecture. There were 457 neurons in the first hidden layer, followed by 20% dropout, 128 neurons with 20% dropout and 64 neurons with 10% dropout with the output layer containing a *sigmoid* activation function. All other layers used the *ReLU* activation function. The minimum validation loss was monitored with *patience* set to 5, and *batch size* to 64 as early stopping was implemented.

2.2.6.2 Subset 2

Subset 2 comprised of 1,327,104 spectra. Quaternary mixture combinations were created with the drug as buprenorphine and naltrexone and the diluents as acetaminophen, caffeine, procaine, and maltose. This resulted in 8 compound mixtures and a complete description can be found in **Table 2.6.** The same architecture and parameters described in **Section 2.2.6.1** were selected to create CNN models for compound mixtures and compound class mixtures.

Table 2. 6. Subset 2 mixtures.

Compound Mixtures	**Compound Class Mixtures**
Buprenorphine -Acetaminophen – Caffeine - Maltose	Opiate antagonist- Analgesic- Stimulant- Anesthetic
Buprenorphine- Acetaminophen _Caffeine- Procaine	Opiate antagonist- Analgesic- Stimulant- Sugar
Buprenorphine- Acetaminophen- Maltose- Procaine	Opiate antagonist- Analgesic- Sugar- Anesthetic
Buprenorphine- Caffeine- Maltose- Procaine	Opiate antagonist- Stimulant- Sugar- Anesthetic
Naltrexone- Acetaminophen- Caffeine- Maltose	Opioid- Analgesic- Stimulant- Anesthetic
Naltrexone- Acetaminophen- Caffeine- Procaine	Opioid- Analgesic- Stimulant- Sugar

Compound Mixtures	Compound Class Mixtures
Naltrexone- Acetaminophen- Maltose- Procaine	Opioid- Analgesic- Sugar- Anesthetic
Naltrexone- Caffeine- Maltose- Procaine	Opioid- Stimulant- Sugar- Anesthetic

The NN models had the same architecture with 228 neurons in the first hidden layer followed by 10% dropout, 152 neurons in the second layer with 10% dropout, an output layer with the *sigmoid* activation function and the *ReLU* activation function in the other layers. The *batch size* was 32, *patience* set to 5 and the minimum *validation loss* monitored for early stopping during training of the models.

2.2.6.3 Subset 3

The quaternary mixtures in subset 4 contained codeine and morphine as drugs, and acetaminophen, caffeine, lidocaine, maltose as diluents. A total of 8 compound mixture classes (**Table 2.7**) were created with 1,327,104 spectra. The architectures of the CNN models described in **Section 2.2.6.1** were used to evaluate the data in subset 3.

Table 2. 7. Subset 3 mixtures.

Compound Mixtures	Compound Class Mixtures
Codeine- Acetaminophen- Caffeine- Lidocaine	Opioid- Analgesic- Stimulant- Anesthetic
Codeine- Acetaminophen- Caffeine- Maltose	Opioid- Analgesic- Stimulant- Sugar
Codeine- Acetaminophen- Lidocaine- Maltose	Opioid- Analgesic- Anesthetic- Sugar
Codeine- Caffeine- Lidocaine- Maltose	Opioid- Stimulant- Anesthetic- Sugar
Morphine- Acetaminophen- Caffeine- Lidocaine	
Morphine- Acetaminophen- Caffeine- Maltose	
Morphine- Acetaminophen- Lidocaine- Maltose	
Morphine- Caffeine- Lidocaine- Maltose	

The NN model created to evaluate the data by compound mixtures contained 304 neurons in the first hidden layer with 10% *dropout*, 76 in the second layer with 10% *dropout*, 152 in the third layer with 10% *dropout*, and 76 in the fourth layer with 10% *dropout*. The *sigmoid* activation function was used in the output layer, and the *ReLU* activation function in all other layers. Early stopping was implemented by monitoring the minimum *validation loss*, *patience* set to 5, and a *batch size* of 64. The compound class mixtures model was similar, but the first, second and third hidden layers contained 228, 57, and 114 neurons, respectively. The optimized *batch size* was 32.

A summary of the methods is shown in **Figure 2.1.**

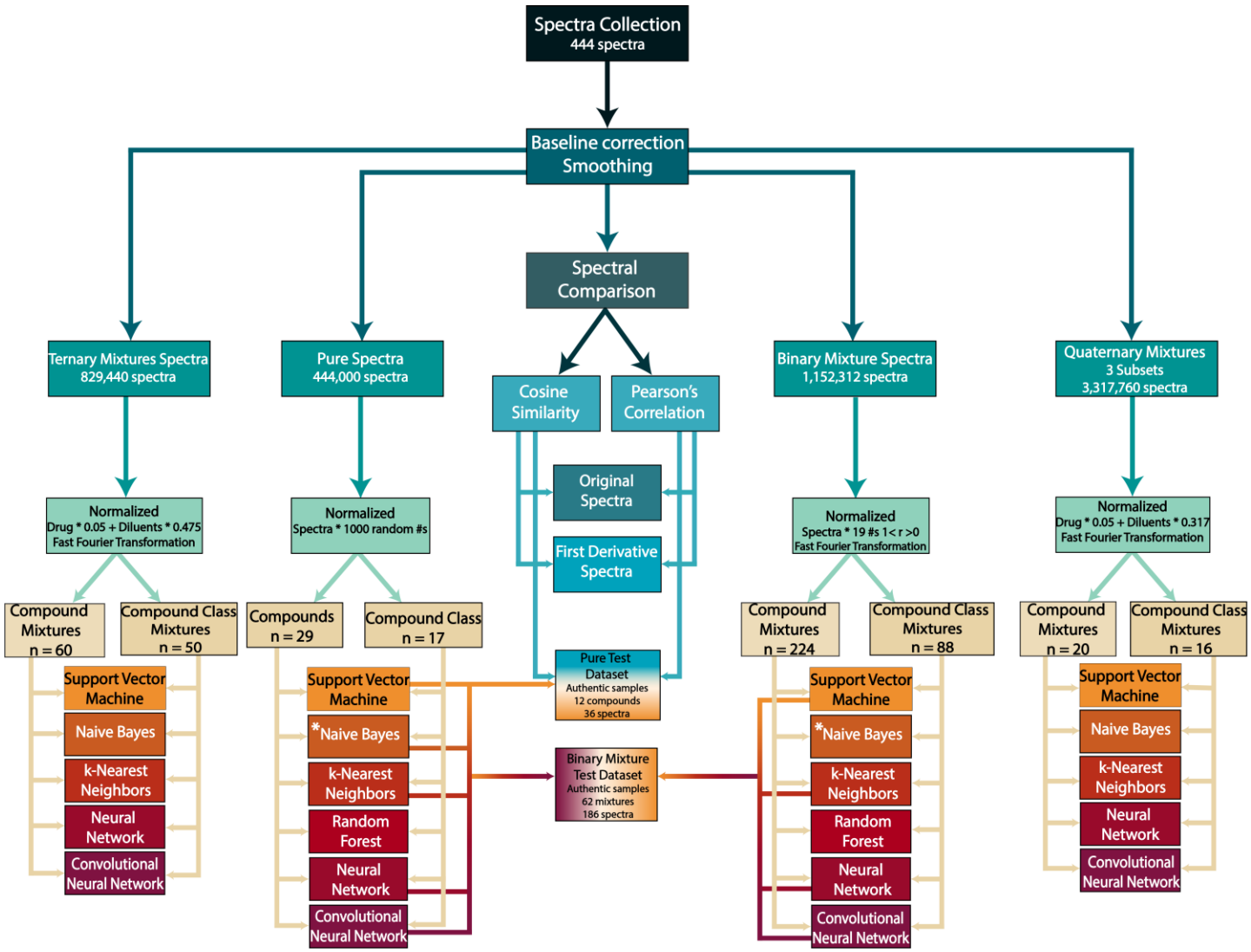

Figure 2. 1. Summary of the workflow used in this study. *— The Naïve Bayes algorithm was not used to evaluate the authentic pure test and authentic binary mixture datasets. All simulated datasets excluding the pure spectra dataset included Fast Fourier transformed data. The Quaternary mixture dataset contained a total of 3,317,760 spectra and was divided into 3 subsets: subset 1 contained 663,552 spectra with 4 compound mixtures and 4 compound class mixtures; subset 2 contained 1,327,104 spectra with 8 compound mixtures and 8 compound class mixtures; and subset 3 contained 1,327,104 spectra with 8 compound mixtures and 4 compound class mixtures.

2.3.0 Results

2.3.1 Spectra Creation and Comparison

A visual representation of the pure simulated spectra and binary, ternary, and quaternary mixtures recreation is shown in **Figure 2.2.** Mixtures were created to represent complex combinations of drugs and diluents that represent common street drugs as well as worst case scenarios. Multiplication of the pure spectra by numbers between 0 and 1 resulted in a relative suppression or scaling of the signal intensities (**Figure 2.2A)**. **Figure 2.2B** shows the individual spectrum of maltose and morphine and the differences in the number, shape, and intensity of the peaks characteristic of each compound. When the mixtures were simulated, the peak at 1640 cm^{-1} for morphine decreased relative to the diluent— maltose, when the ratio of maltose to morphine was higher (**Figure 2.2C**). For example, when the morphine spectrum was multiplied by 0.90 and the maltose spectrum multiplied by 0.10, then combined, the resulting spectrum demonstrated more features similar to morphine. **Figure 2.2D** shows the effect of applying the Fast Fourier transformation to the spectra. Some peak intensities are higher whereas others are lower than those in the original spectrum. Additionally, noise is added in random portions of the spectrum. **Figure 2.2E** and **2.2F** demonstrate the spectrum of a ternary and quaternary mixture, respectively. The deliberate suppression of the drug spectrum in relation to the diluents in both the ternary and quaternary mixture makes it difficult to identify the Raman bands unique to the drugs—codeine for the ternary mixture, and buprenorphine for the quaternary mixture.

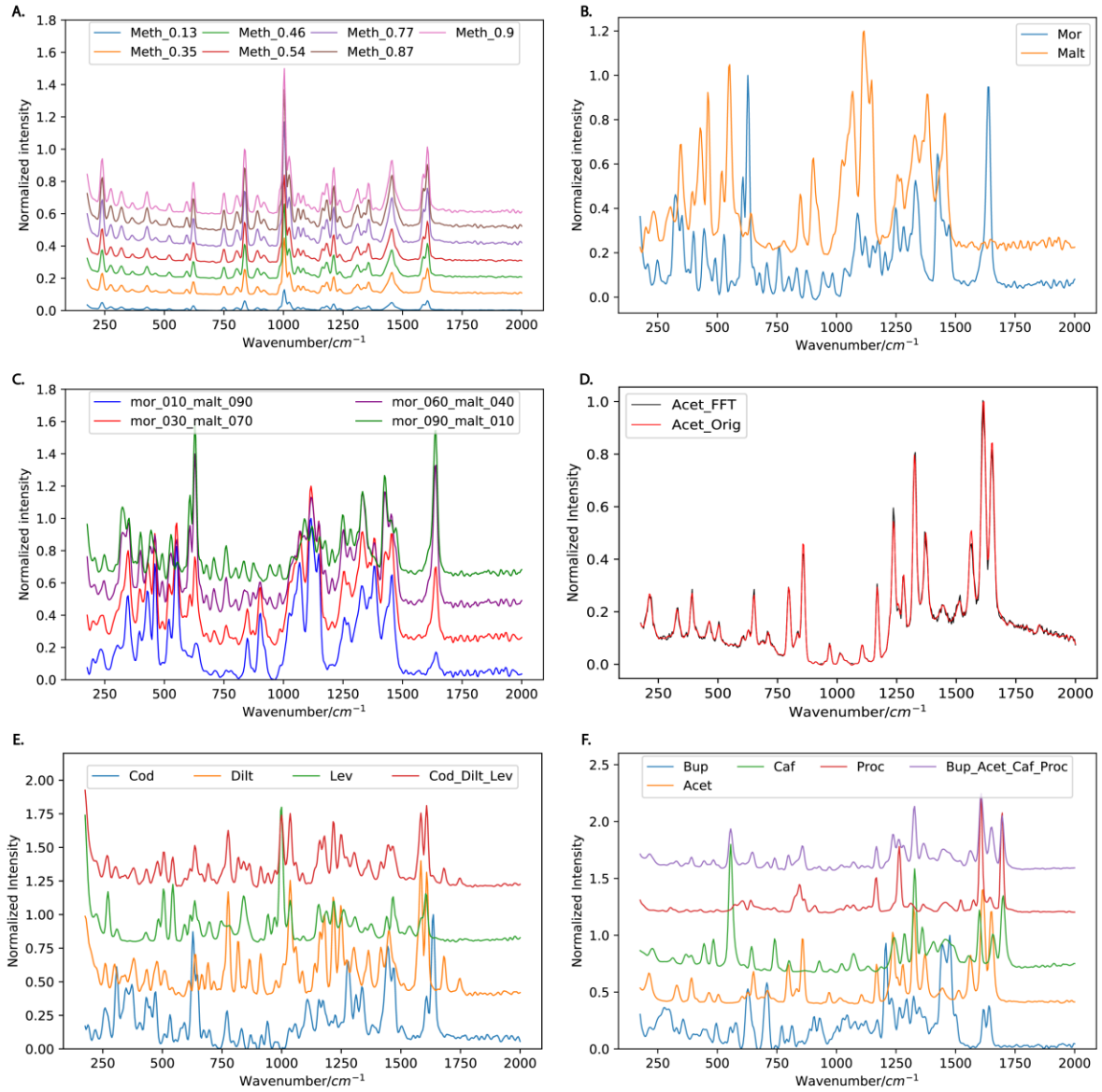

Figure 2. 2. (A)– Illustration of the resulting spectra when a methamphetamine (Meth) spectrum is multiplied by 0.13, 0.35, 0.46, 0.54, 0.77, 0.87, 0.90. (B)–Comparison of maltose (Malt) and morphine (Mor) spectrum. (C)– Illustrations of the resulting simulated spectra for morphine (multiplied by 0.1, 0.3, 0.6, 0.9) and maltose (multiplied by 0.9, 0.7, 0.4, 0.1). (D)– The spectrum of acetaminophen before (Acet_Orig) and after Fast Fourier transformation (Acet_FFT). (E)– Creation of a ternary mixture of codeine, diltiazem, and levamisole with the codeine signal suppressed to 5% of the original spectrum. (F)–Creation of a quaternary mixture containing buprenorphine, acetaminophen, caffeine, and procaine with 5% suppression of the buprenorphine signal.

The cosine similarity and Pearson's correlation coefficient for the authentic pure set is shown in **Figure 2.3**. Although lower scores were observed when making comparisons of the first derivative spectra, all scores were greater than 0.90 with the cosine similarity, and greater than 0.86 with the Pearson's correlation. Comparisons on the pure test set using the cosine similarity resulted in methamphetamine having the highest similarity to diphenhydramine (0.820), and sorbitol having the highest similarity to mannitol (0.878). When comparisons were made using the first derivative algorithm combining the cosine similarity, the results were the same between mannitol and sorbitol, but the score was 0.640. Diphenhydramine was also most similar to fentanyl (0.717) using the first derivative comparison. The Pearson's correlation resulted in mannitol and sorbitol being most similar (0.817 and 0.640 for the original spectra and first derivative spectra algorithms respectively). Fentanyl and methamphetamine were also reported as the closest compounds to diphenhydramine. Although the first derivative provides lower correlation scores than the original spectral correlations, they are not markedly different.

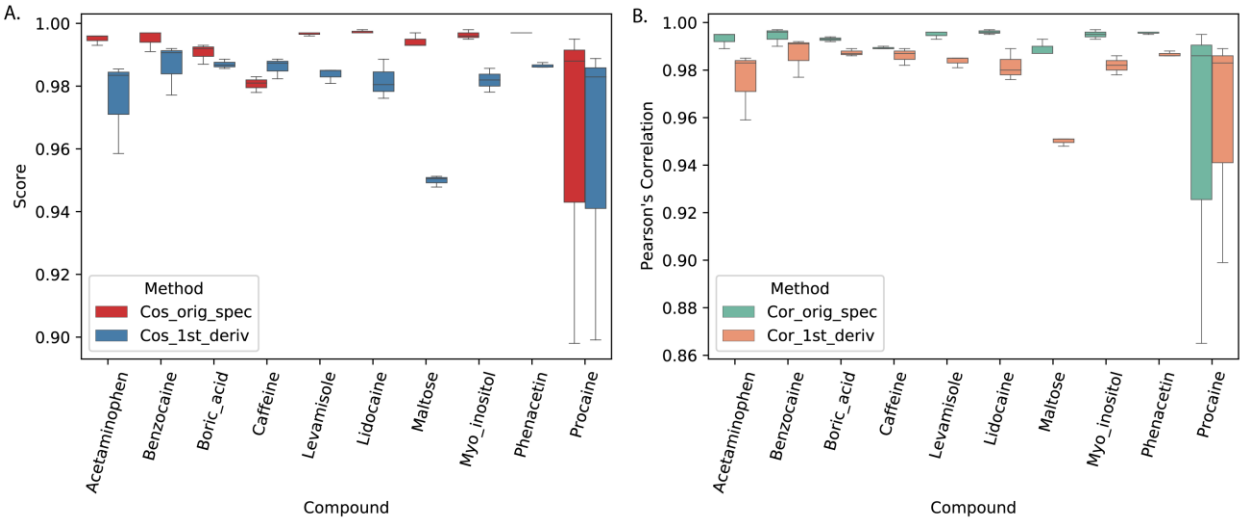

Figure 2. 3. Distribution of cosine scores (A), and correlation coefficients (B) of the test data. The scores for the comparisons between the original spectra and first derivative spectra are shown. Diphenhydramine and mannitol are not included since they were not present in the database.

2.3.2 Pure Spectra

Exploratory analysis of the 444 pure spectra using PCA of the original spectra and the first derivative spectra is shown in **Figure 2.4.** Plots of the first two principal components of the original

spectra labeled by compound and class show overlap of the clusters making PCA a challenge for classification of this dataset. The explained variance in the first two components were 34% and 9%. Although some clusters are more separated when the first derivative of the spectra is computed (**Figure 2.4C, 2.4D**), others still overlap. Linear discriminant analysis (LDA) results in higher separation of the classes, but overlap is still observed for few drugs and classes (**Figure 2.5**). As a result, neither PCA nor LDA were used for further evaluation of the data in this study. Various machine learning algorithms were then evaluated in the pure spectra dataset, as explained below.

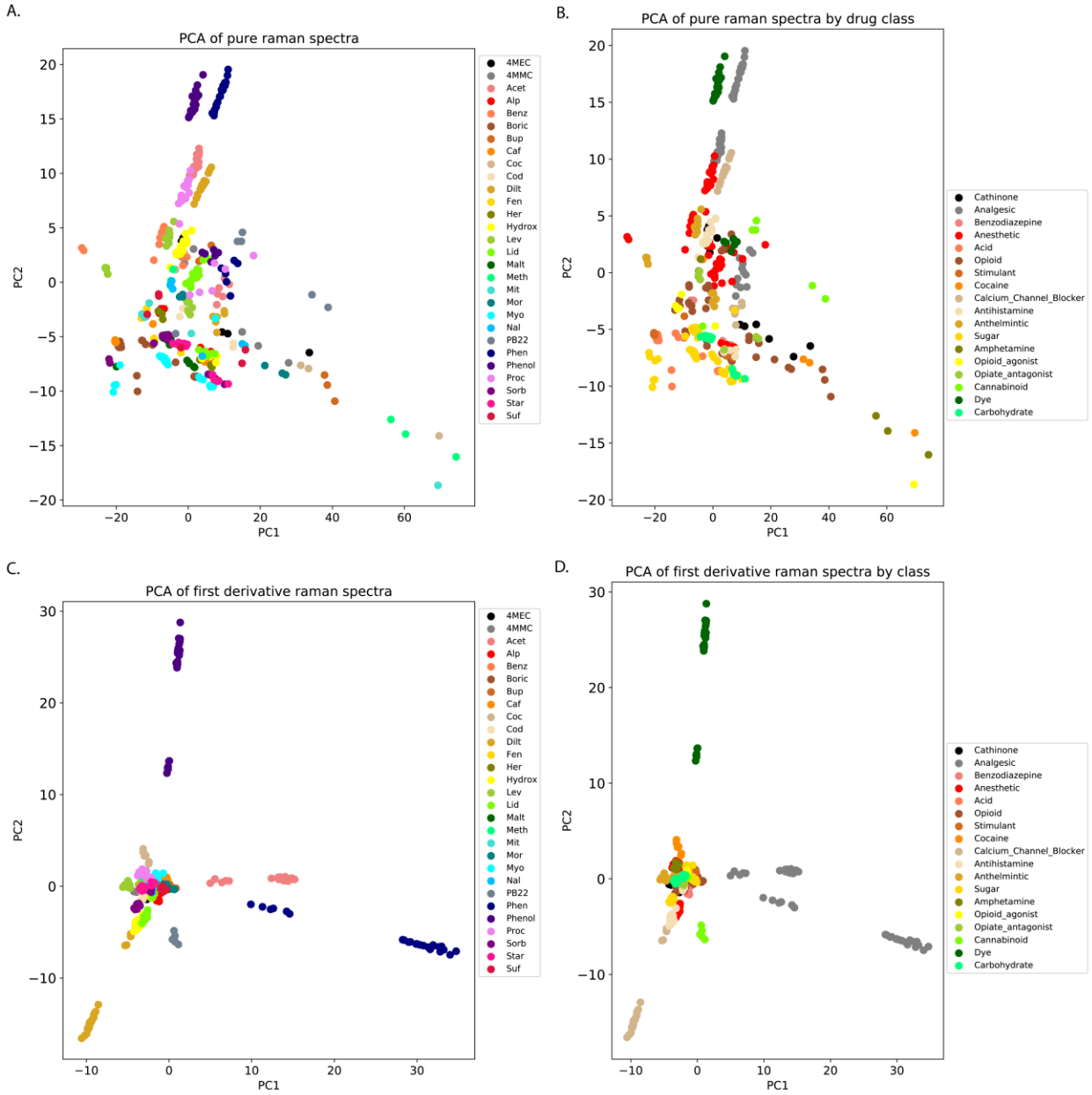

Figure 2. 4. Principal component analysis on the 444 spectra acquired using the TacticID instrument. (A)–Original spectra labeled by compound. (B) – Original spectra labeled by compound class. Note there are 18 compound classes used here for illustration. (C) –First derivative spectra labeled by compound. (D) –First derivative spectra labeled by compound class.

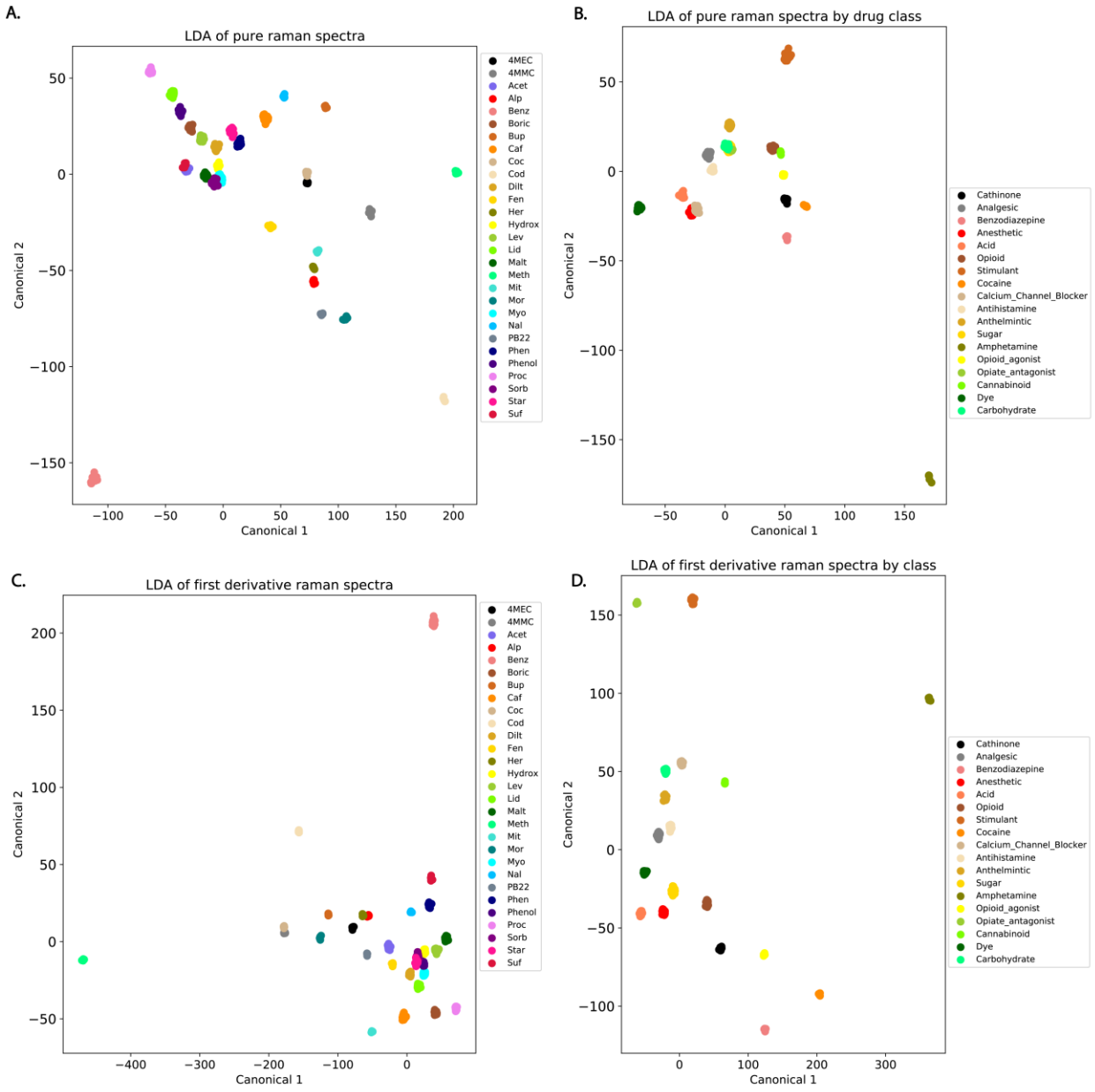

Figure 2. 5. Linear discriminant analysis of the 444 pure spectra. A– Canonical plot for the original spectra labeled by compounds. Variance in the canonical variable 1 is 23% and 15% in canonical variable 2. B– Canonical plot of the original spectra for the compound classes. The variance in the two canonical variables were 24% and 15%. C–Canonical plot of the first derivative spectra labeled by compound. The variance in the two canonical variables were 26% and 14%. D– Canonical plot for the first derivative spectra labeled by class. The variance in the two canonical variables were 24% and 21%. Note that for illustration, there are 18 classes in B and C.

The performance of the method was evaluated as correct identification or accuracy. Correct identification was evaluated for the authentic datasets (pure and binary mixtures) where True positives and False negatives were considered. The models created from the simulated data were evaluated using accuracy. True positive (T_p), False positive (F_p), and their respective True negative (T_n) and False negative (F_n) were used in the calculation of accuracy. Accuracy is given by **Equation 2.4.** Precision or the positive predictive value is given by **Equation 2.5**. Recall, true positive rate, or sensitivity is given by **Equation 2.6.** The F1-score—the harmonic mean of precision and recall is given by **Equation 2.7**.

$$Accuracy = \frac{T_p + T_n}{T_p + T_n + F_p + F_n} \qquad \boldsymbol{Equation\ 2.4}$$

$$Precision(P) = \frac{T_p}{T_p + F_p} \qquad \textbf{Equation 2.5}$$

$$Recall(R) = \frac{T_p}{T_p + F_n} \qquad \textbf{Equation 2.6}$$

$$F1 - score = 2 * \frac{P * R}{P + R} \qquad \boldsymbol{Equation\ 2.7}$$

The average accuracies of the kNN, RF and CNN algorithms for compound and compound class were 100% (**Table 2.8).** The SVM resulted in 99% accuracy for both models whereas the NN resulted in 98% for the compound model and 99% for the class model. The NB models resulted in the lowest accuracies for both models—68% for compound and 67% for compound class.

All models except the NB algorithm were used to evaluate the authentic pure set. Only the CNN resulted in 100% correct identification for both compound and class (**Table 2.8).** This also included correctly classifying diphenhydramine and mannitol by compound class even though they were not included in the training data. However, they were misclassified by compound because the training data did not contain their labels. The RF model resulted in correct identifications of

97% for compounds and 94% for compound classes. The next best model—kNN, resulted in 93% correct identification for compounds and 86% for compound classes. The model with the lowest correct identification for reporting compounds and class was the SVM with 80% and 56%, respectively. Although at least 80% correct compound identification in the top 3 hits was observed for all models, only the CNN resulted in the top hit corresponding to the ground truth compounds.

Complete classification reports can be found in **Tables 2.9 – 2.19**. Macro average is the accuracy of each label is calculated, and the unweighted mean is reported. Imbalance is not considered. Weighted average is the average accuracy of all labels, weighted by the number of true instances for each label.

Table 2. 8. Comparison of the algorithms' accuracy and evaluation of the models on an authentic pure test dataset. The pure test set accuracy is based on compound's presence in the top three hits.

	kNN		**NB**		**RF**		**SVM**		**NN**		**CNN**	
	Compound	**Class**	**Compound**	**Class**	**Compound**	**Class**	**Compound**	**Class**	**Compound**	**Class**	**Compound**	**Class**
Model Accuracy (%)	100	100	68	67	100	100	99	99	98	99	100	100
Pure Test Set Correct identification (%)	93	86	---	---	97	94	80	56	90	86	100	100

Table 2. 9. KNN Pure 444000 compound accuracy.

	Precision	**Recall**	**F1-score**	**Support**
4-MEC	0.998	1.000	0.999	1200
4-MMC	1.000	0.999	1.000	1200
Acetaminophen	1.000	1.000	1.000	4800
Alprazolam	0.998	1.000	0.999	1200
Benzocaine	1.000	1.000	1.000	4800
Boric acid	1.000	1.000	1.000	4800
Buprenorphine	1.000	1.000	1.000	1200
Caffeine	1.000	1.000	1.000	4800

	Precision	Recall	F1-score	Support
Cocaine	0.998	1.000	0.999	1200
Codeine	1.000	1.000	1.000	1200
Diltiazem	1.000	1.000	1.000	4800
Fentanyl	0.999	0.999	0.999	1200
Heroin	0.998	1.000	0.999	1200
Hydroxyzine	1.000	1.000	1.000	4800
Levamisole	1.000	1.000	1.000	4800
Lidocaine	1.000	1.000	1.000	4800
Maltose	1.000	1.000	1.000	4800
Methamphetamine	0.999	0.998	0.999	1200
Mitragynine	0.998	0.994	0.996	1200
Morphine	0.999	1.000	1.000	1200
Myo-inositol	1.000	1.000	1.000	4800
Naltrexone	1.000	0.999	1.000	1200
PB-22	1.000	0.998	0.999	1200
Phenacetin	1.000	1.000	1.000	4800
Phenolphthalein	1.000	1.000	1.000	4800
Procaine	1.000	1.000	1.000	4800
Sorbitol	1.000	1.000	1.000	4800
Starch	1.000	1.000	1.000	4800
Sufentanil	1.000	1.000	1.000	1200
accuracy	**1.000**	**1.000**	**1.000**	**1.000**
macro avg	**1.000**	**1.000**	**1.000**	**88800**
weighted avg	**1.000**	**1.000**	**1.000**	**88800**

Table 2. 10. KNN Pure 444000 compound class accuracy.

	Precision	Recall	F1-score	Support
Acid	1.000	1.000	1.000	4800
Amphetamine	0.998	1.000	0.999	1200

	Precision	Recall	F1-score	Support
Analgesic	1.000	1.000	1.000	9600
Anesthetic	1.000	1.000	1.000	14400
Anthelmintic	1.000	1.000	1.000	4800
Antihistamine	1.000	1.000	1.000	4800
Benzodiazepine	0.999	1.000	1.000	1200
Calcium channel blocker	1.000	1.000	1.000	4800
Cannabinoid	0.993	0.999	0.996	1200
Carbohydrate	1.000	1.000	1.000	4800
Cathinone	1.000	1.000	1.000	2400
Cocaine	1.000	0.998	0.999	1200
Dye	1.000	1.000	1.000	4800
Opiate	1.000	1.000	1.000	1200
Opioid	1.000	0.999	0.999	8400
Stimulant	1.000	1.000	1.000	4800
Sugar	1.000	1.000	1.000	14400
accuracy	**1.000**	**1.000**	**1.000**	**1.000**
macro avg	**0.999**	**1.000**	**1.000**	**88800**
weighted avg	**1.000**	**1.000**	**1.000**	**88800**

Table 2. 11. NB Pure 444000 compound accuracy.

	Precision	Recall	F1-score	Support
4-MEC	0.766	0.698	0.730	1200
4-MMC	0.758	0.698	0.727	1200
Acetaminophen	1.000	0.740	0.850	4800
Alprazolam	0.665	0.620	0.642	1200
Benzocaine	0.340	0.954	0.502	4800
Boric acid	0.357	0.705	0.473	4800
Buprenorphine	0.888	0.649	0.750	1200
Caffeine	0.954	0.545	0.694	4800
Cocaine	0.940	0.644	0.765	1200

	Precision	Recall	F1-score	Support
Codeine	0.916	0.731	0.813	1200
Diltiazem	1.000	0.674	0.806	4800
Fentanyl	0.390	0.436	0.412	1200
Heroin	0.728	0.629	0.675	1200
Hydroxyzine	0.901	0.671	0.769	4800
Levamisole	0.654	0.718	0.684	4800
Lidocaine	1.000	0.654	0.791	4800
Maltose	0.837	0.632	0.720	4800
Methamphetamine	0.855	0.478	0.613	1200
Mitragynine	0.102	0.345	0.158	1200
Morphine	1.000	0.664	0.798	1200
Myo-inositol	0.702	0.621	0.659	4800
Naltrexone	0.758	0.635	0.691	1200
PB-22	0.506	0.763	0.608	1200
Phenacetin	0.936	0.792	0.858	4800
Phenolphthalein	1.000	0.839	0.913	4800
Procaine	0.876	0.731	0.797	4800
Sorbitol	0.813	0.517	0.632	4800
Starch	1.000	0.685	0.813	4800
Sufentanil	0.508	0.571	0.538	1200
accuracy	**0.682**	**0.682**	**0.682**	**0.682**
macro avg	**0.764**	**0.657**	**0.686**	**88800**
weighted avg	**0.801**	**0.682**	**0.713**	**88800**

Table 2. 12. NB Pure 444000 compound class accuracy.

	Precision	Recall	F1-score	Support
Acid	0.224	0.898	0.358	4800
Amphetamine	0.724	0.508	0.597	1200
Analgesic	0.819	0.827	0.823	9600
Anesthetic	0.979	0.566	0.717	14400
Anthelmintic	0.671	0.726	0.697	4800

	Precision	Recall	F1-score	Support
Antihistamine	0.838	0.658	0.737	4800
Benzodiazepine	0.640	0.567	0.601	1200
Calcium channel blocker	1.000	0.685	0.813	4800
Cannabinoid	0.561	0.685	0.617	1200
Carbohydrate	0.899	0.666	0.765	4800
Cathinone	0.459	0.827	0.590	2400
Cocaine	0.761	0.617	0.681	1200
Dye	1.000	0.872	0.932	4800
Opiate	0.572	0.633	0.601	1200
Opioid	0.490	0.500	0.495	8400
Stimulant	0.953	0.595	0.733	4800
Sugar	0.890	0.615	0.728	14400
accuracy	**0.667**	**0.667**	**0.667**	**0.667**
macro avg	**0.734**	**0.673**	**0.676**	**88800**
weighted avg	**0.796**	**0.667**	**0.700**	**88800**

Table 2. 13. SVM Pure 444000 compound accuracy.

	Precision	Recall	F1-score	Support
4-MEC	1.000	0.981	0.990	1200
4-MMC	1.000	0.974	0.987	1200
Acetaminophen	1.000	0.992	0.996	4800
Alprazolam	1.000	0.981	0.990	1200
Benzocaine	0.900	1.000	0.947	4800
Boric acid	0.988	0.998	0.993	4800
Buprenorphine	1.000	0.990	0.995	1200
Caffeine	1.000	0.994	0.997	4800
Cocaine	1.000	0.986	0.993	1200
Codeine	1.000	0.991	0.995	1200
Diltiazem	1.000	0.995	0.997	4800
Fentanyl	1.000	0.990	0.995	1200
Heroin	1.000	0.988	0.994	1200

	Precision	Recall	F1-score	Support
Hydroxyzine	0.988	0.996	0.992	4800
Levamisole	0.999	0.994	0.996	4800
Lidocaine	1.000	0.992	0.996	4800
Maltose	1.000	0.994	0.997	4800
Methamphetamine	1.000	0.983	0.992	1200
Mitragynine	0.998	0.982	0.990	1200
Morphine	1.000	0.984	0.992	1200
Myo-inositol	1.000	0.995	0.997	4800
Naltrexone	1.000	0.990	0.995	1200
PB-22	1.000	0.981	0.990	1200
Phenacetin	1.000	0.991	0.996	4800
Phenolphthalein	1.000	0.993	0.996	4800
Procaine	0.997	0.993	0.995	4800
Sorbitol	0.998	0.992	0.995	4800
Starch	1.000	0.994	0.997	4800
Sufentanil	1.000	0.987	0.993	1200
accuracy	**0.992**	**0.992**	**0.992**	**0.992**
macro avg	**0.995**	**0.990**	**0.992**	**88800**
weighted avg	**0.993**	**0.992**	**0.993**	**88800**

Table 2. 14. SVM Pure 444000 compound class accuracy.

	Precision	Recall	F1-score	Support
Acid	1.000	0.989	0.994	4800
Amphetamine	1.000	0.984	0.992	1200
Analgesic	1.000	0.993	0.997	9600
Anesthetic	0.963	1.000	0.981	14400
Anthelmintic	1.000	0.992	0.996	4800
Antihistamine	1.000	0.990	0.995	4800
Benzodiazepine	1.000	0.980	0.990	1200
Calcium channel blocker	1.000	0.994	0.997	4800
Cannabinoid	1.000	0.973	0.986	1200

	Precision	Recall	F1-score	Support
Carbohydrate	1.000	0.991	0.996	4800
Cathinone	1.000	0.985	0.993	2400
Cocaine	1.000	0.984	0.992	1200
Dye	1.000	0.993	0.996	4800
Opiate	1.000	0.984	0.992	1200
Opioid	0.996	0.992	0.994	8400
Stimulant	1.000	0.993	0.996	4800
Sugar	0.998	0.996	0.997	14400
accuracy	**0.993**	**0.993**	**0.993**	**0.993**
macro avg	**0.997**	**0.989**	**0.993**	**88800**
weighted avg	**0.993**	**0.993**	**0.993**	**88800**

Table 2. 15. RF Pure 444000 compound accuracy.

	Precision	Recall	F1-score	Support
4-MEC	1.000	1.000	1.000	1200
4-MMC	1.000	1.000	1.000	1200
Acetaminophen	1.000	1.000	1.000	4800
Alprazolam	1.000	1.000	1.000	1200
Benzocaine	1.000	1.000	1.000	4800
Boric acid	1.000	1.000	1.000	4800
Buprenorphine	1.000	1.000	1.000	1200
Caffeine	1.000	1.000	1.000	4800
Cocaine	1.000	1.000	1.000	1200
Codeine	1.000	1.000	1.000	1200
Diltiazem	1.000	1.000	1.000	4800
Fentanyl	1.000	1.000	1.000	1200
Heroin	0.999	1.000	1.000	1200
Hydroxyzine	1.000	1.000	1.000	4800
Levamisole	1.000	1.000	1.000	4800
Lidocaine	1.000	1.000	1.000	4800
Maltose	1.000	1.000	1.000	4800

	Precision	Recall	F1-score	Support
Methamphetamine	1.000	1.000	1.000	1200
Mitragynine	1.000	0.997	0.998	1200
Morphine	1.000	1.000	1.000	1200
Myo-inositol	1.000	1.000	1.000	4800
Naltrexone	1.000	1.000	1.000	1200
PB-22	0.998	1.000	0.999	1200
Phenacetin	1.000	1.000	1.000	4800
Phenolphthalein	1.000	1.000	1.000	4800
Procaine	1.000	1.000	1.000	4800
Sorbitol	1.000	1.000	1.000	4800
Starch	1.000	1.000	1.000	4800
Sufentanil	1.000	1.000	1.000	1200
accuracy	**1.000**	**1.000**	**1.000**	**1.000**
macro avg	**1.000**	**1.000**	**1.000**	**88800**
weighted avg	**1.000**	**1.000**	**1.000**	**88800**

Table 2. 16. RF Pure 444000 compound class accuracy.

	Precision	Recall	F1-score	Support
Acid	1.000	1.000	1.000	4800
Amphetamine	1.000	0.998	0.999	1200
Analgesic	1.000	1.000	1.000	9600
Anesthetic	1.000	1.000	1.000	14400
Anthelmintic	1.000	1.000	1.000	4800
Antihistamine	1.000	1.000	1.000	4800
Benzodiazepine	1.000	0.999	1.000	1200
Calcium channel blocker	1.000	1.000	1.000	4800
Cannabinoid	1.000	0.997	0.998	1200
Carbohydrate	1.000	1.000	1.000	4800
Cathinone	1.000	1.000	1.000	2400
Cocaine	1.000	0.998	0.999	1200
Dye	1.000	1.000	1.000	4800

	Precision	Recall	F1-score	Support
Opiate	1.000	0.995	0.997	1200
Opioid	0.998	1.000	0.999	8400
Stimulant	1.000	1.000	1.000	4800
Sugar	1.000	1.000	1.000	14400
accuracy	**1.000**	**1.000**	**1.000**	**1.000**
macro avg	**1.000**	**0.999**	**1.000**	**88800**
weighted avg	**1.000**	**1.000**	**1.000**	**88800**

Table 2. 17. NN Pure 444000 compound accuracy.

	Precision	Recall	F1-score	Support
4-MEC	1.000	0.971	0.985	1200
4-MMC	1.000	0.968	0.983	1200
Acetaminophen	0.998	0.991	0.995	4800
Alprazolam	0.999	0.971	0.985	1200
Benzocaine	0.998	0.985	0.992	4800
Boric acid	0.996	0.993	0.994	4800
Buprenorphine	0.992	0.980	0.986	1200
Caffeine	0.982	0.983	0.983	4800
Cocaine	0.894	0.984	0.937	1200
Codeine	0.943	0.977	0.959	1200
Diltiazem	0.993	0.989	0.991	4800
Fentanyl	0.899	0.978	0.937	1200
Heroin	1.000	0.973	0.986	1200
Hydroxyzine	0.895	1.000	0.944	4800
Levamisole	0.999	0.986	0.993	4800
Lidocaine	0.997	0.989	0.993	4800
Maltose	0.988	0.994	0.991	4800
Methamphetamine	1.000	0.861	0.925	1200
Mitragynine	1.000	0.856	0.922	1200
Morphine	0.999	0.910	0.952	1200
Myo-inositol	1.000	0.989	0.994	4800

	Precision	Recall	F1-score	Support
Naltrexone	1.000	0.982	0.991	1200
PB-22	1.000	0.969	0.984	1200
Phenacetin	0.996	0.990	0.993	4800
Phenolphthalein	1.000	0.991	0.996	4800
Procaine	0.944	0.999	0.970	4800
Sorbitol	0.999	0.995	0.997	4800
Starch	1.000	0.984	0.992	4800
Sufentanil	1.000	0.973	0.986	1200
accuracy	**0.984**	**0.984**	**0.984**	**0.984**
macro avg	**0.983**	**0.973**	**0.977**	**88800**
weighted avg	**0.985**	**0.984**	**0.984**	**88800**

Table 2. 18. NN Pure 444000 compound class accuracy.

	Precision	Recall	F1-score	Support
Acid	1.000	0.988	0.994	4800
Amphetamine	1.000	0.976	0.988	1200
Analgesic	0.981	0.998	0.990	9600
Anesthetic	0.996	0.997	0.996	14400
Anthelmintic	1.000	0.989	0.995	4800
Antihistamine	1.000	0.979	0.989	4800
Benzodiazepine	0.998	0.975	0.987	1200
Calcium channel blocker	0.990	0.993	0.992	4800
Cannabinoid	1.000	0.961	0.980	1200
Carbohydrate	1.000	0.994	0.997	4800
Cathinone	1.000	0.945	0.972	2400
Cocaine	1.000	0.982	0.991	1200
Dye	1.000	0.991	0.996	4800
Opiate	1.000	0.982	0.991	1200
Opioid	0.938	1.000	0.968	8400
Stimulant	1.000	0.988	0.994	4800
Sugar	1.000	0.992	0.996	14400

	Precision	Recall	F1-score	Support
accuracy	**0.990**	**0.990**	**0.990**	**0.990**
macro avg	**0.994**	**0.984**	**0.989**	**88800**
weighted avg	**0.991**	**0.990**	**0.991**	**88800**

Table 2. 19. CNN Pure 444000 compound accuracy.

	Precision	Recall	F1-score	Support
4-MEC	1.000	0.993	0.997	1200
4-MMC	0.993	0.998	0.996	1200
Acetaminophen	0.986	1.000	0.993	4800
Alprazolam	1.000	0.998	0.999	1200
Benzocaine	1.000	0.999	1.000	4800
Boric acid	1.000	0.999	1.000	4800
Buprenorphine	1.000	1.000	1.000	1200
Caffeine	1.000	0.999	1.000	4800
Cocaine	1.000	1.000	1.000	1200
Codeine	1.000	1.000	1.000	1200
Diltiazem	1.000	0.998	0.999	4800
Fentanyl	1.000	0.999	1.000	1200
Heroin	1.000	0.999	1.000	1200
Hydroxyzine	1.000	1.000	1.000	4800
Levamisole	1.000	0.999	1.000	4800
Lidocaine	1.000	0.999	0.999	4800
Maltose	1.000	0.999	0.999	4800
Methamphetamine	1.000	0.998	0.999	1200
Mitragynine	0.997	0.997	0.997	1200
Morphine	1.000	0.999	1.000	1200
Myo-inositol	1.000	0.999	1.000	4800
Naltrexone	1.000	1.000	1.000	1200
PB-22	1.000	0.997	0.998	1200
Phenacetin	1.000	0.999	0.999	4800
Phenolphthalein	1.000	1.000	1.000	4800

	Precision	Recall	F1-score	Support
Procaine	1.000	0.999	1.000	4800
Sorbitol	1.000	1.000	1.000	4800
Starch	1.000	1.000	1.000	4800
Sufentanil	1.000	0.998	0.999	1200
accuracy	**0.999**	**0.999**	**0.999**	**0.999**
macro avg	**0.999**	**0.999**	**0.999**	**88800**
weighted avg	**0.999**	**0.999**	**0.999**	**88800**

The accuracy and loss plots during training and testing of the CNN model are shown in **Figure 2.6**. Although the model was created with 100 epochs, the implementation of early stopping to prevent overfitting meant that after 25 to 30 epochs, the training automatically stopped. The training accuracy remained between 99.7 and 99.9% after 5 epochs for the compound model (**Figure 2.6A)**. The testing accuracy fluctuated between 99.6 and 99.9% while the training loss continued to decrease from 0.030 to 0.005. A similar pattern was observed for the compound class model, but the testing accuracy fluctuated between 99.5 and 99.9% after 30 epochs.0.030 to 0.005.

A similar pattern was observed for the compound class model, but the testing accuracy fluctuated between 99.5 and 99.9% after 30 epochs.

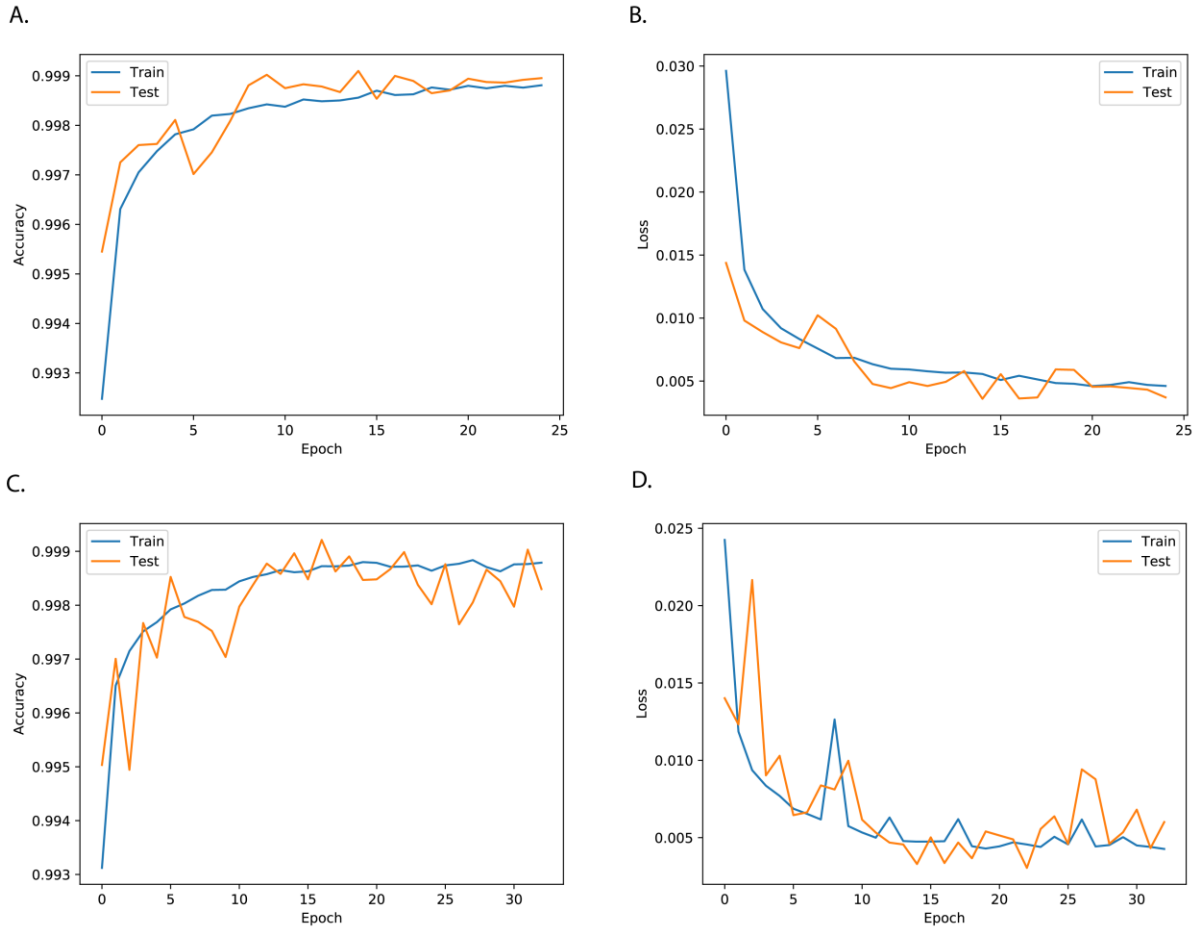

Figure 2. 6. Accuracy and validation loss plots for the CNN developed for the simulated pure spectra. A- Accuracy plot on compounds, B- Loss during compound algorithm training, C- Accuracy during compound class model training, D- Loss during compound class training.

2.3.3 Binary Mixtures

All models demonstrated at least 95% accuracy for compound mixtures or class mixtures except NB which had 47% accuracy with class mixtures (**Table 2.20**). The RF, NB and CNN all had

100% accuracy with the compound mixtures whereas only the RF, and CNN resulted in 100% accuracy for the class mixtures model.

Table 2. 20. Reported accuracy for the algorithms used to evaluate the simulated binary mixtures dataset. The NB and RF algorithms were only evaluated on binary mix #1 (spectra multiplied by numbers between 0.05 and 0.95).

	kNN		**NB**		**RF**		**SVM**		**NN**		**CNN**	
	Compound Mixtures	**Class Mixtures**	**Compound Mixtures**	**Class Mixtures**	**Compound Mixtures**	**Class Mixtures**	**Compound Mixtures**	**Class Mixtures**	**Compound Mixtures**	**Class Mixtures**	**Compound Mixtures**	**Class Mixtures**
Accuracy (%)	98	99	100	47	100	100	99	99	95	97	100	100

Training for the CNN algorithm stopped after 17 and 16 epochs for the compound mixtures, and class mixtures model, respectively. **Figure 2.7** demonstrates an increase in training and testing accuracies while the loss decreased, indicating no overfitting.

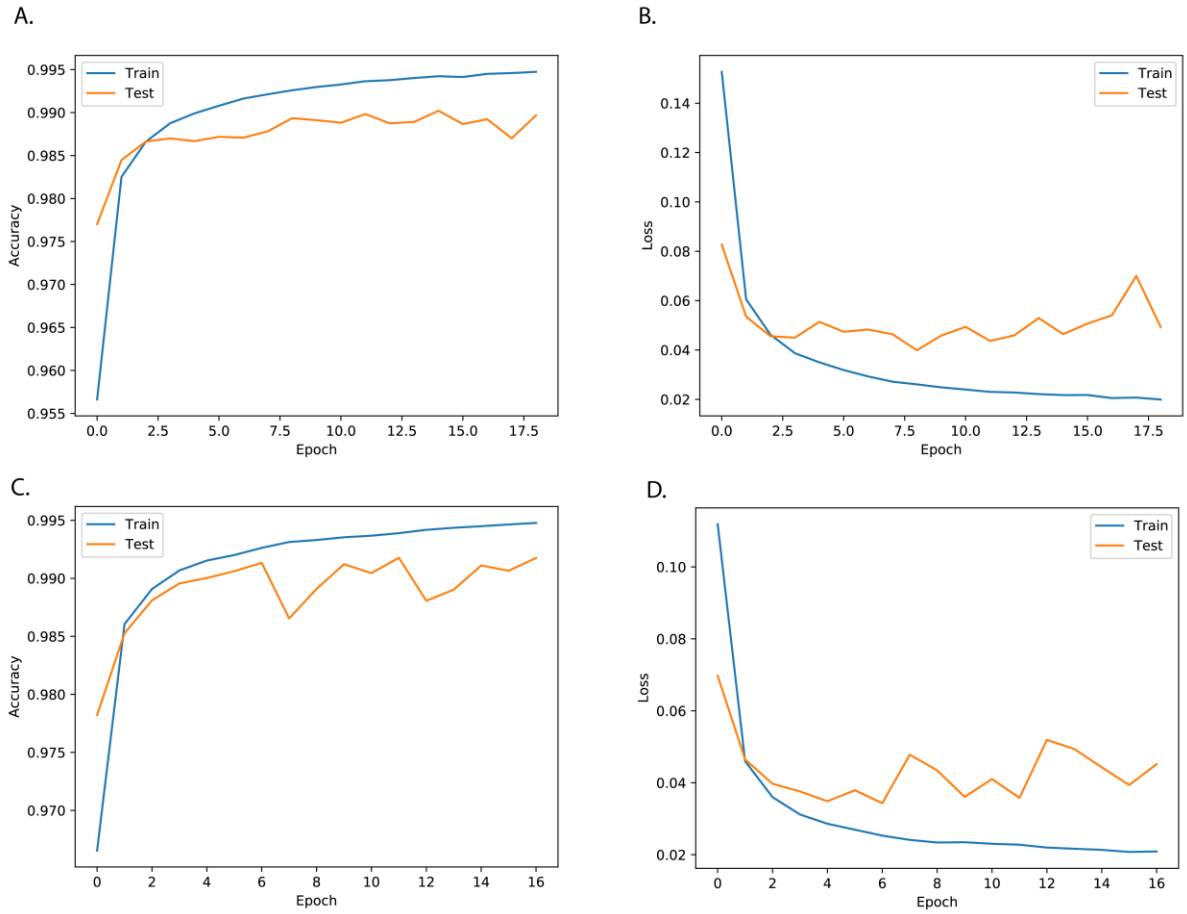

Figure 2. 7. Accuracy and validation loss plots for the CNN developed for the simulated mixtures. A- accuracy plot on compound mixtures model, B- Loss during compound mixtures model training, C- Accuracy during compound class mixtures model training, and D- Loss during compound class mixtures model training.

2.3.4 Application to Authentic In-house Binary Mixtures

The correct identification rates for the authentic in-house mixtures when using selected models was compared to results previously reported for the TacticID Raman [150]. The reported identification rates in **Table 2.21** considers the presence of the ground truth in the top 3 hits. The top 3 hits were determined based on the classification probability as shown in **Table 2.22.** For example, a mixture containing morphine and maltose resulted in the correct mixture as hit #1 because of the highest probability they belonged to that class. However, the ground truth was reported as hit #2 in one instance (**Table 2.22**) with a probability of 0.003.

The authentic in-house mixtures were evaluated using the developed pure spectra algorithms to demonstrate the importance of model selection based on the application. The SVM and RF models resulted in the highest correct identifications for both drug and diluent in the top 3 hits—26% and 16%, respectively (**Table 2.21**). The SVM was the only algorithm that outperformed the HQI, with 51% correct identification for drug only compared to 30% with the HQI. Although, the Raman instrument does not report the class of unknown compounds, the pure spectra algorithms by compound class all provided correct identifications greater than 74% for diluents only and performed poorly for drug classification (≤54%).

Table 2. 21. Correct identification rates of the in-house binary mixtures dataset using the pure spectra algorithms for classification. The results are based on the presence of the mixtures in the top 3 hits.

	HQI	**kNN**		**RF**		**SVM**		**NN**		**CNN**	
Correct Identification (ID, %)		**Compound Mixtures**	**Class Mixtures**	**Compound Mixtures**	**Class Mixtures**	**Compound Mixtures**	**Class Mixtures**	**Compound Mixtures**	**Class Mixtures**	**Compound Mixtures**	**Class Mixtures**
Drug	30	24	19	24	42	51	54	15	12	30	22
Diluent	89	80	81	89	96	74	77	75	77	75	78
Drug and Diluent	19	5	1	16	38	26	32	2	1	5	1
At least one compound/ class	99	99	99	97	100	99	98	88	89	100	100

Table 2. 22. Example of generated table for CNN drug algorithm evaluation on in-house mixtures. (Mor- morphine, malt- maltose, 4MEC- methylethcathinone, 4MMC- 4-methylmethcathinone).

Ground Truth	**Hit #1**	**Hit #2**	**Hit #2**	**Hit #1 Probability**	**Hit #2 Probability**	**Hit #3 Probability**
Mor– Malt	Mor–Malt	4MMC–Malt	4MEC–Malt	0.996	0.004	0.000
Mor–Malt	Mor–Malt	4MMC–Malt	4MEC–Malt	0.986	0.014	0.000
Mor–Malt	4MMC–Malt	Mor–Malt	4MEC–Malt	0.997	0.003	0.000

The correct identification improved when the binary mixtures models were used to assess the authentic in-house mixtures. All binary mixtures models demonstrated correct identifications at

least double that which was observed with the Raman instrument (**Table 2.23**). Greater than 70% correct drug classification was observed for most algorithms compared to 30% with the HQI, and greater than 90% correct diluent classification for most algorithms as compared to 89% identification of the diluent with the HQI. Moreover, all the algorithms were able to correctly detect at least one compound or class in the mixture. The class mixtures correct identification rates cannot be compared with the Raman instrument because the instrument only reports the drug based on spectral similarity. However, the CNN and NN performed better than the other algorithms for drug class identification with 78% and 77%, respectively. The correct diluent class identification was ≥90% for all algorithms.

Table 2. 23. Correct identification rates for the in-house binary mixtures using the simulated binary mixtures algorithms in comparison to the Raman instrument built-in hit quality index (HQI). The NB models were not evaluated as the other algorithms resulted in higher identification rates for both compound and compound class. The RF algorithm was not evaluated on the in-house mixtures. The correct identification was based on the true compound/ class being in the top 3 hits.

	HQI	**kNN**		**SVM**		**NN**		**CNN**	
		Compound Mixtures	**Class Mixtures**	**Compound Mixtures**	**Class Mixtures**	**Compound Mixtures**	**Class Mixtures**	**Compound Mixtures**	**Class Mixtures**
Drug (%)	30	59	60	61	73	73	77	69	78
Diluent (%)	89	90	90	94	95	92	95	95	93
Both (%)	19	49	50	55	68	65	72	64	72
At least one compound/Class (%)	99	100	100	100	100	100	100	100	100

2.3.5 Ternary and Quaternary Mixtures

Molecular analysis of multiple component mixtures can be challenging using portable Raman spectroscopy as the signal of compounds in a lower percentage can be masked by compounds that are present in higher percentages. Therefore, investigating the performance of the algorithms on more complex mixtures is critical in understanding their applicability as screening tools.

In general, the tested algorithms successfully identified ternary mixtures. An example of the accuracy and validation loss plots during training and testing the ternary mixtures CNN algorithm

is shown is **Figure 2.8**. Training stopped after 16 – 20 epochs when the validation loss no longer decreased, and when the accuracy remained between 98.5% and 99.6%.

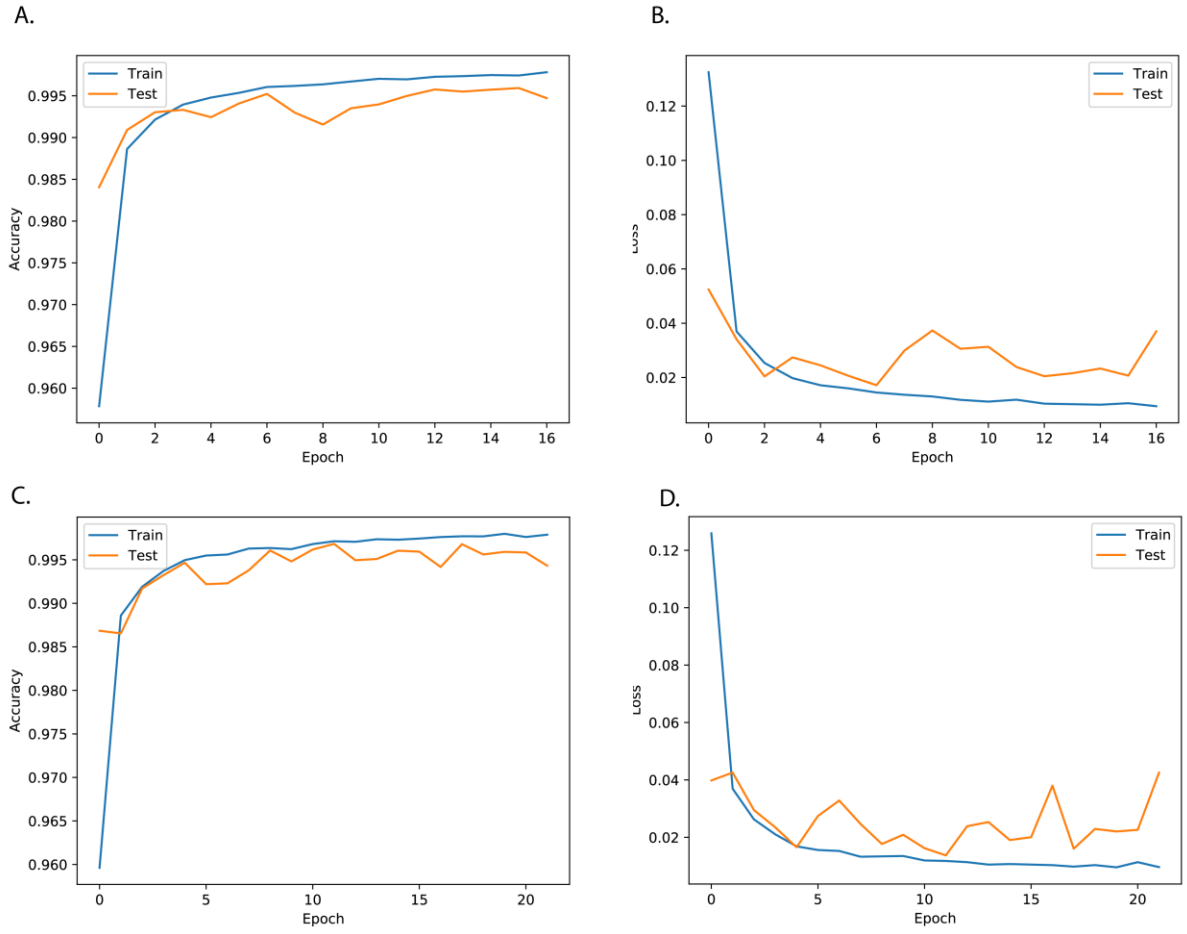

Figure 2. 8. Accuracy and validation loss plots for the CNN developed for the ternary mixtures. A- accuracy plot on compound mixtures model, B- Loss during compound mixtures model training, C- Accuracy during compound class mixtures model training, and D- Loss during compound class mixtures model training.

Evaluation of ternary mixtures using selected algorithms resulted in the kNN performing the worst with 83% accuracy for compound mixtures and 84% for compound class mixtures (**Table 2.24**).

An accuracy greater than 95% was observed with all other models with the CNN's performance at 100%.

Table 2. 24. Accuracy of ternary mixtures models.

	kNN		SVM		NN		CNN	
	Compound Mixtures	**Class Mixtures**	**Compound Mixtures**	**Class Mixtures**	**Compound Mixtures**	**Class Mixtures**	**Compound Mixtures**	**Class Mixtures**
Accuracy (%)	83	84	99	99	95	99	100	100

Interestingly, accuracy of identification of quaternary mixtures ranged from 93 to 100%, depending on the model and subset. The accuracy for all models on subset 1 was 100%, at least 99% on subset 2, and at least 93% on subset 3 (**Table 2.25**). The lowest accuracy for the compound mixtures model was observed with the NN.

Table 2. 25. Accuracy of quaternary mixtures models.

	kNN		SVM		NN		CNN	
	Compound Mixtures	**Class Mixtures**	**Compound Mixtures**	**Class Mixtures**	**Compound Mixtures**	**Class Mixtures**	**Compound Mixtures**	**Class Mixtures**
Subset 1 Accuracy (%)	100	100	100	100	100	100	100	100
Subset 2 Accuracy (%)	100	100	100	100	99	100	100	100
Subset 3 Accuracy (%)	97	100	99	100	93	100	99	100

2.4.0 Discussion

The CNN algorithm performed better than the other algorithms in detecting the authentic pure test compounds and their class with 100% correct identification (**Table 2.1**). The RF algorithm also produced a comparable but lower correct identification of 97%. The use of a *linear* kernel with the SVM models suggested our data was linearly separable due to the high accuracies observed in this study. The inclusion of a model trained by compound class proved to be useful in understanding the potential identity of an unknown compound when the HQI search results in no matches. This is particularly useful when Raman is used as a quick screening tool for drug identification. The two examples used in this study—diphenhydramine and mannitol, were correctly classified by their compound class using the CNN model, even though they were misclassified when tested using the compound model. Discrimination of three novel psychoactive substances (NPS)

families—12 fentanyl related compounds, 8 synthetic cathinones, and 10 synthetic cannabinoids, was achieved using PCA [19]. The authors' intended use of this application was for law enforcement and customs officers where a diversity of controlled substances or counterfeits is encountered. The challenge with the use of PCA is when compounds of other drug families are encountered, accuracy can suffer. We demonstrate in **Figure 2.4** the difficulty in separating multiple clusters using PCA and we believe it is not the ideal method for classification although it can be used for feature selection with other algorithms. LDA provided better class separation than PCA and reasonable accuracy—96%, 88%, 91%, and 78 for single compounds, single classes, binary compound mixtures, and binary compound class mixtures, respectively, but emphasis was given to machine learning classifiers due to their higher accuracies with more complex datasets. Organic molecules which are structurally different by a functional group are of interest especially in forensic science, where new drug analogues are constantly emerging as a way of evading local laws and regulations. Although our study is not focused on differentiating between functional groups, a study using CNN demonstrated 100% accuracy in discriminating between toluene, aniline, o-xylene which differ by the number and position of a methyl group [146].

In many laboratories especially in forensic science, the ability to identify a controlled substance from seized materials using portable Raman instruments can provide more effective decision-making onsite and more efficient processing of cases at points of entry, such as customs. However, it is a challenge because most drug cases involve impure substances where the controlled drug is of a lower percentage making detection by conventional Raman difficult. For this reason the use of portable Raman is considered a screening tool requiring further confirmation using an additional technique [10]. During a presumptive stage, accuracies above 70% are acceptable to inform the user about a potential drug or compound of interest. The rapid and non-destructive nature of portable Raman makes it an ideal technique to make quick sampling and investigative decisions at the point of contact, with minimal sample manipulation and under safe conditions to the operators. Similarly, in counterfeit pharmaceutical products, the high percentage of excipients may mask the active pharmaceutical ingredients. Therefore, we decided to calculate correct identification of the in-house binary mixtures test set based on its presence in the top three hits, accounting for uncertainties in classification. The instrument's accuracy for detecting the drug—a controlled substance in the mixtures, using the HQI algorithm was 30%, and lower than all the evaluated machine learning algorithms **(Table 2.21).** The NN and CNN models resulted in the highest correct

identification rate—73% and 69% for drug only, and 65% and 64% for both compounds, respectively.

The success of the CNN algorithm for pure compounds and mixtures has been supported by several studies [126–128, 143, 145, 146, 148, 153]. In one study, a smart Raman instrument was developed and the reported accuracy for ternary mixtures was 85.7% but 100% was observed with our CNN algorithm although the tested compounds were different [143]. The architecture of the CNN model reported by the authors contained 9 layers possibly due to the complexity of the acquired spectra, and incorporated dropout to prevent overfitting. Our CNN model consisted of no more than 5 layers, and without dropout as there was no indication of overfitting. Additionally, the authors only reported compound mixtures, but we also report compound class mixtures. However, despite the algorithm used, sampling is also important. Some studies used solvent mixtures which allows for a more homogeneous sampling which results in spectra that better represent the contents. Fan *et al* evaluated binary mixtures of polyacrylamide and sodium acetate but at a 1:1 ratio with a 100% true positive rate [127]. Our test mixtures included ratios of 1:4, 1:7, 1:10 and 1:20 where the controlled drug was present in a smaller percentage, simulating what can be expected in street drugs. The correct identification rates for the drug in the authentic mixtures decreased as the drug: diluent ratios increased with all algorithms, demonstrating the difficulty in detecting low concentration compounds in mixtures. Although, several measurements are required when performing analysis using portable Raman instruments to account for inhomogeneous samples, the acquired data may still be unrepresentative of the compounds in the mixture. One method that addresses this issue is the orbital raster scanning technique which allows the Raman instrument's laser to sweep over large areas of the sample to yield an average spectrum [157, 158]. However, evaluating the accuracy of this technique with machine learning would have to be studied and compared to conventional Raman instruments. The simulated complex mixtures data demonstrated that if measurements capture all components in a sample, the algorithm will detect them with high accuracy. An alternative to conventional Raman—surface enhanced Raman spectroscopy (SERS) requires collection of a small sample dissolved in a solvent prior to analysis. This technique can provide more representative information about the components of a mixture even when the target substance is in low quantities, but can be risky when performed outside a controlled environment if the operator is exposed to unknown compounds [90, 159, 160].

A comparison of the effect of training with the mixtures models (**Table 2.23)** or pure models (**Table 2.21**) to predict the compounds in the test mixtures demonstrated the importance of having the appropriate model in the library. For example, if ternary mixtures are being tested, the models should be trained on ternary mixtures. If the pure model which returns a single compound is used on mixtures, a result for the compound most representative of the spectrum will result, as demonstrated by the accuracy of the diluent in **Table 2.21.** Additionally, the algorithms detected differences in spectra of ternary and quaternary mixtures, that would otherwise be challenging to observe by inspection, with high accuracies (~ 83-100%, **Table 2.24 and 2.25**). Depending on the application, if the number of component mixtures is known, algorithms can be designed to meet this expectation. For example, if the number of mixtures in street drugs does not typically exceed 5 compounds, then training algorithms to detect more than 4 components would not be necessary.

We propose the use of models created to report single compounds, single compound classes, binary, ternary, and quaternary mixtures using the CNN algorithm due to the high correct identification rates and accuracy reported in this study. Instead of implementing these classification techniques post processing, they can be incorporated into portable instruments and depending on the application, provide both spectral correlation information using the HQI, cosine similarity or Pearson's correlation, and classification as demonstrated by the proposed workflow in **Figure 2.9**. One advantage of this classification and reporting workflow, is the gain of feedback to the end-user. When the identity of a compound is unknown and misclassified by the conventional HQI, having a built-in CNN algorithm can provide additional information about drug classes and potential mixtures. For example, when pure PB-22 was analyzed using the portable Raman instrument, it was reported as BB22 using the HQI due to the similarity between their spectra. Nonetheless, using the machine learning algorithm for compound class classified it as a synthetic cannabinoid even though it was absent from the library.

It should be noted that depending on the application, the proposed approach still has some limitations. For example, in the pharmaceutical industry where purer compounds are encountered and Raman is the primary technique used, instead of using the top three hits (**Table 2.22**), the top hit might be more important. On the other hand, in forensic science, where portable Raman is used as a screening method, it might be acceptable to consider the top three hits as potential compounds since confirmation using a secondary technique would be required before reporting components

of seized materials. One of the drawbacks of using machine learning algorithms on large datasets is that it requires high computing capabilities as observed with Random Forests in this study. However, given portable instruments such as the TacticID have Wi-Fi capabilities, access to a server can be used to train the algorithms on new data and be used to perform searches. In future studies, other data augmentation parameters such as Raman shift offset can be used in training the models to increase their robustness. Additionally, creation of authentic ternary and quaternary mixtures can be created to demonstrate the capability of the algorithms as more complex drug: diluent mixtures have previously reported in casework [73].

Machine learning which detects minor differences in spectra of complex mixtures outperformed the HQI algorithm incorporated in a portable Raman system. Implementation of machine learning algorithms capable of detecting single compounds, mixtures, and their classes can provide useful screening information about unknown compounds or molecules. Although, our proposed approach provides a probability for each hit, when needed, a spectral correlation technique can be used. Furthermore, having these methods built into the instrument eliminates the need to first export the data for post processing, and does not require separate libraries to be installed on the instrument as models can be trained offline then transferred to the device. Reporting the accuracy of the models as shown in **Figure 2.9**, size of the training, and testing data results in more transparent reporting of results. The concept proposed in this study will therefore benefit applications where portable Raman instruments are used for compound screening including forensic science, medicine, and pharmaceutical industries.

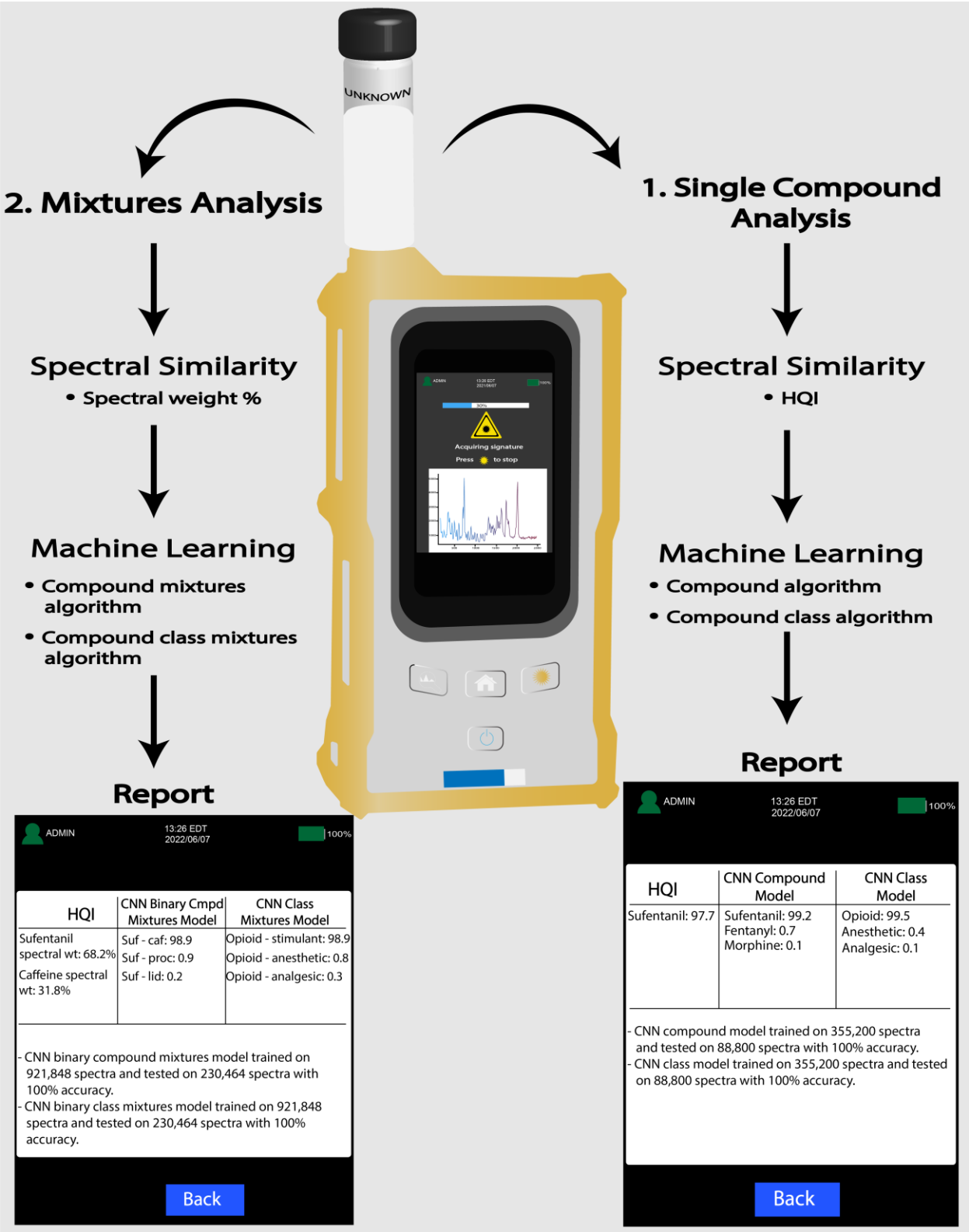

Figure 2. 9. An example of a workflow that can be implemented in portable Raman instruments. If the intended application requires a numerical value for spectral correlation, a similarity metric

can provide a HQI for pure compounds and spectral weight for mixtures. Machine learning algorithms can also be incorporated for identification of the compounds and their classes. In the final report, a summary of the potential hits and their respective class probabilities is reported.

2.5.0 Conclusions

Six machine learning algorithms—kNN, NB, RF, SVM, NN, and CNN were investigated and compared to a portable Raman instrument's accuracy in detecting pure powders, binary, ternary, and quaternary mixtures in this study. The CNN performed better than all algorithms with 100% correct identification for pure substances by compound and class. Both the NN and CNN resulted in superior correct identification on the authentic binary mixtures data— 65% and 64%, respectively in detecting both compounds in comparison to 19% observed in the portable Raman instrument. Improved accuracy in the binary simulated mixtures was observed, ranging from 83 to 100%, depending on the model and algorithm used, with superior performance observed for CNN. The CNN also provided the highest accuracy on the ternary and quaternary mixtures—100%, demonstrating its ability to provide compound and class information on samples that simulate common seized drugs formulations.

We propose the use of the HQI for spectral correlation and CNN models in portable Raman instruments to provide preliminary information about the identity of a compound and its class. Incorporating machine learning algorithms into portable Raman systems can enhance the response and feedback provided to law enforcement and scientists at the laboratory and onsite, facilitating more efficient and safer decision-making during sampling and investigative stages. The methods proposed here are broadly applicable to other materials and disciplines that use Raman spectroscopy as a rapid method for point-of-contact analysis.

Chapter 3: Evaluation of Fentanyl Toxicity and Metabolism using a Zebrafish Model

Reproduced with additions and permission from Wiley and Travon Cooman, Sadie A. Bergeron, Rebecca Coltogirone, Eric Horstick, Luis Arroyo, *Journal of Applied Toxicology*, Vol. 42 (2022): 706-714. DOI #: 10.1002/jat.4253

3.1.0 Introduction

The United States of America continues to experience an opioid epidemic fueled by not only prescription opioids, but also their illegally synthesized analogues. Notably, synthetic opioids are emerging at an alarming rate and has highlighted the lack of knowledge about their toxicity. Currently, many of these compounds are scheduled under the Administrative Controlled Substances Code 9850 [161] with minimal prior study. High throughput models are therefore useful in evaluating the toxic effects of multiple drugs. Although *in vitro* cell culture models are available, they do not always translate to *in vivo* toxicity due to differences in absorption, distribution, metabolism, and excretion of xenobiotics [162]. *In vivo* models such as rodents, are more expensive, and do not allow for high throughput experiments, and are time consuming. The zebrafish model is a popular, cost-effective, and high throughput model used to study drug toxicity and metabolism due to their similarities to human [39, 43, 50, 163–165]. The organization for economic cooperation and development (OECD) developed guidelines for testing acute or lethal toxicity of chemicals on zebrafish larvae and listed the endpoints as coagulation, lack of somite formation, lack of tail detachment from the yolk sac, and lack of heartbeat [33].

Zebrafish have homologous opioidergic genes to human [166] and have therefore been used as a model for behavioral studies with morphine [167], buprenorphine [168] and tramadol [169], where hyperactivity was observed with all drugs. Fentanyl—a potent opioid, when consumed may cause difficulty breathing and loss of consciousness in humans [170, 171]. Similar effects were reported by Zaig *et al.*, when they investigated fentanyl respiratory depression in zebrafish larvae by monitoring the fish mandible movement [172]. Anatomical phenotypes have been used to observe toxicity for multiple classes of drugs which affect human [35, 173], but few studies evaluate opioid toxicity or metabolism. One study reported death and malformation of embryos when exposed to 100 nM morphine [174] while another reported pericardial edema and tail malformation when larvae were exposed to furanoyl-1-benzyl-4-anilinopiperidine (Fu-BAP) [175]—a fentanyl

analogue. Tramadol metabolism was studied via microinjection [169], and two fentanyl analogues— cyclopropanoyl-1-benzyl-4'-fluoro-4-anilinopiperidine and Fu-BAP [175] were characterized in zebrafish. However, no study evaluated both toxicity and metabolism simultaneously as the fish developed from 24 to 96 hours post fertilization (hpf).

Here we investigate the toxicity and metabolism of fentanyl in zebrafish larvae. A single assay was utilized to observe diverse morphological phenotypes, as well as the ability of embryos and larvae to metabolize fentanyl when dosed through rearing-media. This approach provides foundational knowledge to further elucidate fentanyl's mechanism of action in fish and to translate the observations to human.

3.2.0 Materials and Method

3.2.1 Chemicals

United States Pharmacopeia fentanyl citrate (CAS #: 990-73-8, >99% purity, verified by Gas Chromatography Mass Spectrometry), 0.1 M sodium hydroxide, Tris base, 1 M 4-(2-hydroxyethyl)-1-piperazineethanesulfonic acid (HEPES) buffer and magnesium sulfate ($MgSO_4 \cdot 7H_2O$) were purchased from Sigma Aldrich (St. Louis, MO). Methanol, ammonium formate, formic acid, hexanes, sodium chloride (NaCl) and potassium chloride (KCl) were purchased from Fisher Chemical (Waltham, MA). Calcium chloride ($CaCl_2$) was purchased from LabChem (PA). Tricaine (MS-222) was purchased from Syndel (Nanaimo, Canada). Deionized water was acquired from a Direct-Q® 3UV Millipore Sigma system (Burlington, MA). Fentanyl, norfentanyl, β-hydroxyfentanyl, and despropionyl fentanyl (4-ANPP) were obtained from Cayman Chemical (Ann Arbor, MI).

3.2.2 Method

3.2.2.1 Embryo Toxicity Study

Adult wild-type zebrafish breeders (TL strain) were acquired from several generations of breeding in our laboratory facility at West Virginia University. Adult fish were raised on a flow-through system [176]. Daily and weekly water checks for optimal conditions included pH—7.0-8.0, conductivity—600 – 800 µS/cm, temperature—27 – 30°C, chlorine—0 ppm, ammonia—0 ppm, nitrate—<10 ppm, nitrite—0 ppm, hardness—80 – 300 ppm, alkalinity—50 – 150 ppm. Fertilized

eggs were collected during the first hour of light period (14/10 hour light on/off) and incubated in embryo media (5 µM NaCl, 0.17 µM KCl, 0.33 µM $CaCl_2$, 0.33 µM $MgSO_4 \cdot 7H_2O$, 1 M HEPES) with a final pH of 7.4. Fertilized eggs <10 hours post fertilization (hpf) were placed in a 96 well-plate with one egg per well. Excess media was removed and 24 eggs per treatment level were exposed to 200 µL fentanyl solution dissolved in embryo media. The treatment levels recommended by the OECD [33] as a starting point included: 0, 0.01, 0.1, 1, 10, 100 µM, with the addition of 50 µM. The experiment was performed in triplicate (n = 72 eggs per level) with each replicate on a different day. The treatment groups were randomly placed on each plate and each well-plate contained a negative control. The plates were incubated at 28- 29 °C (VWR 1535 general purpose incubator, Radnor, PA) under a 14/10 hour light on/off period. Observations were made using a Leica MF205A FA stereomicroscope (Wetzlar, Germany) at 24, 48, 72 and 96 hours post dosing (hpd) and the media was collected, stored at -20°C for metabolite analysis and replenished each day. Phenotype observations included: yolk extension malformation, yolk extension length, tail malformation, tail degree of curvature, pericardial edema, pericardial edema size, and swim bladder inflation whereas endpoint observations included: egg coagulation, lack of somite formation, lack of heartbeat, and tail non-detachment. Data for lack of somite formation and tail-yolk non-detachment are not presented because few embryos were observed with these characteristics. All experiments were performed in accordance with the West Virginia University Institutional Animal Care and Use Committee and the ARRIVE guidelines [177].

The percentage of coagulated eggs after 24 hpd was calculated in **Equation (3.1)**.

$$Coagulation(\%) = \frac{Number\ of\ coagulated\ eggs\ per\ treatment\ level}{Total\ eggs\ per\ treatment} * 100 \qquad \textbf{Equation (3.1)}$$

The embryos which survived were recorded for each treatment level daily. To normalize survival, the number of deaths at 0 µM were subtracted from each level and reported as a percentage of the number of surviving embryos at 0 µM.

Hatching was recorded at 48, 72 and 96 hpd. The percentage of embryos hatched at each time was calculated as shown in **Equations (3.2, 3.3, 3.4)**, where H_{48}, H_{72}, and H_{96} are the percentage of hatching by 48, 72 and 96 hpd, respectively.

$$H_{48}(\%) = \frac{Number\ hatched\ at\ 48\ hpd}{Number\ survived\ at\ 48\ hpd} * 100$$ **Equation (3.2)**

$$H_{72}(\%) = \frac{Number\ hatched\ at\ 48\ hpd + 72\ hpd}{Number\ survived\ at\ 72\ hpd} * 100$$ **Equation (3.3)**

$$H_{96}(\%) = \frac{Number\ hatched\ at\ 48\ hpd + 72\ hpd + 96\ hpd}{Number\ survived\ at\ 96\ hpd} * 100$$ **Equation (3.4)**

In one replicate, some larvae were missing tails at levels not limited to the negative control. These larvae were omitted from the calculations for yolk extension length, pericardial edema size, degree of tail curvature, and swim bladder inflation. A correction for the observed malformations in the yolk extension, pericardium, and tail was done by subtracting the number observed at 0 µM from each treatment level.

The percentage of larvae with malformed yolk extension, tail, and pericardium at 48, 72, and 96 hpd were calculated as shown in **Equation (3.5)**.

$$Malformation(\%) = \frac{Number\ of\ malformed\ larvae}{Number\ of\ larvae\ survived}$$ **Equation (3.5)**

At 96 hpd, the larvae were anesthetized with MS-222 (1 mg/mL) in Tris buffer (pH 7), then imaged using a Leica MF205 FA stereoscope. The images were calibrated and processed in Adobe Photoshop CC 2018. The yolk extension length was measured using the Measurement Tool as shown in **Figure 3.1A**. To measure tail curvature, a straight line measuring 0 degrees was drawn from the otolith closest to the tail, then a second line was drawn through the spine as shown in **Figure 3.1B**. The angle between the lines was recorded as the degree of curvature. The size of pericardial edema was measured using the Record Measurement and Quick Selection tools in Adobe Photoshop CC 2018. These malformation measurements were compared to the measurements from the negative control.

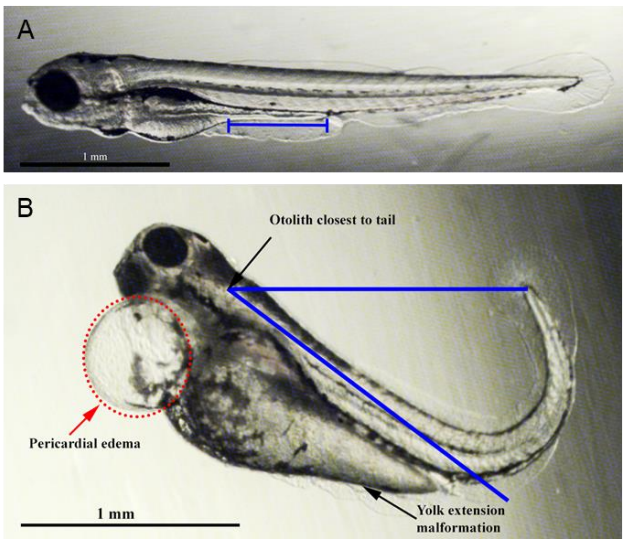

Figure 3. 1. (A)- annotation of yolk extension length; (B)- measurement of pericardial edema and degree of spinal curvature.

The percentage of larvae with fully inflated swim bladder at 96 hpd was calculated using **Equation (3.6)**.

$$Swim\ bladder\ inflation(\%) = \frac{Number\ of\ inflated\ swim\ bladder}{Number\ survived\ H_{96}} \qquad \textbf{Equation (3.6)}$$

One-way analysis of variance (ANOVA) was used to analyze the data when all assumptions were met, and post-hoc testing with Tukey's honestly significant differences (HSD) test. Kruskal-Wallis test was used alternatively when the assumption of normality was violated and Dunn's test for post-hoc testing using the Benjamini and Hochberg (BH) procedure to control the false discovery rate (FDR) [178]. Statistical analyses were performed using R v 4.0.3, R Studio v 1.4.1103 and the packages— *rstatix* v 0.6.0[179] and *DescTools* v 0.99.39 [180].

3.2.2.2 Metabolism Study

The stored media from the toxicity study was thawed and pooled per concentration and observation time. A liquid-liquid extraction procedure was performed using 1 mL hexanes and 150 µL 0.1 M sodium hydroxide. The samples were vortexed and centrifuged for five minutes. The organic layer was dried under nitrogen gas at 50ºC and reconstituted with 100 µL methanol. Analysis was performed using an Agilent 6470A triple quadrupole coupled to a 1290 Infinity II Liquid Chromatography System (Agilent Technologies, Santa Clara, CA). Mobile phase A consisted of water in 0.1% formic acid, and 5 mM ammonium formate, whereas mobile phase B consisted of

methanol in 0.1% formic acid. A Hypersil GOLD™ C18 (30 mm x 2.1 mm x 3 µm) column with a guard column holder and 5 µm drop-in guard cartridge (ThermoFisher Scientific, Waltham, MA) were used. Fentanyl, norfentanyl, β-hydroxy fentanyl and 4-ANPP were monitored in dynamic multiple reaction monitoring mode and the instrument operated in positive electrospray ionization mode for the transitions in **Table 3.1**. The fragmentor voltage for fentanyl, 4-ANPP, Norfentanyl and β-hydroxy fentanyl were 122, 107, 98, and 107 V, respectively. The cell accelerator voltage was 4 V for all compounds. The source parameters were as follows: gas temperature—325°C, gas flow—9 L/min, nebulizer pressure—30 psi, sheath gas heater temperature—350°C, sheath gas flow—10 L/min, capillary voltage—3500 V, nozzle voltage—500 V. The elution gradient system was as follows: 5% B ramped until 3.5 min, 40% B ramped until 4.5 min, 70% B held until 8.0 min, then ramped to 80% B until 8.5 min, and ramped down to 5% B until 9 min. The flow rate was 0.3 mL/min and the volume of injected sample was 1 µL. Data analysis was performed using MassHunter B.08.00 (Agilent Technologies).

Table 3. 1. Monitored transitions for fentanyl and metabolites.

Compound	**Precursor ion (*m/z*)**	**Product ions (*m/z*)**	**Collision Energy (V)**
Fentanyl	**337.2**	**188.0**^{Q}	24
		105.0	48
		77.0	100
4-ANPP	**281.2**	**188.0**^{Q}	16
		105.0	36
		77.0	80
Norfentanyl	**233.2**	**84.0**^{Q}	20
		56.0	32
		55.0	48
β-hydroxy fentanyl	**353.2**	**91.0**^{Q}	52
		204.0	24
		186.0	28

Q- quantifier ion (used to monitor peak areas of each metabolite)

3.3.0 Results

3.3.1 Embryo Toxicity Study

Fentanyl causes malformations in zebrafish larvae, with the severity increasing at higher concentrations (**Figure 3.2**). No pericardium, tail, and yolk extension malformations were observed at 0 µM, whereas these phenotypes were more visible at 50 and 100 µM.

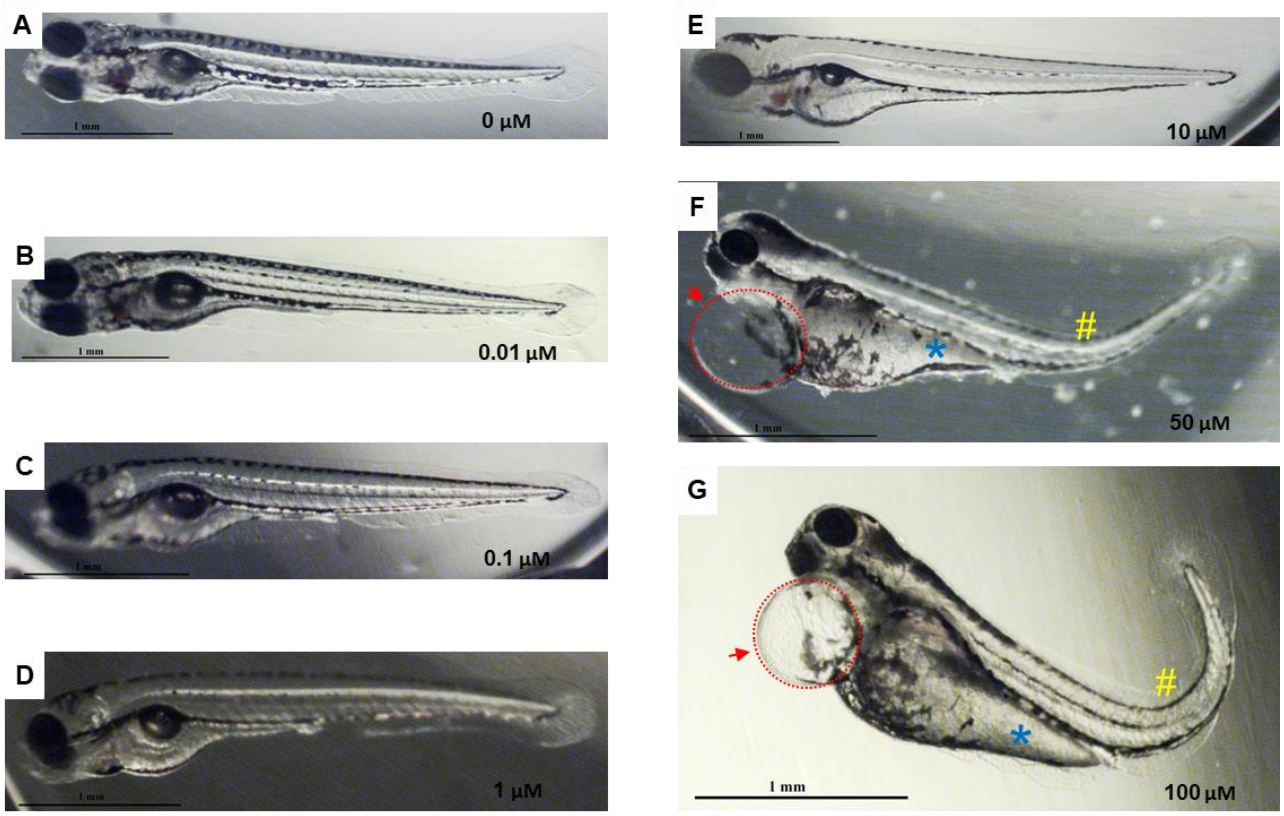

Figure 3. 2. Comparison of zebrafish larvae at 96 hpd. (A) 0 µM, (B) 0.01 µM, (C) 0.1 µM, (D) 1 µM, (E) 10 µM, (F) 50 µM, and (G) 100 µM. Pericardium (→), spine (#), and yolk extension malformation (*) are visible in (F) and (G).

Survival

Although fentanyl affected mortality, the tested concentrations did not result in 100% mortality up to 96 hpd. Higher mortality was observed at concentrations ≥ 0.1 µM (**Figure 3.3**). Whereas a statistically significant difference was detected between concentrations, none was detected between observation times (**Figure 3.4**).

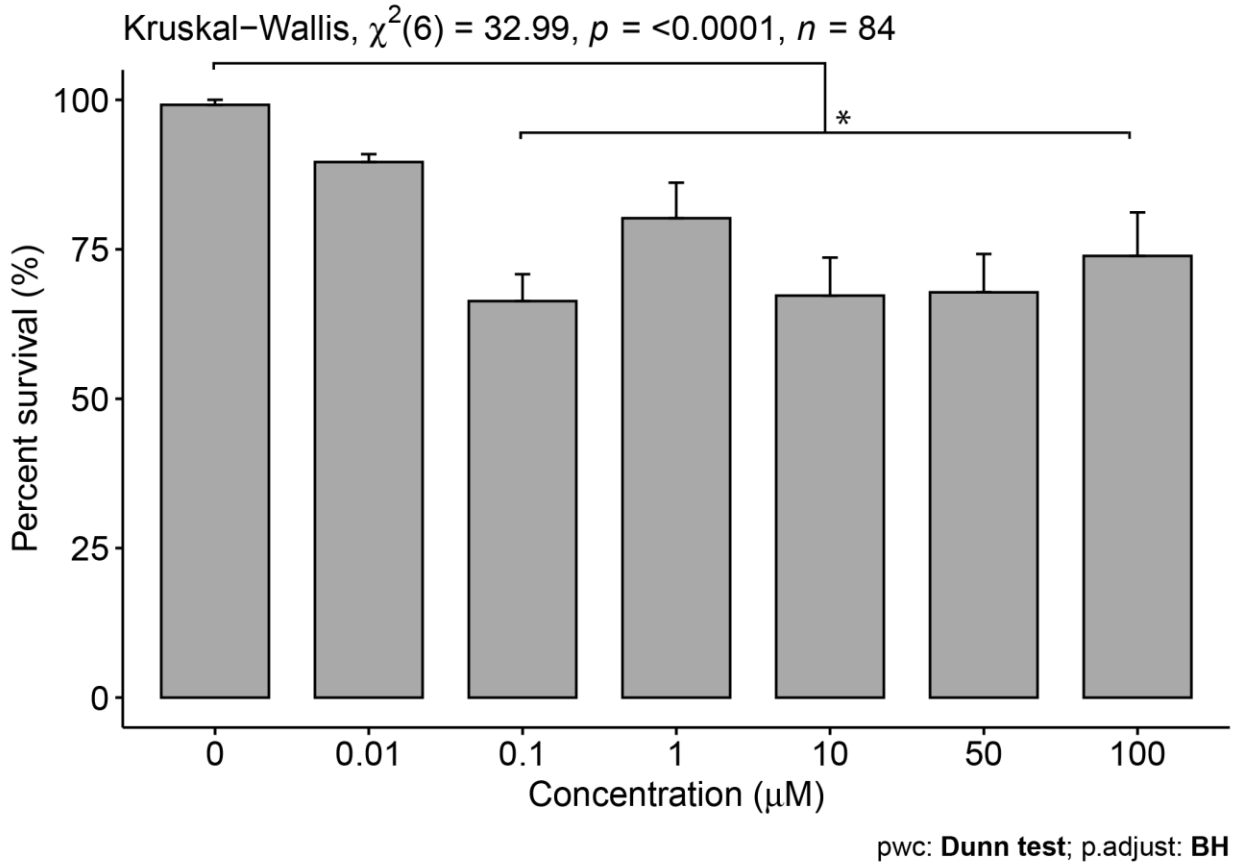

Figure 3. 3. Percentage of embryo survival in relation to fentanyl concentration (*-α < 0.05). Significant differences were observed between 0 μM and concentrations ≥0.1.

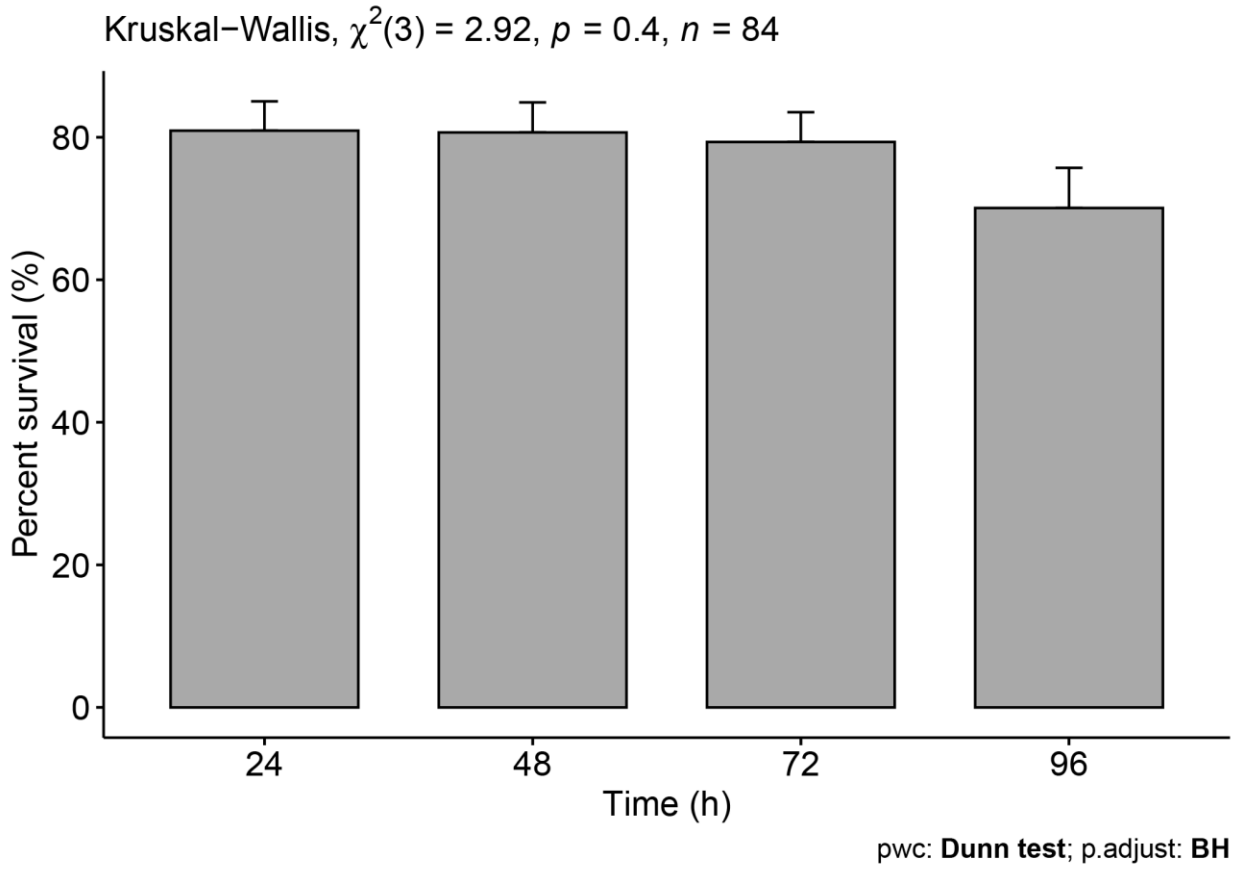

Figure 3. 4. Percentage of embryo survival in relation to time. No statistically significant difference observed between times.

Pericardial malformation

Our study used pericardial edema and edema size quantification to understand the toxic effect of fentanyl. Fentanyl exposure during early development induces pericardial malformation (**Figure 3.5**). Time did not have a significant effect on the percentage of pericardium malformations (**Figure 3.6**), but an average of 28% and 29% malformations were observed at 72 and 96 hpd, respectively.

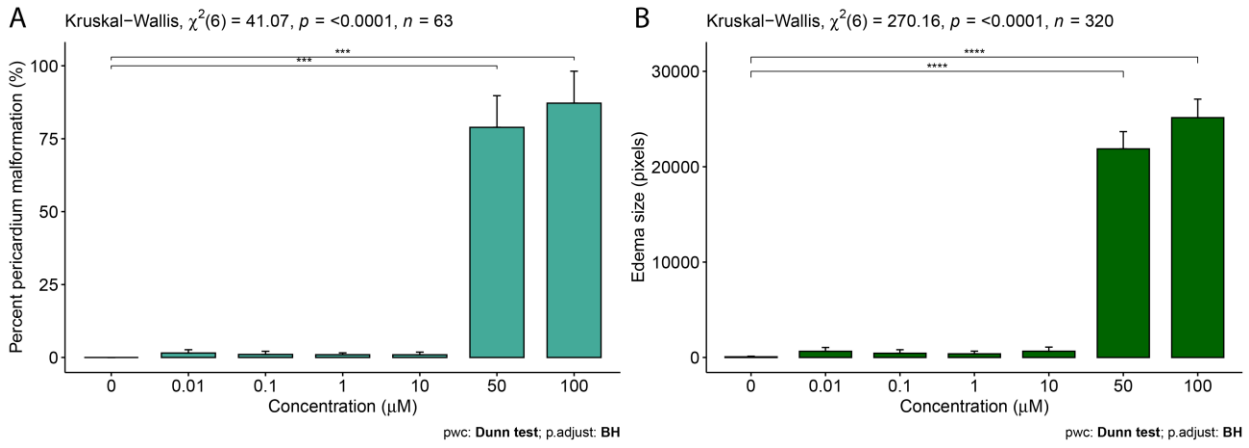

Figure 3. 5. The effect of concentration (A) on pericardial edema. The effect of concentration on edema size (B) (***- α = 0.001, ****- α = 0.0001).

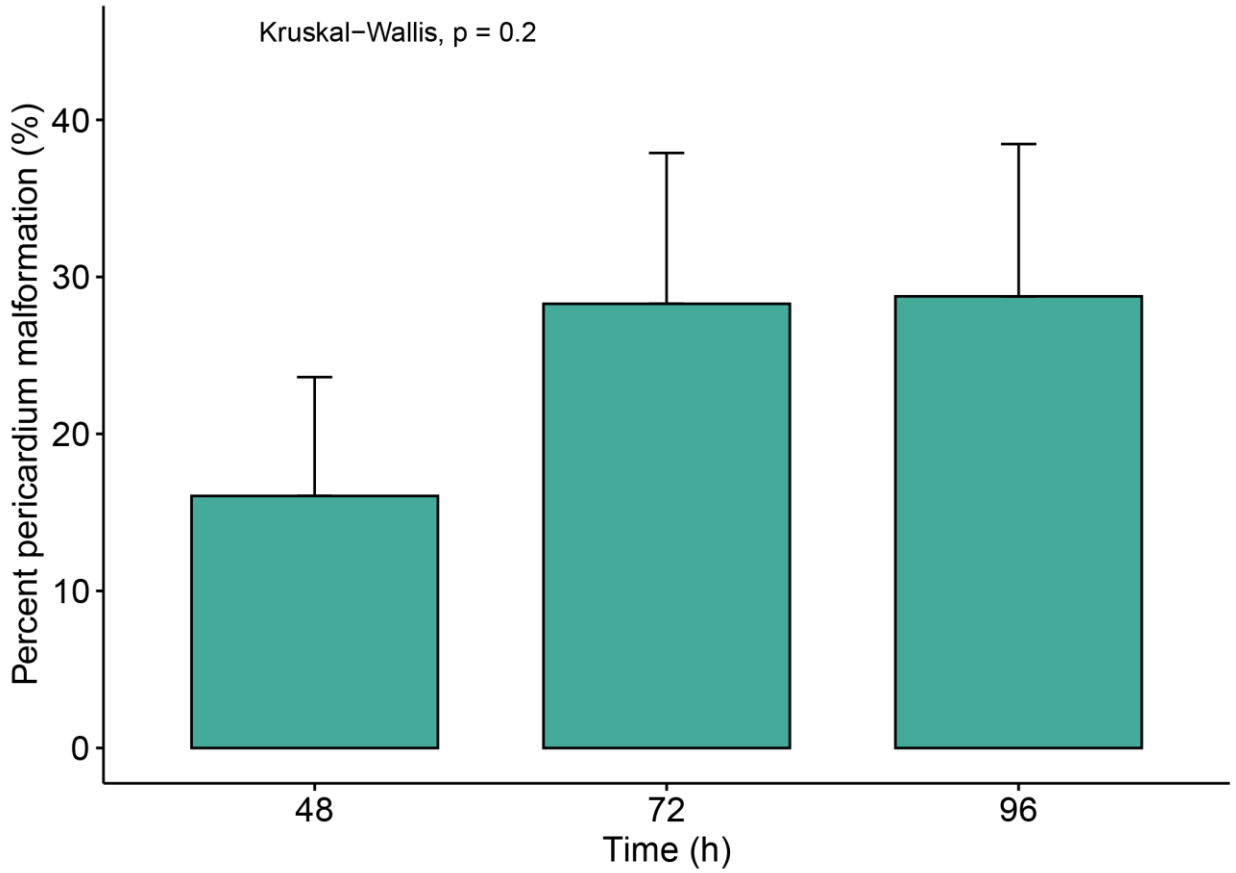

Figure 3. 6. The effect of fentanyl exposure duration on pericardium malformation. No statistically significant differences were detected.

Yolk extension malformation

Although incubation time did not affect yolk extension (**Figure 3.8**), fentanyl concentrations affected the typical absorption of the yolk (**Figure 3.7**). In comparison to the control group, only 50 µM (α = 0.001) and 100 µM (α = 0.0001) groups were significantly deformed. Further quantification of this malformation by measuring the yolk extension length at 96 hpd confirmed these observations (**Figure 3.7B**), subsequently contributing to the impaired development of zebrafish larvae. However, yolk extension length between 0 µM and 0.1 µM were significantly different but no differences were detected at 1 and 10 µM.

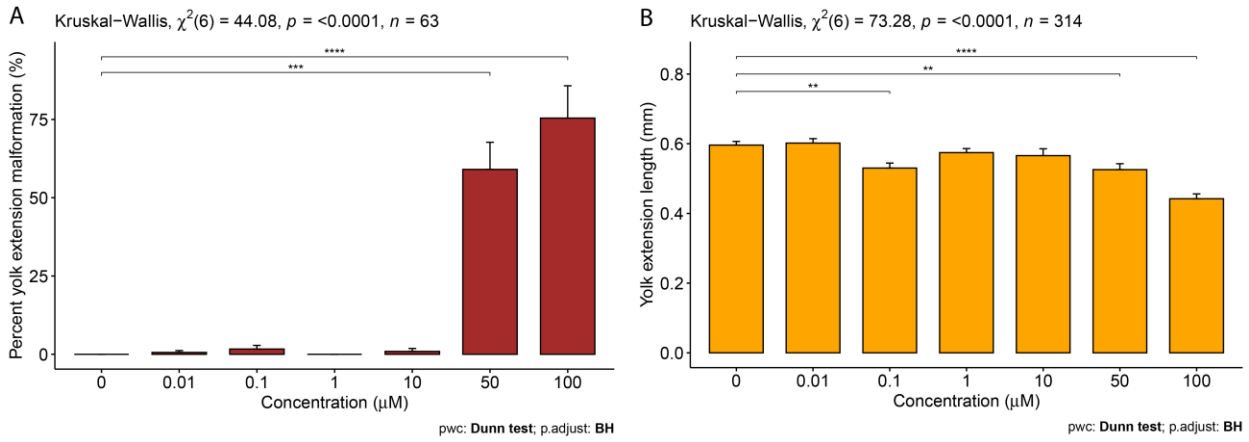

Figure 3. 7. Percentage of yolk extension malformation in relation to concentration (A) and further quantification of yolk extension length (mm) (B)(**- α = 0.01, ***- α = 0.001, ****- α = 0.0001).

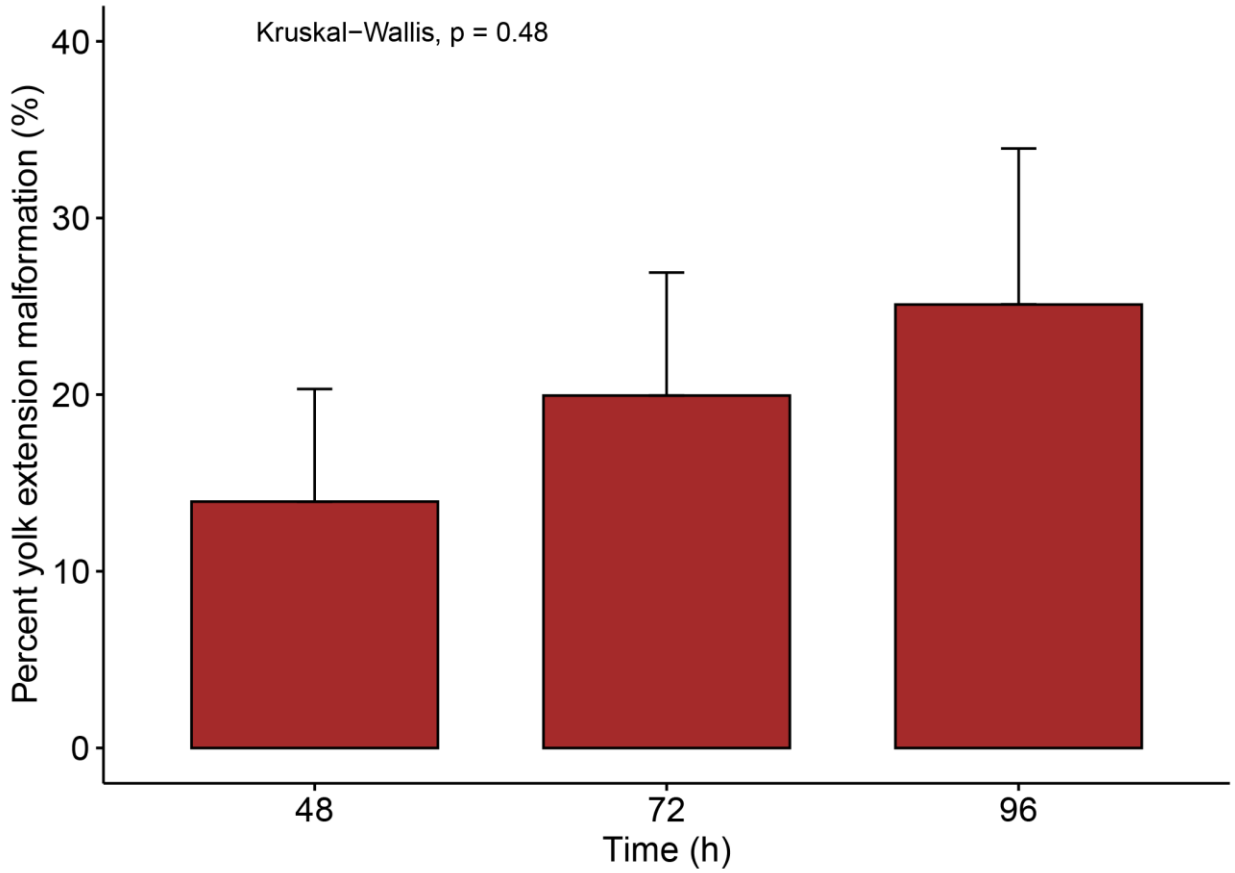

Figure 3. 8. The effect of fentanyl exposure duration on yolk extension malformation.

Tail malformation

As adult zebrafish age, they may develop spinal deformities resulting in curvature of the vertebral column [181], making it an ideal degenerative spinal disease model. Moreover, developing larvae also display spinal deformities upon exposure to toxic chemicals by either upward or downward tail curvature [182–187]—a common phenotype observed in developmental toxicity assays. An average of 13% tail malformations were observed at 96 hpd, higher than 48 (4%) and 72 (4%) hpd (**Figure 3.9**). However, no statistically significant difference was detected between these times (**Figure 3.10**). Conversely, higher fentanyl concentrations had a significant effect on percent tail malformation and tail curvature (**Figure 3.9**). The mean tail curvature for the negative control was 0.4° whereas at 50 and 100 µM, tail curvature was 3.6° and 11.8°, respectively. A previous study demonstrated neuroinflammation as a cause of spinal curvature [188]. Although spinal curvature

is a possible outcome from inflammation in our study, future studies will help elucidate the mechanism.

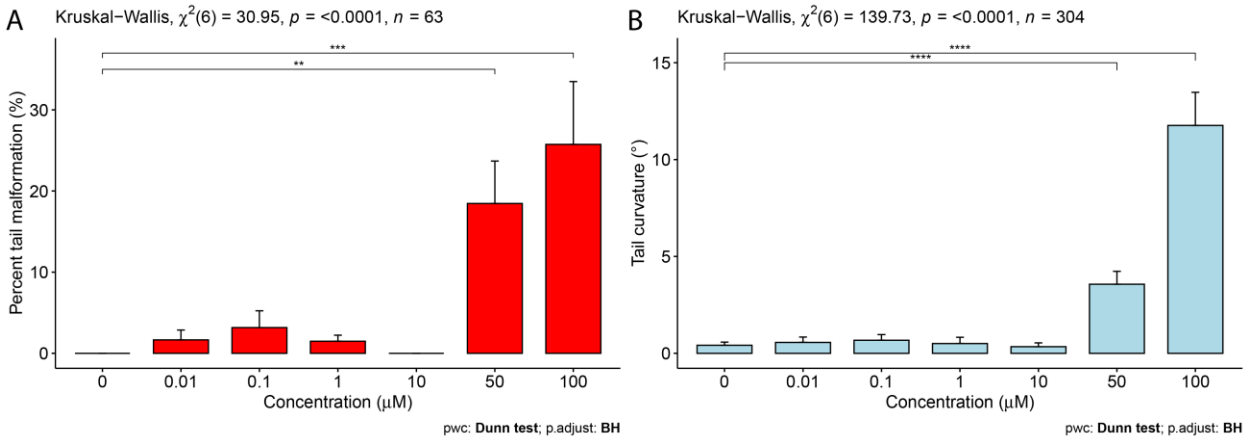

Figure 3. 9. The effect of concentration (A) on tail malformation percentage. The extent of tail curvature at 96 hpd (B). **- α = 0.01, ***- α = 0.001, ****- α = 0.0001.

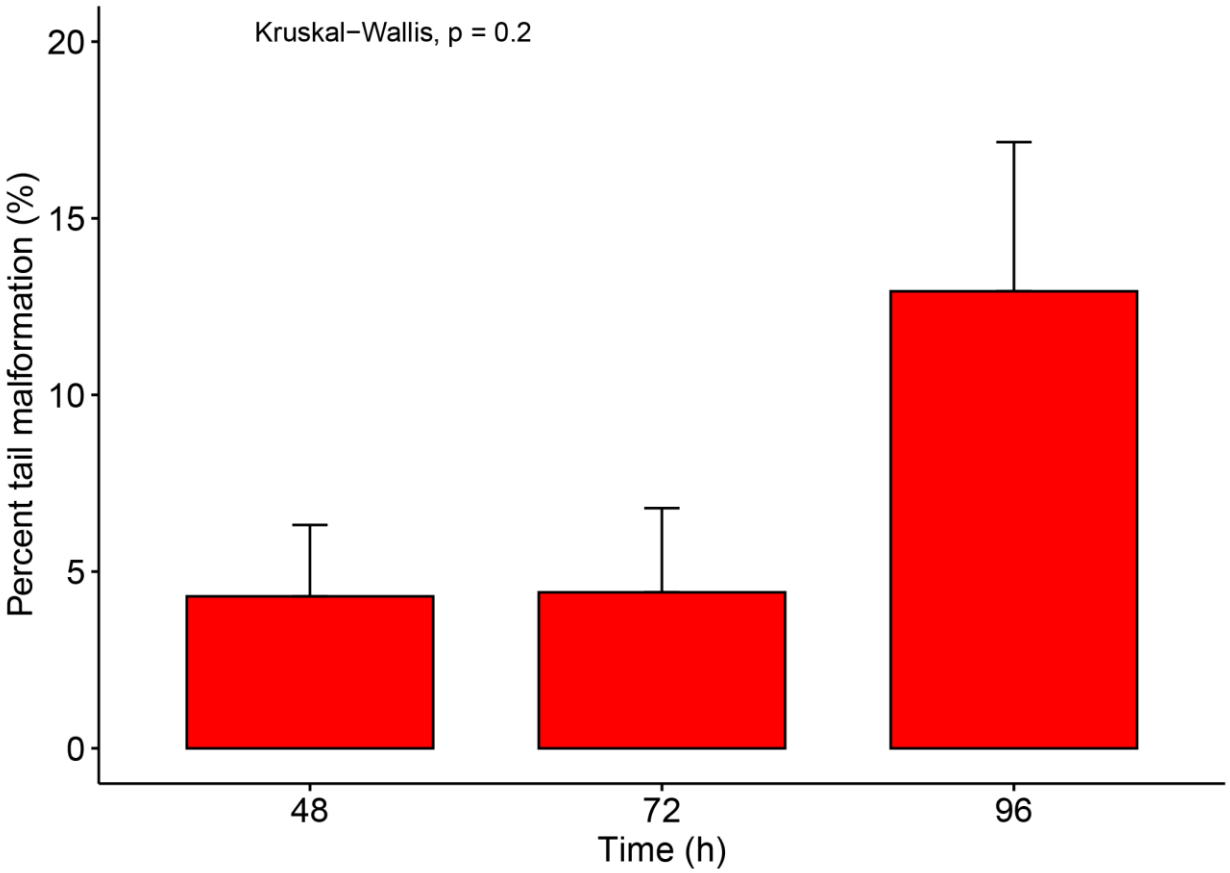

Figure 3. 10. Tail malformation from fentanyl exposure duration.

Swim bladder inflation

Zebrafish use their swim bladder to regulate buoyancy and balance in the water column by expending minimal energy [189]. Inflation of the swim bladder occurs at 96 – 120 hpf via air gulping at the water surface [190, 191]. In our study, only 75% of larvae at 96 hpd in the negative control showed fully inflated swim bladders yet was fully inhibited at 50 and 100 µM. Pairwise comparison to the negative treatment resulted in statistically significant differences being detected at 10, 50 and 100 µM (**Figure 3.11**). A previous study demonstrated that blood circulation was crucial in swim bladder development and the authors hypothesized that swim bladder inflation was secondary to heart malformations [192]. Further research is required to understand the mechanistic effects of fentanyl on swim bladder inflation.

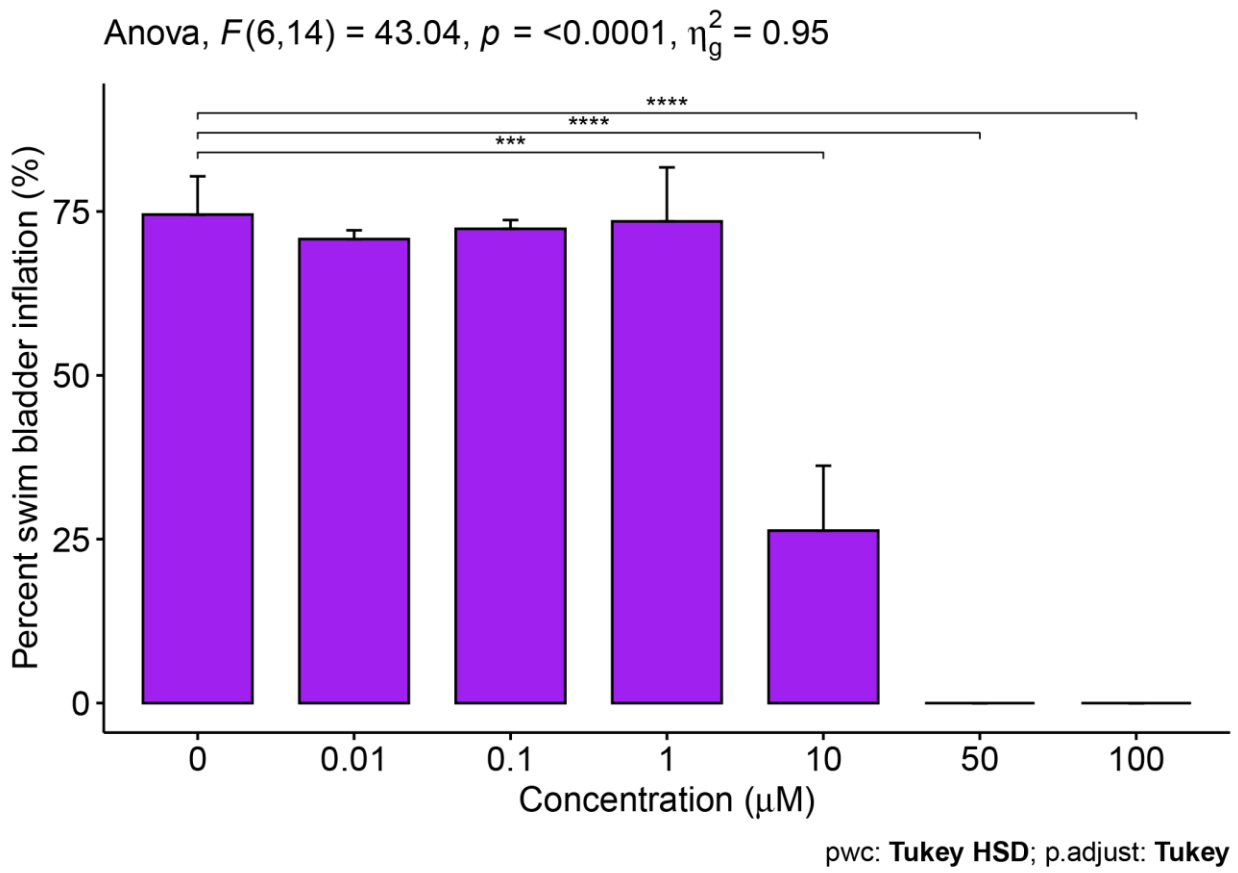

Figure 3. 11. The effect of concentration on swim bladder inflation. *-α = 0.05, ***- α = 0.001, ****- α = 0.0001.

Hatching

Hatching begins after 48 hpf [44]. Fentanyl exposure did not significantly influence hatching (**Figure 3.12**), but a statistically significant difference was detected between 48 hpf and 72 hpf with a higher percentage of hatching (92%) being observed at 72 hours between all groups (**Figure 3.13**).

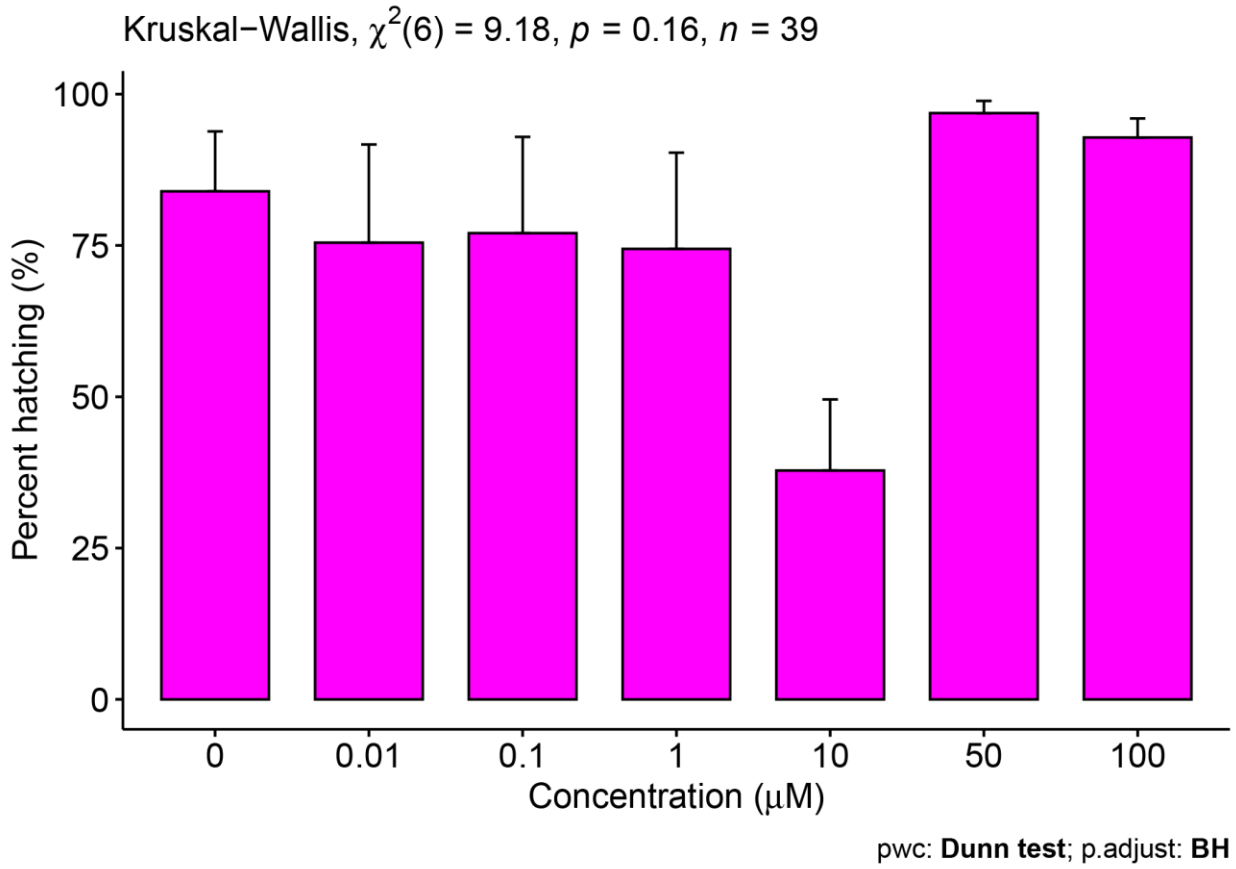

Figure 3. 12. Hatching percentage in relation to concentration.

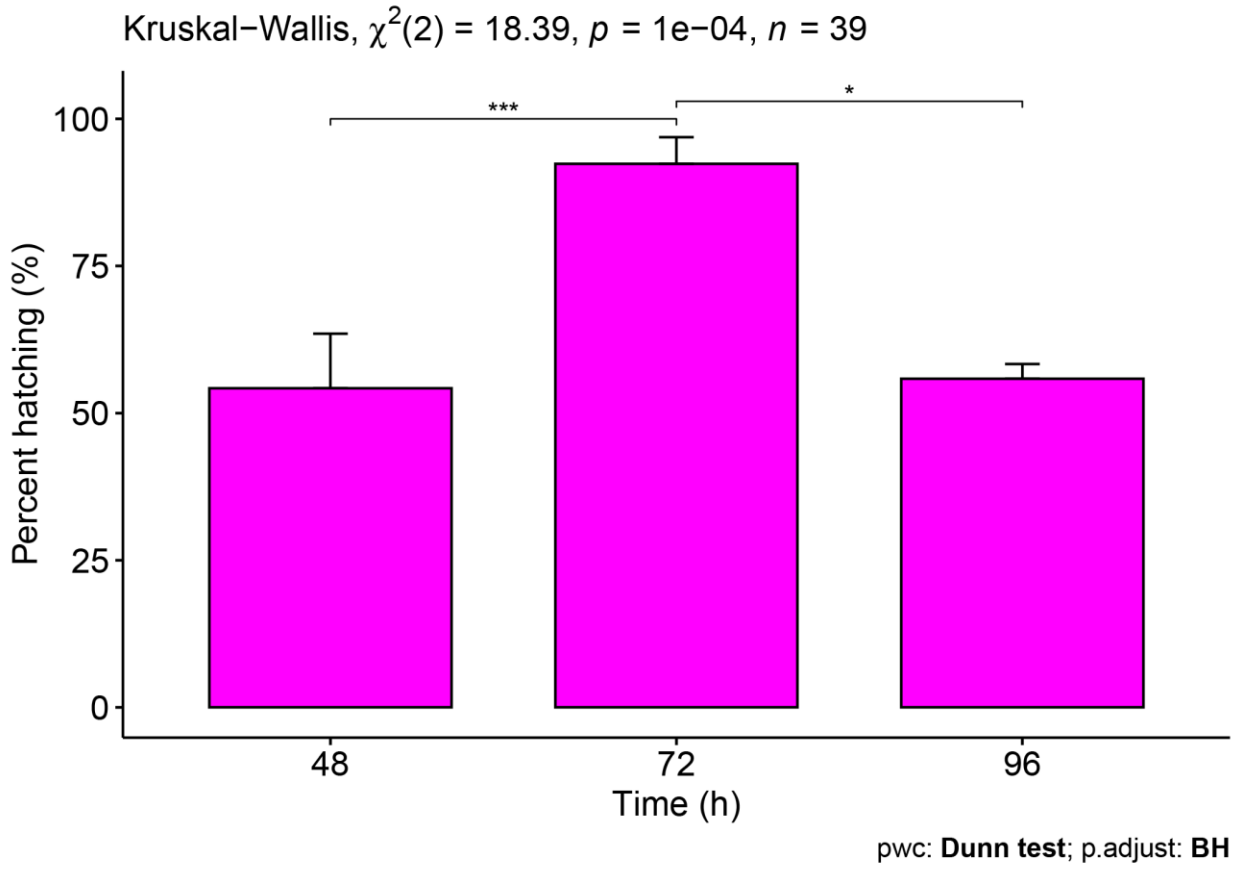

Figure 3. 13. Percent hatching due to fentanyl exposure. *-α = 0.05, ***- α = 0.001.

3.3.2 Metabolism Study

The liver is the major site of metabolism in human. *In vitro* metabolomics studies use human liver microsomes and hepatocytes to elucidate metabolism of novel compound exposure. Metabolomics studies in zebrafish provide not only metabolism data, but also toxicity data as we demonstrate. Adult fish, larvae of varying ages, fish media, and whole organism analysis have been used for metabolite screening. Using a targeted metabolomics approach, we reported three of the major metabolites of fentanyl as early as 24 hpf. 4-ANPP (**Figure 3.14A**), and β-hydroxy fentanyl (**Figure 3.14C**) were detected when larvae were exposed to fentanyl at 1, 10, 50 and 100 µM. Norfentanyl (**Figure 3.14E**) was observed in one sample at 0.1 µM and in all other samples ≥1 µM at all observed times. No metabolites were observed in the negative control or at 0.01 µM (**Figure 3.14**). Here, the reported metabolites in zebrafish have also been detected in human with norfentanyl as the primary metabolite in human. The concentrations at 50 and 100 µM were the

most effective at causing deformities in larvae, but the highest peak areas of the metabolites were observed at these levels.

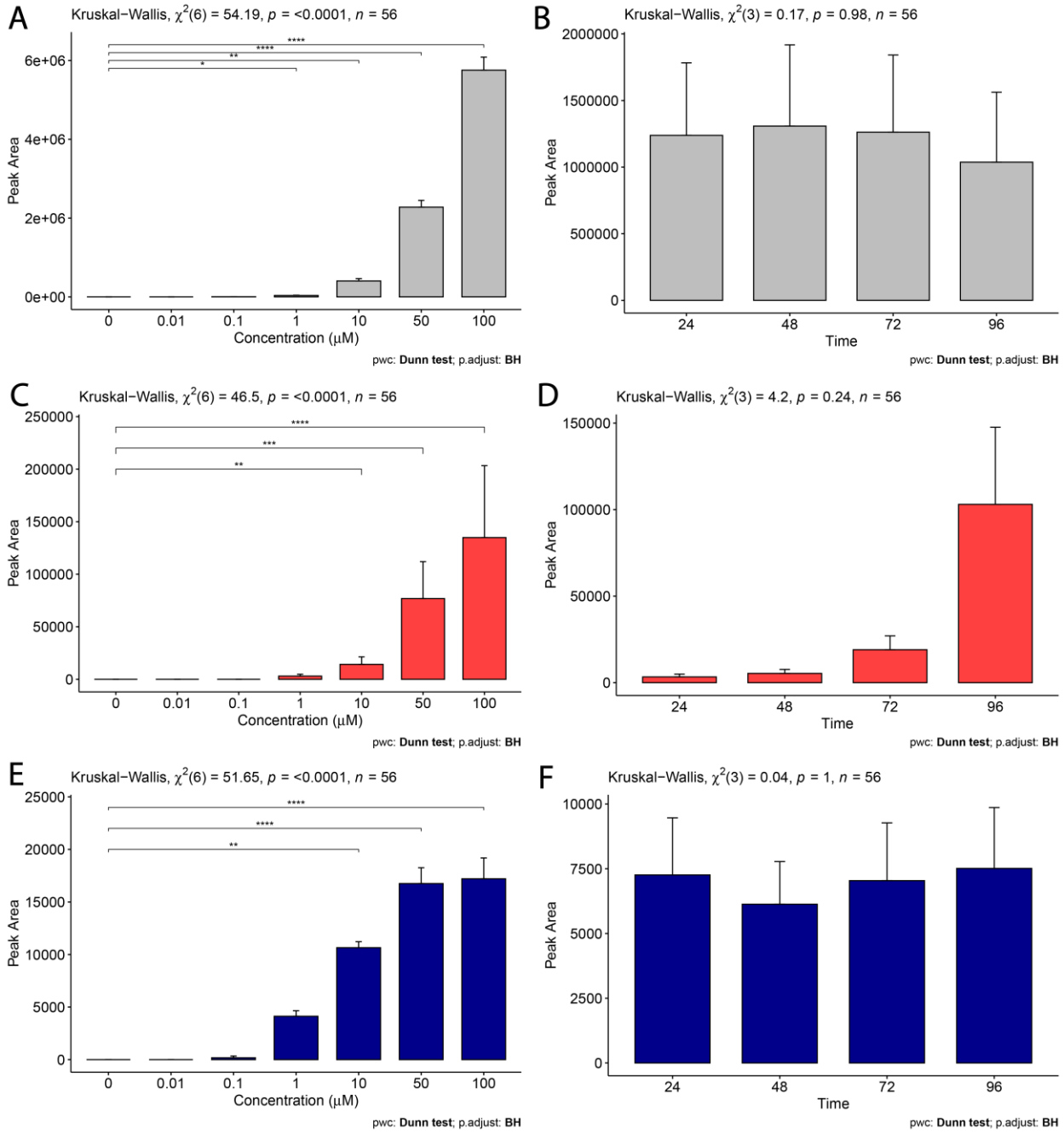

Figure 3. 14. The concentrations 0- 100 µM represent that of fentanyl administered to zebrafish larvae. 4-ANPP was not detected at 0.01 and 0.1 µM (A). The concentrations at 50 and 100 µM produced the highest metabolite peak areas for 4-ANPP(A) but no significant difference was observed over time (B). Significantly higher β-hydroxy fentanyl peak areas were observed at

concentrations ≥10 μM (C) but no statistical differences were detected between the treatment times (D) when the peak areas at the investigated concentrations were combined. The concentrations ≥10 μM produced significantly higher peak areas for norfentanyl (E) but no significant differences were observed in relation to time (F). *-α = 0.05, **- α = 0.01, ***- α = 0.001, ****- α = 0.0001.

3.4.0 Discussion

This study presented three metabolites of fentanyl—4-ANPP, β-hydroxyfentanyl, and norfentanyl produced by zebrafish at all stages of development between 0 and 96 hpf investigated, and the significant morphological defects to the larvae and embryos (0-72 h) at fentanyl concentrations above 10 μM. A previous study investigated the toxicity of opioids, including fentanyl in zebrafish larvae but reported metabolic data for only tramadol and butyrfentanyl [193]. Here, a single assay was used to evaluate toxicity and metabolism of fentanyl, further strengthening the case for zebrafish as an *in vivo* model for opioid studies.

Upward tail curvature and pericardium malformations (**Figure 3.2**) in our study were similar to those previously observed when larvae were exposed to Fu-BAP—a fentanyl analogue [175], yet, observations were not quantified and focused on identifying a maximum tolerated concentration. While these endpoints provide valuable information, they do not account for morphological defects which may lead to further investigations into the chemicals' mechanism of action and translation to human. For this reason, we quantified additional observations and provided statistical analyses to further explain the effect of fentanyl on the observed phenotypes.

Cardiotoxicity was one of the major factors affecting survival of zebrafish larvae, with significant effects observed at 50 and 100 μM (**Figure 3.5**). The world health organization reported cardiovascular disease as the leading cause of death globally [194], making this an active research field. In recent years, the zebrafish model has gained popularity for cardiology studies due to the translucent nature of the heart as it develops [195, 196]. Heart rate [197] and morphological defects [35, 198–200] have been used to demonstrate the toxicity of chemicals on heart development in zebrafish. Bradycardia and respiratory depression have been reported as the main cause of opioid overdose in humans [201]. In zebrafish larvae, fentanyl caused analgesia and respiratory

depression [172]. Although heart rate and respiratory depression were not quantified in our study, larvae movement was reduced when exposed to higher concentrations of fentanyl.

Larvae are reliant on their yolk sac until they start feeding—4-5 days post fertilization [202]. A normal larva as shown in **Figure 3.2A**, absorbs the yolk as it develops. Exposure to toxic compounds can result in a shortening of the yolk extension or abnormal rate of nutrient metabolism and uptake [203] (**Figure 3.2G**). Zebrafish have been proposed as a model to elucidate the toxic effects of chemicals during human development and the metabolic birth defects observed in infants [204]. The transparent nature of zebrafish embryos allow for easy visualization of nutrient uptake and distribution through fluorescence assays [205, 206]. However, confirmation of metabolites using secondary methods as mass spectrometry, as we have presented can provide further support for metabolic rates. In our study, significant abnormal yolk extension occurred at 50 and 100 µM (**Figure 3.7**), the same concentrations where pericardial edema was observed, and where higher metabolites detected (**Figure 3.14**). It is possible that the larvae are preferentially metabolizing fentanyl which may be inhibiting yolk metabolism at such high concentrations. Although zebrafish have complementary xenobiotic metabolizing enzymes to human, the cytochrome P450 (CYP) families 1- 4 have greater sequence diversity [207, 208]. CYP3A65, the zebrafish orthologue to CYP3A4 in human—which metabolizes fentanyl to norfentanyl [53], is 54% similar [208], possibly accounting for the differences in the major metabolite between species. Therefore, to gain full understanding of the impact of fentanyl on nutrient uptake in zebrafish, and to extend this knowledge to human, further research is required to isolate the enzyme metabolizing fentanyl in zebrafish.

One limitation of our research was not quantifying the internal concentration of fentanyl metabolites in zebrafish larvae and evaluating the metabolites' effects on the observed phenotypes. Further investigations would be required to understand any correlations between the concentrations of these metabolites and toxicological effects. Differences in glucose metabolism after fasting were reported in various adult zebrafish strains as well as behavioral variation in wild type strains [209, 210]. Therefore, future zebrafish strain variation studies can be performed to compare the phenotypes and metabolic differences upon fentanyl exposure to understand if one strain provides more reproducible and robust results than another.

3.5.0 Conclusions

We present an *in vivo* vertebrate model to evaluate toxicity and metabolism of fentanyl. Fentanyl disrupted in a dose-dependent manner five out of seven morphological parameters observed—survival, yolk extension, tail, pericardium malformation, and swim bladder inflation, but no effect on coagulation and hatching. A targeted metabolomics approach showed that three metabolites of fentanyl were detected at each observation time and concentration. In addition to opioid zebrafish behavioral studies [211], a combination of developmental defects and metabolite analysis can provide greater insight into the effects of drugs.

Chapter 4: The metabolism of valerylfentanyl using human liver microsomes and zebrafish larvae

Reproduced with additions and permission from Wiley and Travon Cooman, Brianna Hoover, Brianna Sauvé, Sadie A. Bergeron, Natalia Quinete, Piero Gardinali, Luis Arroyo, *Drug Testing and Analysis*, DOI #: 10.1002/dta.3233

4.1.0 Introduction

Fentanyl and novel synthetic opioids (NSOs) are continuously impacting the workload of multiple sectors including law enforcement, first responders and forensic toxicology personnel [212]. The large number of overdose deaths associated with these types of compounds have reached epidemic proportions in recent years. At the front end, the high potency of fentanyl analogs requires trained personnel on the correct use of personal protection equipment, and to properly respond in emergency situations. At the laboratory level, the isolation, identification and quantification of NSOs in biological specimens can be challenging due to the time required for method development, the need of high-end mass spectrometry instrumentation, and the availability of standard reference materials for confirmation. NSOs are illicitly manufactured and sold as other common drugs or laced into known drug entities to cause harm. In some instances, they are consumed without knowledge of the contents and the dosage by the user, resulting in unexpected effects or overdoses. From 2014 to 2016, the overdose deaths from fentanyl or its analogs increased from 9% to 41% [213]. Between July and December of 2016, fentanyl analogs accounted for 20% of overdose deaths [213]. Additionally, from July to December of 2018, 19.4% of opioid-involved overdose death cases were reported to contain one or more fentanyl analogs, one of which was valerylfentanyl, which appeared in 0.5% of those cases [214].

In the 1980s, researchers recognized the need for reference materials to confirm the identity of fentanyl analogues and to evaluate their potency, therefore synthesizing many of which are re-emerging today [215, 216]. Valerylfentanyl was included as one of these compounds and since then it has been detected in wastewater effluents, postmortem samples, or in seized drugs in North America, Australia, Europe and Asia [56, 217–221]. **Figure 4.1** shows the structure of valerylfentanyl, a homologue of fentanyl, differing by 28 Da. A study of valerylfentanyl in monkeys showed that it was equipotent to morphine [216]. Another study in rats measured the binding affinity at the opioid receptors and demonstrated the highest affinity—53.0 ± 5.13 nM at

the μ opioid receptor compared to fentanyl—2.76 ± 0.38 nM [222]. In addition to the limited investigations of the toxicity of valerylfentanyl, pharmacokinetics data are lacking. The zebrafish model is emerging as a model for drug metabolism since they have similar enzymes as humans including cytochrome P450s (CYP) [223]. Zebrafish (*Danio rerio*) have a fully sequenced genome with 70% homology to humans, high fecundity, short generation time (about 3 months), rapid embryonic development (48 hours), and external fertilization, which makes visualization of developing internal organs easy [224, 225]. Additionally, they have opioid receptors similar to humans and have been used as a human disease model [166, 196, 226]. Studies have been performed to investigate metabolite markers for synthetic cannabinoids [227], human performance enhancing drugs [50, 228], synthetic cathinones [163] and opioids [175, 193] using the zebrafish model. More recently, we utilized the zebrafish model as a single assay for the toxicity and metabolism of fentanyl, and detected norfentanyl, β-hydroxyfentanyl, and 4-anilino-*N*-phenethylpiperidine (4-ANPP) from 24 to 96 hours post fertilization[229], providing additional support for their ability to metabolize opioids.

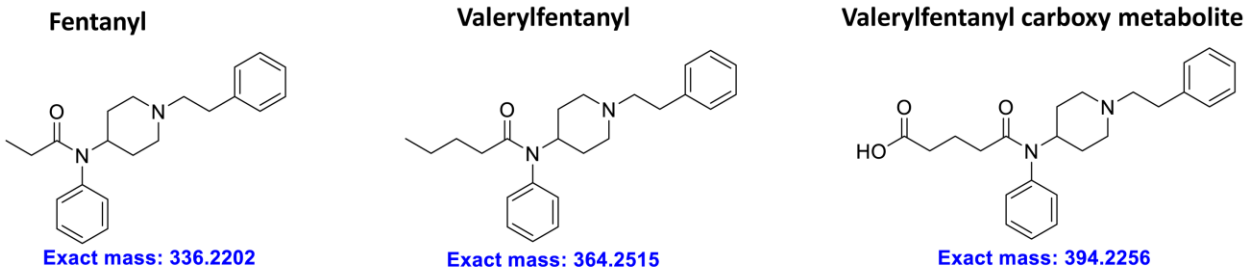

Figure 4. 1. Structural comparison between fentanyl, valerylfentanyl and the commercially available metabolite of valerylfentanyl— valerylfentanyl carboxy metabolite.

Despite valerylfentanyl being a scheduled I drug, it is still consumed illegally. When a parent drug is not detected in a biological specimen, a marker metabolite can be used to determine if the parent was consumed. To our knowledge, no published studies have evaluated the metabolism of valerylfentanyl, although valerylfentanyl carboxy metabolite (**Figure 4.1**) is sold commercially as its marker metabolite. In this study, we compare the metabolism of valerylfentanyl in human liver

microsomes and zebrafish. We also analyze an authentic liver specimen for valerylfentanyl and metabolites.

4.2.0 Experimental

4.2.1 Chemicals and Reagents

Valerylfentanyl hydrochloride, valerylfentanyl carboxy metabolite, and 4-ANPP standards were purchased from Cayman Chemical Company (Ann Arbor, MI, USA). NADPH regenerating system solutions A ($NADP^+$, Glucose-6-phosphate, and $MgCl_2$) and B (Glucose-6-phosphate dehydrogenase in sodium citrate), and 0.5 M potassium phosphate buffer, pH 7.4, were purchased from Corning (Woburn, MA, USA). HPLC grade methanol, HPLC grade water, acetonitrile, ammonium formate, sodium chloride (NaCl), formic acid, and potassium chloride (KCl) were purchased from Fisher Chemical (Waltham, MA). Calcium chloride ($CaCl_2$) was acquired from LabChem (PA). Uridine 5'-diphosphoglucuronic acid (UDPGA), tris base, 4-(2-hydroxyethyl)- 1-piperazineethanesulfonic acid (HEPES) buffer and magnesium sulfate ($MgSO_4 \cdot 7H_2O$) were purchased from Sigma Aldrich (St. Louis, MO, USA). Pooled human liver microsomes (20 mg/mL) were purchased from Thermo Fisher Scientific (Waltham, MA, USA).

4.2.2 Microsome Study

The microsome incubation was performed as previously described [230]. The human liver microsome (HLM) suspension was thawed at 37°C. The reaction mixture contained 780 µL distilled water, 100 µL 0.5 M potassium phosphate buffer, pH 7.4, 50 µL of solution A, and 10 µL of 19.3 mM UDPGA. The suspension was pre-incubated using a Thermal Mixer (ThermoFisher Scientific®; Waltham, MA, USA) at 37°C and 800 rpm for 3 minutes. 10 µL of solution B and 50 µL of HLM suspension were added to initiate the reaction. Aliquots of 300 µL were collected at 0, 150, and 300 minutes and were quenched with 300 µL ice-cold acetonitrile. The samples were centrifuged at 10,000 rpm for 5 minutes. The supernatant was extracted from the samples and placed into a 0.2 µm Nanosep water wettable hydrophilic polytetrafluoroethylene (ww PTFE) centrifugal device (Pall Life Sciences, Port Washington, NY, USA) due to their low protein binding ability. The samples were dried under nitrogen gas at 40°C and reconstituted with 200 µL

methanol. The reconstituted samples were centrifuged again at 10,000 rpm for 1 minute, and the supernatant transferred to LC vials. The experiment was performed in triplicate.

4.2.3 Zebrafish Study

All zebrafish experimental procedures were reviewed and approved by the West Virginia University IACUC. Adult wild-type zebrafish breeders (TL strain) were crossed, fertilized eggs collected and larvae were raised from 5-30 days post fertilization (dpf) on a flow-through housing system on a 14h/10h light/dark cycle at 28.5°C. Daily and weekly checks were performed to maintain the following conditions: pH—7.0 to 8.0, conductivity—600- 800 µS/cm, alkalinity—50- 150 ppm, chlorine—0 ppm, ammonia—0 ppm, nitrate—<200 ppm [231], nitrite—0 ppm, temperature—27- 30°C, and hardness—80- 300 ppm. Ten 30 dpf juvenile zebrafish were dosed with 3 mL of 50 µM valerylfentanyl dissolved in E3 media (5-µM NaCl, 0.17-µM KCl, 0.33-µM $CaCl_2$, 0.33-µM $MgSO_4 \cdot 7H_2O$, 1 M HEPES, at pH 7.4). At about 30 dpf, larvae begin to metamorphosize into juvenile zebrafish—having most adult characteristics, and have fully formed organs crucial for drug metabolism [232]. The experiment was performed in triplicate (n = 30) and dosing occurred in a six-well plate. A negative control also contained 10x 30 dpf zebrafish in media containing no drug. Incubation occurred for 24 hours, after which the fish were euthanized by rapid chilling in ice-cold water per the American Veterinary Medical Association guidelines [233]. The collected media was extracted by adding 1 mL to an Oasis PRiME MCX 3cc solid phase extraction cartridge (Waters Corporation, Milford, MA) using a positive pressure manifold system (United Chemical Technologies, Inc., Bristol, PA). After the sample was loaded, 1 mL of methanol: ammonium hydroxide (95:5) was used for elution. The eluent was dried under nitrogen at 40°C, reconstituted with 100 µL methanol. The collected fish tissue was extracted using the same technique described for the microsome study above.

4.2.4 Instrumental Analysis

All samples were analyzed using a high-resolution mass spectrometer (HRMS)—Q-Exactive - Orbitrap mass spectrometer coupled with a PAL HTC Accela autosampler and Accela1250 pump (ThermoFisher Scientific; Waltham, MA, USA). A Hypersil GOLD™ C18 (30 mm x 2.1 mm x 3 µm) column with a guard column holder and 5 µm drop-in guard cartridge (ThermoFisher Scientific, Waltham, MA) were used. Mobile phase B consisted of methanol whereas mobile phase D consisted of water in 0.1% formic acid. The gradient system was as follows: 5% mobile phase

B ramped to 10% at 0.1 min and held until 0.6 min, ramped to 95% until 10.5 min, ramped down to 10% at 11 min and back to 5% at 13 min. The flow rate was kept at 300 µL/min.

Data were acquired using full MS and data dependent (ddMS^2) using the optimized parameters listed in **Table 4.1.** The normalized collision energy was 30 V. Compound Discoverer version 3.2.0.421 (ThermoFisher Scientific; Waltham, MA, USA) and XCalibur™ version 2.2 (ThermoFisher Scientific®; Waltham, MA, USA) were used for metabolite profiling. The phase I transformations used in Compound Discoverer workflow included dehydration, desaturation, hydration, nitro reduction, oxidation, and reduction and phase II transformations included glucuronide conjugation and sulfation. The mass error for metabolite analysis was set to a maximum threshold of 10 ppm. A standard containing valerylfentanyl, 4-ANPP, and valerylfentanyl carboxy metabolite was injected at the beginning of the run and after every 20 injections to verify the mass error was within the set threshold.

Table 4. 1. Q-Exactive -Orbitrap mass spectrometer full MS/ddMS2 parameters used for metabolite identification.

General	
Runtime	0-13 min
Polarity	Positive
Full MS	
Resolution	70,000
AGC target	1,000,000
Maximum IT	200 ms
Scan Range	70-700 *m/z*
ddMS^2	
Resolution	35,000
AGC target	100,000
Maximum IT	50 ms
Loop count	5
Isolation window	2 m/z
Collision energy	30 V

The samples were also analyzed using an Agilent 6470A triple quadrupole mass spectrometer coupled to a 1290 Infinity II Liquid Chromatography System (Agilent Technologies, Santa Clara, CA). Mobile phase A consisted of water in 0.1% formic acid and 5-mM ammonium formate, whereas mobile phase B consisted of methanol in 0.1% formic acid. The gradient program was as follows: 5% B until 3.5 mins, 40% B until 9.0 mins, ramped back to 5% B at 9.5 mins and held until 11 mins. The flow rate was 0.3 mL/min and 1 µL sample was injected for analysis. Valerylfentanyl, 4-ANPP, valerylfentanyl carboxy metabolite, and selected newly proposed metabolites of valerylfentanyl were detected in multiple reaction monitoring mode. The transitions and instrumental conditions can be found in **Table 4.2**.

Table 4. 2. Compounds and monitored transitions by LC-MS/MS. Cell accelerator voltage was set to 4 V, and the dwell time was 20 ms. The source parameters included: gas temperature- 325°C, gas flow- 9 L/min, nebulizer pressure- 9 psi, sheath gas temperature- 349°C, sheath gas flow- 8 L/min, capillary- 3500 V, nozzle- 500 V.

Compound	**Precursor (*m/z*)**	**Ions (*m/z*)**	**Fragmentor voltage (V)**	**Collision energy (V)**	**RT**
Valeryl fentanyl	365.3	77.0	127	100	6.702
		105.0	127	48	
		188.0	127	24	
Valeryl fentanyl carboxy metabolite (M19)	395.2	77.0	141	100	4.921
		105.0	141	56	
		188.1	141	28	
4ANPP (M6)	281.2	77.0	107	80	4.938
		105.0	107	36	
		188.0	107	16	

Compound	Precursor (*m/z*)	Ions (*m/z*)	Fragmentor voltage (V)	Collision energy (V)	RT
Valeryl norfentanyl (M10)	261.2	84.0	98	20	5.717
		177.1	98	16	
		178.0	98	16	
M7/M8/M9	381.3	91.0	107	56	4.932
		105.0	107	52	5.336
		188.1	107	28	5.597
M12/14	381.3	91.0	107	56	6.091
		105.0	107	52	6.420
		204.1	107	24	
M16/M18	381.3	105.0	107	52	7.248
		204.1	107	24	7.538

4.2.5 Authentic Specimen Analysis

A previously analyzed postmortem liver sample positive for valerylfentanyl [221] was reanalyzed using the Q-Exactive orbitrap and the triple quadrupole for metabolites of valerylfentanyl. The liver specimen acquired from the Office of the Chief Medical Examiner in West Virginia was a drug related overdose death case. Refer to Cox *et al*. for further details about the validation procedure used in extracting the authentic specimen [221].

4.3.0 Results and Discussion

The metabolism of valerylfentanyl was elucidated using both human liver microsomes and juvenile zebrafish. Nineteen metabolites were detected in the HLM model (**Table 4.3)**, with two confirmed using reference standards—M6 (4-ANPP) and M19 (valerylfentanyl carboxy metabolite). The major metabolites in the HLM model were valeryl norfentanyl (M10) and hydroxy valerylfentanyl (M7, M14) whereas in zebrafish the three major metabolites were M10, M12 and M7.

The most prevalent biotransformation was mono hydroxylation, although dihydroxylation, reduction and *N*-dealkylation were observed (**Figure 4.2**). In the zebrafish model, only M10, M7,

M12, M14, M16, and M18 were detected using HRMS possibly due to the lower dose (50 µM) and instrument sensitivity in comparison to the microsome model (dosed at 100 µM), but targeted analysis of higher abundance metabolites observed in the HLMs using QqQ resulted in M6, M7/8/9/12, M10, M14/16, M18, and M19 (**Figure 4.2)**. The microsome model is commonly used as a cost-effective alternative to elucidate the metabolism of novel drugs of abuse, but the findings are not always reflective of *in vivo* results [162]. Microsomes are subcellular fragments, highly purified to contain cytochrome P450 (CYP) drug metabolizing enzymes providing quick metabolic data but do not contain drug transporters which affects therapeutic efficacy, absorption, distribution, and elimination [234]. Zebrafish provide a whole organism model that can help elucidate these mechanisms with stronger biological systems relevance.

In the fish samples, the peak intensity of valeryl norfentanyl (M10) was 2.6% of valerylfentanyl, and valerylfentanyl carboxy metabolite (M19)—a minor metabolite commercially available as valerylfentanyl metabolite, was 0.9% of valeryl norfentanyl (M10). The ratios in the microsome sample varied because the incubation times were different. A longer incubation time resulted in a lower parent drug to metabolite ratio. M19 was detected only after analysis on the QqQ and was 0.4% of the M10 metabolite peak. The ratio of M7/M10 was 60% and 63% for the HLM samples and zebrafish, respectively, whereas the M8/M10 ratio was 11% and 20% for the microsome and zebrafish assays, respectively. However, quantifying these metabolites and evaluating the statistical significance would be required to demonstrate any meaningful model differences such as enzyme effects on metabolism. No metabolites were detected in the negative controls.

Table 4. 3. Summary of detected metabolites. The [M+H]+ and selected diagnostic ions correspond to the experimental accurate mass. The metabolites are listed as M1 to M18 according to the retention times, but also ranked from major to minor metabolite based on the average peak area. The mass error of M19 is based on the reference standard.

Compound	**Formula**	**Mass $[M+H]^+$**	**Mass Error (ppm)**	**RT (mins)**	**Peak Area**	**Selected Diagnostic ions (*m/z*)**	**Rank**
Valerylfentanyl	$C_{24}H_{32}N_2O$	365.2607	5.5	7.26	1.81×10^{10}	188.1445, 105.0704, 244.1708, 281.2028	---
M1	$C_{13}H_{19}NO$	206.1552	6.3	3.21	1.36×10^{8}	188.1446, 105.0705, 146.0607, 134.0972	11

Compound	Formula	Mass $[M+H]^+$	Mass Error (ppm)	RT (mins)	Peak Area	Selected Diagnostic ions (*m/z*)	Rank
M2	$C_{16}H_{24}N_2O_2$	277.1927	5.8	3.80	5.20×10^7	84.0813, 177.1397, 194.1188, 259.1820	14
M3	$C_{19}H_{24}N_2O$	297.1978	5.7	4.28	1.41×10^7	204.1395, 134.0972, 186.1289, 279.1873	17
M4	$C_{19}H_{24}N_2O$	297.1978	5.7	4.74	4.84×10^7	204.1395, 134.0972, 186.1289, 279.1872	16
M5	$C_{24}H_{32}N_2O_3$	397.2511	6.3	5.07	1.02×10^8	204.1397, 186.1291, 279.1874, 297.1978	12
†M6	$C_{19}H_{24}N_2$	281.2029	6.0	5.43	7.50×10^8	188.1445, 105.0705, 134.0973, 146.0974	5
†M7	$C_{24}H_{32}N_2O_2$	381.2558	5.5	5.71	2.53×10^9	188.1445, 105.0705, 260.1660, 363.2450	2
†M8	$C_{24}H_{32}N_2O_2$	381.2557	5.2	5.98	7.17×10^8	188.1445, 105.0705, 260.1658, 363.2451	6
†M9	$C_{24}H_{32}N_2O_2$	381.2558	5.5	6.17	3.41×10^8	188.1445, 105.0705, 281.2028, 194.1185	8
†M10	$C_{16}H_{24}N_2O$	261.1977	6.1	6.32	4.59×10^{10}	84.0813, 177.1397, 178.1239, 244.1709	1
M11	$C_{24}H_{30}N_2O_3$	379.2404	6.3	6.45	5.08×10^6	188.1447, 105.0706, 258.1504, 281.2029	18
†M12	$C_{24}H_{32}N_2O_2$	381.2560	6.0	6.71	3.83×10^8	204.1396, 121.0655, 261.1977, 297.1979	7
M13	$C_{24}H_{30}N_2O$	363.2454	6.3	6.87	1.92×10^8	188.1446, 105.0705, 242.1554, 281.2030	9
†M14	$C_{24}H_{32}N_2O_2$	381.2560	6.0	7.03	1.71×10^9	204.1396, 186.1289, 279.1872, 363.2453	3
M15	$C_{24}H_{32}N_2O_3$	397.251	6.0	7.10	8.57×10^7	121.0655, 277.1927, 193.1348, 202.1239	13
†M16	$C_{24}H_{32}N_2O_2$	381.2559	5.8	7.52	1.64×10^8	189.1386, 105.0705, 204.1395, 297.1978	10
M17	$C_{24}H_{32}N_2O_3$	397.2513	6.8	7.77	5.00×10^7	202.1240, 244.1711, 220.1347, 379.2405	15
†M18	$C_{24}H_{32}N_2O_2$	381.2559	5.8	7.93	9.17×10^8	186.1289, 105.0705, 273.1977, 204.1396	4
*†M19	$C_{24}H_{30}N_2O_3$	395.2356	6.8	---	---	188.1429, 105.0702, 274.1433, 349.2274	---

*M19 was not detected by HRMS analysis, therefore no retention time or peak area is reported.
†These metabolites were detected in both zebrafish and microsome models.

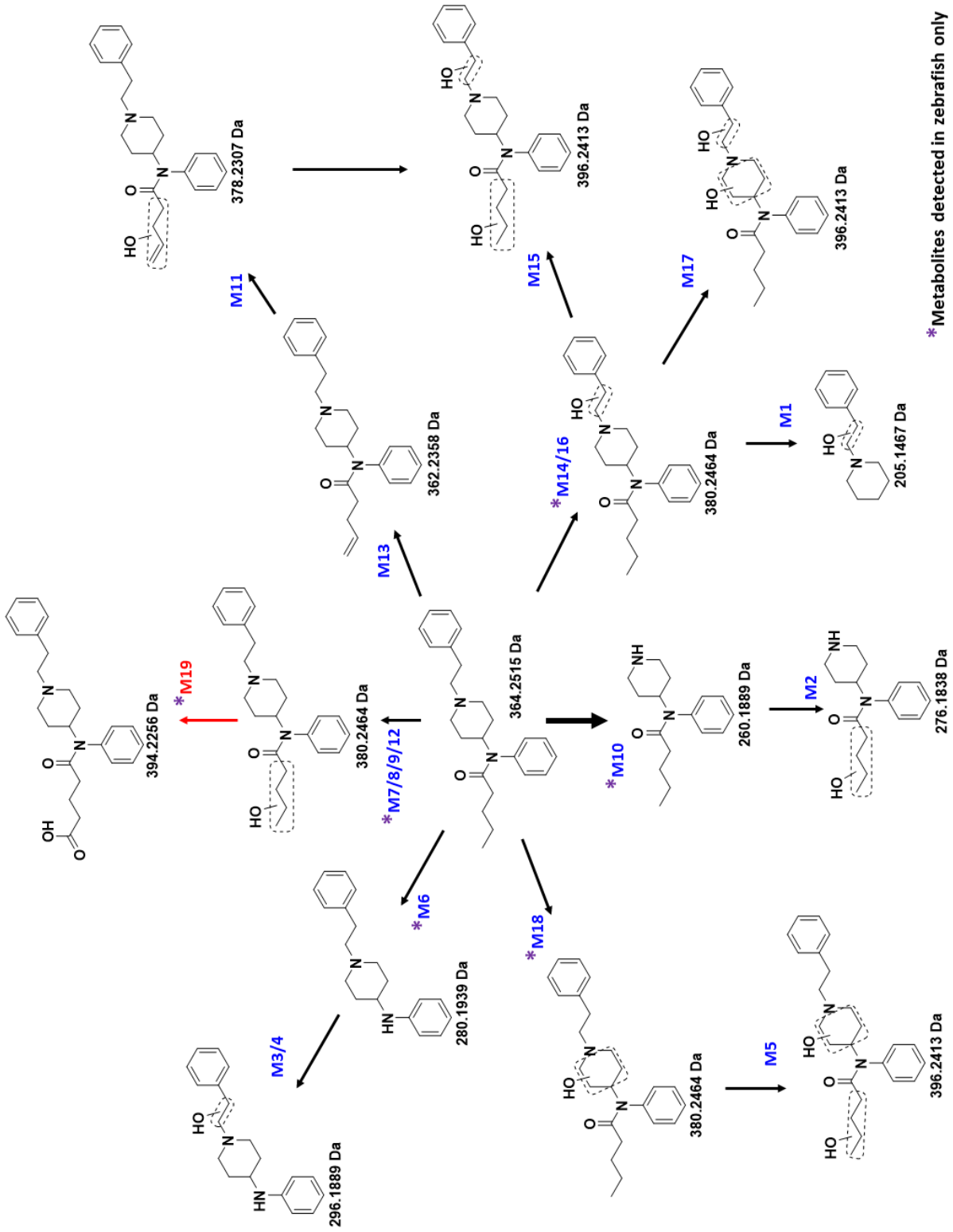

Figure 4. 2. Proposed metabolic pathway of valerylfentanyl. M19 was detected only by QqQ analysis.

The primary purpose of metabolism is for elimination of substances which may result in toxic effects to the body. This is achieved by enzymatically modifying the drug, thereby increasing its polarity relative to the drug. **Figure 4.3** shows the order of elution of the major metabolites of valerylfentanyl detected in the microsome samples analyzed via HRMS. The extracted ion chromatogram of the metabolites observed in the zebrafish assay via QqQ analysis is shown in **Figure 4.4**. The hydroxylated metabolite M7/8/9 eluted before the dealkylated metabolite M10, whereas M14 eluted after M10. Interestingly, two other proposed hydroxylated metabolites-M16/18 eluted after the parent drug but were minor metabolites. Previous studies have also demonstrated metabolites can elute later than the parent compound [235–238].

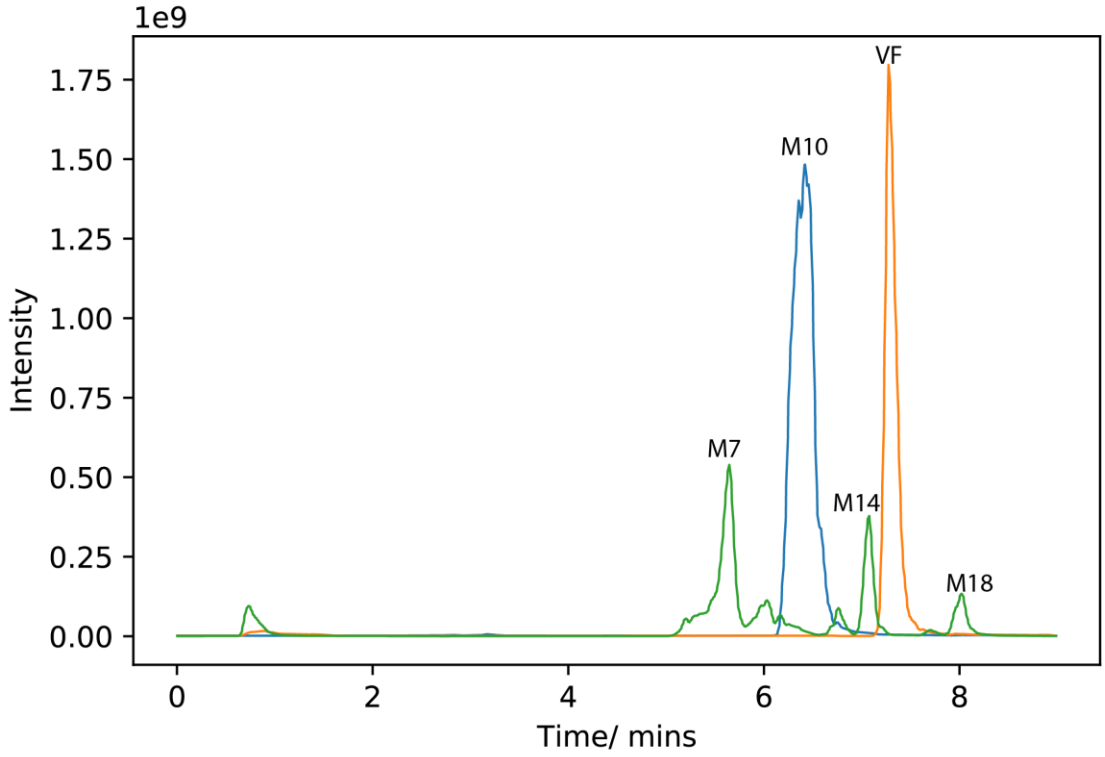

Figure 4. 3. Extracted ion chromatogram for the major metabolites of valerylfentanyl detected in the human liver microsome assay.

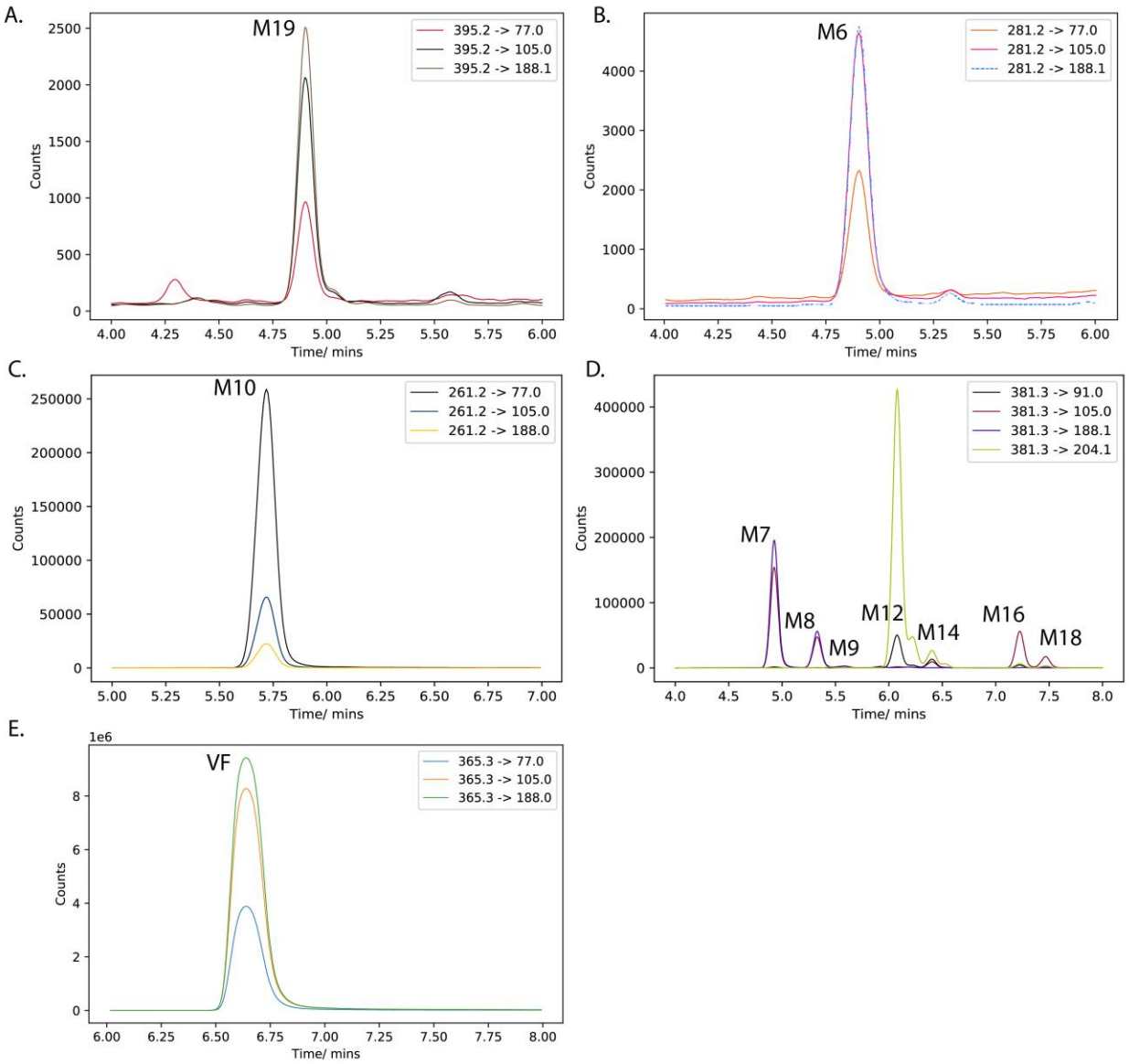

Figure 4. 4. Valerylfentanyl metabolites detected in the zebrafish assay using MRM transitions on the QqQ.

Figure 4.5 shows the spectra of valerylfentanyl and valerylfentanyl carboxy metabolite (M19) standards. The product ion at *m/z* 188, observed in both spectra is common to many fentanyl related compounds and the pathways through the intermediate at *m/z* 281 and *m/z* 216 have been described [239, 240]. Similar to the 216 ion proposed as forming through charge stabilization on the tertiary carbocation, it is likely *m/z* at 244 is formed through the same mechanism [241]. However, the product ion at *m/z* 244 was proposed as an intermediate for the formation of *m/z* 188 in fentanyl through a propionyl transfer to the piperidine moiety [239]. Although valerylfentanyl contains a

pentanoyl moiety and is 28 Da more than fentanyl, if a similar rearrangement were to occur, a product ion at *m/z* 272 ($C_{18}H_{26}NO^+$) may have been observed even though the product ion at *m/z* 218.1553—$C_{14}H_{20}NO^+$ (6.4 ppm mass error) suggests that it is the result of this rearrangement. This does not imply *m/z* 272 is a precursor to *m/z* 218 but if this is the preferred pathway, its abundance was negligible. The product ions at *m/z* 105, *m/z* 134, *m/z* 146, *m/z* 188, and *m/z* 281 similar for M19 and valerylfentanyl, are common to fentanyl analogues. Additional ions for M19 (**Table 4.3**) were observed at *m/z* 377—$C_{24}H_{29}N_2O_2^+$, a loss of H_2O—18 Da; *m/z* 349—$C_{23}H_{29}N_2O^+$, a loss of CH_2O_2—46 Da, and *m/z* 274—$C_{16}H_{20}NO_3^+$, a loss $C_8H_{11}N$—121 Da.

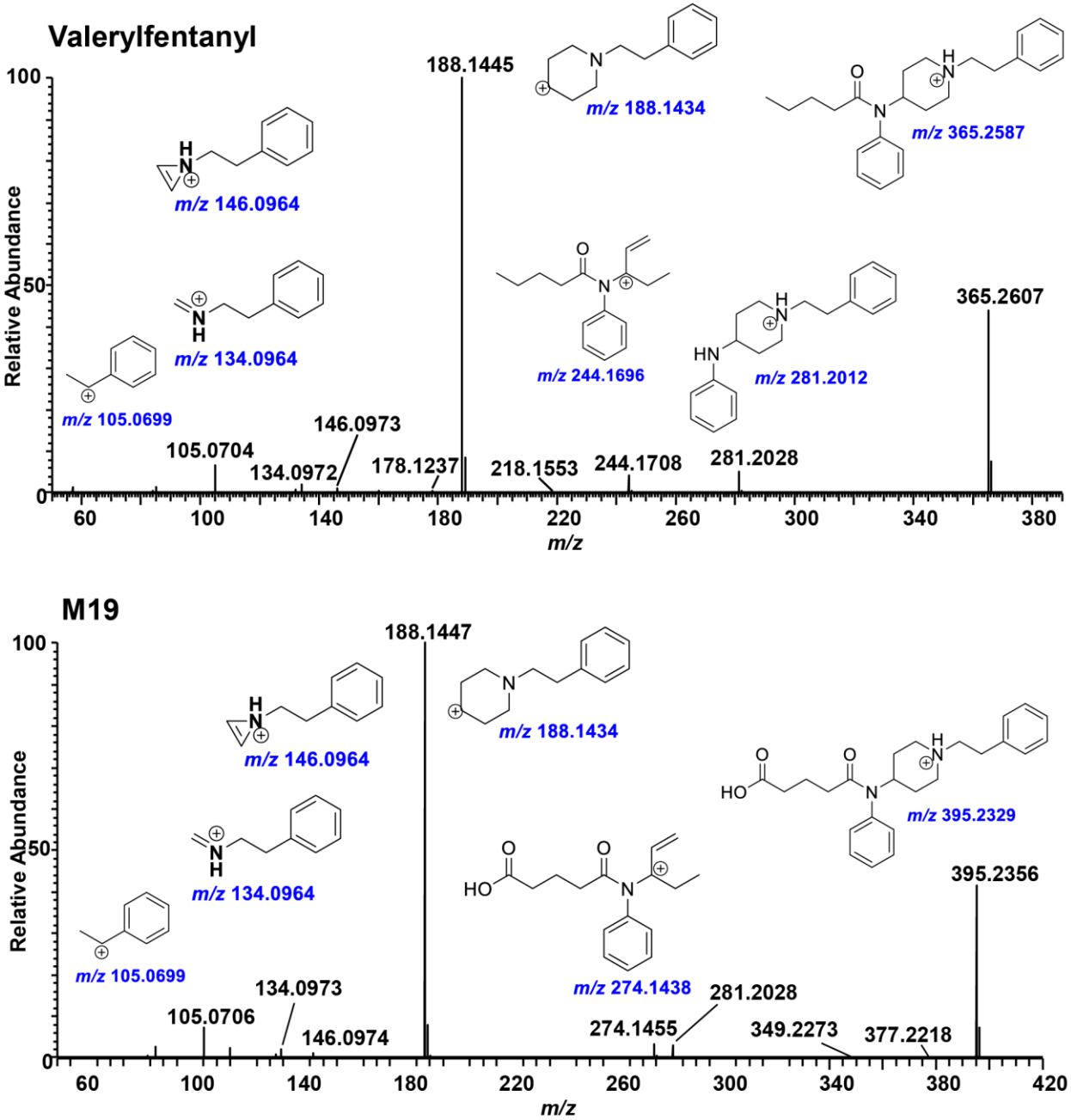

Figure 4. 5. Mass spectra of valerylfentanyl and valerylfentanyl carboxy metabolite (M19) standards (Collision energy (CE) = 30 V).

The spectra of the most abundant metabolites M10 and M7 are shown in **Figure 4.6.** The base peak for M10 is the piperidinylium ion at *m/z* 84. The product ion at *m/z* 244—$C_{16}H_{22}NO^+$, formed by a loss of NH_3—17 Da from the precursor ion at *m/z* 261 also observed for valerylfentanyl. A loss of C_5H_9N—83 Da from the precursor ion resulted in a product ion at *m/z* 178, but a loss of

pent-1-en-1-one—C_5H_8O, 84 Da resulted in the ion at *m/z* 177. The proposed precursor ion for M7 is a result of mono hydroxylation on the pentanoyl group. The base peak is observed at *m/z* 188. A loss of H_2O—18 Da from the precursor ion resulted in *m/z* 363—$C_{16}H_{22}N_2O^+$. Subsequently, the loss of 1-phenethyl-1,2,3,6-tetrahydropyridine ($C_{13}H_{17}N$)—187 Da resulted in the formation of the observed ion at *m/z* 176. Although this is not a favorable pathway, it supports hydroxylation on the pentanoyl group. Similarly, the product ion at *m/z* 260—a loss of 2-phenylethan-1-amine ($C_8H_{11}N$), 121 Da, provides evidence for this metabolite.

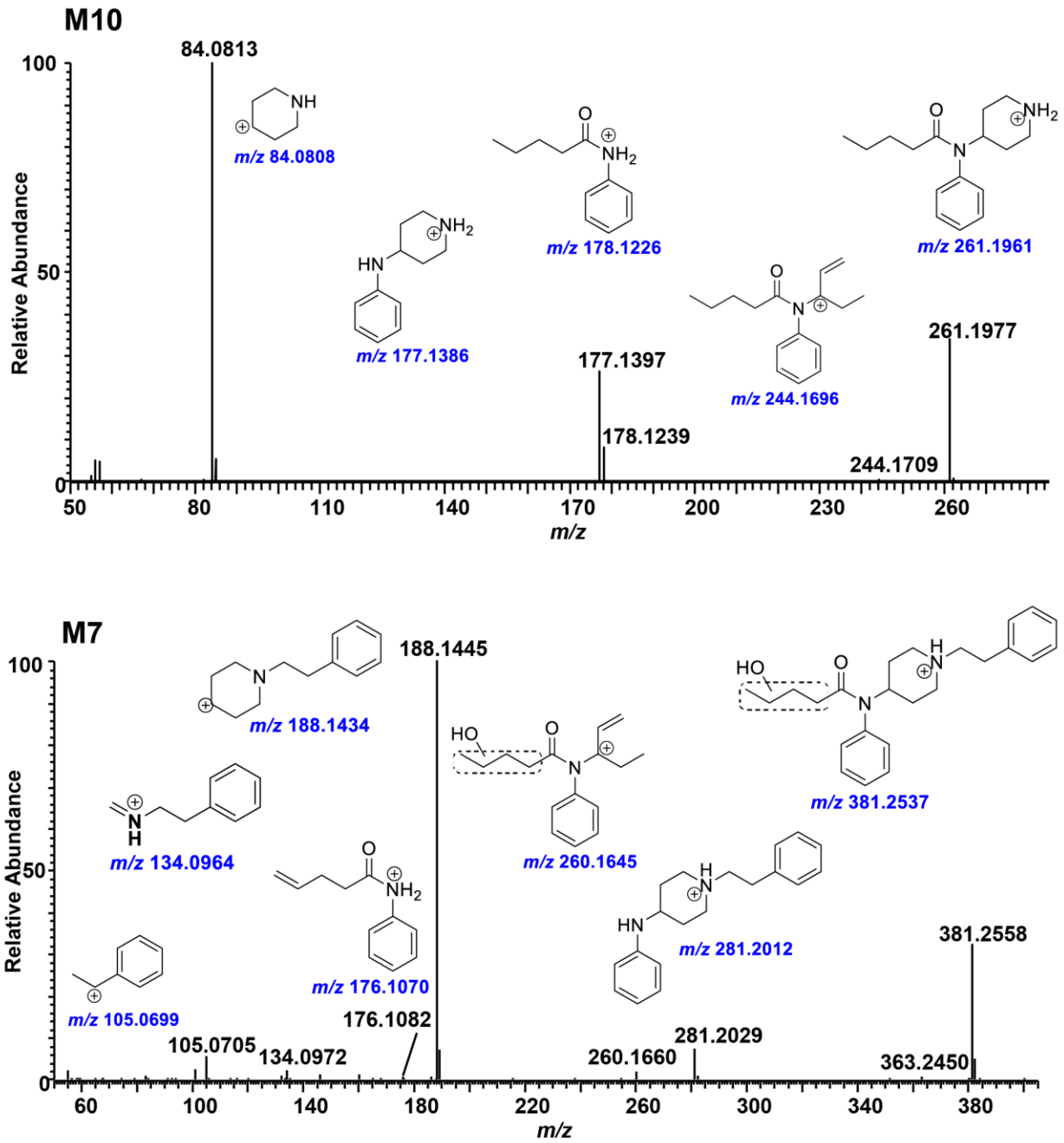

Figure 4. 6. Mass spectra of M10 (valeryl norfentanyl) and M7 (CE = 30 V).

The metabolites M14 and M18 as shown in **Figure 4.7** are isomers. Whereas the base peak for M14 is the product ion at *m/z* 204, the base peak for M18 is observed at *m/z* 186. Despite the low abundance of the ion at *m/z* 188, the product ions at *m/z* 105, *m/z* 134, *m/z* 146, *m/z* 160 are common to both metabolites. However, the difference between these metabolites is the position of the hydroxyl group (**Figure 4.2**). The proposed structure of M14 is a result of hydroxylation on the

alkyl group of the phenethylpiperidine moiety whereas M18 is hydroxylated on the piperidine ring. Both M14 and M18 show a loss of H_2O—18 Da for a product ion at *m/z* 363 but is more prominent in M14. Subsequently, the loss of $C_5H_{10}O$—86 Da resulted in the product ion at *m/z* 279 which may be isomeric in both spectra due to the position where dehydration occurs. Furthermore, the loss of aniline—C_6H_7N, 93 Da resulted in the isomeric product ion at *m/z* 186, following the pathway *m/z* 381→ 363 → 279 → 186. The product ion at *m/z* 204 was also observed for both metabolites and follows the pathway *m/z* 381→ 297— loss of $C_5H_{10}O$, 86 Da → 204—loss of aniline. The product ion at *m/z* 105 was the third most intense ion for M18 whereas it was one of the least abundant for M14. This may have been due to the difficulty to form *m/z* 105 when a hydroxyl group is present on the alkyl group of the phenethylpiperidine moiety (M14) compared to its presence on the piperidine ring (M18). The product ion at *m/z* 273— $C_{17}H_{25}N_2O^+$ in **Figure 4.7,** M18 was also observed in the valerylfentanyl standard spectrum but at 0.013% of the *m/z* 188 base peak. In order for the 1-methylene-4-(*N*-phenylpentanamido)piperidin-1-ium ion to form from M18, a loss of C_7H_8O —108 Da is expected, whereas a loss of C_7H_8—92 Da is expected for valerylfentanyl.

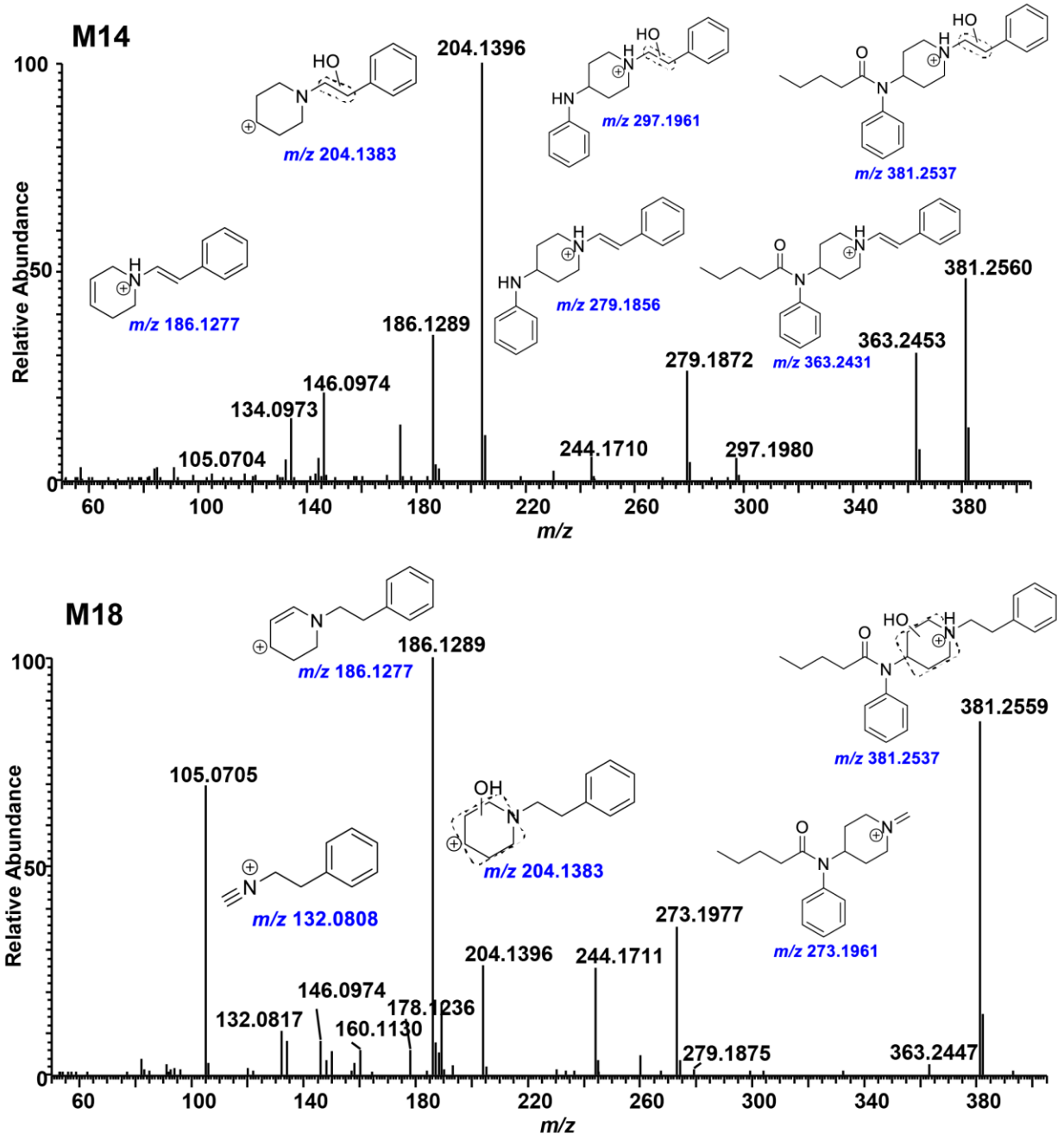

Figure 4. 7. Mass spectra of metabolites M14 and M18 (CE = 30 V).

The spectra of M6 (4-ANPP) and M8 are shown in **Figure 4.8**. M6 is a precursor to many fentanyl analogues where modification occurs on the amide group of fentanyl [242]. Therefore, it can be found as an impurity in street drugs containing fentanyl related compounds and is also an amide hydrolyzed metabolite of fentanyl analogues modified on the amide group [243]. Although it is not ideal as a marker metabolite, when detected in toxicological specimen, it can indicate the

presence of fentanyl analogues. The product ions observed in the mass spectrum of M6 were also observed for valerylfentanyl (**Figure 4.5**) and the characterization of the ions have been described [239].

Other mono hydroxylated valerylfentanyl isomeric metabolites included M8 (**Figure 4.8**), M9, M12 (**Figure 4.9**) and M16 (**Figure 4.10**). The mass spectra of M8 and M9 are similar due to hydroxylation occurring on the pentanoyl group and the explanation for the product ions are similar to M7 discussed above (**Figure 4.6**). The spectrum of M12 and M14 have *m/z* 204 as the base peak but the distribution of the product ions is different. Whereas M14 has a product ion at *m/z* 363, indicating a loss of H_2O, no *m/z* 363 was observed in M12. This indicates M12 is hydroxylated on either aromatic ring of valerylfentanyl. The presence of the product ion at *m/z* 261(**Figure 4.9,** M12)— a loss of C_8H_8O, 120 Da indicates the hydroxyl group is on the aromatic ring of the phenethylpiperidine moiety which is further supported by the product ion at *m/z* 121 ($C_8H_9O^+$) which corresponds to the hydroxy-phenethanylium ion—a loss of C_5H_9N, 83 Da if produced via the product ion at *m/z* 204.

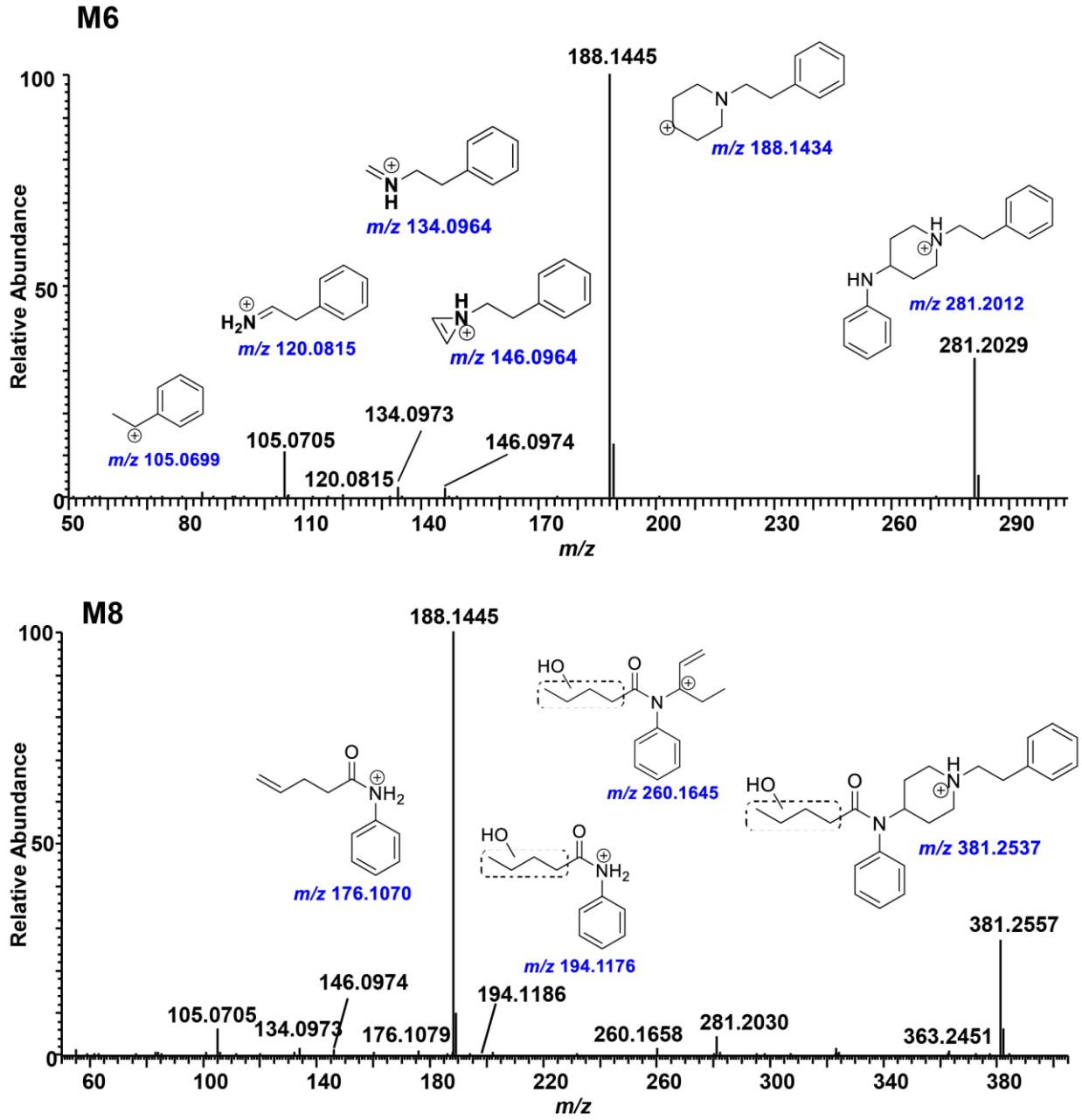

Figure 4. 8. Mass spectra of M6 (4-ANPP) and M8 (CE = 30 V).

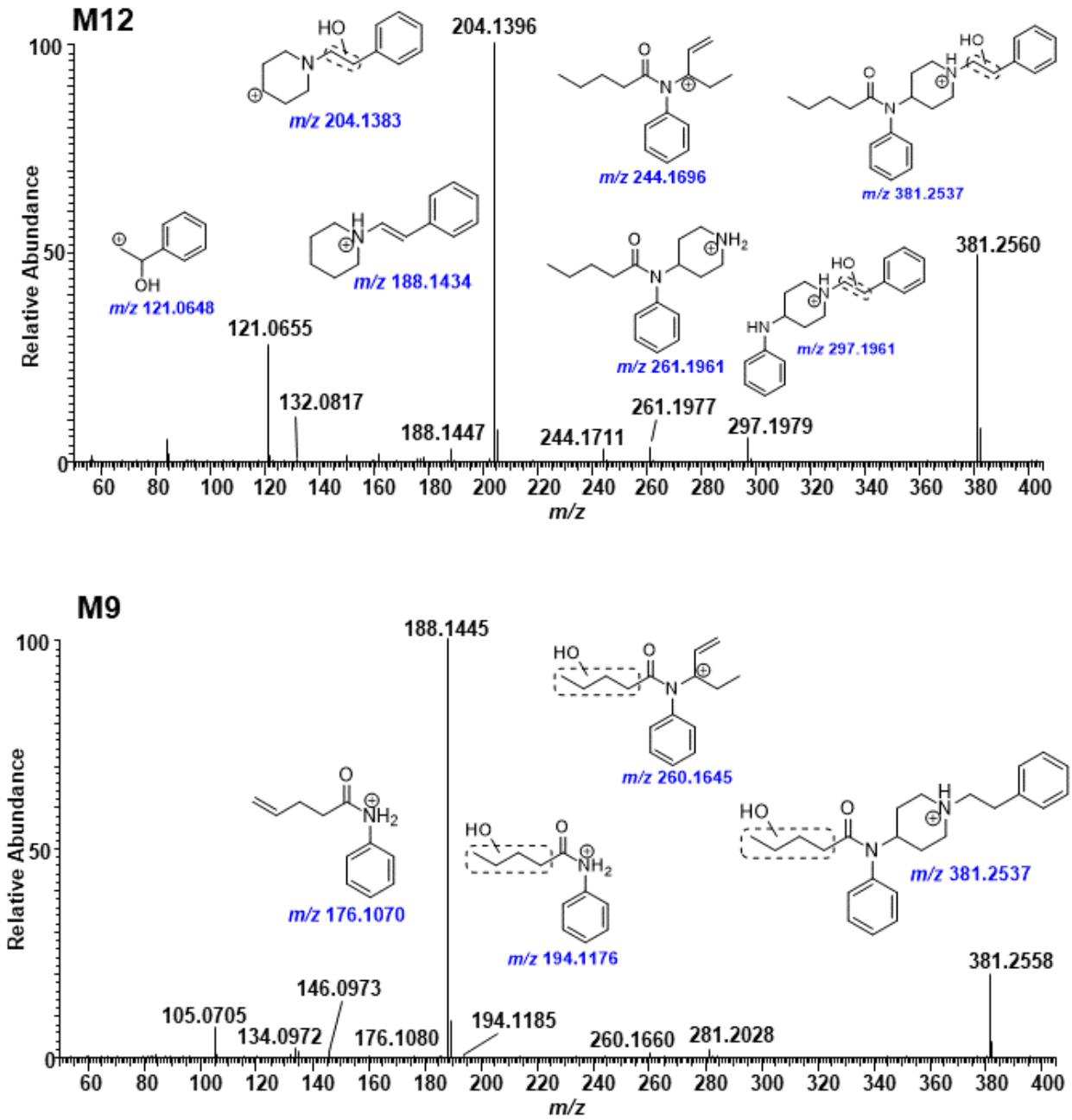

Figure 4. 9. Mass spectra of M12 and M9 (CE = 30 V).

Figure 4.10 shows the mass spectra of the desaturated metabolite, M13 and another mono hydroxylated valerylfentanyl metabolite, M16. Although similar product ions as the other mono hydroxylated metabolites were observed for M16, such as *m/z* 363, *m/z* 297, *m/z* 279, *m/z* 204, *m/z* 188, *m/z* 186, the protonated precursor ion at *m/z* 381 was the base peak, followed by *m/z* 189 ($C_{12}H_{17}N_2^+$). A loss of pent-1-en-1-one— C_5H_8O, 84 Da from the product ion at *m/z* 273 resulted

in *m/z* 189. The base peak for M13 and most product ions were similar to valerylfentanyl. However, the product ion at *m/z* 242 and *m/z* 176 indicate the desaturation occurred on the pentanoyl group. The position of the double bond in the proposed structures is only for illustration purposes.

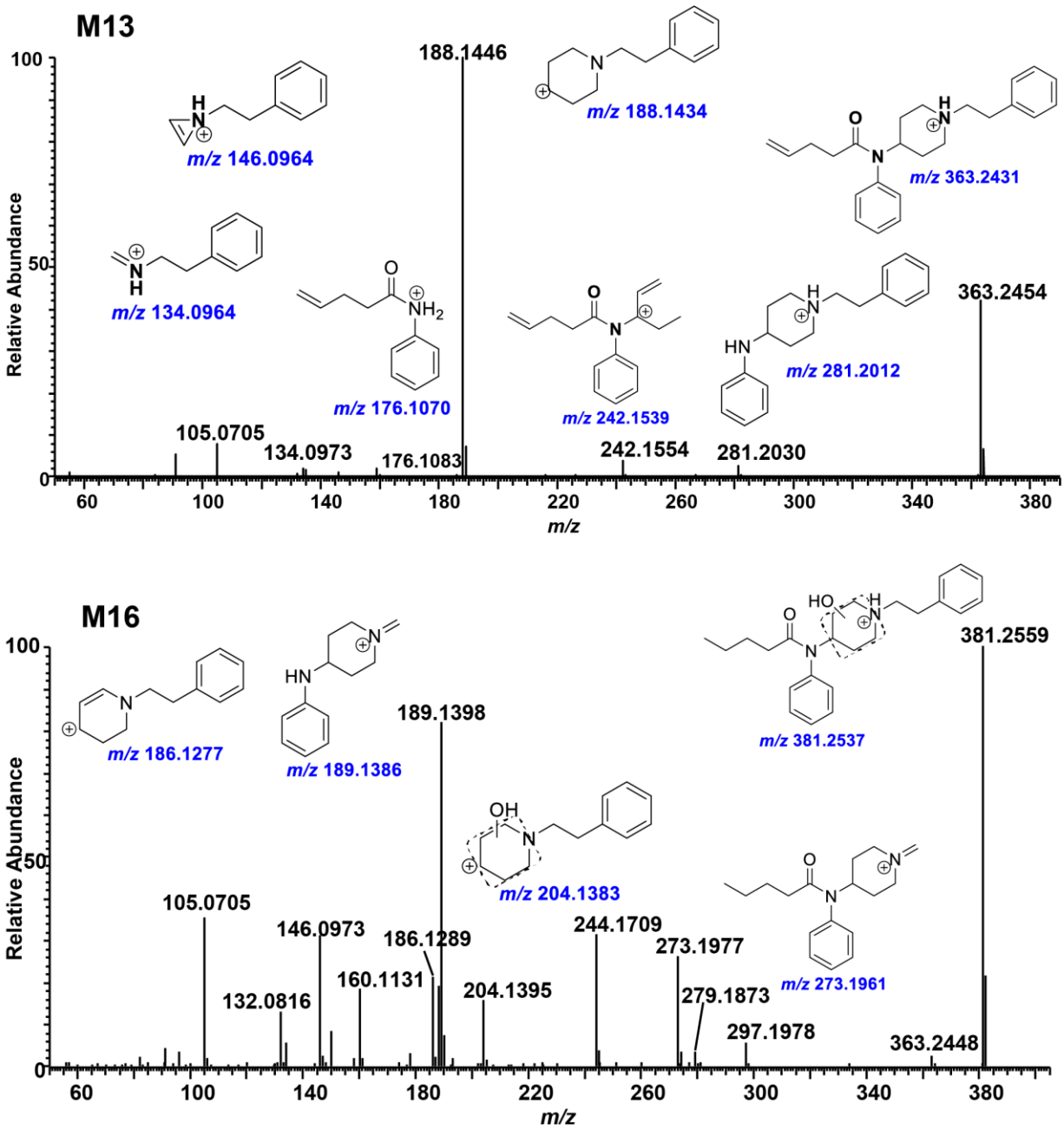

Figure 4. 10. Mass spectra of M13 and M16 (CE = 30 V).

The spectra of the minor metabolites hydroxy-phenethylpiperidine (M1) and di-hydroxy valerylfentanyl (M5) are shown in **Figure 4.11**. M1 was the earliest eluting metabolite detected (3.21 mins). However, similar to 4-ANPP (M6), it would not be a marker metabolite for valerylfentanyl as it is common to other fentanyl analogues where substitution occurs on the amide group. The mass spectrum is also similar to 4-ANPP, but the base peak is the protonated precursor ion—*m/z* 206. A loss of H_2O, 18 Da from M5 protonated precursor ion—*m/z* 397 resulted in the product ion at *m/z* 379. A subsequent loss of C_5H_6O, 82 Da resulted in *m/z* 297, and dehydration—loss of 18 Da, resulted in *m/z* 279. The base peak at *m/z* 204 indicates at least one hydroxyl group is present on the piperidine moiety and the hydroxypentylidyne-oxonium ion ($C_5H_9O_2^+$) at *m/z* 101 indicates another hydroxyl group on the pentanoyl group. Furthermore, the observed *m/z* 121 ($C_8H_9O^+$), supports the other hydroxyl group on the alkyl chain of the phenethylpiperidine moiety.

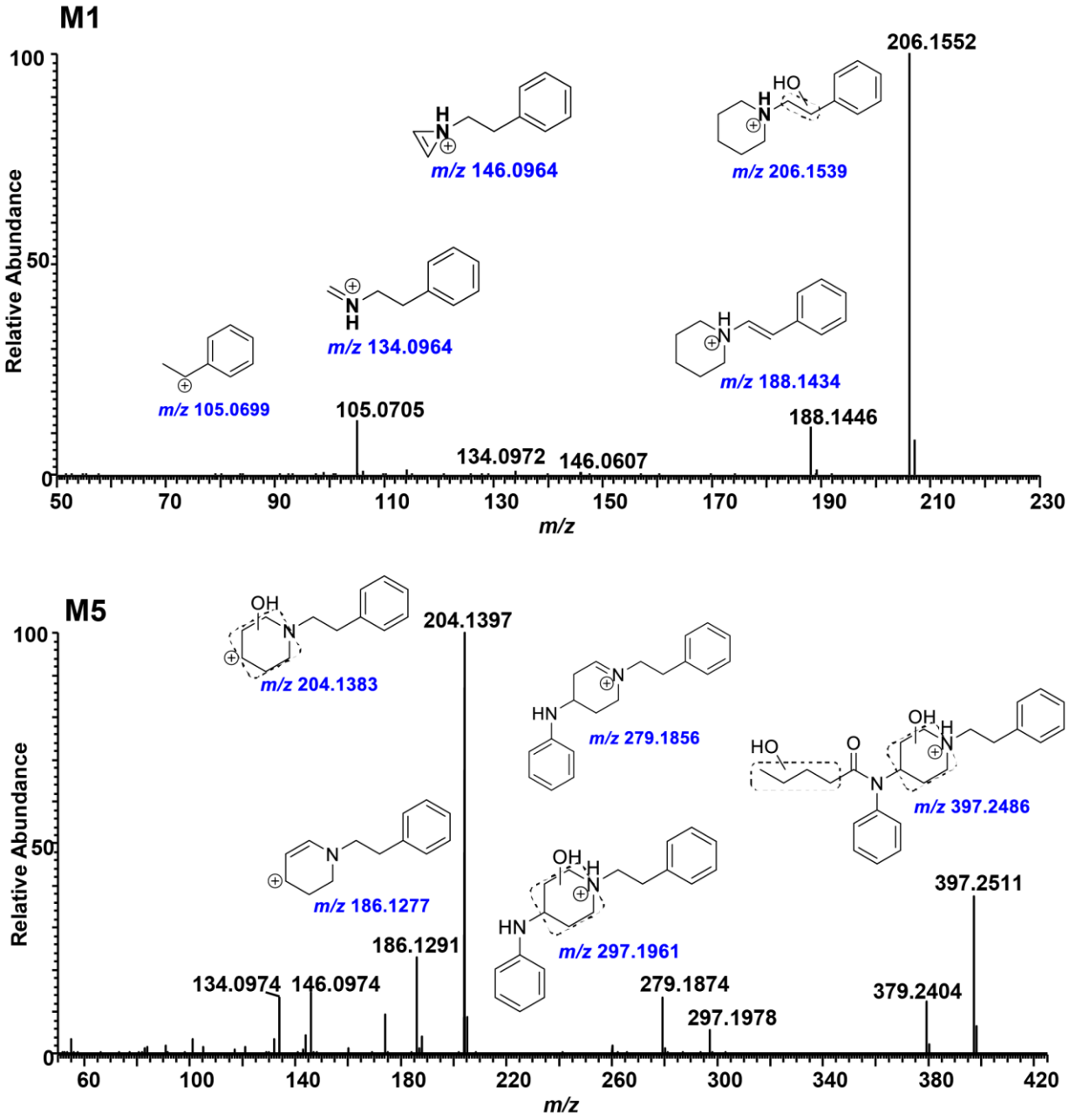

Figure 4. 11. Mass spectra of M1 and M5 (CE = 30 V).

Two isomers of the di-hydroxylated metabolite M5, eluted at 7.10 min (M15) and 7.77 mins (M17) and were both less abundant than M5. The mass spectrum of M15 is shown in **Figure 4.15**. The base peak is observed at *m/z* 121, $C_8H_9O^+$ and corresponds to a loss of C_5H_9N—83 Da from the product ion at *m/z* 204. The product ion at *m/z* 202 was more intense than *m/z* 204 and corresponds

to $C_{13}H_{16}NO^+$—a loss of 18 Da from *m/z* 220 ($C_{13}H_{18}NO_2^+$). The second most intense product ion was observed at *m/z* 277—$C_{16}H_{25}N_2O_2^+$, and resulted from the loss of C_8H_8O, 120 Da from the protonated precursor ion at *m/z* 397. A subsequent loss of NH_3—17 Da resulted in *m/z* 260 ($C_{16}H_{22}NO_2^+$). A loss of C_5H_8O, 84 Da from *m/z* 277 resulted in third most abundant product ion at *m/z* 193—$C_{11}H_{17}N_2O^+$ providing support for hydroxylation on the piperidine ring. Furthermore, *m/z* 295 ($C_{19}H_{23}N_2O^+$) was observed, indicating dehydration on the piperidine ring.

M17 shows the precursor ion *m/z* 397 as the base peak and *m/z* 202 as the second most prominent in **Figure 4.13**. The product ion at *m/z* 220— $C_{13}H_{18}NO_2^+$, indicates the presence of dihydroxylation occurring on the phenethylpiperidine moiety. A loss of water from this product ion results in the favorable formation of *m/z* 202—$C_{13}H_{16}NO^+$, and subsequent loss of a second water molecule resulted in the product ion at *m/z* 184.

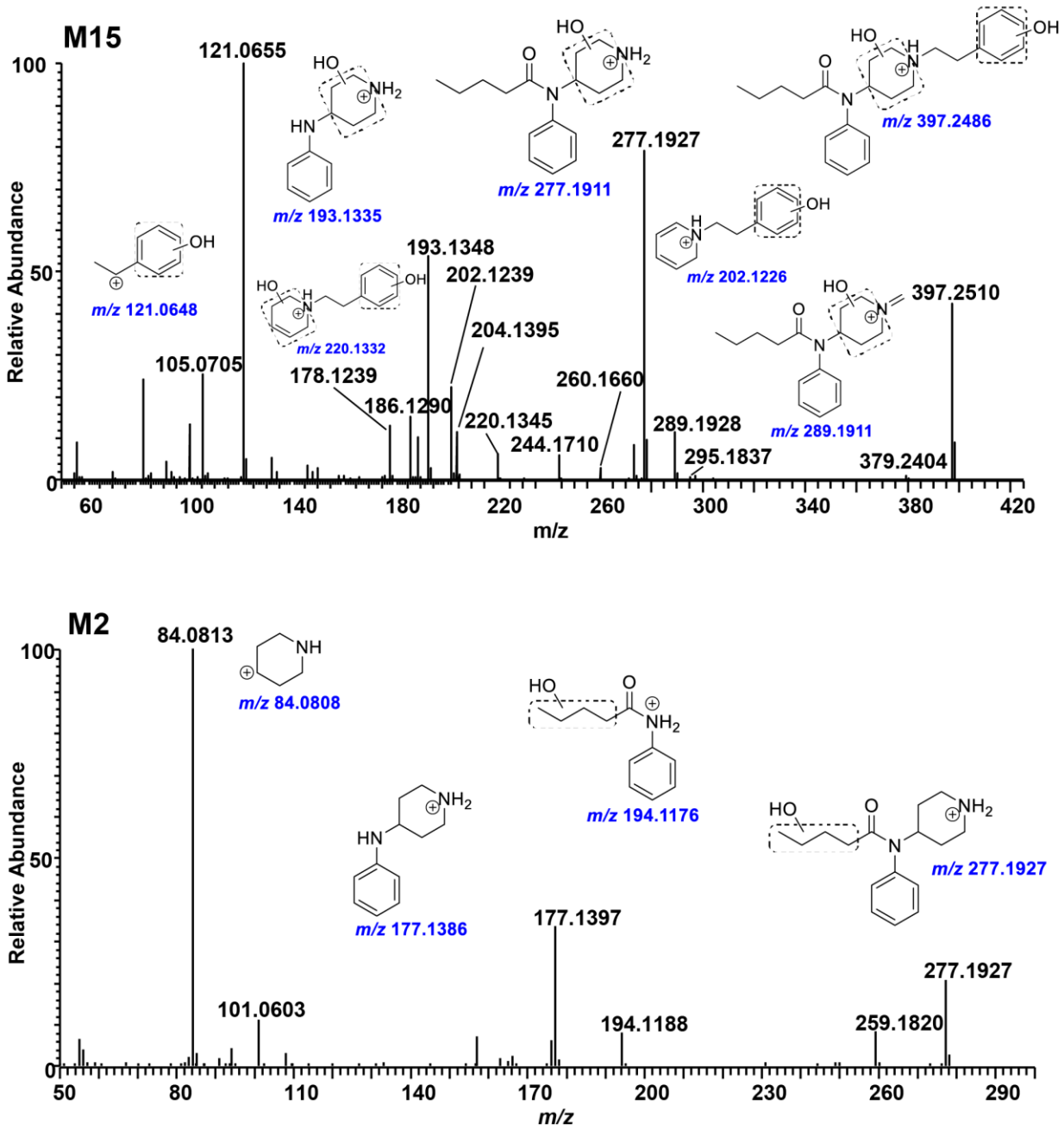

Figure 4. 12. Mass spectra of M15 and M2 (CE = 30 V).

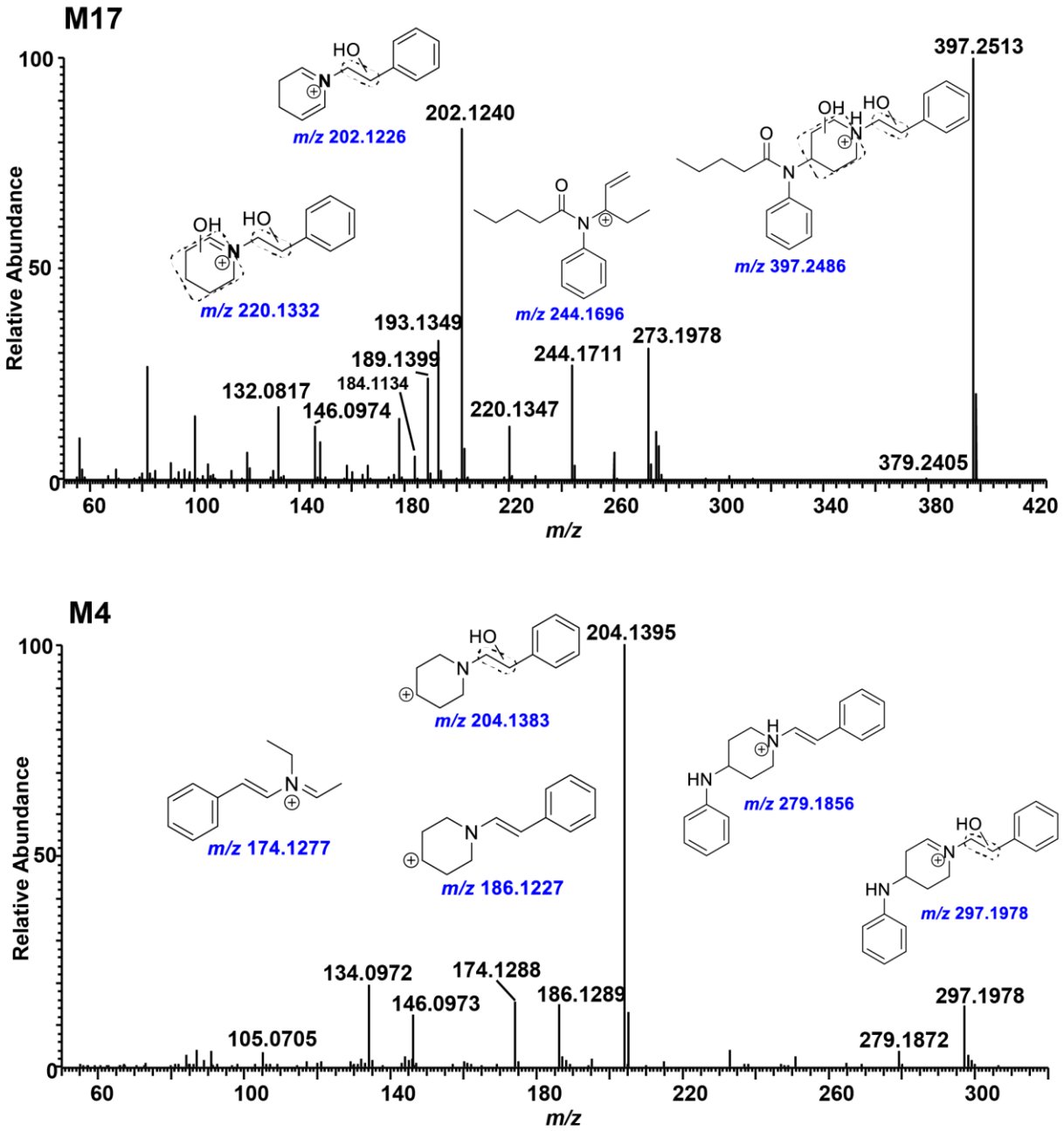

Figure 4. 13. Mass spectra of M17 and M4 (CE = 30 V).

Hydroxylation of the major metabolite M10, and minor metabolite M6 produced highly polar metabolites M2, M3 and M4 (**Figure 4.2**). The mass spectrum of M2, shown in **Figure 4.12** consisted of product ions similar to M10 (**Figure 4.6**). For example, the base peak in both spectra was *m/z* 84. However, the product ion at *m/z* 259 indicates a loss of H_2O, 18 Da and a further loss

of pentadienone, C_5H_6O—82 Da resulted in the observed product ion at *m/z* 177. A loss of hydroxypentenone, $C_5H_8O_2$—100 Da from the protonated precursor ion can also produce *m/z* 177. The observed product ions at *m/z* 101—$C_5H_9O_2^+$, *m/z* 194—$C_{11}H_{16}NO_2^+$, and *m/z* 94—$C_6H_8N^+$ also indicate hydroxylation of M10 occurred on the pentanoyl group. The mass spectra of M4 (**Figure 4.13**) and M3 (**Figure 4.14)** consist of similar product ions and abundance as they are isomers with hydroxylation occurring on the ethylbenzene group. The base peak was observed for both metabolites at *m/z* 204 and was discussed above for metabolites hydroxylated at a similar position such as M12, M14, M16, and M18. The product ion at *m/z* 121 observed in the spectra also supports the hydroxylation of M6.

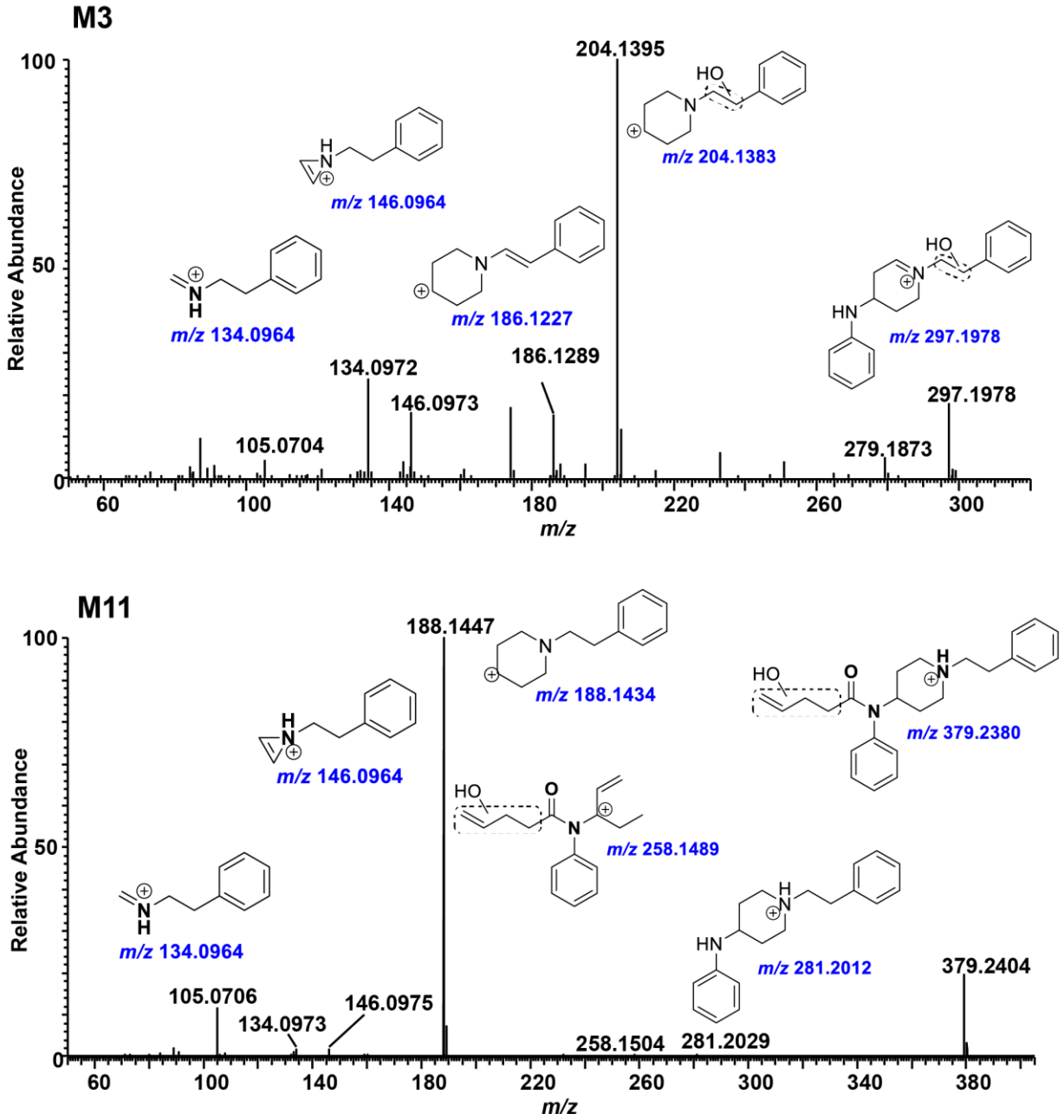

Figure 4. 14. Mass spectra of M3 and M11 (CE = 30 V).

Hydroxylation of M13 resulted in M11. The mass spectrum of M11 is shown in **Figure 4.14**. The product ions at *m/z* 188, 281, 146, 134, and 105, also observed for valerylfentanyl (**Figure 4.5**) were present for M11 indicating modification occurred on the amide group of valerylfentanyl.

However, the product ion at *m/z* 258—$C_{16}H_{20}NO_2^+$ indicated hydroxylation occurred on the amide group.

Analysis of the authentic sample by HRMS resulted in fentanyl and valerylfentanyl being detected. However, 4-ANPP (M6), β-hydroxyfentanyl, norfentanyl, morphine, and methamphetamine were detected using a triple quadrupole mass spectrometer operating in multiple reaction monitoring mode (MRM) mode. A compound sharing the same transitions—381.3→105 and 381.3→188.1, in a similar ratio as M7 and occurring at the same retention time was detected in the authentic sample (**Figure 4.15**). This was not detected via HRMS, possibly due to the lower sensitivity of the Orbitrap. The availability of reference standards would be vital in confirming this metabolite. Butyrfentanyl, structurally similar to valerylfentanyl was found to undergo extensive metabolism with the hydroxylated and carboxylated metabolites detected when a postmortem sample was analyzed, but the anticipated major metabolite—nor butyrfentanyl was only detected as a minor metabolite [235]. The authentic liver specimen analyzed in this study corresponded potentially to M7—the hydroxylated metabolite of valerylfentanyl, but the expected valeryl norfentanyl metabolite was not observed. However, further analysis of postmortem and antemortem specimen would be required to understand if there are differences in the detected metabolites of valerylfentanyl compared to our results.

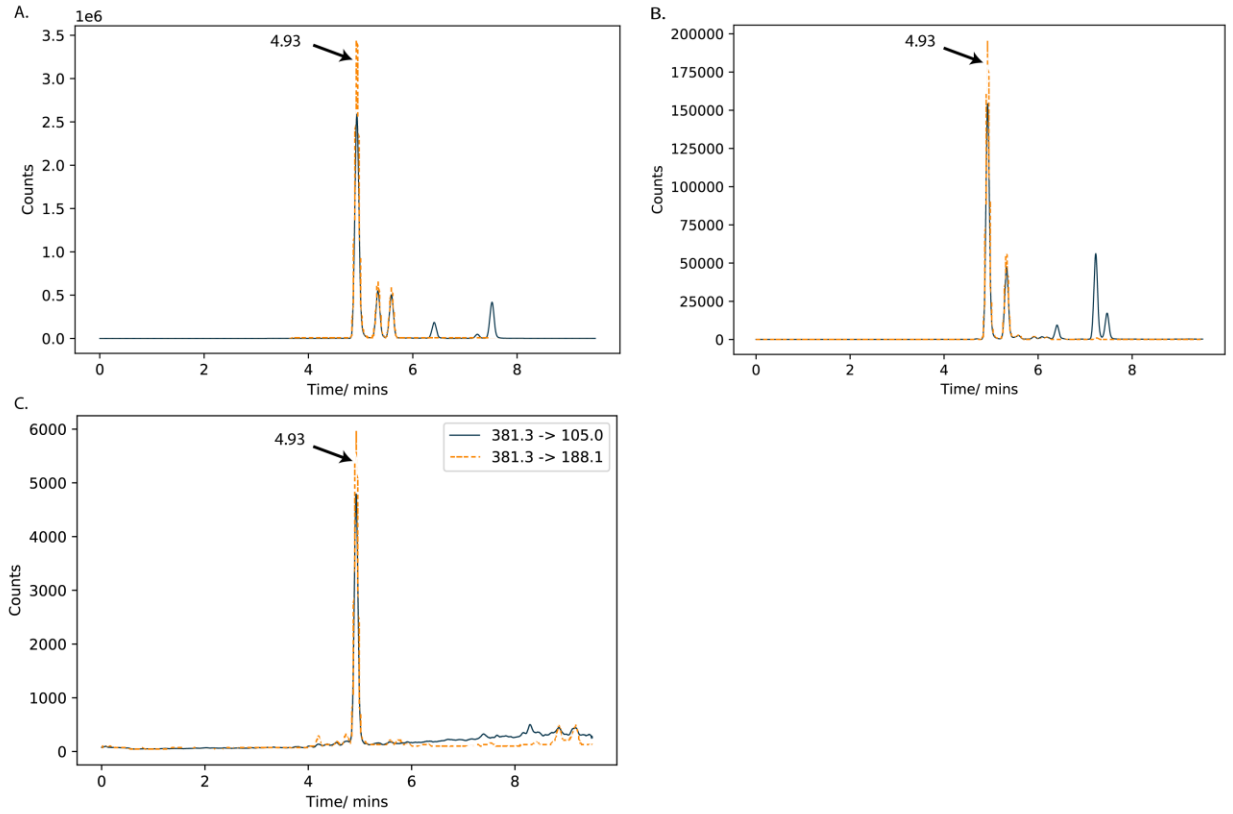

Figure 4. 15. Chromatograms showing the monitored transitions: 381.3 → 105.0 and 381.3 → 188.1 similar to M7 for (A)—Human liver microsome study, (B)—Zebrafish study, and (C)—Authentic liver sample. The retention times (4.93 min) are the same in each sample. A higher abundance is present in the microsome sample compared to the zebrafish and authentic sample.

Studies of other fentanyl analogues using *in vitro* methods such as HLM and hepatocytes have demonstrated *N*-dealkylation and hydroxylation as prevalent metabolic pathways [235, 236, 244]. Furthermore, fentanyl studies demonstrated that human liver derived CYP3A4 had a high contribution to *N*-dealkylation [53, 245]. Butyrfentanyl—which contains a butanoyl group compared to valerylfentanyl which contains a pentanoyl group, also demonstrated *N*-dealkylation as the major pathway with enzymatic contributions mainly from CYP3A4, and minor contributions from CYP1A2, 2C8 and 2C19 [235]. Although the extent of the human CYP enzymes responsible for the metabolism of valerylfentanyl have not been evaluated, it is possible the contributions are similar to butyrfentanyl. Kirla *et al.* reported zebrafish larvae metabolized butyrfentanyl similar to human but the metabolites were not fully described [193]. The authors also suggest CYP3A4 was responsible for butyrfentanyl metabolism in zebrafish. However, *cyp3a65* in zebrafish was

identified as the human CYP3A4 orthologue [47] and the role of both enzymes in valerylfentanyl or butyrfentanyl metabolism is yet to be evaluated for a comprehensive understanding of the metabolism differences between the two species.

4.4.0 Conclusion

As fentanyl analogues continue to emerge, elucidation of marker metabolites, and selection of an appropriate model that reflect human metabolism are critical. In this study we used a common *in vitro* model, human liver microsomes, and compared the major metabolites of valerylfentanyl to an *in vivo* zebrafish model. *N*-dealkylation, and hydroxylation observed with fentanyl analogues were the primary biotransformations. Although 19 metabolites were detected using the human liver microsome model, we propose the two major metabolites M10—valeryl norfentanyl and M7—hydroxy valerylfentanyl as marker metabolites for valerylfentanyl as they can be discriminated from other fentanyl analogs. The commercially available metabolite M19—valerylfentanyl carboxy metabolite, was detected as a minor metabolite only after analysis by tandem mass spectrometry. Whereas this metabolite provides evidence for the consumption of valerylfentanyl, its low presence makes it a poor marker metabolite. The major metabolites in the microsome model were highly corroborated by the zebrafish model, providing support for zebrafish as a model for metabolism of fentanyl related compounds.

General Conclusions

Measures to mitigate and understand the adverse effects of novel psychoactive substances and other common drugs of abuse to users, first responders, or forensic science personnel are constantly being studied. In the first phase of this project the detection of these substances was evaluated using a portable, rapid, non-destructive, safe technique commercially available. A novel approach which utilized both Raman and DART-MS was implemented for seized drug analysis. After demonstrating that portable Raman resulted in poor accuracy for mixtures, machine learning was implemented to classify compounds by drug name and drug class. In the second phase, a single zebrafish assay was developed to investigate the toxicity and metabolism of opioids, providing critical information for drug metabolite markers and a foundation to extend the toxic effects observed in zebrafish to the relationships in human. The findings in this dissertation demonstrate the need to improve the accuracy of rapid onsite techniques and greater understanding of the effects of NPS on human.

Portable Raman analysis is advantageous over many onsite drug testing strategies because of its ability to analyze unknown substances through certain packaging types, thereby reducing the risk of exposure, and can assist in decreasing drug backlogs. However, issues such as fluorescence, and analysis of multicomponent mixtures may affect the instrument's overall accuracy. The benefits of orthogonal methods as DART-MS to improve Raman results were demonstrated in chapter 1. Analysis of solid drug/diluent standards using a combination of the two techniques resulted in 96% drug accuracy, 100% diluent accuracy, and 96% two-part mixtures accuracy. Authentic case samples which contained multiple drugs were assessed using both methods. Diluents which contain poor sensitivity using DART-MS such as sugars were easier to detect using Raman. Drugs, which were typically present in lower concentrations were detected easier using DART-MS. The accuracy of the portable Raman was 44%, DART-MS—74%, and the combination of both techniques—83%. Future work can extend Raman and DART-MS analysis to other drugs of abuse and NPS. Moreover, evaluation of other techniques in detecting multicomponent mixtures such as SERS and the use of Raman instruments containing a 1064 nm laser to combat fluorescence can be studied in future work.

Analysis of in-house binary mixtures using the portable Raman instrument only, resulted in 30% correct identification for drugs, 89% for diluents, and 19% for both drugs and diluents. For this

reason, machine learning was implemented in chapter 2 as a method of improving the instrument's accuracy. Machine learning and deep learning methods have been increasingly utilized as classification methods in instances where the human judgment in detecting spectral differences may suffer. Out of the six machine and deep learning methods—kNN, NB, RF, SVM, NN, and CNN, higher accuracies were observed with CNN models—69% for drug, 95% for diluent, 64% for both drug and diluent classification compared to the portable Raman instrument's built-in algorithm—30% for drug, 89% for diluent, 19% for both drug and diluent classification. Although binary, ternary and quaternary mixtures were evaluated, future studies can include more complex mixtures. This work can also be extended to SERS which is advantageous over conventional Raman by having higher sensitivity to low drug concentrations in complex mixtures. Initial identification of unknown compounds can be challenging. Therefore, the substances evaluated in chapter 2 were not only classified by the drug name for pure substances, or drug mixtures, but also by compound class for pure substances and class mixtures for multiple component substances. When compounds in binary mixtures were classified by drug class (for example, fentanyl's drug class is opioid) using CNN models, the correct classification was 78%, 93% and 72% for drug class, diluent class, and both compound classes, respectively. The presumptive results can help drug analysts better understand the substance they have encountered and provide guidance for further investigations. Future work will include a graphical user interface to incorporate the algorithms developed in this study. Providing pre-trained models to users of the TaticID instrument will give them the capability to add compounds and re-train the model as their database increases. The algorithms presented in this work were multiclass which allows a spectrum prediction to belong to only one class. Even though probabilities can be used to report the top three hits for an unknown, it may result in lower accuracy for reporting all components in mixtures. Therefore, multilabel classification algorithms—which can result in a spectrum prediction to belong to multiple classes, can be explored to compare the accuracy when analyzing mixtures.

Chapters 3 and 4 investigates an *in vivo* model for opioid metabolism and toxicity. Zebrafish have emerged as whole organism model to study human disease and functions. Their genetic similarities to human and cost-effective approaches to maintain them increase their tendency as research animals over rodents in many labs. Although *in vitro* models such as human liver microsomes can provide pharmacologic data, they do not always reflect *in vivo* effects crucial for understanding human function. Fentanyl, one drug responsible for many drug overdose cases in the United States

of America was evaluated in chapter 3. A single assay was presented to evaluate fentanyl's toxicity and metabolism in zebrafish larvae (0 - 96 hpf). Major phenotypic effects included heart, yolk extension and spinal malformation in a dose dependent manner. These findings warrant further investigations into the mechanism of action, methods of reducing these effects or even reversing them. This can provide vital information to first responders and medical personnel when treating overdosed patients. Additionally, analysis of the zebrafish media detected fentanyl metabolites—4ANPP, norfentanyl, and β-hydroxyfentanyl, all of which have also been observed in human and microsomal studies.

After demonstrating zebrafish larvae were capable of metabolizing fentanyl, an uncharacterized fentanyl analogue—valerylfentanyl was evaluated using 30 dpf zebrafish in chapter 4. The zebrafish data was compared to human liver microsomes and analyzed using high resolution mass spectrometry. *N*-dealkylation, and hydroxylation were the primary biotransformations. Nineteen metabolites were detected using the human liver microsome model and many of these metabolites were observed in the zebrafish assay. The two major metabolites M10—valeryl norfentanyl and M7—hydroxy valeryl fentanyl were proposed as marker metabolites for valerylfentanyl. Future work will include evaluating the toxic effects of valerylfentanyl on zebrafish larvae and comparing the data to fentanyl. Furthermore, the toxicity of fentanyl metabolites such as 4ANPP, norfentanyl, β-hydroxyfentanyl, and metabolites of valerylfentanyl will be assessed. Extending the zebrafish assay to newer emerging synthetic opioids would also be crucial in providing support for this alternative model for human toxicity and metabolism.

This work has therefore demonstrated that reliance on similarity metrics built into portable Raman instruments do not always result in high accuracy when drug mixtures are analyzed, but the implementation of machine learning algorithms improve identification of multicomponent mixtures. More accurate preliminary drug screening techniques can help reduce backlogs in forensic chemistry laboratories because when field tests are performed, only suspected controlled substances would be sent for confirmation to the laboratory. The second major contribution of this work was the development of a single zebrafish model as an alternative to investigate drug toxicity and metabolism, laying the foundation for future mechanism of action studies that can be translated to human. The genetic similarities between zebrafish and humans, the observed phenotypic effects such as respiratory depression due to fentanyl overdose in both species, and

the detection of similar fentanyl metabolites in both species provide strong evidence for zebrafish as a toxicity and metabolism model. Extension of this work to novel drugs will alert users of a drug's potency and elucidate marker metabolites that can be incorporated in screening of human specimens at forensic toxicology laboratories.

References

1. Toole KE, Fu S, Shimmon RG, et al (2012) Color tests for the preliminary identification of methcathinone and analogues of methcathinone. Microgram J 9:27–32

2. Lieblein D, McMahon ME, Leary PE, et al (2018) A Comparison of Portable Infrared Spectrometers, Portable Raman Spectrometers, and Color-Based Field Tests for the On-Scene Analysis of Cocaine. Spectroscopy 33:20–28

3. Brown H, Oktem B, Windom A, et al (2016) Direct Analysis in Real Time (DART) and a portable mass spectrometer for rapid identification of common and designer drugs on-site. Forensic Chem 1:66–73. https://doi.org/10.1016/j.forc.2016.07.002

4. Wang J (2002) Portable electrochemical systems. TrAC Trends Anal Chem 21:226–232. https://doi.org/10.1016/S0165-9936(02)00402-8

5. de Araujo WR, Cardoso TMG, da Rocha RG, et al (2018) Portable analytical platforms for forensic chemistry: A review. Anal Chim Acta 1034:1–21. https://doi.org/10.1016/j.aca.2018.06.014

6. Das RS, Agrawal YK (2011) Raman spectroscopy: Recent advancements, techniques and applications. Vib Spectrosc 57:163–176. https://doi.org/10.1016/j.vibspec.2011.08.003

7. de Oliveira Penido CAF, Pacheco MTT, Lednev IK, Silveira L (2016) Raman spectroscopy in forensic analysis: identification of cocaine and other illegal drugs of abuse. J Raman Spectrosc 47:28–38. https://doi.org/10.1002/jrs.4864

8. Chan KLA (2019) An Introduction to Infra-red and R aman Spectroscopies for Pharmaceutical and Biomedical Studies. Biomol Bioanal Tech Theory, Methodol Appl 307–331

9. Zou P (2015) Choosing the most suitable laser wavelength for your Raman application. vol 1:1–6

10. SWGDRUG (2016) Scientific Working Group for the Analysis of Seized Drugs (SWGDRUG) recommendations. United States Department of Justice Drug Enforcement Administration …

11. Kudelski A (2008) Analytical applications of Raman spectroscopy. Talanta 76:1–8. https://doi.org/10.1016/j.talanta.2008.02.042

12. Harvey SD, Vucelick ME, Lee RN, Wright BW (2002) Blind field test evaluation of Raman spectroscopy as a forensic tool. Forensic Sci Int 125:12–21. https://doi.org/https://doi.org/10.1016/S0379-0738(01)00615-6

13. Hargreaves MD, Page K, Munshi T, et al (2008) Analysis of seized drugs using portable Raman spectroscopy in an airport environment—a proof of principle study. J Raman Spectrosc 39:873–880. https://doi.org/10.1002/jrs.1926

14. De Gelder J, Vandenabeele P, Govaert F, Moens L (2005) Forensic analysis of automotive paints by Raman spectroscopy. J Raman Spectrosc 36:1059–1067. https://doi.org/10.1002/jrs.1408

15. Hoehse M, Paul A, Gornushkin I, Panne U (2012) Multivariate classification of pigments and inks using combined Raman spectroscopy and LIBS. Anal Bioanal Chem 402:1443–1450. https://doi.org/10.1007/s00216-011-5287-6

16. Izake EL (2010) Forensic and homeland security applications of modern portable Raman spectroscopy. Forensic Sci Int 202:1–8. https://doi.org/10.1016/j.forsciint.2010.03.020

17. UNODC (2017) Guidelines on handheld raman field identification devices for seized material

18. Guirguis A (2017) Identification and Classification of New Psychoactive Substances Using Raman Spectroscopy and Chemometrics

19. Omar J, Slowikowski B, Guillou C, et al (2019) Identification of new psychoactive substances (NPS) by Raman spectroscopy. J Raman Spectrosc 50:41–51. https://doi.org/10.1002/jrs.5496

20. Weng S, Dong R, Zhu Z, et al (2018) Dynamic surface-enhanced Raman spectroscopy and Chemometric methods for fast detection and intelligent identification of methamphetamine and 3, 4-Methylenedioxy methamphetamine in human urine. Spectrochim Acta Part A Mol Biomol Spectrosc 189:1–7. https://doi.org/10.1016/j.saa.2017.08.004

21. O'Connell M-L, Ryder AG, Leger MN, Howley T (2010) Qualitative Analysis Using Raman Spectroscopy and Chemometrics: A Comprehensive Model System for Narcotics Analysis. Appl Spectrosc 64:1109–1121. https://doi.org/10.1366/000370210792973541

22. Streisinger G, Walker C, Dower N, et al (1981) Production of clones of homozygous diploid zebra fish (Brachydanio rerio). Nature 291:293–296. https://doi.org/10.1038/291293a0

23. Vargesson NA (2007) Zebrafish in Manual of Animal Technology

24. Delaney M, Follet C, Ryan N, et al (2002) Social Interaction and Distribution of Female Zebrafish (Danio rerio) in a Large Aquarium. Biol Bull 203:240–241. https://doi.org/10.2307/1543418

25. Spence R, Fatema MK, Reichard M, et al (2006) The distribution and habitat preferences of the zebrafish in Bangladesh. J Fish Biol 69:1435–1448. https://doi.org/10.1111/j.1095-8649.2006.01206.x

26. Moorman SJ (2001) Development of Sensory Systems in Zebrafish (Donio rerio) . ILAR J 42:292–298. https://doi.org/10.1093/ilar.42.4.292

27. Spence R, Gerlach G, Lawrence C, Smith C (2008) The behaviour and ecology of the zebrafish, Danio rerio. Biol Rev 83:13–34. https://doi.org/10.1111/j.1469-185X.2007.00030.x

28. Ruhl N, McRobert SP, Currie WJS (2009) Shoaling preferences and the effects of sex ratio on spawning and aggression in small laboratory populations of zebrafish (Danio rerio). Lab Anim (NY) 38:264–269

29. Matthews M, Trevarrow B, Matthews J (2002) A virtual tour of the guide for zebrafish users. Resource 31:34–40

30. Fleming A (2007) Zebrafish as an alternative model organism for disease modelling and drug discovery: implications for the 3Rs. NC3Rs 10:1–7

31. Kamel M, Ninov N (2017) Catching new targets in metabolic disease with a zebrafish. Curr Opin Pharmacol 37:41–50

32. Kirla KT, Groh KJ, Poetzsch M, et al (2018) Importance of Toxicokinetics to Assess the Utility of Zebrafish Larvae as Model for Psychoactive Drug Screening Using Meta-Chlorophenylpiperazine (mCPP) as Example. Front Pharmacol 9:414. https://doi.org/10.3389/fphar.2018.00414

33. OECD (2013) Test No. 236: Fish Embryo Acute Toxicity (FET) Test. OECD

34. Zoupa M, Machera K (2017) Zebrafish as an Alternative Vertebrate Model for Investigating Developmental Toxicity-The Triadimefon Example. Int J Mol Sci 18:817. https://doi.org/10.3390/ijms18040817

35. Cornet C, Calzolari S, Miñana-Prieto R, et al (2017) ZeGlobalTox: An Innovative Approach to Address Organ Drug Toxicity Using Zebrafish. Int J Mol Sci 18:. https://doi.org/10.3390/ijms18040864

36. Gonzalez-Nunez V, Rodríguez RE (2009) The zebrafish: a model to study the endogenous mechanisms of pain. ILAR J 50:373–386

37. Santoro MM (2014) Zebrafish as a model to explore cell metabolism. Trends Endocrinol Metab 25:546–554. https://doi.org/10.1016/j.tem.2014.06.003

38. Howe K, Clark MD, Torroja CF, et al (2013) The zebrafish reference genome sequence and its relationship to the human genome. Nature 496:498–503. https://doi.org/10.1038/nature12111

39. Jones HS, Trollope HT, Hutchinson TH, et al (2012) Metabolism of ibuprofen in zebrafish larvae. Xenobiotica 42:1069–1075. https://doi.org/10.3109/00498254.2012.684410

40. Chng HT, Ho HK, Yap CW, et al (2012) An Investigation of the Bioactivation Potential and Metabolism Profile of Zebrafish versus Human. J Biomol Screen 17:974–986. https://doi.org/10.1177/1087057112447305

41. Richter LHJ, Herrmann J, Andreas A, et al (2019) Tools for studying the metabolism of new psychoactive substances for toxicological screening purposes – A comparative study using pooled human liver S9, HepaRG cells, and zebrafish larvae. Toxicol Lett 305:73–80. https://doi.org/10.1016/j.toxlet.2019.01.010

42. Xu D, Zhang W, Li J, et al (2019) Analysis of AMB-FUBINACA Biotransformation Pathways in Human Liver Microsome and Zebrafish Systems by Liquid Chromatography-High Resolution Mass Spectrometry. Front Chem 7:240. https://doi.org/10.3389/fchem.2019.00240

43. Matos RR, Martucci MEP, de Anselmo CS, et al (2020) Pharmacokinetic study of xylazine in a zebrafish water tank, a human-like surrogate, by liquid chromatography Q-Orbitrap mass spectrometry. Forensic Toxicol 38:108–121. https://doi.org/10.1007/s11419-019-00493-y

44. Kimmel CB, Ballard WW, Kimmel SR, et al (1995) Stages of embryonic development of the zebrafish. Dev Dyn 203:253–310. https://doi.org/10.1002/aja.1002030302

45. Field HA, Ober EA, Roeser T, Stainier DYR (2003) Formation of the digestive system in zebrafish. I. liver morphogenesis. Dev Biol 253:279–290. https://doi.org/10.1016/S0012-1606(02)00017-9

46. Saad M, Cavanaugh K, Verbueken E, et al (2016) Xenobiotic metabolism in the zebrafish: a review of the spatiotemporal distribution, modulation and activity of Cytochrome P450 families 1 to 3. J Toxicol Sci 41:1–11. https://doi.org/10.2131/jts.41.1

47. Verbueken E, Alsop D, Saad M, et al (2017) In vitro biotransformation of two human CYP3A probe substrates and their inhibition during early zebrafish development. Int J Mol Sci 18:217. https://doi.org/10.3390/ijms18010217

48. Parliament E, Council E (2010) DIRECTIVE 2010/63/EU on the protection of animals used for scientific purposes. EU Off J L276:

49. Santoriello C, Zon LI (2012) Hooked! Modeling human disease in zebrafish. J Clin Invest 122:2337–2343. https://doi.org/10.1172/JCI60434

50. de Souza Anselmo C, Sardela VF, Matias BF, et al (2017) Is zebrafish (Danio rerio) a tool for human-like metabolism study? Drug Test Anal 9:1685–1694. https://doi.org/10.1002/dta.2318

51. Green CJ, Charlton CA, Wang L-M, et al (2017) The isolation of primary hepatocytes from human tissue: optimising the use of small non-encapsulated liver resection surplus.

Cell Tissue Bank 18:597–604. https://doi.org/10.1007/s10561-017-9641-6

52. Li AP (2005) Preclinical in vitro screening assays for drug-like properties. Drug Discov today Technol 2:179–185

53. Feierman DE, Lasker JM (1996) Metabolism of fentanyl, a synthetic opioid analgesic, by human liver microsomes. Role of CYP3A4. Drug Metab Dispos 24:932–9

54. Asha S, Vidyavathi M (2010) Role of Human Liver Microsomes in In Vitro Metabolism of Drugs—A Review. Appl Biochem Biotechnol 160:1699–1722. https://doi.org/10.1007/s12010-009-8689-6

55. Ton E, Stevens C, Moorman P, et al (2021) Thirteen cases of valeryl fentanyl in Michigan: a call for expanding opioid testing. Am J Forensic Med Pathol 42:367–372

56. Walsh E, Forni A, Pardi J, Cooper G (2021) Acute Intoxications Involving Valerylfentanyl Identified at the New York City Office of Chief Medical Examiner. J Anal Toxicol

57. U.S. Drug Enforcement Administration Diversion Control Division (2019) National Forensic Laboratory Information System:NFLIS-Drug 2019 Annual Report

58. Philp M, Fu S (2018) A review of chemical ‘spot’ tests: A presumptive illicit drug identification technique. Drug Test Anal 10:95–108. https://doi.org/10.1002/dta.2300

59. Ali EMA, Edwards HGM (2014) Screening of textiles for contraband drugs using portable Raman spectroscopy and chemometrics. J Raman Spectrosc 45:253–258. https://doi.org/10.1002/jrs.4444

60. Brewster VL, Edwards HGM, Hargreaves MD, Munshi T (2009) Identification of the date-rape drug GHB and its precursor GBL by Raman spectroscopy. Drug Test Anal 1:25–31. https://doi.org/10.1002/dta.11

61. Burnett AD, Edwards HGM, Hargreaves MD, et al (2011) A forensic case study: the detection of contraband drugs in carrier solutions by Raman spectroscopy. Drug Test Anal 3:539–543. https://doi.org/10.1002/dta.169

62. Hakonen A, Wu K, Stenbæk Schmidt M, et al (2018) Detecting forensic substances using

commercially available SERS substrates and handheld Raman spectrometers. Talanta 189:649–652. https://doi.org/10.1016/j.talanta.2018.07.009

63. Dégardin K, Guillemain A, Roggo Y (2017) Comprehensive Study of a Handheld Raman Spectrometer for the Analysis of Counterfeits of Solid-Dosage Form Medicines. J Spectrosc 2017:1–13. https://doi.org/10.1155/2017/3154035

64. Sisco E, Verkouteren J, Staymates J, Lawrence J (2017) Rapid detection of fentanyl, fentanyl analogues, and opioids for on-site or laboratory based drug seizure screening using thermal desorption DART-MS and ion mobility spectrometry. Forensic Chem 4:108–115. https://doi.org/10.1016/j.forc.2017.04.001

65. Sisco E, Forbes TP, Staymates ME, Gillen G (2016) Rapid analysis of trace drugs and metabolites using a thermal desorption DART-MS configuration. Anal Methods 8:6494–6499. https://doi.org/10.1039/C6AY01851C

66. Lesiak AD, Shepard JR (2014) Recent advances in forensic drug analysis by DART-MS. Bioanalysis 6:819–842. https://doi.org/10.4155/bio.14.31

67. Sisco E, Robinson EL, Burns A, Mead R (2019) What's in the bag? Analysis of exterior drug packaging by TD-DART-MS to predict the contents. Forensic Sci Int 304:109939. https://doi.org/10.1016/j.forsciint.2019.109939

68. Grange AH, Sovocool GW (2011) Detection of illicit drugs on surfaces using direct analysis in real time (DART) time-of-flight mass spectrometry. Rapid Commun Mass Spectrom 25:1271–1281. https://doi.org/10.1002/rcm.5009

69. Sisco E, Forbes TP (2021) Forensic applications of DART-MS: A review of recent literature. Forensic Chem 22:100294. https://doi.org/10.1016/j.forc.2020.100294

70. Steiner RR, Larson RL (2009) Validation of the Direct Analysis in Real Time Source for Use in Forensic Drug Screening. J Forensic Sci 54:617–622. https://doi.org/https://doi.org/10.1111/j.1556-4029.2009.01006.x

71. ASTM International (2014) E1683-02 Standard Practice for Testing the Performance of Scanning Raman Spectrometers

72. ASTM International (2014) E1840- 96 Standard Guide for Raman Shift Standards for Spectrometer Calibration

73. Fiorentin TR, Krotulski AJ, Martin DM, et al (2019) Detection of Cutting Agents in Drug-Positive Seized Exhibits within the United States. J Forensic Sci 64:888–896. https://doi.org/10.1111/1556-4029.13968

74. Administration DE (2018) National drug threat assessment (2018). US Departament of Justice

75. Administration DE (2019) National Drug Threat Assessment 2019

76. Drug Enforcement Administration D.O.J (2018) 2016 Heroin Domestic Monitor Program

77. Miserez B, Ayrton O, Ramsey J (2014) Analysis of purity and cutting agents in street mephedrone samples from South Wales. Forensic Toxicol 32:305–310. https://doi.org/10.1007/s11419-014-0232-y

78. Guirguis A, Corkery JM, Stair JL, et al (2017) Intended and unintended use of cathinone mixtures. Hum Psychopharmacol Clin Exp 32:e2598. https://doi.org/10.1002/hup.2598

79. Lian R, Wu Z, Lv X, et al (2017) Rapid screening of abused drugs by direct analysis in real time (DART) coupled to time-of-flight mass spectrometry (TOF-MS) combined with ion mobility spectrometry (IMS). Forensic Sci Int 279:268–280. https://doi.org/10.1016/j.forsciint.2017.07.010

80. Gwak S, Almirall JR (2015) Rapid screening of 35 new psychoactive substances by ion mobility spectrometry (IMS) and direct analysis in real time (DART) coupled to quadrupole time-of-flight mass spectrometry (QTOF-MS). https://doi.org/10.1002/dta.1783

81. Park J-K, Park A, Yang SK, et al (2017) Raman spectrum identification based on the correlation score using the weighted segmental hit quality index. Analyst 142:380–388. https://doi.org/10.1039/C6AN02315K

82. Gryniewicz-Ruzicka CM, Rodriguez JD, Arzhantsev S, et al (2012) Libraries, classifiers, and quantifiers: A comparison of chemometric methods for the analysis of Raman spectra

of contaminated pharmaceutical materials. J Pharm Biomed Anal 61:191–198. https://doi.org/10.1016/j.jpba.2011.12.002

83. Rodriguez JD, Westenberger BJ, Buhse LF, Kauffman JF (2011) Standardization of Raman spectra for transfer of spectral libraries across different instruments. Analyst 136:4232. https://doi.org/10.1039/c1an15636e

84. Kudlacek O, Hofmaier T, Luf A, et al (2017) Cocaine adulteration. J Chem Neuroanat 83–84:75–81. https://doi.org/10.1016/j.jchemneu.2017.06.001

85. Broséus J, Gentile N, Bonadio Pont F, et al (2015) Qualitative, quantitative and temporal study of cutting agents for cocaine and heroin over 9 years. Forensic Sci Int 257:307–313. https://doi.org/10.1016/j.forsciint.2015.09.014

86. Schneider S, Meys F (2011) Analysis of illicit cocaine and heroin samples seized in Luxembourg from 2005–2010. Forensic Sci Int 212:242–246. https://doi.org/10.1016/j.forsciint.2011.06.027

87. European Monitoring Centre for Drugs and Drug Addiction (2020) European Drug Report: Trends and Developments

88. System NFLI (2021) NFLIS-Drug 2020 Midyear Report

89. Penido CAFO, Pacheco MTT, Zângaro RA, Silveira L (2015) Identification of Different Forms of Cocaine and Substances Used in Adulteration Using Near-infrared Raman Spectroscopy and Infrared Absorption Spectroscopy. J Forensic Sci 60:171–178. https://doi.org/10.1111/1556-4029.12666

90. Haddad A, Green O, Lombardi JR (2019) Detection of fentanyl in binary mixtures with cocaine by use of surface-enhanced Raman spectroscopy. Spectrosc Lett 52:462–472. https://doi.org/10.1080/00387010.2019.1671871

91. Green TC, Park JN, Gilbert M, et al (2020) An assessment of the limits of detection, sensitivity and specificity of three devices for public health-based drug checking of fentanyl in street-acquired samples. Int J Drug Policy 77:102661. https://doi.org/10.1016/j.drugpo.2020.102661

92. Forensic Technology Center of Excellence (2018) Landscape Study of Field Portable Devices for Presumptive Drug Testing

93. Spicher C, Yeatman T, Alford I, Waugh L (2016) The Evaluation of Portable Handheld Raman Systems for the Presumptive Identification of Narcotics: Thermo Scientific TruNarc® and Chemring Detection Systems PGR-1064®. Marshall Univ

94. Roberts ES, Boudreau BA, Brown DW, et al (2016) Analysis of carbohydrates in Fusarium verticillioides using size-exclusion HPLC – DRI and direct analysis in real time ionization – time-of-flight – mass spectrometry (DART-MS). Anal Methods 8:673–681. https://doi.org/10.1039/C5AY01666E

95. Bourgeois J-P, Vorlet O (2018) Low-cost Portable Raman Instrument, a Tool toward Counterfeit Medication Identification. Chimia (Aarau) 72:905. https://doi.org/10.2533/chimia.2018.905

96. Vandenabeele P, Edwards HGM, Jehlička J (2014) The role of mobile instrumentation in novel applications of Raman spectroscopy: archaeometry, geosciences, and forensics. Chem Soc Rev 43:2628–2649. https://doi.org/10.1039/C3CS60263J

97. Fedick PW, Pu F, Morato NM, Cooks RG (2020) Identification and Confirmation of Fentanyls on Paper using Portable Surface Enhanced Raman Spectroscopy and Paper Spray Ionization Mass Spectrometry. J Am Soc Mass Spectrom 31:735–741. https://doi.org/10.1021/jasms.0c00004

98. Salles MO, Meloni GN, de Araujo WR, Paixão TRLC (2014) Explosive colorimetric discrimination using a smartphone, paper device and chemometrical approach. Anal Methods 6:2047–2052. https://doi.org/10.1039/C3AY41727A

99. Martinez AW, Phillips ST, Butte MJ, Whitesides GM (2007) Patterned Paper as a Platform for Inexpensive, Low-Volume, Portable Bioassays. Angew Chemie Int Ed 46:1318–1320. https://doi.org/10.1002/anie.200603817

100. Domingos E, de Carvalho TC, Pereira I, et al (2017) Paper spray ionization mass spectrometry applied to forensic chemistry – drugs of abuse, inks and questioned documents. Anal Methods 9:4400–4409. https://doi.org/10.1039/C7AY01091E

101. O'Leary AE, Oberacher H, Hall SE, Mulligan CC (2015) Combining a portable, tandem mass spectrometer with automated library searching – an important step towards streamlined, on-site identification of forensic evidence. Anal Methods 7:3331–3339. https://doi.org/10.1039/C4AY02778G

102. O'Leary AE, Hall SE, Vircks KE, Mulligan CC (2015) Monitoring the clandestine synthesis of methamphetamine in real-time with ambient sampling, portable mass spectrometry. Anal Methods 7:7156–7163. https://doi.org/10.1039/C5AY00511F

103. Ali EMA, Edwards HGM (2017) The detection of flunitrazepam in beverages using portable Raman spectroscopy. Drug Test Anal 9:256–259. https://doi.org/10.1002/dta.1969

104. Tsujikawa K, Yamamuro T, Kuwayama K, et al (2014) Application of a portable near infrared spectrometer for presumptive identification of psychoactive drugs. Forensic Sci Int 242:162–171. https://doi.org/10.1016/j.forsciint.2014.05.020

105. Kammrath BW, Leary PE, Reffner JA (2021) Forensic Applications of Portable Spectrometers. In: Portable Spectroscopy and Spectrometry. Wiley, pp 125–147

106. Pleus S, Schauer S, Jendrike N, et al (2021) Proof of Concept for a New Raman-Based Prototype for Noninvasive Glucose Monitoring. J Diabetes Sci Technol 15:11–18. https://doi.org/10.1177/1932296820947112

107. Pandey R, Paidi SK, Valdez TA, et al (2017) Noninvasive Monitoring of Blood Glucose with Raman Spectroscopy. Acc Chem Res 50:264–272. https://doi.org/10.1021/acs.accounts.6b00472

108. Zavaleta C, de la Zerda A, Liu Z, et al (2008) Noninvasive Raman Spectroscopy in Living Mice for Evaluation of Tumor Targeting with Carbon Nanotubes. Nano Lett 8:2800–2805. https://doi.org/10.1021/nl801362a

109. Cletus B, Olds W, Izake EL, et al (2012) Combined time- and space-resolved Raman spectrometer for the non-invasive depth profiling of chemical hazards. Anal Bioanal Chem 403:255–263. https://doi.org/10.1007/s00216-012-5792-2

110. Agilent Technologies Agilent Resolve Raman.

https://www.agilent.com/cs/library/brochures/5991-8867EN_Resolve_brochure_CPOD-web.pdf

111. Ellis DI, Eccles R, Xu Y, et al (2017) Through-container, extremely low concentration detection of multiple chemical markers of counterfeit alcohol using a handheld SORS device. Sci Rep 7:12082. https://doi.org/10.1038/s41598-017-12263-0

112. Jehlička J, Vítek P, Edwards HGM, et al (2009) Application of portable Raman instruments for fast and non-destructive detection of minerals on outcrops. Spectrochim Acta Part A Mol Biomol Spectrosc 73:410–419. https://doi.org/10.1016/j.saa.2008.09.004

113. Jehlička J, Edwards HGM, Culka A (2010) Using portable Raman spectrometers for the identification of organic compounds at low temperatures and high altitudes: exobiological applications. Philos Trans R Soc A Math Phys Eng Sci 368:3109–3125. https://doi.org/10.1098/rsta.2010.0075

114. Hargreaves MD, Macleod NA, Brewster VL, et al (2009) Application of portable Raman spectroscopy and benchtop spatially offset Raman spectroscopy to interrogate concealed biomaterials. J Raman Spectrosc 40:1875–1880. https://doi.org/10.1002/jrs.2335

115. Beganović A, Hawthorne L, Bach K, Huck C (2019) Critical Review on the Utilization of Handheld and Portable Raman Spectrometry in Meat Science. Foods 8:49. https://doi.org/10.3390/foods8020049

116. Yildiz Tiryaki G, Ayvaz H (2017) Quantification of soybean oil adulteration in extra virgin olive oil using portable raman spectroscopy. J Food Meas Charact 11:523–529. https://doi.org/10.1007/s11694-016-9419-8

117. Guzmán E, Baeten V, Pierna JAF, García-Mesa JA (2012) A portable Raman sensor for the rapid discrimination of olives according to fruit quality. Talanta 93:94–98. https://doi.org/10.1016/j.talanta.2012.01.053

118. Nieuwoudt MK, Holroyd SE, McGoverin CM, et al (2016) Rapid, sensitive, and reproducible screening of liquid milk for adulterants using a portable Raman spectrometer and a simple, optimized sample well. J Dairy Sci 99:7821–7831. https://doi.org/10.3168/jds.2016-11100

119. Tondepu C, Toth R, Navin C V, et al (2017) Screening of unapproved drugs using portable Raman spectroscopy. Anal Chim Acta 973:75–81. https://doi.org/10.1016/j.aca.2017.04.016

120. Lu F, Weng X, Chai Y, et al (2013) A novel identification system for counterfeit drugs based on portable Raman spectroscopy. Chemom Intell Lab Syst 127:63–69. https://doi.org/10.1016/j.chemolab.2013.06.001

121. Keller MD, Vargis E, Mahadevan-Jansen A, et al (2011) Development of a spatially offset Raman spectroscopy probe for breast tumor surgical margin evaluation. J Biomed Opt 16:1–9. https://doi.org/10.1117/1.3600708

122. Bratchenko IA, Bratchenko LA, Moryatov AA, et al (2021) In vivo diagnosis of skin cancer with a portable Raman spectroscopic device. Exp Dermatol 30:652–663. https://doi.org/10.1111/exd.14301

123. Cui S, Zhang S, Yue S (2018) Raman Spectroscopy and Imaging for Cancer Diagnosis. J Healthc Eng 2018:8619342. https://doi.org/10.1155/2018/8619342

124. Bakeev KA, Chimenti R V (2013) Pros and cons of using correlation versus multivariate algorithms for material identification via handheld spectroscopy. Eur Pharm Rev 1:

125. Samuel AZ, Mukojima R, Horii S, et al (2021) On Selecting a Suitable Spectral Matching Method for Automated Analytical Applications of Raman Spectroscopy. ACS Omega 6:2060–2065. https://doi.org/10.1021/acsomega.0c05041

126. Weng S, Yuan H, Zhang X, et al (2020) Deep learning networks for the recognition and quantitation of surface-enhanced Raman spectroscopy. Analyst 145:4827–4835. https://doi.org/10.1039/D0AN00492H

127. Fan X, Ming W, Zeng H, et al (2019) Deep learning-based component identification for the Raman spectra of mixtures. Analyst 144:1789–1798. https://doi.org/10.1039/C8AN02212G

128. Acquarelli J, van Laarhoven T, Gerretzen J, et al (2017) Convolutional neural networks for vibrational spectroscopic data analysis. Anal Chim Acta 954:22–31. https://doi.org/https://doi.org/10.1016/j.aca.2016.12.010

129. Been F, Roggo Y, Degardin K, et al (2011) Profiling of counterfeit medicines by vibrational spectroscopy. Forensic Sci Int 211:83–100. https://doi.org/10.1016/j.forsciint.2011.04.023

130. Noonan KY, Tonge LA, Fenton OS, et al (2009) Rapid Classification of Simulated Street Drug Mixtures Using Raman Spectroscopy and Principal Component Analysis. Appl Spectrosc 63:742–747. https://doi.org/10.1366/000370209788701008

131. Srivastava HK, Wolfgang S, Rodriguez JD (2016) Expanding the analytical toolbox for identity testing of pharmaceutical ingredients: Spectroscopic screening of dextrose using portable Raman and near infrared spectrometers. Anal Chim Acta 914:91–99. https://doi.org/10.1016/j.aca.2016.01.061

132. Zhang Z (2016) Introduction to machine learning: k-nearest neighbors. Ann Transl Med 4:218–218. https://doi.org/10.21037/atm.2016.03.37

133. Ben-Hur A, Weston J (2010) A User's Guide to Support Vector Machines. In: Data mining techniques for the life sciences. Springer, pp 223–239

134. O'Connell M-L, Howley T, Ryder AG, et al (2005) Classification of a target analyte in solid mixtures using principal component analysis, support vector machines, and Raman spectroscopy. In: Byrne HJ, Lewis E, MacCraith BD, et al (eds) Proc.SPIE. p 340

135. Zhang X-F, Zou M-Q, Qi X-H, et al (2011) Quantitative detection of adulterated olive oil by Raman spectroscopy and chemometrics. J Raman Spectrosc 42:1784–1788. https://doi.org/10.1002/jrs.2933

136. Dong J, Hong M, Xu Y, Zheng X (2019) A practical convolutional neural network model for discriminating Raman spectra of human and animal blood. J Chemom 33:1–12. https://doi.org/10.1002/cem.3184

137. Langley P, Iba W, Thompson K (1992) An analysis of Bayesian classifiers. In: Aaai. Citeseer, pp 223–228

138. Cutler A, Cutler DR, Stevens JR (2012) Random Forests. In: Zhang C, Ma Y (eds) Ensemble Machine Learning. Springer US, Boston, MA, pp 157–175

139. Li M, Xu Y, Men J, et al (2021) Hybrid variable selection strategy coupled with random forest (RF) for quantitative analysis of methanol in methanol-gasoline via Raman spectroscopy. Spectrochim Acta Part A Mol Biomol Spectrosc 251:119430. https://doi.org/10.1016/j.saa.2021.119430

140. Breiman L (2001) Random forests. Mach Learn 45:5–32

141. Abraham A (2005) Artificial neural networks. Handb Meas Syst Des

142. Gogul I, Kumar VS (2017) Flower species recognition system using convolution neural networks and transfer learning. In: 2017 Fourth International Conference on Signal Processing, Communication and Networking (ICSCN). IEEE, pp 1–6

143. Chandler LL, Huang B, Mu T (2019) A smart handheld Raman spectrometer with cloud and AI deep learning algorithm for mixture analysis. In: Crocombe RA, Profeta LT, Azad AK (eds) Next-Generation Spectroscopic Technologies XII. SPIE, p 7

144. Reisner LA, Cao A, Pandya AK (2011) An integrated software system for processing, analyzing, and classifying Raman spectra. Chemom Intell Lab Syst 105:83–90. https://doi.org/10.1016/j.chemolab.2010.09.011

145. Mozaffari MH, Tay L-L (2020) Anomaly detection using 1D convolutional neural networks for surface enhanced raman scattering. In: SPIE Future Sensing Technologies. International Society for Optics and Photonics, p 115250S

146. Mozaffari MH, Tay L-L (2021) Raman spectral analysis of mixtures with one-dimensional convolutional neural network. arXiv Prepr arXiv210605316

147. Mazurek S, Szostak R (2009) Quantification of atorvastatin calcium in tablets by FT-Raman spectroscopy. J Pharm Biomed Anal 49:168–172. https://doi.org/10.1016/j.jpba.2008.10.015

148. Fu X, Zhong L, Cao Y, et al (2021) Quantitative analysis of excipient dominated drug formulations by Raman spectroscopy combined with deep learning. Anal Methods 13:64–68. https://doi.org/10.1039/D0AY01874K

149. Karunathilaka SR, Yakes BJ, He K, et al (2018) First use of handheld Raman

spectroscopic devices and on-board chemometric analysis for the detection of milk powder adulteration. Food Control 92:137–146. https://doi.org/10.1016/j.foodcont.2018.04.046

150. Cooman T, Ott CE, Dalzell KA, et al (2021) Screening of seized drugs utilizing portable Raman spectroscopy and direct analysis in real time-mass spectrometry (DART-MS). Forensic Chem 25:100352. https://doi.org/10.1016/j.forc.2021.100352

151. Virtanen P, Gommers R, Oliphant TE, et al (2020) SciPy 1.0: fundamental algorithms for scientific computing in Python. Nat Methods 17:261–272

152. Bjerrum EJ, Glahder M, Skov T (2017) Data augmentation of spectral data for convolutional neural network (CNN) based deep chemometrics. arXiv Prepr arXiv171001927

153. Wahl J, Sjödahl M, Ramser K (2020) Single-Step Preprocessing of Raman Spectra Using Convolutional Neural Networks. Appl Spectrosc 74:427–438. https://doi.org/10.1177/0003702819888949

154. Pedregosa, F., Varoquaux, G., Gramfort, A., Michel, V., Thirion, B., Grisel, O., Blondel, M., Prettenhofer, P., Weiss, R., Dubourg, V., Vanderplas, J., Passos, A., Cournapeau, D., Brucher, M., Perrot, M., Duchesnay E (2011) Scikit-learn: Machine Learning in Python. J Mach Learn Res 12:2825–2830

155. Abadi M, Barham P, Chen J, et al (2016) Tensorflow: A system for large-scale machine learning. In: 12th {USENIX} symposium on operating systems design and implementation ({OSDI} 16). pp 265–283

156. Srivastava N, Hinton G, Krizhevsky A, et al (2014) Dropout: a simple way to prevent neural networks from overfitting. J Mach Learn Res 15:1929–1958

157. Mansouri MA, Sacré P-Y, Coïc L, et al (2020) Quantitation of active pharmaceutical ingredient through the packaging using Raman handheld spectrophotometers: A comparison study. Talanta 207:120306. https://doi.org/10.1016/j.talanta.2019.120306

158. Coic L, Sacré P-Y, Dispas A, et al (2020) Evaluation of the analytical performances of two Raman handheld spectrophotometers for pharmaceutical solid dosage form

quantitation. Talanta 214:120888. https://doi.org/10.1016/j.talanta.2020.120888

159. Haddad A, Comanescu MA, Green O, et al (2018) Detection and Quantitation of Trace Fentanyl in Heroin by Surface-Enhanced Raman Spectroscopy. Anal Chem 90:12678–12685. https://doi.org/10.1021/acs.analchem.8b02909

160. Leonard J, Haddad A, Green O, et al (2017) SERS, Raman, and DFT analyses of fentanyl and carfentanil: Toward detection of trace samples. J Raman Spectrosc 48:1323–1329. https://doi.org/10.1002/jrs.5220

161. Drug EA (2018) Schedules of Controlled Substances: Temporary Placement of Fentanyl-Related Substances in Schedule I. Temporary amendment; temporary scheduling order. Fed Regist 83:5188

162. McGrath P, Li C-Q (2008) Zebrafish: a predictive model for assessing drug-induced toxicity. Drug Discov Today 13:394–401. https://doi.org/10.1016/j.drudis.2008.03.002

163. Prado E, Matos RR, de Lima Gomes GM, et al (2021) Metabolism of synthetic cathinones through the zebrafish water tank model: a promising tool for forensic toxicology laboratories. Forensic Toxicol 39:73–88. https://doi.org/10.1007/s11419-020-00543-w

164. Sardela VF, Sardela PDO, Lisboa RR, et al (2020) Comprehensive Zebrafish Water Tank Experiment for Metabolic Studies of Testolactone. Zebrafish 17:104–111. https://doi.org/10.1089/zeb.2019.1791

165. Gamse JT, Gorelick DA (2016) Mixtures, Metabolites, and Mechanisms: Understanding Toxicology Using Zebrafish. Zebrafish 13:377–378. https://doi.org/10.1089/zeb.2016.1370

166. Bao W, Volgin AD, Alpyshov ET, et al (2019) Opioid Neurobiology, Neurogenetics and Neuropharmacology in Zebrafish. Neuroscience 404:218–232. https://doi.org/10.1016/j.neuroscience.2019.01.045

167. Lopez-Luna J, Al-Jubouri Q, Al-Nuaimy W, Sneddon LU (2017) Reduction in activity by noxious chemical stimulation is ameliorated by immersion in analgesic drugs in zebrafish. J Exp Biol 220:1451 LP – 1458. https://doi.org/10.1242/jeb.146969

168. Curtright A, Rosser M, Goh S, et al (2015) Modeling nociception in zebrafish: a way forward for unbiased analgesic discovery. PLoS One 10:e0116766

169. Zhuo H, Jin H, Peng H, Huang H (2016) Distribution, pharmacokinetics and primary metabolism model of tramadol in zebrafish. Mol Med Rep 14:5644–5652. https://doi.org/10.3892/mmr.2016.5956

170. NIDA (2019) Fentanyl DrugFacts. https://www.drugabuse.gov/publications/drugfacts/fentanyl

171. Somerville NJ, O'Donnell J, Gladden RM, et al (2017) Characteristics of Fentanyl Overdose - Massachusetts, 2014-2016. MMWR Morb Mortal Wkly Rep 66:382–386. https://doi.org/10.15585/mmwr.mm6614a2

172. Zaig S, Scarpellini C, Montandon G (2020) Respiratory depression and analgesia by opioid drugs in freely-behaving larval zebrafish. bioRxiv 2020.09.30.320267. https://doi.org/10.1101/2020.09.30.320267

173. He J-H, Guo S-Y, Zhu F, et al (2013) A zebrafish phenotypic assay for assessing drug-induced hepatotoxicity. J Pharmacol Toxicol Methods 67:25–32. https://doi.org/10.1016/j.vascn.2012.10.003

174. Sanchez-Simon FM, Arenzana FJ, Rodriguez RE (2010) In vivo effects of morphine on neuronal fate and opioid receptor expression in zebrafish embryos. Eur J Neurosci 32:550–559. https://doi.org/10.1111/j.1460-9568.2010.07317.x

175. Gampfer TM, Wagmann L, Park YM, et al (2020) Toxicokinetics and toxicodynamics of the fentanyl homologs cyclopropanoyl-1-benzyl-4´-fluoro-4-anilinopiperidine and furanoyl-1-benzyl-4-anilinopiperidine. Arch Toxicol 94:2009–2025. https://doi.org/10.1007/s00204-020-02726-1

176. Lawrence C, Mason T (2012) Zebrafish housing systems: a review of basic operating principles and considerations for design and functionality. ILAR J 53:179–191. https://doi.org/10.1093/ilar.53.2.179

177. Kilkenny C, Browne WJ, Cuthill IC, et al (2010) Improving Bioscience Research Reporting: The ARRIVE Guidelines for Reporting Animal Research. PLoS Biol

8:e1000412. https://doi.org/10.1371/journal.pbio.1000412

178. Benjamini Y, Hochberg Y (1995) Controlling the false discovery rate: a practical and powerful approach to multiple testing. J R Stat Soc Ser B 57:289–300

179. Kassambara A (2020) Rstatix: pipe-friendly framework for basic statistical tests. R Packag version 06 0

180. Signorell A, Aho K, Alfons A, et al (2019) DescTools: Tools for Descriptive Statistics (R package version 0.99. 39)[Computer software]

181. Hayes AJ, Reynolds S, Nowell MA, et al (2013) Spinal deformity in aged zebrafish is accompanied by degenerative changes to their vertebrae that resemble osteoarthritis. PLoS One 8:e75787

182. Li J, Zhang Y, Liu K, et al (2018) Xiaoaiping Induces Developmental Toxicity in Zebrafish Embryos Through Activation of ER Stress, Apoptosis and the Wnt Pathway. Front. Pharmacol. 9:1250

183. Roy NM, Zambrzycka E, Santangelo J (2017) Butyl benzyl phthalate (BBP) induces caudal defects during embryonic development. Environ Toxicol Pharmacol 56:129–135. https://doi.org/10.1016/j.etap.2017.09.009

184. Wu Y, Yang Q, Chen M, et al (2018) Fenbuconazole exposure impacts the development of zebrafish embryos. Ecotoxicol Environ Saf 158:293–299. https://doi.org/10.1016/j.ecoenv.2018.04.048

185. Wu Y, Zuo Z, Chen M, et al (2018) The developmental effects of low-level procymidone towards zebrafish embryos and involved mechanism. Chemosphere 193:928–935. https://doi.org/10.1016/j.chemosphere.2017.11.105

186. Xu H, Liu X, Jia Y, et al (2018) Fipronil-induced toxic effects in zebrafish (Danio rerio) larvae by using digital gene expression profiling. Sci Total Environ 639:550–559. https://doi.org/10.1016/j.scitotenv.2018.05.159

187. Qian L, Liu J, Lin Z, et al (2020) Evaluation of the spinal effects of phthalates in a zebrafish embryo assay. Chemosphere 249:126144.

https://doi.org/10.1016/j.chemosphere.2020.126144

188. Van Gennip JLM, Boswell CW, Ciruna B (2018) Neuroinflammatory signals drive spinal curve formation in zebrafish models of idiopathic scoliosis. Sci Adv 4:eaav1781. https://doi.org/10.1126/sciadv.aav1781

189. Robertson GN, Lindsey BW, Dumbarton TC, et al (2008) The contribution of the swimbladder to buoyancy in the adult zebrafish (Danio rerio): A morphometric analysis. J Morphol 269:666–673. https://doi.org/10.1002/jmor.10610

190. Goolish EM, Okutake K (1999) Lack of gas bladder inflation by the larvae of zebrafish in the absence of an air-water interface. J Fish Biol 55:1054–1063. https://doi.org/10.1111/j.1095-8649.1999.tb00740.x

191. Winata CL, Korzh S, Kondrychyn I, et al (2009) Development of zebrafish swimbladder: The requirement of Hedgehog signaling in specification and organization of the three tissue layers. Dev Biol 331:222–236. https://doi.org/10.1016/j.ydbio.2009.04.035

192. Winata CL, Korzh S, Kondrychyn I, et al (2010) The role of vasculature and blood circulation in zebrafish swimbladder development. BMC Dev Biol 10:3. https://doi.org/10.1186/1471-213X-10-3

193. Kirla KT, Erhart C, Groh KJ, et al (2021) Zebrafish early life stages as alternative model to study ‘designer drugs’: Concordance with mammals in response to opioids. Toxicol Appl Pharmacol 419:115483. https://doi.org/10.1016/j.taap.2021.115483

194. World Health Organization (2020) The top 10 causes of death. https://www.who.int/news-room/fact-sheets/detail/the-top-10-causes-of-death

195. Bakkers J (2011) Zebrafish as a model to study cardiac development and human cardiac disease. Cardiovasc Res 91:279–288. https://doi.org/10.1093/cvr/cvr098

196. Bournele D, Beis D (2016) Zebrafish models of cardiovascular disease. Heart Fail Rev 21:803–813. https://doi.org/10.1007/s10741-016-9579-y

197. Burns CG, Milan DJ, Grande EJ, et al (2005) High-throughput assay for small molecules that modulate zebrafish embryonic heart rate. Nat Chem Biol 1:263–264.

https://doi.org/10.1038/nchembio732

198. Seok S-H, Baek M-W, Lee H-Y, et al (2008) In vivo alternative testing with zebrafish in ecotoxicology. J Vet Sci 9:351. https://doi.org/10.4142/jvs.2008.9.4.351

199. Prasch AL (2003) Aryl Hydrocarbon Receptor 2 Mediates 2,3,7,8-Tetrachlorodibenzo-p-dioxin Developmental Toxicity in Zebrafish. Toxicol Sci 76:138–150. https://doi.org/10.1093/toxsci/kfg202

200. Han Y, Zhang J, Qian J, Hu C (2015) Cardiotoxicity evaluation of anthracyclines in zebrafish (Danio rerio). J Appl Toxicol 35:241–252. https://doi.org/10.1002/jat.3007

201. Pattinson KTS (2008) Opioids and the control of respiration. Br J Anaesth 100:747–758. https://doi.org/10.1093/bja/aen094

202. Wilson C (2012) Aspects of Larval Rearing. ILAR J 53:169–178. https://doi.org/10.1093/ilar.53.2.169

203. Raldúa D, André M, Babin PJ (2008) Clofibrate and gemfibrozil induce an embryonic malabsorption syndrome in zebrafish. Toxicol Appl Pharmacol 228:301–314. https://doi.org/10.1016/j.taap.2007.11.016

204. Sant KE, Timme-Laragy AR (2018) Zebrafish as a Model for Toxicological Perturbation of Yolk and Nutrition in the Early Embryo. Curr Environ Heal reports 5:125–133. https://doi.org/10.1007/s40572-018-0183-2

205. Miyares RL, de Rezende VB, Farber SA (2014) Zebrafish yolk lipid processing: a tractable tool for the study of vertebrate lipid transport and metabolism. Dis Model & Mech 7:915 LP – 927. https://doi.org/10.1242/dmm.015800

206. Marín-Juez R, Rovira M, Crespo D, et al (2015) GLUT2-Mediated Glucose Uptake and Availability Are Required for Embryonic Brain Development in Zebrafish. J Cereb Blood Flow Metab 35:74–85. https://doi.org/10.1038/jcbfm.2014.171

207. Poon KL, Wang X, Ng AS, et al (2017) Humanizing the zebrafish liver shifts drug metabolic profiles and improves pharmacokinetics of CYP3A4 substrates. Arch Toxicol 91:1187–1197. https://doi.org/10.1007/s00204-016-1789-5

208. Goldstone J V, McArthur AG, Kubota A, et al (2010) Identification and developmental expression of the full complement of Cytochrome P450 genes in Zebrafish. BMC Genomics 11:643. https://doi.org/10.1186/1471-2164-11-643

209. Audira G, Siregar P, Strungaru S-A, et al (2020) Which Zebrafish Strains Are More Suitable to Perform Behavioral Studies? A Comprehensive Comparison by Phenomic Approach. Biology (Basel) 9:200. https://doi.org/10.3390/biology9080200

210. Meyer BM, Froehlich JM, Galt NJ, Biga PR (2013) Inbred strains of zebrafish exhibit variation in growth performance and myostatin expression following fasting. Comp Biochem Physiol Part A Mol Integr Physiol 164:1–9. https://doi.org/10.1016/j.cbpa.2012.10.004

211. Bossé GD, Peterson RT (2017) Development of an opioid self-administration assay to study drug seeking in zebrafish. Behav Brain Res 335:158–166. https://doi.org/10.1016/j.bbr.2017.08.001

212. Armenian P, Vo KT, Barr-Walker J, Lynch KL (2018) Fentanyl, fentanyl analogs and novel synthetic opioids: A comprehensive review. Neuropharmacology 134:121–132. https://doi.org/https://doi.org/10.1016/j.neuropharm.2017.10.016

213. Sarah Sanders, Christina Mullins, Samantha Batdorf, Faisal Reza, James Jeffries, Nathan Wood, Laura Hunt KO (2017) 2016 WV Overdose Fatality Analysis: Healthcare Systems Utilization, Risk Factors, and Opportunities for Intervention

214. O'Donnell J, Gladden MR, Goldberger BA, et al (2020) Opioid-Involved Overdose Deaths with Fentanyl or Fentanyl Analogs Detected-28 States and the District of Columbia. Morb Mortal Wkly Rep 69:271–273

215. Carroll FI, Boldt KG, Huang PT, et al (1989) Synthesis of Fentanyl Analogs. Probl Drug Depend 1989 497

216. Aceto MD, Bowman ER, Harris LS, May EL (1987) Dependence studies of new compounds in the rhesus monkey, rat and mouse (1987). Probl Drug Depend 485–542

217. WHO (2019) Critical Review Report: Valerylfentanyl

218. Christine Stevens, Erinn Ton, Michael Markey PJ (2020) Ten Cases of Valeryl Fentanyl in Southwest Michigan

219. Administration DE (2017) NFLIS Brief: Fentanyl and Fentanyl-Related Substances Reported in NFLIS, 2015–2016. Natl Forensic Lab Inf Syst

220. Bade R, Abdelaziz A, Nguyen L, et al (2020) Determination of 21 synthetic cathinones, phenethylamines, amphetamines and opioids in influent wastewater using liquid chromatography coupled to tandem mass spectrometry. Talanta 208:120479. https://doi.org/10.1016/j.talanta.2019.120479

221. Cox J, Mathison K, Ott C, et al (2021) Quantitation and Validation of 34 Fentanyl Analogs from Liver Tissue Using a QuEChERS Extraction and LC–MS-MS Analysis. J Anal Toxicol. https://doi.org/10.1093/jat/bkab009

222. Baumann MH, Kopajtic TA, Madras BK (2018) Pharmacological Research as a Key Component in Mitigating the Opioid Overdose Crisis. Trends Pharmacol Sci 39:995–998. https://doi.org/10.1016/j.tips.2018.09.006

223. Saad M, Matheeussen A, Bijttebier S, et al (2017) In vitro CYP-mediated drug metabolism in the zebrafish (embryo) using human reference compounds. Toxicol Vitr 42:329–336. https://doi.org/10.1016/j.tiv.2017.05.009

224. Teame T, Zhang Z, Ran C, et al (2019) The use of zebrafish (Danio rerio) as biomedical models. Anim Front 9:68–77. https://doi.org/10.1093/af/vfz020

225. Van Wijk RC, Krekels EHJ, Hankemeier T, et al (2017) Systems pharmacology of hepatic metabolism in zebrafish larvae. https://doi.org/10.1016/j.ddmod.2017.04.003

226. Hill AJ, Teraoka H, Heideman W, Peterson RE (2005) Zebrafish as a Model Vertebrate for Investigating Chemical Toxicity. Toxicol Sci 86:6–19. https://doi.org/10.1093/toxsci/kfi110

227. Hei H, Wang J, Zhang W, et al (2020) Study of the in vitro and in vivo metabolism of a novel synthetic cannabinoid PX-2 in human liver microsomes and zebrafish. Int J Mass Spectrom 456:116388. https://doi.org/https://doi.org/10.1016/j.ijms.2020.116388

228. Sardela VF, Anselmo C de S, Nunes IK da C, et al (2018) Zebrafish (<scp> *Danio rerio* </scp>) water tank model for the investigation of drug metabolism: Progress, outlook, and challenges. Drug Test Anal 10:1657–1669. https://doi.org/10.1002/dta.2523

229. Cooman T, Bergeron SA, Coltogirone R, et al (2021) Evaluation of fentanyl toxicity and metabolism using a zebrafish model. J Appl Toxicol. https://doi.org/10.1002/jat.4253

230. Cooman T, Bell S (2019) In vitro metabolism of the synthetic cannabinoids PX-1, PX-2, and PX-3 by high-resolution mass spectrometry and their clearance rates in human liver microsomes. Rapid Commun Mass Spectrom 33:1816–1825. https://doi.org/10.1002/rcm.8543

231. Learmonth C, Carvalho AP (2015) Acute and Chronic Toxicity of Nitrate to Early Life Stages of Zebrafish--Setting Nitrate Safety Levels for Zebrafish Rearing. Zebrafish 12:305–311. https://doi.org/10.1089/zeb.2015.1098

232. Parichy DM, Elizondo MR, Mills MG, et al (2009) Normal table of postembryonic zebrafish development: Staging by externally visible anatomy of the living fish. Dev Dyn 238:2975–3015. https://doi.org/https://doi.org/10.1002/dvdy.22113

233. Underwood W, Anthony R (2013) AVMA guidelines for the euthanasia of animals: 2020 edition. Retrieved on March 30:2001–2020

234. Zhang Y, Bachmeier C, Miller DW (2003) In vitro and in vivo models for assessing drug efflux transporter activity. Adv Drug Deliv Rev 55:31–51

235. Steuer AE, Williner E, Staeheli SN, Kraemer T (2017) Studies on the metabolism of the fentanyl-derived designer drug butyrfentanyl in human in vitro liver preparations and authentic human samples using liquid chromatography-high resolution mass spectrometry (LC-HRMS). Drug Test Anal 9:1085–1092. https://doi.org/10.1002/dta.2111

236. Feasel MG, Wohlfarth A, Nilles JM, et al (2016) Metabolism of Carfentanil, an Ultra-Potent Opioid, in Human Liver Microsomes and Human Hepatocytes by High-Resolution Mass Spectrometry. AAPS J 18:1489–1499. https://doi.org/10.1208/s12248-016-9963-5

237. Di Trana A, Brunetti P, Giorgetti R, et al (2021) In silico prediction, LC-HRMS/MS analysis, and targeted/untargeted data-mining workflow for the profiling of phenylfentanyl

in vitro metabolites. Talanta 235:122740. https://doi.org/10.1016/j.talanta.2021.122740

238. Nordmeier F, Richter LHJ, Schmidt PH, et al (2019) Studies on the in vitro and in vivo metabolism of the synthetic opioids U-51754, U-47931E, and methoxyacetylfentanyl using hyphenated high-resolution mass spectrometry. Sci Rep 9:13774. https://doi.org/10.1038/s41598-019-50196-y

239. Davidson JT, Sasiene ZJ, Jackson GP (2020) The characterization of isobaric product ions of fentanyl using multi-stage mass spectrometry, high-resolution mass spectrometry and isotopic labeling. Drug Test Anal 12:496–503. https://doi.org/10.1002/dta.2758

240. Wichitnithad W, McManus TJ, Callery PS (2010) Identification of isobaric product ions in electrospray ionization mass spectra of fentanyl using multistage mass spectrometry and deuterium labeling. Rapid Commun Mass Spectrom 24:2547–2553. https://doi.org/https://doi.org/10.1002/rcm.4673

241. Thevis M, Geyer H, Bahr D, Schänzer W (2005) Identification of fentanyl, alfentanil, sufentanil, remifentanil and their major metabolites in human urine by liquid chromatography/tandem mass spectrometry for doping control purposes. Eur J Mass Spectrom 11:419–427

242. Valdez CA, Leif RN, Mayer BP (2014) An efficient, optimized synthesis of fentanyl and related analogs. PLoS One 9:e108250

243. Wilde M, Pichini S, Pacifici R, et al (2019) Metabolic Pathways and Potencies of New Fentanyl Analogs. Front Pharmacol 10:238. https://doi.org/10.3389/fphar.2019.00238

244. Kanamori T, Togawa Iwata Y, Segawa H, et al (2018) Metabolism of Fentanyl and Acetylfentanyl in Human-Induced Pluripotent Stem Cell-Derived Hepatocytes. Biol Pharm Bull 41:106–114. https://doi.org/10.1248/bpb.b17-00709

245. Tateishi T, Krivoruk Y, Ueng Y-F, et al (1996) Identification of Human Liver Cytochrome P-450 3A4 as the Enzyme Responsible for Fentanyl and Sufentanil N-Dealkylation. Anesth Analg 82:

Curriculum vitae

Travon Cooman

Education:

- **West Virginia University**, Morgantown, West Virginia, USA
  - **Doctor of Philosophy in Forensic Science** (May 2019 — May 2022)
  - Advisor: Dr. Luis Arroyo
  - Dissertation: Integration of spectroscopic and mass spectrometric tools for the analysis of novel psychoactive substances in forensic and toxicology applications

  - **Master of Science in Forensic and Investigative Science** (August 2017 — May 2019)
  - Advisor: Dr. Suzanne Bell
  - Thesis: *In vitro* metabolism of the synthetic cannabinoids PX-1, PX-2, PX-3 and a comparison of their clearance rates in human liver microsomes

- **Illinois Institute of Technology**, Chicago, Illinois, USA
  - Bachelor of Science in Biochemistry (August 2011 — May 2014)

Scholarships:

- Presidential scholar, Illinois Institute of Technology (August 2011 — May 2014)

Professional Memberships:

- Midwest Association for Toxicology and Therapeutic Drug Monitoring (2022—)
- Caribbean Association of Forensic Sciences (2021— present)
- American Chemical Society (2020 — present)

Publications:

[6] **T. Cooman**, B. Hoover, B. Sauvé, S.A. Bergeron, N. Quinete, P. Gardinali, and L. Arroyo "The metabolism of valeryl fentanyl using human liver microsomes and zebrafish larvae," *Drug Testing and Analysis*, Jan 2022. Doi:10.1002/dta.3233

[5] **T. Cooman**, T. Trejos, A.H. Romero, and L.E. Arroyo "Implementing machine learning for the identification and classification of compound mixtures in portable Raman instruments," *Chemical Physics Letters*, vol.787, Dec 2021. Doi:10.1016/j.cplett.2021.139283

[4] **T. Cooman**, S.A. Bergeron, R. Coltogirone, E. Horstick, and L. Arroyo "Evaluation of fentanyl toxicity and metabolism using a zebrafish model," *Journal of Applied Toxicology*, vol.42, Oct 2021. Doi:10.1002/jat.4253

[3] **T. Cooman**, C.E. Ott, K.A. Dalzell, A. Burns, E. Sisco, and L.E. Arroyo "Screening of seized drugs utilizing portable Raman spectroscopy and direct analysis in real time-mass spectrometry (DART-MS)," *Forensic Chemistry*, vol.25, Aug 2021. Doi:10.1016/j.forc.2021.100352

[2] **T. Cooman**, H. Santos, J. Cox, J.F. Allochio Filho, K.B. Borges, W. Romão, and L.E. Arroyo-Mora "Development, validation and evaluation of a quantitative method for the analysis of twenty-four new psychoactive substances in oral fluid by LC–MS/MS," *Forensic Chemistry*, vol.19, Jun 2020. Doi:10.1016/j.forc.2020.100231

[1] **T. Cooman**, and S. Bell, "*In vitro* metabolism of the synthetic cannabinoids PX–1, PX–2, and PX–3 by high resolution mass spectrometry and their clearance rates in human liver microsomes," *Rapid Communications in Mass Spectrometry*, vol. 33, Issue. 23, pp. 1816–1825, Jul 2019. Doi:10.1002/rcm.8543

Presentations:

[9] **T. Cooman**, B. Hoover, B. Sauvé, S.A. Bergeron, N. Quinete, P. Gardinali, and L. Arroyo. "Zebrafish—an alternative drug metabolism model for valerylfentanyl," Platform presentation at the *Midwest Association for Toxicology and Therapeutic Drug Monitoring (MATT)* Conference, Kalamazoo, Michigan, USA, April 2022.

[8] **T. Cooman**, S.A. Bergeron, R. Coltogirone, E. Horstick, and L. Arroyo. "Evaluation of fentanyl toxicity and metabolism using a zebrafish model," Poster presentation at the *Midwest Association for Toxicology and Therapeutic Drug Monitoring (MATT)* Conference, Kalamazoo, Michigan, USA, April 2022.

[7] Katherine Davis, Collin Kustera, **T. Cooman**, Brianna Sauve, Brianna Hoover, S.A. Bergeron, and L. Arroyo. "Comparison of furanyl fentanyl metabolism in zebrafish and human liver microsomes," Poster presentation at the *Midwest Association for Toxicology and Therapeutic Drug Monitoring (MATT)* Conference, Kalamazoo, Michigan, USA, April 2022.

[6] **T. Cooman**, C.E. Ott, K.A. Dalzell, A. Burns, E. Sisco, L.E. Arroyo. "Seized drugs analysis using a portable Raman instrument and Direct Analysis in Real-Time Mass Spectrometry," Poster presentation at *2022 Current Trends Forensic Symposium- Seized Drugs Analysis*, Online. Jan 2022.

[5] **T. Cooman**, S.A. Bergeron, R. Coltogirone, E. Horstick, L. Arroyo "Zebrafish as a toxicology and metabolism model for opioids," Lecture at *3rd Brazilian Winter School of Forensic Sciences*, Online. Oct 2021.

[4] **T. Cooman**, C.E. Ott, K.A. Dalzell, A. Burns, E. Sisco, L.E. Arroyo. "Portable Raman Spectroscopy and Mass Spectrometry Techniques for the analysis of Seized Drugs: TacticID®and AccuTOF™-DART," Poster presentation in Proceedings of the *Pittsburgh Conference on Analytical Chemistry and Applied Spectroscopy*, Online, Mar 2021.

[3] **T. Cooman**, S. Bergeron, R. Coltogirone, E. Horstick, L. Arroyo "Zebrafish as a model to study toxicity and metabolism of fentanyl," Lecture at *Crossing Forensic Borders Symposium*, Online. Jan 2021.

[2] **T. Cooman,** S. Bell, "Metabolite elucidation of the synthetic cannabinoids: PX-1, PX-2, PX-2 in human liver microsomes," Platform presentation in Proceedings of the *Mid-Atlantic Association of Forensic Scientists (MAAFS)* Conference, Morgantown, West Virginia, USA, May 2019.

[1] **T. Cooman**, S. Bell, "In vitro metabolism of the synthetic cannabinoids: PX-1, PX-2, PX-3 and a comparison of their clearance rates in human liver microsomes.," Platform presentation in Proceedings of the *Midwest Association for Toxicology and Therapeutic Drug Monitoring (MATT)* Conference, Cleveland, Ohio, USA, Apr 2019.